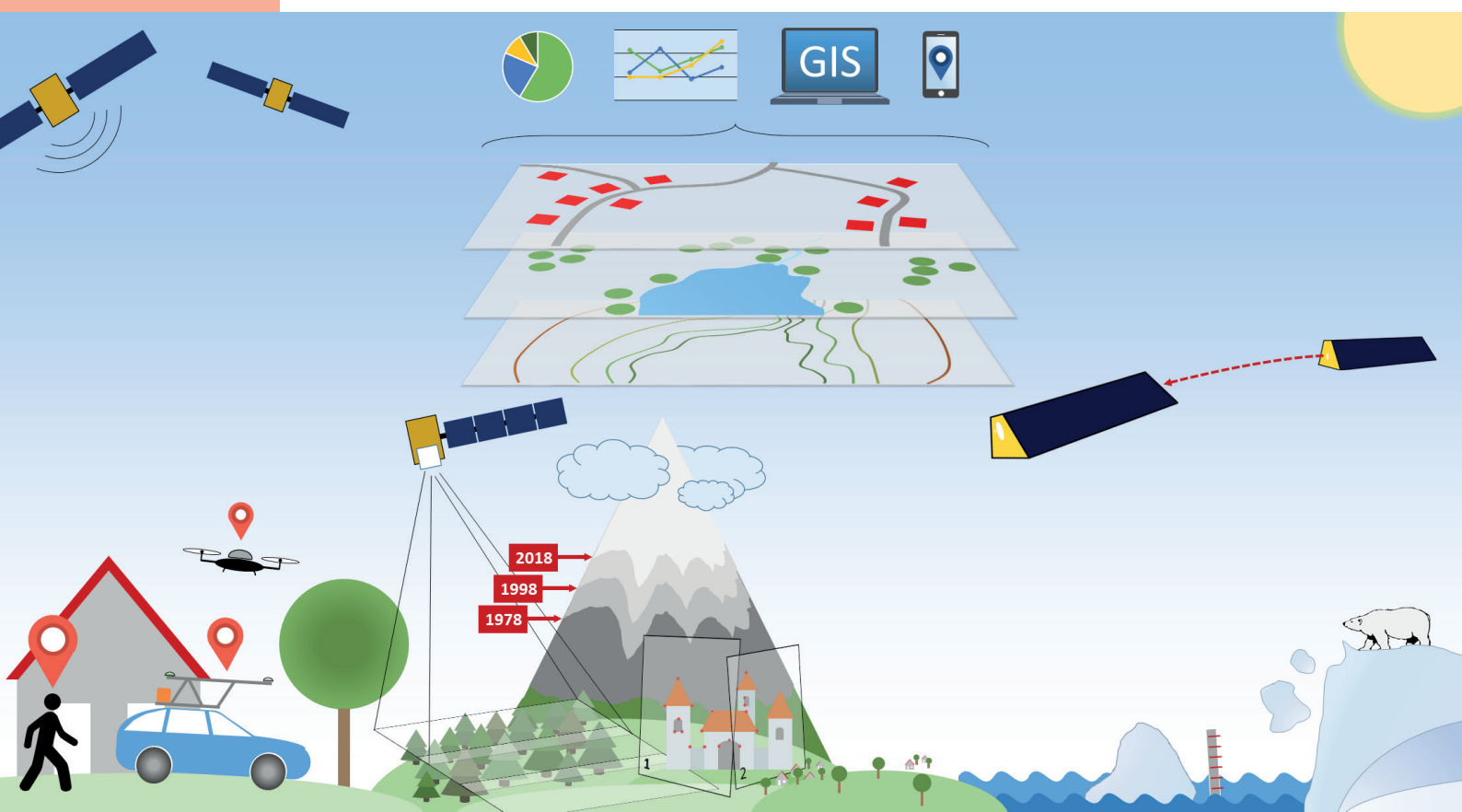Matthias Ellmer

Contributions to GRACE Gravity Field Recovery

Improvements in Dynamic Orbit Integration, Stochastic Modelling of the Antenna Offset Correction, and Co-Estimation of Satellite Orientations

GEOD 1

MONOGRAPHIC SERIES TU GRAZ
GEODESY

Matthias Ellmer

Contributions to GRACE Gravity Field Recovery

Improvements in Dynamic Orbit Integration, Stochastic Modelling of the Antenna Offset Correction, and Co-Estimation of Satellite Orientations

Monographic Series TU Graz

Geodesy

Series Editor

Univ.-Prof. Dr.-Ing. Torsten Mayer-Gürr
Ao.Univ.-Prof. Dipl.-Ing. Dr.techn. Manfred Wieser
Univ.-Prof. Dr.rer.nat. Dipl.-Forstwirt Mathias Schardt
Ass.Prof. Dipl.-Ing. (FH) Dr.techn. Johannes Scholz

Monographic Series TU Graz

Geodesy   **Volume 1**

Matthias Ellmer

Contributions to GRACE Gravity Field Recovery

Improvements in Dynamic Orbit Integration, Stochastic Modelling of the Antenna Offset Correction, and Co-Estimation of Satellite Orientations

Abstract

Time series of global GRACE-derived surface mass variations have become an invaluable data source in the field of Earth system science. Prominent examples of subject areas that have particularly benefited from GRACE data are the study of the continental hydrological cycle, the cryosphere, and the global ocean mass balance. The work presented within this thesis is part of the community-wide effort to improve the quality of global gravity field solutions based on GRACE satellite-to-satellite tracking observations. Specifically, it is part of and builds on the ITSG-Grace2016 series of gravity field solutions.

The research within this thesis is divided into three main subjects: the study of numerical effects in the dynamic orbit integration necessary in computing GRACE gravity fields; the description and rigorous evaluation of the effect of the spacecraft orientation uncertainty on a correction applied to the GRACE inter-satellite ranging observable; and the co-estimation of improved satellite orientations within the least squares adjustment for the gravity field parameters.

Regarding the topic of dynamic orbits, a modified Encke approach is introduced which allows for the integration of dynamic orbits at a numerical resolution that is shown to be sufficient for GRACE-FO processing. To this end, the classical osculating Encke ellipse is replaced with a rigorously optimized reference ellipse parametrised in equinoctial elements. The dynamic orbit integrated based on this algorithm and parametrisation is shown to exhaust machine precision over a large part of the resulting orbits' frequency spectrum.

Complete covariance matrices for the satellite orientation are propagated to the GRACE KBR antenna offset correction. The propagated covariance matrices describe the non-stationary contribution of noise in the satellite orientation observations on the correction applied to the inter-satellite ranging observations. This information is incorporated into the estimation of a complete stochastic model for the inter-satellite ranging observations, which is computed anew for each month of data. The improved stochastic model better describes the noise found in real observations, and can thus contribute in the determination of better gravity field solutions.

The covariance information for the satellite orientation is further used in the co-estimation of improved orientation parameters in the least squares adjustment for the gravity field parameters. Departing from the assumption of error-free and fixed satellite orientations leads to a reduction in temporal variability of the recovered gravity fields over the oceans. This methodology further improves estimates of the KBR antenna phase centre coordinates.

Acknowledgements

Without the help, guidance, encouragement, and support of the people surrounding me this work would not have been possible, and I am deeply thankful to them.

First and foremost my sincere gratitude is directed at my supervisor, Prof. Torsten Mayer-Gürr. I want to thank him for always having an open door and helpful advice, and for allowing me the space to follow my own interests and intuitions in this research. I could not have asked for a better supervisor. I also want to express my thankfulness to my external examiner, Prof. Nico Sneeuw, for his efforts in reviewing this thesis.

Further, I want to express my gratitude to my colleagues at the working group. First and foremost thank you to my office mate Andreas, for always being willing to bounce ideas back and forth, your helpful criticisms, and sharp mind. Thank you Sebastian, for having my back during the final months of writing this thesis. To Bianca, thank you for always guiding me when I was in danger of getting lost in the bureaucracy. To them and all other colleagues present and past: I want to say thank you for an always stimulating, pleasant, and fun working environment, and of course all of the refreshing breaks at the foosball table. I will miss you.

A large thank you is owed to my family. To my parents for instilling scientific curiosity and a sense of adventure in me, for giving me a start in life that allowed me to reach this milestone. To my siblings for always being there when I needed them.

Finally, I want to especially thank the two people most important to me throughout these years in Graz. Thank you Thomas, for all your friendship and support. Thank you Heather, for your sacrifices, for everything.

Thank you.

Ellmer

Contents

List of Figures

List of Tables

Introduction

<div style="text-align: right">1</div>

The Gravity Recovery and Climate Experiment (GRACE) twin satellite mission was a joint NASA and DLR Earth observation mission, directed at detecting mass transport signals in the Earth system at an unprecedented accuracy. The mission was an overwhelming success, collecting data during its operational period spanning from April 2002 until end of science operations in June 2017, much exceeding the initial goal of 5 years of data acquisition.

The successor mission to GRACE, Gravity Recovery and Climate Experiment Follow-On (GRACE-FO), was successfully launched on May 22, 2018, and is expected to continue the time series established by GRACE into the future. Further, GRACE-FO will serve as a technology demonstrator for advanced instrumentation, use of which could be made in possible future satellite gravimetry missions.

This work has a three-fold purpose. First, the stability of the current state-of-the-art orbit integration technique used for GRACE processing is analysed. These results are then compared to the requirements of GRACE-FO and possible future gravity missions. Improvements to the orbit integration algorithm are proposed and implemented, making it suitable for GRACE-FO processing. Second, an attempt is made to introduce a stochastic model of GRACE orientation observations into the gravity field determination, the impact of which is studied in the context of the current GRACE mission. This is done in hope of improving the quality of the existing time series of GRACE gravity field solutions. Third, the newly introduced stochastic information is exploited in the co-estimation of satellite orientations and gravity field parameters in a total least squares adjustment. All of this is achieved within the context of the gravity field processing strategy employed at IfG, which is the Institute of Geodesy at Graz University of Technology, where the ITSG-Grace2016 series of gravity field solutions was computed.

Chapters 2 to 6 give background on some of the relevant concepts, terminology, and algorithms. This is then followed by the three chapters 7 to 9 which detail the author's contributions to the aforementioned fields of orbit integration, stochastic modelling, and parameter estimation in the context of GRACE. The individual chapters are as follows:

Chapter 2 gives information on the employed notation, basic concepts such as the least squares adjustment, variance propagation, parameter elimination, variance component estimation, and specific interpolation techniques used in later chapters. This chapter is held general in nature, and its contents should be mostly familiar to readers with a background in satellite gravimetry.

Chapter 3 outlines the fundamentals of gravity signals in the Earth system and how they relate to the goals of GRACE. Some of the most fundamental disturbing factors for GRACE observations are presented, followed by a short introduction on the representation of gravitational potentials and their analysis.

Chapter 4 mainly serves to give comprehensive background on the GRACE satellites, their construction, and instrumentation. Some of the most relevant reference frames are introduced, and the reader is referred to the authoritative sources for complete information on the satellites. Special consideration is made to give a thorough introduction to the observation geometry of the GRACE constellation, as this specific aspect of the mission is of primary importance to later parts of this thesis.

Chapter 5 gives details on the technique of dynamic orbit integration through variational equations, with a specific focus on their implementation at IfG. The variational equations form the basis of both the ITSG-Grace2016 and the ITSG-Grace2018 series of gravity field solutions.

Chapter 6 aims to give a detailed description of the state of the art of gravity field processing at IfG, specifically the ITSG-Grace2016 time series of gravity fields. This series can be considered the basis of this thesis, although the contents of chapter 7 were already included in the final ITSG-Grace2016 processing chain. The functional model for all GRACE-based observables is derived, followed by a detailed description of the process used to estimate realistic stochastic models for GRACE observations, which is a feature unique to the ITSG-Grace series of gravity field solutions. Finally, the use of these stochastic models to determine a full monthly gravity field is outlined.

The focus of chapter 7 is the improvement of the dynamic orbit integration based on variational equations, as outlined in chapter 5. First, a criteria is developed to quantify the quality of a dynamic orbit solution based on its convergence behaviour. This is followed by a description of the proposed improved algorithm, the heart of which is a generalization of the well-known orbit integration technique due to Encke. This approach is extended through rigorous optimization of the initial satellite state used for orbit integration. The improvements in dynamic orbit quality due to this new algorithm are analysed using the example of GRACE, and some observations are made on the applicability of the algorithm to GRACE-FO and other satellite missions.

Chapter 8 gives a thorough analysis of the effects of uncertainty in the satellite orientation on the GRACE observables. This is followed by the development of a stochastic model for these effects, based on existing full covariance information on the satellite orientation as derived in chapter 6, and its application to the processing chain of ITSG-Grace2016. The impact on the estimated stochastic model as well as a time series of post-fit residuals is analysed, and the observed changes and improvements are discussed.

Chapter 9 uses the orientation uncertainty information and updated stochastic model derived in chapter 8 to co-estimate improved satellite orientations together with the primary goal, the Stokes coefficients describing the monthly gravity fields. This estimation is prefaced by a comparison of two different formalisms used to consider

uncertainty in independent variables in a least squares adjustment. The application of these formalisms to GRACE is described, followed by a detailed analysis of the results both in terms of estimated satellite orientations and in terms of estimated gravity field solutions.

Chapter 10 marks the end of the main body, summarizing the findings and giving an outlook on possible future avenues for research in this area.

Mathematical Theory and Notation

<div style="text-align: right">2</div>

This chapter will give a short overview of the most important mathematical concepts used throughout this thesis. It is written under the assumption that the reader is familiar with the basic concepts of linear algebra and adjustment theory. A review of the foundations of the employed concepts will serve as a setting to define the nomenclature and notation used in the remaining document.

2.1 Variables and Derivatives

Scalars are set in regular type as in "x", while vectors are set in bold type as in "$\boldsymbol{x}$". Matrices are set in bold type as well, but denoted by capital letters like "$\boldsymbol{X}$". For derivatives of non-scaler operands, the numerator notation is chosen. In this notation, the derivative of a scalar y with respect to a vector

$$\boldsymbol{x} = \begin{bmatrix} x_0 & x_1 & \ldots & x_n \end{bmatrix}^{\mathsf{T}} \tag{2.1.1}$$

is written as

$$\frac{\partial y}{\partial \boldsymbol{x}} = \begin{bmatrix} \dfrac{\partial y}{\partial x_0} & \dfrac{\partial y}{\partial x_1} & \ldots & \dfrac{\partial y}{\partial x_n} \end{bmatrix} . \tag{2.1.2}$$

The derivative of $\boldsymbol{x}$ with regard to another vector

$$\boldsymbol{y} = \begin{bmatrix} y_0 & y_1 & \ldots & y_m \end{bmatrix}^{\mathsf{T}} \tag{2.1.3}$$

is

$$\frac{\partial \boldsymbol{x}}{\partial \boldsymbol{y}} = \begin{bmatrix} \dfrac{\partial x_0}{\partial y_0} & \dfrac{\partial x_0}{\partial y_1} & \ldots & \dfrac{\partial x_0}{\partial y_m} \\[2ex] \dfrac{\partial x_1}{\partial y_0} & \dfrac{\partial x_1}{\partial y_1} & \ldots & \dfrac{\partial x_1}{\partial y_m} \\[2ex] \vdots & \vdots & \ddots & \vdots \\[2ex] \dfrac{\partial x_n}{\partial y_0} & \dfrac{\partial x_n}{\partial y_1} & \ldots & \dfrac{\partial x_n}{\partial y_m} \end{bmatrix}_{n+1 \times m+1} . \tag{2.1.4}$$

For vector by matrix derivatives, the *vec()*-operator is used, which stacks the columns of a matrix. For a $k+1 \times l+1$ matrix

$$M = \begin{bmatrix} m_{00} & m_{01} & \cdots & m_{0l} \\ m_{10} & m_{11} & \cdots & m_{1l} \\ \vdots & \vdots & \ddots & \vdots \\ m_{k0} & m_{k1} & \cdots & m_{kl} \end{bmatrix}_{k+1 \times l+1} \tag{2.1.5}$$

this is

$$\mathrm{vec}\,(M) = \begin{bmatrix} m_{00} \ldots m_{k0} & m_{01} \ldots m_{k1} & \cdots & m_{0l} \ldots m_{kl} \end{bmatrix}^{\mathsf{T}} . \tag{2.1.6}$$

The vector by matrix derivative is then, equivalently to eq. (2.1.4), written as

$$\frac{\partial x}{\partial \,\mathrm{vec}\,(M)} = \begin{bmatrix} \dfrac{\partial x_0}{\partial m_{00}} & \dfrac{\partial x_0}{\partial m_{10}} & \cdots & \dfrac{\partial x_0}{\partial m_{kl}} \\ \dfrac{\partial x_1}{\partial m_{00}} & \dfrac{\partial x_1}{\partial m_{10}} & \cdots & \dfrac{\partial x_1}{\partial m_{kl}} \\ \vdots & \vdots & \ddots & \vdots \\ \dfrac{\partial x_n}{\partial m_{00}} & \dfrac{\partial x_n}{\partial m_{10}} & \cdots & \dfrac{\partial x_n}{\partial m_{kl}} \end{bmatrix}_{n+1 \times (k+1)\cdot(l+1)} . \tag{2.1.7}$$

For differentiation of matrices by scalars, such as the often occurring time derivatives, Lagrange's notation using parentheses may be used for brevity, such that

$$\frac{\partial^n M}{\partial t^n} = M^{(m)} \tag{2.1.8}$$

is the *m*-th derivative and

$$\int M \,\partial t^n = M^{(-m)} \tag{2.1.9}$$

is the *m*-th antiderivative.

For a time series of scaler or matrix values a variable with an explicit time point given, such as $x(t)$, shall refer to that single epoch. The variable given without a specific time shall refer to the complete time series

$$x = \begin{bmatrix} x(t_0)^{\mathsf{T}} & x(t_1)^{\mathsf{T}} & \cdots & x(t_n)^{\mathsf{T}} \end{bmatrix}^{\mathsf{T}} . \tag{2.1.10}$$

2.2 Least Squares Adjustment

The fundamental concept in this thesis is the least squares adjustment (LSA), an algorithm to determine the values of some set of *parameters x* that "best" fit some

other set of *observations l*. The parameters are connected to the observations through a functional model $l = f(x)$. Exhaustive descriptions of this algorithm can for example be found in Koch (1997) and Niemeier (2008).

The algorithm prescribes the computation of a *design matrix*, denoted A, as the Jacobian of the observations with regard to the parameters

$$A = \left. \frac{\partial f(x)}{\partial x} \right|_{x_0} \tag{2.2.1}$$

at some initial value for the parameters x_0. With this linearisation, an equation system

$$\Delta l = A \Delta x + e \tag{2.2.2}$$

is set up, where e is the vector of *residuals*, the misfit of the observations with the prediction made by the model, and $\Delta l = l - f(x_0)$ the *reduced observations*. Given a matrix of observation weights P, the least squares solution of eq. (2.2.2) is

$$\Delta \hat{x} = \left(A^\mathsf{T} P A \right)^{-1} A^\mathsf{T} P \Delta l . \tag{2.2.3}$$

The *adjusted* vector of parameters $\Delta \hat{x}$ is that solution to eq. (2.2.2) that minimizes the weighted square sum of residuals $e^\mathsf{T} P e$. The desired parameters are then $\hat{x} = x_0 + \Delta \hat{x}$. This process of linearisation and adjustment must be iterated until the additions to the parameters $\Delta \hat{x}$ are small, signalling convergence. In case the functional relationship $f(x)$ between observations and parameters is linear, no differences have to be formed and the adjusted parameters can directly be computed as

$$\hat{x} = \left(A^\mathsf{T} P A \right)^{-1} A^\mathsf{T} P l . \tag{2.2.4}$$

The *estimated residuals* of the observations are

$$\hat{e} = l - A \hat{x} . \tag{2.2.5}$$

The weight matrix P is the inverse of the *covariance matrix of the observations* Σ_{ll}:

$$P = \Sigma_{ll}^{-1} \tag{2.2.6}$$

Equation (2.2.4) can be written as

$$N \hat{x} = n \tag{2.2.7}$$

with the *normal equation* of the system

$$N = A^\mathsf{T} P A \tag{2.2.8}$$

and the *right hand side*

$$n = A^\mathsf{T} P l . \tag{2.2.9}$$

Multiple observation groups l_k for the same set of parameters x can be combined at the normal equation level by summation

$$N = \sum_{k=0}^{n} N_k \qquad\qquad n = \sum_{k=0}^{n} n_k \, . \qquad (2.2.10)$$

The *estimated covariance matrix of the adjusted parameters* is the inverse of the normal equation

$$\hat{\Sigma}_{\hat{x}\hat{x}} = N^{-1} \, . \qquad (2.2.11)$$

2.3 Decorrelation

For many problems, the stochastic model for the observations is given or estimated as a covariance matrix Σ_{ll}, and not as the weight matrix P needed to compute eq. (2.2.4). As direct inversion of Σ_{ll} is expensive and, depending on the covariance structure, can be numerically unstable (Björck, 1996), it is desirable to avoid this operation. If the given covariance matrix is positive definite, the Cholesky decomposition

$$\Sigma_{ll} = W^\mathsf{T} W \, , \qquad (2.3.1)$$

exists, with W an upper triangular matrix. With

$$P = \left(W^\mathsf{T} W \right)^{-1} = W^{-1} W^{-\mathsf{T}} \qquad (2.3.2)$$

eq. (2.2.4) is

$$\hat{x} = \left(A^\mathsf{T} W^{-1} W^{-\mathsf{T}} A \right)^{-1} A^\mathsf{T} W^{-1} W^{-\mathsf{T}} l \, . \qquad (2.3.3)$$

With the transformation

$$\bar{A} = W^{-\mathsf{T}} A \, , \qquad\qquad \bar{l} = W^{-\mathsf{T}} l \qquad (2.3.4)$$

this is

$$\hat{x} = \left(\bar{A}^\mathsf{T} \bar{A} \right)^{-1} \bar{A}^\mathsf{T} \bar{l} \, . \qquad (2.3.5)$$

Due to the upper triangular shape of W, the *decorrelated observations* $\bar{l}$ and the *decorrelated observation equations* $\bar{A}$ can be computed without knowing the inverse W^{-1} by solving the system

$$W^\mathsf{T} \bar{x} = x \qquad (2.3.6)$$

through back-substitution. The normal equation and the right hand side are computed from the decorrelated matrices as

$$N = \bar{A}^\mathsf{T} \bar{A} \, , \qquad\qquad n = \bar{A}^\mathsf{T} \bar{l} \, . \qquad (2.3.7)$$

2.4 Parameter Elimination

Given a normal equation system $N\hat{x} = n$ where only some of the parameters $\hat{x}_1$ are of interest and the remaining parameters $\hat{x}_2$ are only necessary for proper modelling of the system, these non-target parameters can be *eliminated* from the system. Let the normal equation system be partitioned as

$$\begin{bmatrix} N_{11} & N_{12} \\ N_{12}^{\mathsf{T}} & N_{22} \end{bmatrix} \begin{bmatrix} \hat{x}_1 \\ \hat{x}_2 \end{bmatrix} = \begin{bmatrix} n_1 \\ n_2 \end{bmatrix} . \tag{2.4.1}$$

Solving the second matrix equation of eq. (2.4.1) for $\hat{x}_2$ gives

$$\hat{x}_2 = N_{22}^{-1} \left(n_2 - N_{12}^{\mathsf{T}} \hat{x}_1 \right) , \tag{2.4.2}$$

assuming that N_{22} is invertible. Equation (2.4.2) can then be inserted into the first equation of eq. (2.4.1), giving

$$\begin{aligned} N_{11}\hat{x}_1 + \quad N_{12} \left(N_{22}^{-1} \left(n_2 - N_{12}^{\mathsf{T}} \hat{x}_1 \right) \right) &= n_1 \\ N_{11}\hat{x}_1 + N_{12}N_{22}^{-1}n_2 - N_{12}N_{22}^{-1}N_{12}^{\mathsf{T}}\hat{x}_1 &= n_1 \\ \left(N_{11} - N_{12}N_{22}^{-1}N_{12}^{\mathsf{T}} \right) \hat{x}_1 &= n_1 - N_{12}N_{22}^{-1}n_2 . \end{aligned} \tag{2.4.3}$$

More compactly, this is $N'\hat{x}_1 = n'$, with

$$N' = N_{11} - N_{12}N_{22}^{-1}N_{12}^{\mathsf{T}} \qquad \text{and} \qquad n' = n_1 - N_{12}N_{22}^{-1}n_2 . \tag{2.4.4}$$

The system eq. (2.4.4) gives the same solution for $\hat{x}_1$ as eq. (2.4.1). Solving for $\hat{x}_1$ in this manner can be advantageous, depending on the structure and size of the initial normal equation system.

2.5 Variance Propagation

Given a functional relationship between some dependent variables y and a set of parameters x with given covariance Σ_{xx}, the covariance matrix of the dependent variables is (e.g. Niemeier, 2008)

$$\Sigma_{yy} = B\Sigma_{xx}B^{\mathsf{T}} \tag{2.5.1}$$

with

$$B = \frac{\partial y}{\partial x} . \tag{2.5.2}$$

2.6 Variance Component Estimation

A problem often encountered when solving for a set of parameters is that the covariance of the observations $\mathbf{\Sigma}_{ll}$ is not exactly known. Similarly, when combining several observation groups at the normal equation level, the relative weight of the observations must be known to compute the optimal solution $\hat{x}$. One approach to determine these unknown weights and correlations is to treat them as unknown parameters in the adjustment problem and co-estimate the weights in an iterative procedure. This is known as variance component estimation (VCE). The outline in this section follows the reasoning given in Niemeier (2008).

The fundamental extension to eq. (2.2.2) is that the single vector of residuals is split into multiple vectors of residuals e_i:

$$l = Ax + e_0 + e_1 + \cdots + e_n. \tag{2.6.1}$$

Each of these residual vectors shall have its own covariance matrix $\mathbf{\Sigma}_i$, each a constituent of the complete covariance of the observations

$$\mathbf{\Sigma}_{ll} = \sum_{i=0}^{n} \mathbf{\Sigma}_i \,. \tag{2.6.2}$$

The structure of $\mathbf{\Sigma}_i$ is given by a known *cofactor matrix* $\mathbf{Q}$, which is then scaled by an unknown *variance factor* σ_i^2. Equation (2.6.2) is then

$$\mathbf{\Sigma}_{ll} = \sum_{i=0}^{n} \sigma_i^2 \mathbf{Q}_i \,. \tag{2.6.3}$$

Using this scheme, an arbitrary covariance matrix $\mathbf{\Sigma}_{ll}$ can be formed by choosing the right cofactor matrices and scaling them appropriately. Given an initial guess for the variance factors the optimal values are determined iteratively by introducing weights $\alpha_i^2 = 1$, writing

$$\mathbf{\Sigma}_{ll} = \sum_{i=0}^{n} \alpha_i^2 \left(\sigma_i^2 \mathbf{Q}_i \right) \,. \tag{2.6.4}$$

After computing the least squares solution of eq. (2.6.1) using this initial covariance matrix, the estimated weights are

$$\hat{\alpha}_i^2 = \frac{\Omega}{s} \,, \tag{2.6.5}$$

with

$$\Omega = \hat{e}^\mathsf{T} \mathbf{\Sigma}_{ll}^{-\mathsf{T}} \mathbf{\Sigma}_i \mathbf{\Sigma}_{ll}^{-1} \hat{e} \tag{2.6.6}$$

and

$$s = \text{trace} \left(\mathbf{R} \mathbf{\Sigma}_i \right) \,, \tag{2.6.7}$$

where R is a symmetric matrix

$$R = \Sigma_{ll}^{-1} - \Sigma_{ll}^{-1} A N^{-1} A^{\mathsf{T}} \Sigma_{ll}^{-\mathsf{T}} . \tag{2.6.8}$$

The estimated variance factors of this iteration

$$\hat{\sigma}_i^2 = \hat{\alpha}_i^2 \sigma_i^2 \tag{2.6.9}$$

are used as the initial value σ_i^2 for the next iteration. When the α_i^2 converge to 1, the σ_i^2 are the desired variance factors for the cofactor matrices Q_i. Iteration is needed due to a simplifying assumption in eq. (2.6.5) that the individual σ_i^2 can be estimated independently. It can be shown that after convergence, the computed σ_i^2 are identical to those resulting from a strict solution (Förstner, 1979).

The algorithm of variance component estimation can also be employed to determine the optimal respective weights of several uncorrelated observation groups l_k of n_k observations each:

$$\begin{bmatrix} l_0 \\ \vdots \\ l_m \end{bmatrix} = \begin{bmatrix} A_0 \\ \vdots \\ A_m \end{bmatrix} x + \begin{bmatrix} e_0 \\ \vdots \\ e_m \end{bmatrix} \tag{2.6.10}$$

Here, each observation group has a cofactor matrix Q_k with an unknown variance factor σ_k^2. The full covariance matrix of all observations is

$$\Sigma_{ll} = \begin{bmatrix} \sigma_0^2 Q_0 & 0 & \cdots & 0 \\ 0 & \ddots & \ddots & \vdots \\ \vdots & \ddots & \ddots & 0 \\ 0 & \cdots & 0 & \sigma_m^2 Q_m \end{bmatrix} . \tag{2.6.11}$$

As the observation groups are assumed to be uncorrelated, all variables pertaining to the other observation groups disappear when inserting into eq. (2.6.5), except for the combined normal equation N:

$$\hat{\alpha}_k^2 = \frac{\hat{e}_k^{\mathsf{T}} \Sigma_k^{-1} \hat{e}_k}{n_k - \mathrm{trace}\left(N_k N^{-1}\right)} \tag{2.6.12}$$

Then, the estimated variance factor for the observation group is

$$\hat{\sigma}_k^2 = \hat{\alpha}_k^2 \sigma_k^2 . \tag{2.6.13}$$

2.7 Interpolation, Numerical Integration, and Numerical Differentiation

Techniques for numerical differentiation, integration, and interpolation of discrete time series of data find many applications in the computation of GRACE gravity field

solutions. Here, a formalism for these operations based on polynomial interpolation is introduced. The derivations in this section follow those given by Mayer-Gürr (2006). Let there be a series of $n + 1$ values $x(t_0) \ldots x(t_n)$ with constant temporal sampling Δt. The coefficients of an n-th degree polynomial

$$x(\tau) = \sum_{k=0}^{n} a_k \tau^k \tag{2.7.1}$$

defined by these supports can be computed by solving the system

$$\underbrace{\begin{bmatrix} x(t_0 + \tau_0) \\ \vdots \\ x(t_0 + \tau_n) \end{bmatrix}}_{\boldsymbol{x}} = \underbrace{\begin{bmatrix} \tau_0^0 & \tau_0^1 & \cdots & \tau_0^n \\ \vdots & \vdots & \ddots & \vdots \\ \tau_n^0 & \tau_n^1 & \cdots & \tau_n^n \end{bmatrix}}_{\boldsymbol{A}} \underbrace{\begin{bmatrix} a_0 \\ \vdots \\ a_n \end{bmatrix}}_{\boldsymbol{a}}, \tag{2.7.2}$$

for the vector $\boldsymbol{a}$, with $\tau_j = j \cdot \Delta t$. This polynomial can then be evaluated at any time τ by inserting into eq. (2.7.1). A longer time series of $k > n + 1$ values can be interpolated by a low degree polynomial applied to a moving segment of the time series, as illustrated in fig. 2.1.
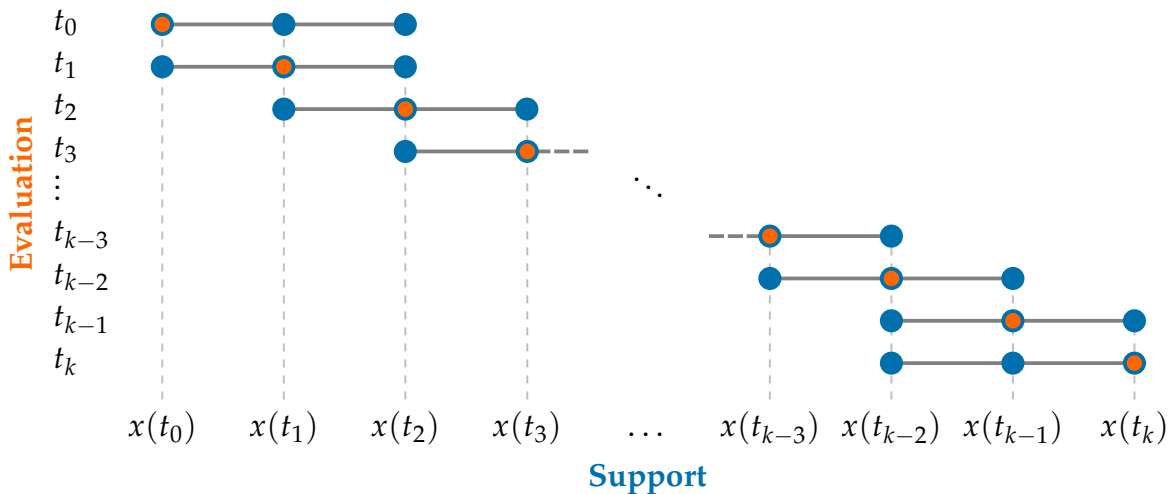
Figure 2.1: Evaluation of an interpolation polynomial of degree $n = 2$. Each polynomial is defined by three supports, and is evaluated at the times marked.

The time series can be smoothed by computing a polynomial of degree $d < n$ from $n + 1$ supports in a least squares adjustment.

The entries of the matrix $\boldsymbol{A}$ are constant, so it is possible to precompute the weights used for interpolation once for a specific combination of polynomial degree and sampling. For the not overdetermined case, the solution to eq. (2.7.2) is

$$\boldsymbol{a} = \boldsymbol{W}\boldsymbol{x}, \tag{2.7.3}$$

with $W = A^{-1}$. Inserting eq. (2.7.3) into eq. (2.7.2), the evaluation of the interpolation polynomial at a specific time t can be written as a vector-matrix-vector product

$$x(\tau) = \boldsymbol{\tau} W \boldsymbol{x} \tag{2.7.4}$$

with $\boldsymbol{\tau} = \begin{bmatrix} \tau^0 \dots \tau^n \end{bmatrix}$ and $\tau = t - t_0$. This has the important property that for a constant value τ, meaning always evaluating the interpolation polynomial at the same fraction of its length, e.g. always at the centre support, the $n+1$ *weights*

$$\overline{\boldsymbol{w}} = \boldsymbol{\tau} W \tag{2.7.5}$$

are constant and only have to be computed once. This is an expression which can be differentiated and integrated analytically. An arbitrary derivative or integral for a time series can be computed using these interpolation polynomials. The m-th time derivative of eq. (2.7.4) is

$$\frac{\partial^m x(\tau)}{\partial \tau^m} = \overline{\boldsymbol{w}}^{(m)} \boldsymbol{x} = \boldsymbol{\tau}^{(m)} W \boldsymbol{x} \ . \tag{2.7.6}$$

The m-th integral is equivalently

$$\int x(\tau) \, \partial \tau^m = \overline{\boldsymbol{w}}^{(-m)} \boldsymbol{x} = \boldsymbol{\tau}^{(-m)} W \boldsymbol{x} \ , \tag{2.7.7}$$

plus some integration constants. Both differentiation and integration can thus be written as a linear operator on a time series $\boldsymbol{x}$ of arbitrary length k, by populating a matrix of dimensions $k \times k$ with the appropriate entries of the respective weight matrices. This would yield a matrix structure similar to what is illustrated in fig. 2.1.

Gravity and Other Signals 3

The GRACE satellites orbit Earth under the influence of a complex interplay of conservative and non-conservative forces.

The most important force, gravity, originates from many overlapping sources, only some of which are of interest when processing data from GRACE. The following sections give an overview of the acting forces and their origins. They are broadly categorized into conservative forces due to direct gravitational fields (section 3.1) and tidal effects (section 3.2), and non-conservative forces (section 3.3).

3.1 Earth's Mean and Time-Variable Gravitational Potential

Earth's gravitational field is determined through the distribution of mass in Earth's volume and immediate vicinity. At time scales for which global gravity observations are available most of Earth's core and mantle mass can be considered static. Current space geodetic methods have neither the spatial nor temporal resolution to resolve the signal that results from its motion. A notable exception is the effect of glacial isostatic adjustment described below. Along the same lines, horizontal crustal motion along Earth's surface is similarly too small to be resolved. Together with the mean state of the remaining non-static masses on Earth, all features with minimum sampling periods longer than the time span covered by the available data are lumped together as Earth's *mean* gravitational field.

Complementary to Earth's mean gravitational field there exists Earth's *time-variable* gravitational field, which encompasses all signals that can be resolved with the current observational record. The time-variable field is described by the superposition of signals at increasingly shorter time spans. At the longer end of this spectrum is the trend, which describes constant-rate change in the gravitational field. Superimposed on the trend are the annual and semi-annual cycle, covering major portions of the inter-annual variability of the gravitational field. All signals at shorter wave lengths make up the *gravity variations*. These are the target signals for GRACE monthly and sub-monthly solutions. Signals at wavelengths shorter than the GRACE minimum sampling period alias into the monthly and sub-monthly solutions. These signals should be reduced by other observations or models as much as possible.

The following paragraphs give an overview of the constituents of the time-variable gravitational field. A more detailed description is given by e.g. Dobslaw et al. (2014).

Atmospheric mass flux The atmospheric mass distribution is changed through winds at a very high frequency in a complex pattern.

Oceanic mass flux Oceanic mass is redistributed by changing currents at a high frequency. Further, the net mass of the ocean can be changed by run-off of continental water and evaporation.

Continental water cycle Net mass is added to the continental mass balance through precipitation and can be lost through run-off, evaporation, or transpiration. Mass is stored and transported in surface water bodies, groundwater systems, and aquifers.

Cryosphere The cryosphere acts mainly as a mass store, with mass flux occurring at longer time scales than in the remaining continental water cycle. Mass is added to the cryosphere through precipitation and freezing, and lost through evaporation and melting with subsequent run-off. The major constituents of the cryosphere are the Antarctic ice caps, continental glaciers, and the Arctic permafrost.

Solid Earth Motion The detectable fractions of solid Earth mass flux are mainly due to seismic and post-seismic activity. Other fluxes in the solid Earth like tidal deformation and glacial isostatic adjustment are described separately.

Glacial Isostatic Adjustment Due to isostatic adjustment, mantle material was displaced from below glaciated land surfaces in the past. After ice masses melt, the crust elastically rebounds towards its initial configuration. Further, the viscous mantle material slowly flows back to the areas it was previously displaced from. Glacial isostatic adjustment (GIA) describes the combination of these two effects.

3.2 Tides and Tidal Effects

In addition to gravitational signals due to processes internal to the Earth system, other solar system bodies induce forces acting on the GRACE satellites through direct and indirect tidal effects. The individual effects are described in more detail in the *IERS Conventions (2010)* (Petit and Luzum, 2010).

Direct tides The gravitational field of other bodies, primarily the Sun and the Moon, induce a tidal potential which directly influences the GRACE satellites. This potential varies with time due to the change in the relative positions of the involved bodies.

Solid Earth tides The direct tidal potential leads to a deformation of the solid Earth body, the resulting mass redistribution leads to a secondary tidal effect, the solid Earth tides.

Ocean tides Similarly, the changing direct tidal potential induces a mass flux in the oceans, with a corresponding gravitational effect from the redistributed masses.

Atmospheric tides Equivalently to the ocean tides, atmospheric masses also move in response to direct tides, with a corresponding gravitational effect.

Pole tides Polar motion, the motion of Earth's rotational axis with respect to its solid body, induces centrifugal forces acting on the solid Earth. These forces in turn

effect mass flux in the solid Earth. The pole tides are the disturbing potential generated due to this mass flux.

Ocean Pole tides Similarly, polar motion indirectly induces mass fluxes in the ocean basins through centrifugal accelerations. These mass redistributions then generate a disturbing potential, the ocean pole tides.

A secondary effect of tidally-induced mass fluxes is *loading*, the displacement of mantle material due to additional weight above the affected area. Where the additional masses first increase the gravitational attraction of the area, the mass loss due to loading reduces the net excess of mass, mitigating the initial effect. Further, *self-attraction* of the additional and displaced masses contribute to the equilibrium state of the system. Due to the constant change in tides and tidally generated effects, such an equilibrium is never reached.

3.3 Non-Conservative Forces

In addition to the various conservative forces due to the effects described above, some non-conservative forces act directly on the GRACE satellites.

Solar radiation pressure When solar radiation interacts with satellite surfaces, momentum is imparted on the satellite. This momentum depends on the area and orientation of the exposed satellite surfaces, as well as the absorption rate of the radiation and the reflectivity of the material.

Earth albedo Similar to solar radiation pressure, radiation reflected by and emitted from Earth's surface also imparts momentum on the satellite.

Atmospheric drag At the altitude of GRACE, the remnant atmosphere slows the satellites through friction. The density of the remnant atmosphere is strongly influenced by solar activity. Atmospheric drag is the most important contributor to the orbital decay of the satellites (Frommknecht, 2008).

3.4 Representation of the Gravitational Potential

Earth's exterior gravitational potential can be described through a series expansion of spherical harmonics coefficients. These are the *Stokes coefficients* c_{nm} and s_{nm} of degree n and order m. The potential is (see e.g. Hofmann-Wellenhof and Moritz, 2005)

$$V(r, \lambda, \theta) = \frac{GM}{R} \sum_{n=0}^{\infty} \left(\frac{R}{r} \right)^{n+1} \sum_{m=0}^{n} [c_{nm} C_{nm}(\lambda, \theta) + s_{nm} S_{nm}(\lambda, \theta)] \qquad (3.4.1)$$

In practice, the expansion is terminated at some finite upper degree N. In eq. (3.4.1), $C_{nm}(\lambda, \theta)$ and $S_{nm}(\lambda, \theta)$ are functionals of the fully normalized Legendre polynomials $\bar{P}_{nm}(\cos\theta)$

$$C_{nm}(\lambda, \theta) = \cos(m\lambda)\,\bar{P}_{nm}(\cos\theta) \tag{3.4.2}$$
$$S_{nm}(\lambda, \theta) = \sin(m\lambda)\,\bar{P}_{nm}(\cos\theta)\;. \tag{3.4.3}$$

The *gravitational attraction* $\boldsymbol{g}$ due to Earth's gravitational potential V is

$$\boldsymbol{g}(r, \lambda, \theta) = \nabla V(r, \lambda, \theta) = \left[\frac{\partial V}{\partial x} \quad \frac{\partial V}{\partial y} \quad \frac{\partial V}{\partial z}\right]^{\mathsf{T}}. \tag{3.4.4}$$

See e.g. Mayer-Gürr (2006) for a compact description of the derivatives in eq. (3.4.4). The gravitational potential is superimposed by other potential fields, the *disturbing potentials T*, some of them due to the effects described in sections 3.1 and 3.2. The largest disturbing potential on Earth is the centrifugal potential Z caused by Earth's rotation. The total potential is then the sum of all contributing potentials, e.g.

$$U = V + \sum_i T_i \tag{3.4.5}$$

3.4.1 Level Surfaces

A gravitational field can be described not only by Stokes coefficients, but also by sets of level surfaces, where

$$U(r, \theta, \lambda) = \text{constant}\;. \tag{3.4.6}$$

One such equipotential surface is the *geoid W*, defined as the equilibrium surface described by the world's oceans if they were at rest and continued through the continents. Specifically, the geoid is the constant level surface described by the above criteria in the potential due to the superposition of Earth's static and centrifugal potential

$$W(r, \theta, \lambda) = V(r, \theta, \lambda) + Z(r, \theta, \lambda) = \text{constant.} \tag{3.4.7}$$

The geoid can be described in the form of *geoid heights*, the height of the geoid level surface with regard to some reference surface, such as the GRS80 reference ellipsoid. The time variability in gravity fields can then be described in terms of changes in the geoid height from one point in time to another.

A more intuitive representation of the temporal variability of the gravity field can be achieved by employing *equivalent water heights (EWHs)*. As many of the short-period changes of the potential are due to hydrological signals, the idea of EWHs is to represent these changes as variations in the thickness of a thin layer of liquid water at Earth's surface (Wahr, Molenaar, and Bryan, 1998).

3.4.2 Degree Amplitudes

When analysing and describing gravity fields, they are often compared to some reference field, usually a mean potential field. This reference field is also given as a series of Stokes coefficients. The *signal degree amplitude* of a gravity field for one degree n, along with its formal error, is defined as

$$\eta_n = \sqrt{\sum_{m=0}^{n} (c_{nm}^2 + s_{nm}^2)} \qquad \text{and} \qquad \sigma_n = \sqrt{\sum_{m=0}^{n} (\sigma_{nm}^2 + \sigma_{nm}^2)} \qquad (3.4.8)$$

where σ_{nm}^2, σ_{nm}^2 are the formal errors of the Stokes coefficients. The *difference degree amplitude* is, with Δc_{nm} and Δs_{nm} the difference of the Stokes coefficients to the reference field,

$$\Delta\eta_n = \sqrt{\sum_{m=0}^{n} (\Delta c_{nm}^2 + \Delta s_{nm}^2)} \, . \qquad (3.4.9)$$

Figure 3.1 shows the signal and difference degree amplitudes of two arbitrary models. The GRACE baseline, a pre-launch estimate of the expected accuracy for GRACE monthly gravity field solutions, is also displayed. This curve will feature in many of the degree amplitude plots in this thesis, without being labelled in the legend each time.
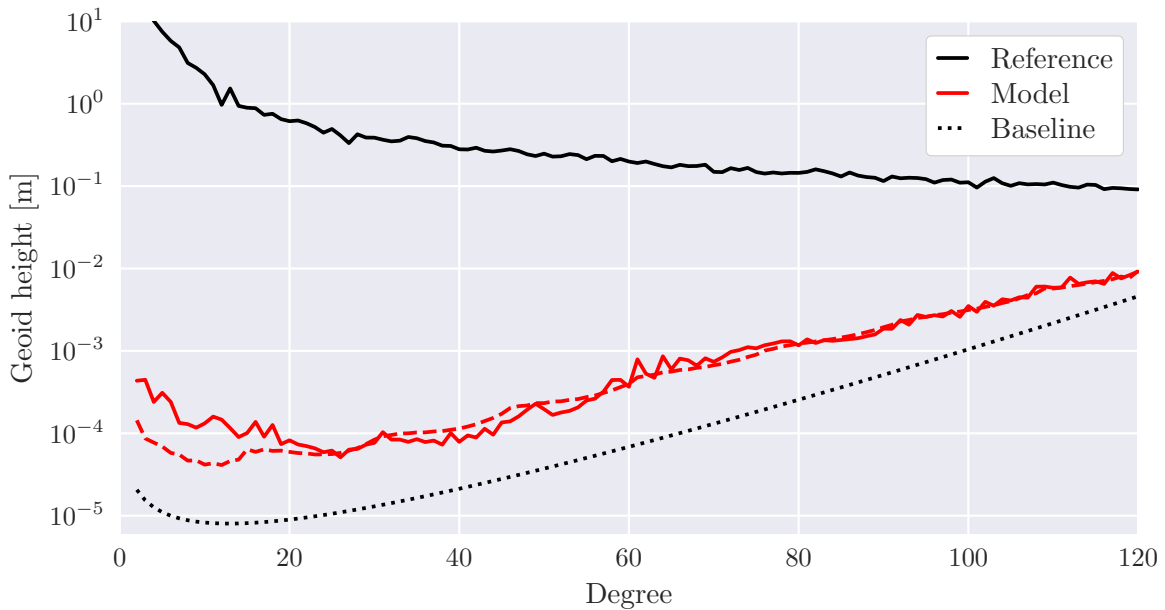
Figure 3.1: Illustration of signal degree amplitudes for a *reference field* and difference degree amplitudes for the analysed *model*.

3.4.3 Coefficient Triangles

The Stokes coefficients and their formal errors can be displayed as *coefficient triangles*. In fig. 3.2a, the deviation of the Stokes coefficients of a monthly GRACE gravity field from a reference static field is shown. The cosine coefficients c_{nm} are shown in the right half of the triangle, with their order increasing with growing distance from the centreline. The sine coefficients s_{nm} are displayed in the left half of the triangle. The degree of the coefficients is zero at the very top of the triangle, and increases in the downward direction. The deviation from the reference field is shown as the base-10 logarithm of the absolute difference from the reference field.

Figure 3.2b shows the base-10 logarithm of the formal errors of the monthly solution. The formal errors clearly show some features which are due to the specific GRACE observation and orbit geometry, such as the bands of increased variance at orders around multiples of ≈ 16.
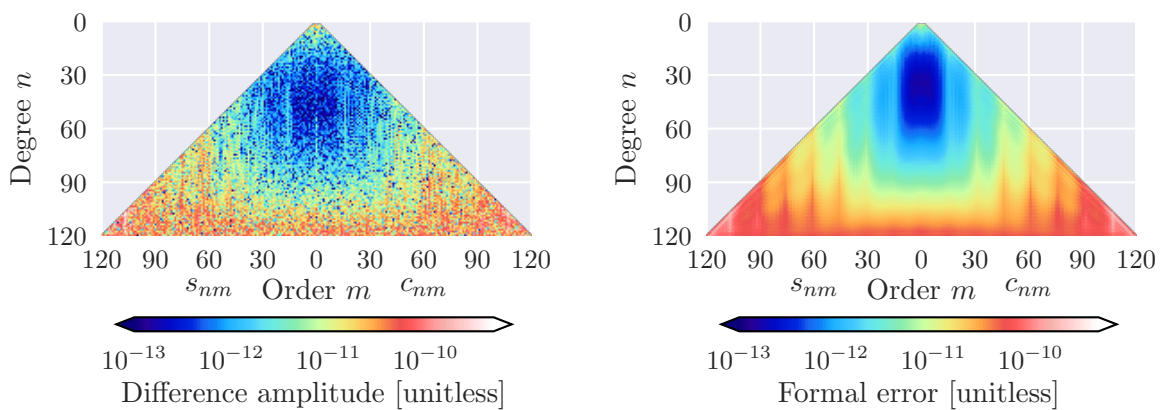
(a) Deviation from a reference field.   (b) Formal errors of Stokes coefficients.

Figure 3.2: GRACE monthly solution Stokes coefficients displayed as coefficient triangles.

3.4.4 Filters

Gravity fields determined through GRACE suffer from distinct correlated errors manifesting as a north-south striping pattern in the spatial domain. These errors are mainly due to the satellites' ground track geometry. There exist many algorithms to filter a gravity field to at least partially remove such aliasing effects, ranging from simple methods of smoothing using a spherical cap to very sophisticated methods considering the complete stochastic information of GRACE gravity fields (Swenson and Wahr, 2006). One implementation of the first approach, smoothing with a spherical cap, is known as a *Gaussian filter* (Jekeli, 1981). A gravity field is filtered using a Gaussian filter by damping the Stokes coefficients with a progressively smaller factor for progressively higher degrees. The damping factor is determined by the *filter radius*
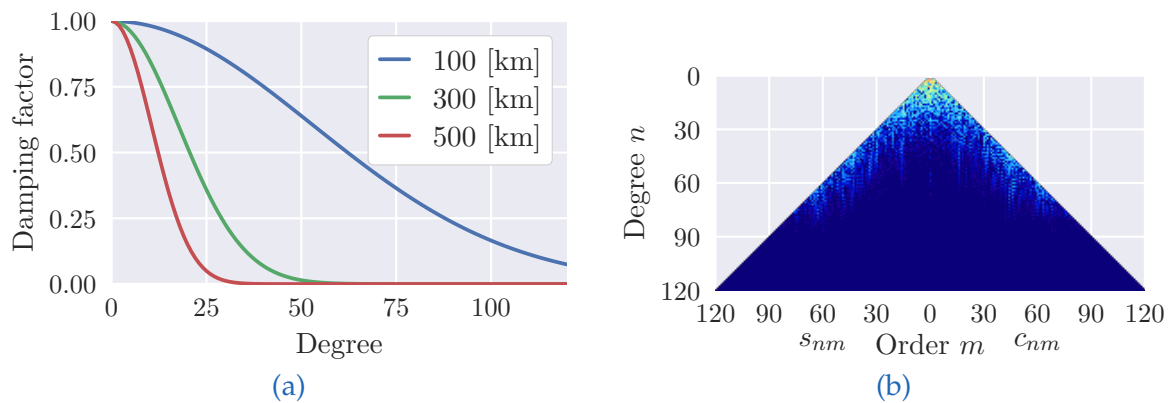
Figure 3.3: (a) Damping factor for Gaussian filters of several radii, and (b) coefficient triangle after filtering with radius $r = 300\,\text{km}$. The scale in (b) is identical to that of fig. 3.2a.

r in such a way that in the spatial domain, the amplitude of the Gaussian spherical cap reaches half its initial amplitude at a distance of the filter radius from its centre. Figure 3.3a shows the damping factor for some example filter radii. Figure 3.3b shows the coefficient triangle for a solution that has been filtered with a Gaussian filter of radius 300 km.

The GRACE Satellites

4

The GRACE twin satellite mission was a joint venture between NASA and DLR with the primary purpose of mapping Earth's mean and time-variable gravitational field. The satellites were launched into near-circular polar orbits at an altitude of approximately 500 km on March 17, 2002 (Tapley et al., 2004). With one satellite trailing the other on its orbit at a distance of roughly 200 km, the satellites primarily observed their position, their separation and its change, and the accelerations due to non-gravitational forces acting on the satellites. From this data, the gravitational acceleration that acts on the satellites can be inferred, allowing scientists to determine Earth's gravitational field. After more than 15 years in orbit, the GRACE science mission ended with the final acquisition of data for gravity field processing in June 2017. This chapter gives a summary of the satellites mission, construction, and instrumentation. For authoritative and detailed descriptions of the satellites, the reader is referred to Bettadpur (2012) and Stanton et al. (1998).

4.1 Construction and Instrumentation

The two GRACE satellites have an elongated prismatic body with dimensions of 3.1 m × 1.9 m × 0.7 m and a mass of 487.2 kg at launch. The satellites are almost identical in construction, differing only in the radio frequencies used for ground communications and the inter-satellite link (Stanton et al., 1998). The GRACE mission realizes both the high-low and low-low variants of the satellite-to-satellite tracking (SST) principle. In addition to flight control and instrument processing hardware, the satellites are equipped with the following science instruments which are of particular interest within the scope of this thesis (compare fig. 4.1):

Accelerometer A three axis accelerometer (ACC) is mounted close to the center of mass (COM) of the satellite. The satellite COM is then calibrated through in-orbit satellite trim manoeuvres to coincide with the accelerometer COM. In addition to linear accelerations, the accelerometer also records angular accelerations in three axes. The accelerometer is used to observe satellite accelerations due to non-conservative forces.

Star Camera Assembly The star camera assembly (SCA) consists of two star camera heads on each satellite, observing different views of the sky. The observations from both heads are combined to determine the satellite attitude.

23
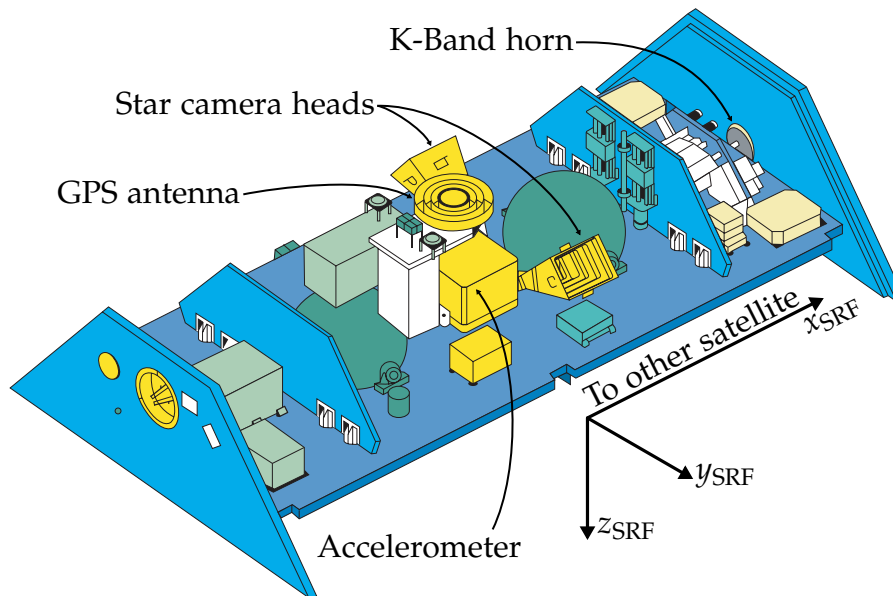
Figure 4.1: Interior view of GRACE with most important instruments. Adapted from NASA (2002).

K/Ka Band Ranging Instrument Mounted on the front panel of the satellite, the K/Ka band ranging instrument (KBR) horn allows for continuous instantaneous observations of the separation of the satellites up to some unknown integer multiple-of-wavelength ambiguity, based on the interferometric principle. Each satellite transmits two carrier signals at specific frequencies in the K and Ka-Band, which are independently tracked by the other satellite. This is referred to as the dual one-way ranging observation, a realization of the low-low satellite-to-satellite tracking (ll-SST) principle. These observations are then combined and corrected to yield observations of the satellites' separation.

Global Positioning System Receiver Realizing the principle of high-low satellite-to-satellite tracking (hl-SST), GRACE is equipped with two primary global positioning system (GPS) antennae, one on the top panel for positioning of the satellite, and one on the rear panel for radio occultation observations.

Laser Retro-reflector Each satellite is equipped with a laser retro-reflector (LRR) for tracking through ground-to-space satellite laser ranging (SLR) observations.

4.2 Reference Frames

During acquisition and processing of GRACE data, several different reference frames are employed. The following paragraphs will give a brief description of the frames that are of particular relevance in this document, a complete and authoritative list can be found in (Bettadpur, 2012).

Science Reference Frame The origin of the science reference frame (SRF) is defined to coincide with the satellite center of mass. The axes of the SRF are parallel to the measurement axes of the accelerometer. The axes are enumerated in such a way that the x-axis of the SRF is the roll axis of the satellite. It is positive in the in-flight direction for the trailing satellite, and negative in the in-flight direction for the leading satellite. During flight, the z-axis (yaw rotation) points roughly nadir. The y-axis (pitch rotation) completes a right-handed coordinate system. The GRACE science data products are released in the SRF.

Star Camera Frame One star camera frame (SCF) is defined for each star camera head on the satellite. The x-axes are parallel to the x-axis of the SRF. The z-axis of each SCF is the optical axis of the respective star camera head. The y-axis completes a right-handed triad.

K-Frame The origin of the K-Frame (KF) coincides with the origin of the SRF. In difference to the SRF, the x-axis of the KF points towards the calibrated antenna phase centre (APC) of the K-band horn, as depicted in fig. 4.2. As such the KF can change with in-orbit K-band calibration manoeuvres. The z-axis of the KF is orthogonal to the x-axis of the KF and the y-axis of the SRF. The y-axis completes the right-handed triad.

Line Of Sight Frame The origin of the line of sight frame (LOSF) coincides with the satellites' SRF origin. The x-axis points towards the other satellite's center of mass. The y-axis is orthogonal to the position vector of the satellite in the celestial reference frame and the x-axis, the z-axis completes a right-handed triad.

Celestial Reference Frame The celestial reference frame (CRF) is an earth-centred, space-fixed reference frame that serves as a quasi-inertial frame for GRACE processing. The chosen realisation of the celestial reference frame is the international celestial reference frame (ICRF) as defined in the *IERS Conventions (2010)* (Petit and Luzum, 2010).

Terrestrial Reference Frame The terrestrial reference frame (TRF) is an earth-centred, earth-fixed reference frame. The chosen realisation of the terrestrial reference frame is the international terrestrial reference frame (ITRF) as defined in the *IERS Conventions (2010)* (Petit and Luzum, 2010).
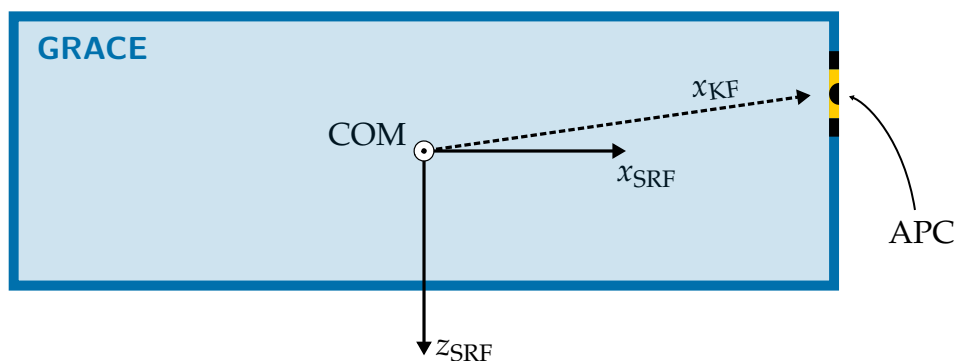
Figure 4.2: Exaggerated depiction of the misalignment of the calibrated KBR antenna phase centre with the SRF x-axis (side view).

4.3 Observation Geometry

The fundamental quantities when describing GRACE observations are the *positions* of the two satellites, r_A and r_B, given in the CRF, and their *orientation* in space R_A and R_B, giving a rotation from the CRF to the respective SRF. The vectorial difference of the satellites' centres of mass is given by

$$u = r_B - r_A . \tag{4.3.1}$$

The satellite *range* is then

$$\rho_{COM} = \|u\| . \tag{4.3.2}$$

This is however not what is observed by the KBR system. The KBR observation is instead the range as observed from the K-band antenna phase centre on GRACE-A to the K-band antenna phase centre on GRACE-B, as illustrated in fig. 4.3. The range as observed by the KBR is in fact

$$\rho_{KBR} = \|(r_B + R_B c_B) - (r_A + R_A c_A)\| , \tag{4.3.3}$$

where $c_{A/B}$ are the calibrated coordinates of the GRACE KBR antenna phase centres given in the respective SRF. More compactly, it is

$$\rho_{KBR} = \|u + v\| \tag{4.3.4}$$

with

$$v = R_B c_B - R_A c_A . \tag{4.3.5}$$

The range observation as made by the KBR is thus too small, and must be corrected with the *antenna offset correction (AOC)*

$$\Delta\rho_{AOC} = \rho_{COM} - \rho_{KBR} = \|u\| - \|u + v\| . \tag{4.3.6}$$

In addition to this purely geometrical correction, the ranging observation must also be corrected for the distance the satellites travelled during the signal time-of-flight,
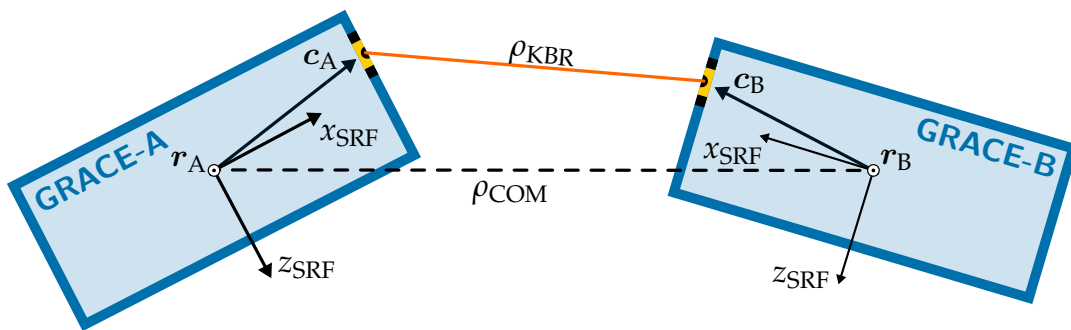
Figure 4.3: Observation geometry of the GRACE KBR measurement.

this is the light-time correction $\Delta\rho_{\text{TOF}}$. Further, a correction for the delay in the KBR signal propagation due to the ionosphere $\Delta\rho_{\text{Iono}}$ is applied. Also considering the unknown ambiguity n due to the interferometric nature of the KBR observation and some random error e, the complete *ranging equation* is (Kim and Tapley, 2002)

$$\rho_{\text{COM}} = \rho_{\text{KBR}} + \Delta\rho_{\text{AOC}} + \Delta\rho_{\text{TOF}} + \Delta\rho_{\text{Iono}} + n + e \, . \tag{4.3.7}$$

GRACE data is often not processed using biased range observations, but using derived range rate or range acceleration observations (Wu, Kruizinga, and Bertiger, 2006). The basis vector of the LOSF is

$$e = \frac{u}{\|u\|} \, . \tag{4.3.8}$$

As a very good approximation, the range rate is the projection of the differential velocity $\dot{u} = \dot{r}_{\text{B}} - \dot{r}_{\text{A}}$ onto the basis vector

$$\dot{\rho}_{\text{COM}} = \langle e, \dot{u} \rangle \, , \tag{4.3.9}$$

while the range acceleration is, with the projection of the differential acceleration $\ddot{u} = \ddot{r}_{\text{B}} - \ddot{r}_{\text{A}}$,

$$\ddot{\rho}_{\text{COM}} = \langle e, \ddot{u} \rangle + \langle \dot{e}, \dot{u} \rangle \, . \tag{4.3.10}$$

The appropriate corrections for range rate or range acceleration observations can be obtained by differentiating the corrections computed for ranges numerically.

In science mode, the satellites are steered in such a way that the KBR antenna phase centres are aligned with the satellite baseline u, their *line of sight (LOS)*, to within a few milliradians. This pointing mode avoids multipath effects in the KBR observations (Kirschner, Montenbruck, and Bettadpur, 2001). In this mode, the x-axes of the respective K-frames are not parallel to the satellite velocity vector, instead the satellites orbit with a pitch angle $\theta_{\text{A/B}}$ of 0.4° to 2.2°, as illustrated in fig. 4.4. In case of perfect steering to this nominal orientation, the LOSF and the KF coincide.
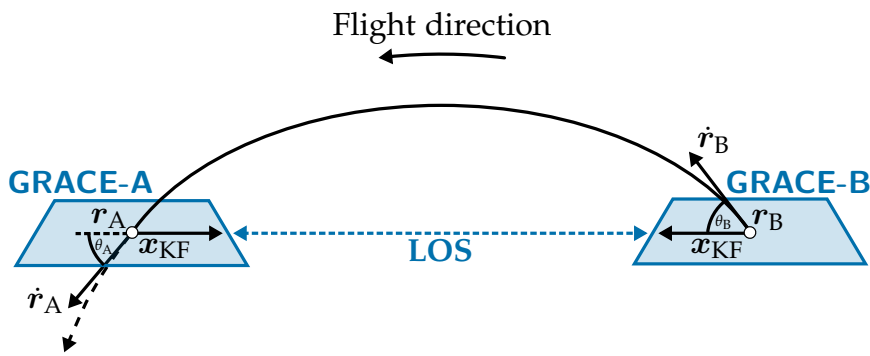
Figure 4.4: In-orbit formation of the GRACE satellites in science mode with pitch bias $\theta_{\text{A/B}}$. Adapted from Kirschner, Montenbruck, and Bettadpur (2001).

4.4 Data Flow

GRACE data is processed in several steps, or levels, before being made available to the science community. This processing occurs under the framework of the SDS, the GRACE Science Data System. *Level* 0 data contains raw decommutated telemetry that has been downloaded from the satellites by the GRACE Raw Data Center at DLR in Neustrelitz. This data is transformed to engineering units by applying sensor calibration factors to yield *level* 1A data. It is then referenced into the SRF, time-tagged, filtered, and down-sampled, which results in *level* 1B data. Level 1A and level 1B data are generated by JPL and GFZ. This is the data source that is available to the general science community, and on which the results in this thesis are based. The gravity field solutions computed from level 1B data are level 2 products. Data products derived from level 2 products, such as mass anomaly grids, are level 3 products.

Variational Equations 5

Determining Stokes coefficients from GRACE data requires a functional model connecting the target parameters to the satellite observations. In ITSG-Grace2016 and this work, *variational equations* (Beutler and Mervart, 2010; Montenbruck and Gill, 2000) are employed to set up the functional model. This approach combines the integration of the spacecraft's dynamic orbit with the set-up of observation equations for Stokes coefficients or other sought parameters in a numerically efficient procedure.

Where kinematic orbits represent discrete epoch-wise position solutions for the spacecraft, dynamic orbits are computed for a complete orbit arc through integration of the accelerations acting on the spacecraft. Positions at a later epoch thus implicitly depend on the spacecraft position at an earlier epoch. Direct position observations of the spacecraft, such as from GPS, may be used to evaluate background force models to yield the accelerations to be integrated, but are not used directly in the computation of the dynamic orbit. Due to the integral nature of the orbit, the spacecraft trajectory is smooth. On account of unavoidable approximation errors, such as from evaluating flawed background models, this smooth trajectory does usually not directly coincide with the true spacecraft position. The divergence increases with growing arc lengths. The smooth dynamic orbit should thus also be fitted to more accurate but less precise observations, such as from GPS (Zehentner and Mayer-Gürr, 2016), to ensure that it is localized correctly. This determination of dynamic orbits in an integrate-and-fit procedure is an essential component in computing gravity field solutions from GRACE satellite-to-satellite tracking observations.

The accelerations that are integrated to yield a dynamic orbit can be broadly categorized into the two groups described in chapter 3: Accelerations due to conservative forces and accelerations due to non-conservative forces. As conservative forces act on all masses of the spacecraft equivalently, they can not be measured by the spacecraft directly. They must be derived from a background model using some approximate position information. This approximation introduces an error in the integrated orbit which can be treated by iterating the integration procedure, using the resulting orbit

of the previous iteration as an input for the next. For spacecraft equipped with an accelerometer, e.g. GRACE, accelerations due to non-conservative forces can be measured directly by this instrument. A change in the computed orbit position from one iteration of orbit determination to the next does not affect the direct accelerometer observations, and so the integrated non-conservative forces do not change between iteration steps. The conservative forces, however, do depend on the spacecraft position. The specific values of the accelerations due to conservative forces being integrated will thus change from one iteration of integration to the next.

The resulting dynamic orbits are then used at multiple steps of the level 1B to level 2 processing chain to compute observation equations for high-low satellite-to-satellite tracking and low-low satellite-to-satellite tracking observations, where they are used as a Taylor point for their linearisation.

The following sections give an overview of the background and process of dynamic orbit integration as implemented at IfG, as well as an introduction to the variational equations and their solution.

5.1 Equation of Motion

The fundamental principle in this work is Newton's second law of motion

$$\boldsymbol{F} = m\ddot{\boldsymbol{r}} \, , \tag{5.1.1}$$

stating that the acceleration experienced by a body is directly proportional to a force $\boldsymbol{F}$ acting on it. Isolating the acceleration in eq. (5.1.1) yields

$$\ddot{\boldsymbol{r}} = \frac{\boldsymbol{F}}{m} = \boldsymbol{f}(t, \boldsymbol{r}(t), \boldsymbol{p}, \ldots) \, , \tag{5.1.2}$$

the *equation of motion*. This equation states that the acceleration experienced by the body, in this case a GRACE spacecraft, is equal to the specific force exerted on it. For GRACE, this is the sum of all conservative and non-conservative forces, as described in chapter 3. As the effective force, the superposition of all component forces, is neither uniform in space nor constant in time, the acceleration in eq. (5.1.2) depends on the time of evaluation t, as well as the position of the spacecraft at this time $\boldsymbol{r}(t)$. Further, it depends on the parameters $\boldsymbol{p}$ of the force-generating functions such as the Stokes coefficients of Earth's gravitational field or the density of the remnant atmosphere, causing drag. Completing this thought, the occurrence of drag in this equation hints to the specific force also being dependent on more factors, namely the orientation of the spacecraft, its cross section, and its velocity $\dot{\boldsymbol{r}}(t)$. When considering albedo and solar radiation pressure, the characteristics of the satellite surface materials and the orientation of the surface elements also become relevant. To simplify this increasingly complex notation, the function describing the specific force is abbreviated to

$$\boldsymbol{f}(t) = \boldsymbol{f}(t, \boldsymbol{r}(t), \boldsymbol{p}, \ldots) \, , \tag{5.1.3}$$

keeping in mind the full breadth of influences contained therein. The analysis of the satellite orbit is limited to a specific interval of time, with start time t_{start} and end time t_{end}. The duration of this interval is $T = t_{\text{end}} - t_{\text{start}}$. Time is normalized to this interval with

$$\tau = \frac{t - t_{\text{start}}}{T} , \tag{5.1.4}$$

giving the compact form of the equation of motion

$$\ddot{\boldsymbol{r}}(\tau) = \boldsymbol{f}(\tau) . \tag{5.1.5}$$

5.1.1 Integrating the Equation of Motion

The position and velocity of the spacecraft can be determined by integrating eq. (5.1.5), giving

$$\ddot{\boldsymbol{r}}(\tau) = \boldsymbol{f}(\tau) \tag{5.1.6}$$

$$\dot{\boldsymbol{r}}(\tau) = \dot{\boldsymbol{r}}_0 + T \int_0^\tau \boldsymbol{f}(\tau')d\tau' \tag{5.1.7}$$

$$\boldsymbol{r}(\tau) = \boldsymbol{r}_0 + \dot{\boldsymbol{r}}_0(\tau T) + T^2 \int_0^\tau (\tau - \tau')\boldsymbol{f}(\tau')d\tau' . \tag{5.1.8}$$

The position $\boldsymbol{r}(\tau)$ and velocity $\dot{\boldsymbol{r}}(\tau)$ depend on unknown initial values $\dot{\boldsymbol{r}}_0$ and $\boldsymbol{r}_0$. Fixing these initial values yields a position and velocity for each epoch $n \in [1, N]$ of the orbit arc (see e.g. Mayer-Gürr, 2006).

The variational equation approach is based on a linearisation of the integrated positions and velocities with regard to the sought force model parameters. In the formalism of the variational equations, the partial derivatives of the spacecraft's position and velocity for all epochs of the orbit arc with regard to the force model parameters appear. These partials are computed efficiently through integration from some initial condition, the explicit evaluation of the complete partials at each epoch is thus avoided. Dynamic orbits then appear as the linear term in a Taylor expansion of the integrated equations of motion (eqs. (5.1.7) and (5.1.8)) necessary when setting up the variational equations.

The position and velocity of the satellite for one epoch are consolidated in the *state vector*

$$\boldsymbol{y}(\tau) = \begin{bmatrix} \boldsymbol{r}(\tau) \\ \dot{\boldsymbol{r}}(\tau) \end{bmatrix} . \tag{5.1.9}$$

Taking the partial derivatives of the satellite state at one epoch with regard to the *initial state* of the satellite

$$\boldsymbol{y}_0 = \begin{bmatrix} \boldsymbol{r}_0 \\ \dot{\boldsymbol{r}}_0 \end{bmatrix} \tag{5.1.10}$$

and the unknown force model parameters p gives the *variational equations* Ω. The variational equations

$$\Omega(\tau) = \begin{bmatrix} S(\tau) & \Phi(\tau) \end{bmatrix} \tag{5.1.11}$$

are divided into the parameter sensitivity matrix

$$S(\tau) = \frac{\partial y(\tau)}{\partial p} = \begin{bmatrix} \dfrac{\partial r(\tau)}{\partial p} \\[2ex] \dfrac{\partial \dot{r}(\tau)}{\partial p} \end{bmatrix} \tag{5.1.12}$$

and the state transition matrix

$$\Phi(\tau) = \frac{\partial y(\tau)}{\partial y_0} = \begin{bmatrix} \dfrac{\partial r(\tau)}{\partial r_0} & \dfrac{\partial r(\tau)}{\partial \dot{r}_0} \\[2ex] \dfrac{\partial \dot{r}(\tau)}{\partial r_0} & \dfrac{\partial \dot{r}(\tau)}{\partial \dot{r}_0} \end{bmatrix} . \tag{5.1.13}$$

The parameter sensitive matrix S describes the influence of a change δp in the force model parameters p on the satellite orbit. This could for example be due to a change in Earth's gravitational potential, or due to a change in the relative position of a celestial body and a resulting disturbance to its tidal potential. The state transition matrix Φ in turn describes the influence of changes in the initial state δy_0 on each epoch of the satellite orbit. The linearisation of the satellite state y about these parameters δp and δy_0 is then

$$\bar{y}(\tau) = y(\tau)|_{p,y_0} + \begin{bmatrix} S(\tau) & \Phi(\tau) \end{bmatrix} \begin{bmatrix} \delta p \\ \delta y_0 \end{bmatrix} . \tag{5.1.14}$$

The *dynamic orbit* is the zero order term of this expansion. The dynamic orbit for the entire arc $\tau \in (0,1]$ can thus be fixed by setting a set of initial conditions y_0 and parameters p. Interestingly, the parameter sensitivity matrices $S(\tau)$, $\tau \in (0,1]$ can be computed through integration having knowledge of its initial state S_0 as well as of the full state transition matrix Φ for all epochs τ. This process is explained later in section 5.3. The full parameter sensitivity matrix can then be used to set up the observation equations for GRACE hl-SST and ll-SST observations, as described in section 6.4.

5.2 Orbit Integration and State Transition Matrix

In order to solve for the sought gravity field parameters in the parameter sensitivity matrix S, the state transition matrix for the complete orbit arc, and thus the dynamic orbit, must be known. These two quantities are computed together through integration.

This integration, and the determination of the dynamic orbit, requires the equations of motion for the satellite to be solved. For the simple potential of a point mass or uniform sphere the equations of motion have a closed solution, described by Kepler's laws of planetary motion. For more complex potential fields, no closed solution exists, and numerical integration methods are used to determine the satellite motion. Classical examples of such numerical methods are Euler's algorithm, the family of Runge-Kutta methods, and multi-step methods of which the Gauss-Jackson family is a prominent example (Berry and Healy, 2004; Beutler and Mervart, 2010). All of these methods have one important characteristic in common: The satellite state is *propagated* from one epoch to the next. This terminology implies that the integral of the acting accelerations over one time interval is formed, and then used to determine the updated satellite state at the end of the interval. In other terms, the new position at the end of the interval is arrived at by extrapolation. For some methods, such as the aforementioned Gauss-Jackson method, the extrapolated state is then corrected through an iterative procedure. This refinement then relies on the previously extrapolated state, and converges on an estimate of the new state at the end of the interval. After completion of this refinement, the integration algorithm moves forward in time to the next interval, and continues the integration following the same procedure.

In the implementation described here, the dynamic orbit is instead determined by continuous numerical integration of all accelerations along an orbit arc. In this integration step the satellite state is not fixed at each epoch. Rather only the changes from one epoch to the next, the integrals in eqs. (5.1.7) and (5.1.8) are computed. In a sense, the orbit is not extrapolated from epoch to epoch, but rather its complete geometry is determined at once. This is achieved by taking advantage of a priori knowledge of all accelerations along the arc, as evaluated from an initial approximate orbit and, depending on the satellite, observed by an on-board accelerometer. For this implementation the definite integrals of the accelerations are efficiently determined using an integration polynomial, as described in section 2.7. The definite integrals for the new positions are then used in conjunction with the satellite states given by the initial approximate orbit to estimate the initial state of the integrated dynamic orbit. The initial state, together with the definite integrals, then completely describes the satellite state for the integrated arc. The following sections describe this algorithm in more detail.

5.2.1 Coarse Approximation

The first iteration of dynamic orbit integration requires a coarse approximation of the spacecraft's orbit, for example a Kepler ellipsis determined from some mean ephemerides, or purely kinematic positions determined from GPS observations. These are the *approximate* positions r_ϵ. The *true* positions of the spacecraft r are unknown, and deviate from the approximate positions by some value ϵ. The employed background models are evaluated at the approximate positions, giving the accelerations from

conservative forces at each epoch:

$$\ddot{r}_\epsilon^{\text{cons}}(\tau) = f(\tau, r_\epsilon(\tau), p) \tag{5.2.1}$$

As GRACE also provides direct accelerometer observations of accelerations due to non-conservative forces, these are added to the accelerations from conservative forces to give the complete approximate accelerations $\ddot{r}_\epsilon$

$$\ddot{r}_\epsilon(\tau) = \ddot{r}_\epsilon^{\text{cons}}(\tau) + \ddot{r}^{\text{ACC}}(\tau) . \tag{5.2.2}$$

Next, the definite integrals from eqs. (5.1.7) and (5.1.8) are computed for the complete arc using integration polynomials as introduced in section 2.7. This gives the integrated velocities and positions

$$\dot{r}_\epsilon^{\text{int}}(\tau) = T \int_0^\tau \ddot{r}_\epsilon(\tau') d\tau' \tag{5.2.3}$$

$$r_\epsilon^{\text{int}}(\tau) = T^2 \int_0^\tau (\tau - \tau') \ddot{r}_\epsilon(\tau') d\tau' . \tag{5.2.4}$$

Back-substituting these quantities into eqs. (5.1.7) and (5.1.8) yields the integrated equations of motion

$$\dot{r}_\epsilon^{\text{dyn}}(\tau) = \dot{r}_0 + \dot{r}_\epsilon^{\text{int}}(\tau) \tag{5.2.5}$$

$$r_\epsilon^{\text{dyn}}(\tau) = r_0 + \tau T \cdot \dot{r}_0 + r_\epsilon^{\text{int}}(\tau) , \tag{5.2.6}$$

where r_ϵ^{dyn} and $\dot{r}_\epsilon^{\text{dyn}}$ are the dynamic orbit computed from the initial approximation of the orbit r_ϵ and $\dot{r}_\epsilon$. The dynamic orbit must now be fixed in space by determining its initial state. To this end, the *approximate state transition matrix* is computed as

$$\bar{\mathbf{\Phi}}(\tau) = \begin{bmatrix} \bar{\mathbf{\Phi}}_r(\tau) \\ \bar{\mathbf{\Phi}}_{\dot{r}}(\tau) \end{bmatrix} = \begin{bmatrix} 1 & \tau T \\ 0 & 1 \end{bmatrix} \tag{5.2.7}$$

by taking the partial derivative of eqs. (5.2.5) and (5.2.6) with regard to the initial state y_0. Although strictly speaking both the position and velocity components must be introduced as observations in the determination of a rigorous least-squares estimate of the initial state $\hat{y}_0$, empirical tests show that it proves sufficient to use positions only at this point. This allows one to neglect the velocity components of the approximate and dynamic orbit in the observation equation system, reducing the complexity of the problem by a small margin. Rearranging eq. (5.2.6) and setting $r_\epsilon^{\text{dyn}} \overset{!}{=} r_\epsilon$ gives

$$r_\epsilon - r_\epsilon^{\text{int}} = \bar{\mathbf{\Phi}}_r y_0 , \tag{5.2.8}$$

which can directly be used to compute an estimate $\hat{y}_0$ for the initial state that best fits the approximate positions r_ϵ in a standard least squares adjustment. The first complete approximate dynamic orbit is then

$$\hat{y} = \bar{\mathbf{\Phi}} \hat{y}_0 + y_\epsilon^{\text{int}} . \tag{5.2.9}$$

This orbit is smooth due to its shape being defined by the integrated accelerations. Its absolute position in space is at this point fixed to be close to the initial approximate orbit as a result of adjusting the initial state $\hat{y}_0$ with eq. (5.2.8).

5.2.2 Refinement

In the determination of the first approximate dynamic orbit, the acting forces due to the background models were evaluated at the *approximate positions* r_ϵ, not the *true positions* of the satellite r. This flaw leads to the derived accelerations deviating from the true accelerations by some amount. In turn, the computed positions r_ϵ^{dyn} also deviate from the true positions. Again evaluating the accelerations at the computed positions must thus lead to accelerations different from those first evaluated at the original approximate positions — the orbit is self-consistent neither in positions nor in accelerations. Mayer-Gürr (2006, section 4.2.4.3) describes a strategy for treating this problem through an iterative approach, but in the context of phrasing the dynamic orbit integration as a boundary value problem. The same approach can be applied to the formulation as an initial value problem used here, with the equivalent apparatus outlined in the following paragraphs.

Two operators for the definite integrals used in the integration of both the spacecraft velocities and positions are introduced as

$$\kappa_{\dot{r}}(\tau) = T \int_0^\tau (\cdot) d\tau' \tag{5.2.10}$$

$$\kappa_r(\tau) = T^2 \int_0^\tau (\tau - \tau')(\cdot) d\tau' . \tag{5.2.11}$$

Phrasing the integrals in terms of polynomial integration, as introduced in section 2.7, the operators $\kappa_{\dot{r}}(\tau)$ and $\kappa_r(\tau)$ can be discretised and written as linear operator matrices $K_r, K_{\dot{r}}$. With these integral operator matrices, eqs. (5.2.3) and (5.2.4) can be written as

$$\dot{r}_\epsilon^{\text{int}} = K_{\dot{r}} \ddot{r}_\epsilon \tag{5.2.12}$$

$$r_\epsilon^{\text{int}} = K_r \ddot{r}_\epsilon , \tag{5.2.13}$$

with $\ddot{r}_\epsilon$ a vector of all accelerations along the orbit arc and r_ϵ^{int} and $\dot{r}_\epsilon^{\text{int}}$ the integrated positions and velocities. Symbolically, the difference between a hypothetical perfect and the actual computed dynamic orbit can be determined by writing eq. (5.2.6) twice, once with the (unknown) true position r as input, and once with the approximate positions r_ϵ:

$$r_\epsilon^{\text{dyn}} = \bar{\Phi}_r y_0 + K_r \ddot{r}_\epsilon \tag{5.2.14}$$

$$r^{\text{dyn}} = \bar{\Phi}_r y_0 + K_r \ddot{r} \tag{5.2.15}$$

Taking the difference of eq. (5.2.14) and eq. (5.2.15) yields

$$r^{\text{dyn}} - r_\epsilon^{\text{dyn}} = K_r (\ddot{r} - \ddot{r}_\epsilon) . \tag{5.2.16}$$

The equation of motion eq. (5.1.5) states that the accelerations acting on the spacecraft are a function of the force $f(r)$. Making this substitution, eq. (5.2.16) can also be written as

$$r^{\text{dyn}} - r_\epsilon^{\text{dyn}} = K_r \left[f(r) - f(r_\epsilon) \right] . \tag{5.2.17}$$

Taking the Taylor expansion of the acting forces $\boldsymbol{f}(\boldsymbol{r})$ up to the linear term, and evaluated at the approximate position $\boldsymbol{r}_\epsilon$ as the Taylor point, gives

$$\boldsymbol{f}(\boldsymbol{r}) = \boldsymbol{f}(\boldsymbol{r}_\epsilon) + \nabla\boldsymbol{f}|_{\boldsymbol{r}_\epsilon} \cdot (\boldsymbol{r} - \boldsymbol{r}_\epsilon) \,. \tag{5.2.18}$$

Inserting eq. (5.2.18) into eq. (5.2.17) gives

$$\begin{aligned}
\boldsymbol{r}^{\text{dyn}} - \boldsymbol{r}_\epsilon^{\text{dyn}} &= \boldsymbol{K}_r \left[\boldsymbol{f}(\boldsymbol{r}_\epsilon) + \nabla\boldsymbol{f}|_{\boldsymbol{r}_\epsilon} \cdot (\boldsymbol{r} - \boldsymbol{r}_\epsilon) - \boldsymbol{f}(\boldsymbol{r}_\epsilon) \right] \\
&= \boldsymbol{K}_r \left[\nabla\boldsymbol{f}|_{\boldsymbol{r}_\epsilon} \cdot (\boldsymbol{r} - \boldsymbol{r}_\epsilon) \right]
\end{aligned} \tag{5.2.19}$$

Here, $\nabla\boldsymbol{f}$ is the Marussi tensor, or gravity tensor. The Marussi tensor is populated with gravity gradients, the second derivative of the force-generating potential. With a Matrix

$$\boldsymbol{T} = \begin{bmatrix} \nabla\boldsymbol{f}(\boldsymbol{r}_\epsilon(\tau_1)) & & 0 \\ & \ddots & \\ 0 & & \nabla\boldsymbol{f}(\boldsymbol{r}_\epsilon(\tau_n))) \end{bmatrix}, \tag{5.2.20}$$

containing the Marussi tensors for all epochs of the orbit arc, eq. (5.2.19) can be written as

$$\boldsymbol{r}^{\text{dyn}} - \boldsymbol{r}_\epsilon^{\text{dyn}} = \boldsymbol{K}_r \boldsymbol{T} (\boldsymbol{r} - \boldsymbol{r}_\epsilon) \,. \tag{5.2.21}$$

Given a correct implementation, the estimated position can be seen as an approximation for the true position, or in other terms $\boldsymbol{r}^{\text{dyn}} \overset{!}{=} \boldsymbol{r}$. Inserting the approximate estimate $\boldsymbol{r}_\epsilon^{\text{dyn}}$ of the position from eq. (5.2.14) into eq. (5.2.21) gives

$$\boldsymbol{r} - \bar{\boldsymbol{\Phi}}_r \boldsymbol{y}_0 - \boldsymbol{K}_r \ddot{\boldsymbol{r}}_\epsilon = \boldsymbol{K}_r \boldsymbol{T} (\boldsymbol{r} - \boldsymbol{r}_\epsilon) \,. \tag{5.2.22}$$

Reducing both sides of this equation by the approximate position $\boldsymbol{r}_\epsilon$ and some reordering gives

$$\boldsymbol{r} - \boldsymbol{r}_\epsilon - \boldsymbol{K}_r \boldsymbol{T} (\boldsymbol{r} - \boldsymbol{r}_\epsilon) = \bar{\boldsymbol{\Phi}}_r \boldsymbol{y}_0 + \boldsymbol{K}_r \ddot{\boldsymbol{r}}_\epsilon - \boldsymbol{r}_\epsilon \,, \tag{5.2.23}$$

which can be solved for the coordinate difference between the true and the approximate positions $\Delta\boldsymbol{r}_\epsilon = \boldsymbol{r} - \boldsymbol{r}_\epsilon$:

$$[\boldsymbol{I} - \boldsymbol{K}_r \boldsymbol{T}] (\boldsymbol{r} - \boldsymbol{r}_\epsilon) = \bar{\boldsymbol{\Phi}}_r \boldsymbol{y}_0 + \boldsymbol{K}_r \ddot{\boldsymbol{r}}_\epsilon - \boldsymbol{r}_\epsilon \tag{5.2.24}$$

$$\Delta\boldsymbol{r}_\epsilon = (\boldsymbol{r} - \boldsymbol{r}_\epsilon) = [\boldsymbol{I} - \boldsymbol{K}_r \boldsymbol{T}]^{-1} [\bar{\boldsymbol{\Phi}}_r \boldsymbol{y}_0 + \boldsymbol{K}_r \ddot{\boldsymbol{r}}_\epsilon - \boldsymbol{r}_\epsilon] \,. \tag{5.2.25}$$

$\Delta\boldsymbol{r}_\epsilon$ is an estimate of the linearisation error made in the dynamic orbit integration due to the initial evaluation of the accelerations from background models at $\boldsymbol{r}_\epsilon$ instead of the true position $\boldsymbol{r}$. Using this estimate, the position of the spacecraft along the arc can then be updated:

$$\boldsymbol{r} = \boldsymbol{r}_\epsilon + \Delta\boldsymbol{r}_\epsilon \tag{5.2.26}$$

5.2.3 State Transition Matrix

In the first derivations of eq. (5.2.7), the approximate state transition matrix $\bar{\Phi}$ is determined by taking the partial of the integrated velocity and position with regard to the initial state of the orbit arc y_0. This approximation neglects that that the terms $\dot{r}_\epsilon^{\text{int}}$ and r_ϵ^{int} also depend on the position along the arc, as they are a result of the integration of the accelerations $\ddot{r}_\epsilon$ evaluated from the force models at the positions r_ϵ. The positions along the arc in turn depend on the initial state, requiring application of the chain rule in the determination of Φ. Again dividing the problem into position and velocity components, the complete state transition matrix for the position Φ_r is arrived at by taking the derivative of eq. (5.1.8) with regard to the initial state y_0, giving

$$\frac{\partial r(\tau)}{\partial y_0} = \frac{\partial (r_0 + \tau T \cdot \dot{r}_0)}{\partial y_0} + T^2 \int_0^\tau (\tau - \tau') \frac{\partial f(\tau')}{\partial y_0} d\tau' . \tag{5.2.27}$$

Application of the chain rule to the derivative of the force function with regard to the initial state yields

$$\frac{\partial f(\tau')}{\partial y_0} = \frac{\partial f(\tau')}{\partial r(\tau')} \frac{\partial r(\tau')}{\partial y_0} \tag{5.2.28}$$

and thus gives, by inserting into eq. (5.2.27),

$$\underbrace{\frac{\partial r(\tau)}{\partial \hat{y}_0}}_{\Phi_r} = \underbrace{\frac{\partial (r_0 + \tau T \cdot \dot{r}_0)}{\partial y_0}}_{\bar{\Phi}_r} + \underbrace{T^2 \int_0^\tau (\tau - \tau')}_{K_r} \underbrace{\frac{\partial f(\tau')}{\partial r(\tau')}}_{T} \underbrace{\frac{\partial r(\tau')}{\partial y_0}}_{\Phi_r} d\tau' . \tag{5.2.29}$$

Here, the polynomial integration matrix K_r, the matrix of Marussi Tensors T, and the initial approximation of the state transition matrix $\bar{\Phi}_r$ can be identified. In addition, the complete state transition matrix Φ also appears on both sides of the equation system. This system can be solved for the complete state transition matrix Φ with

$$\Phi_r = [I - K_r T]^{-1} \bar{\Phi}_r \tag{5.2.30}$$

where the same inverse as previously encountered in eq. (5.2.25) appears. In fact, both eq. (5.2.25) and eq. (5.2.30) are of the form

$$l = [I - K_r T]^{-1} x , \tag{5.2.31}$$

and can thus be solved in a similar fashion. This inverse is of size $3N \times 3N$, containing three position components per epoch. Direct inversion of this matrix is expensive even for moderate arc lengths of a few hours. For arc lengths of 24 h at a sampling of 5 s, as used in ITSG-Grace2016, this inverse alone would be responsible for a large fraction of the computation time in determining the variational equations. The special blocked structure of the inverse can be exploited to solve the system using efficient algorithms. As integration up to time τ only depends on accelerations before that point in time, the discretised integration matrix K_r is only populated on or

below the main block diagonal. Some values appear above the main diagonal due to the evaluation of the integration polynomial at the central support. The matrix of Marussi tensors T is block-diagonal. Each block, one per epoch, has size 3×3. Overall, the Matrix $I - K_r T$ is asymmetric and only populated on or below the main block diagonal. An iterative solver, such as the biconjugate gradient stabilized method (BiCGSTAB) (van der Vorst, 1992), can be used to solve the equation system epoch by epoch. Due to the ability to programmatically exploit the special structure of the inverse in a tailored implementation of the solver, this is magnitudes faster and more efficient than direct inversion. This however comes at the cost of a loss of generality in the solver implementation.

The complete state transition matrix for the velocity $\Phi_{\dot{r}}$ can be arrived at by similarly taking the derivative of eq. (5.1.7) with regard to the initial state. Again using the chain rule, this is

$$
\begin{aligned}
\frac{\partial \dot{r}(\tau)}{\partial y_0} &= \frac{\partial \dot{r}_0}{\partial y_0} + T \int_0^\tau \frac{\partial f(\tau)}{\partial y_0} d\tau' \\
&= \frac{\partial \dot{r}_0}{\partial y_0} + T \int_0^\tau \frac{\partial f(\tau)}{\partial r(\tau)} \frac{\partial r(\tau)}{\partial y_0} d\tau' \ .
\end{aligned}
\tag{5.2.32}
$$

Here, one can identify

$$
\begin{aligned}
\Phi_{\dot{r}} &= \bar{\Phi}_{\dot{r}} + T \int_0^T T(\tau') \Phi_r(\tau') d\tau' \\
&= \bar{\Phi}_{\dot{r}} + K_{\dot{r}} T \Phi_r \\
&= \bar{\Phi}_{\dot{r}} + K_{\dot{r}} \Phi_{\ddot{r}} \ ,
\end{aligned}
\tag{5.2.33}
$$

directly yielding the desired result from the previously computed state transition matrix for the positions Φ_r. In this equation, the state transition matrix for the accelerations $\Phi_{\ddot{r}}$ appears. This matrix can, in analogy to the previous steps, also be derived by taking the derivative of eq. (5.1.6) with regard to the initial state:

$$
\frac{\partial \ddot{r}(\tau)}{\partial y_0} = \frac{\partial f(\tau)}{\partial y_0} \ .
\tag{5.2.34}
$$

Application of the chain rule to the derivative of the force function yields

$$
\frac{\partial \ddot{r}(\tau)}{\partial y_0} = \frac{\partial f(\tau)}{\partial r(\tau)} \frac{\partial r(\tau)}{\partial y_0}
\tag{5.2.35}
$$

in which one can identify the state transition matrix for the accelerations

$$
\Phi_{\ddot{r}} = T \Phi_r \ .
\tag{5.2.36}
$$

5.2.4 Final Estimate

All integrated positions and velocities up to this point were integrated from forces evaluated at the approximate positions $f(r_\epsilon)$, as determined in eq. (5.2.1). An updated

estimate for these accelerations can be computed using the estimated coordinate difference Δr_ϵ from eq. (5.2.25) and the linearisation of the force function from eq. (5.2.18). These are the *corrected* accelerations

$$\ddot{r}_c = \ddot{r}_\epsilon + T\Delta r_\epsilon \, . \tag{5.2.37}$$

These corrected accelerations can then be integrated to corrected velocity and position components using the previously defined integral kernels with

$$\dot{r}_c^{\text{int}} = K_{\dot{r}}\ddot{r}_c \tag{5.2.38}$$

$$r_c^{\text{int}} = K_r\ddot{r}_c \, . \tag{5.2.39}$$

A new estimate for the initial state can be determined by repeating the steps from eq. (5.2.8), but now making use of the knowledge of the complete state transition matrix for the positions $\boldsymbol{\Phi}_r$. One arrives at the system

$$r_\epsilon - r_c^{\text{int}} = \boldsymbol{\Phi}_r y_0 \tag{5.2.40}$$

from which $\hat{y}_0$ can be computed. This newly estimated initial state is then used to fix the positions and velocities of the spacecraft from the reintegrated accelerations, giving the final dynamic orbit:

$$\dot{r} = \boldsymbol{\Phi}_{\dot{r}}\hat{y}_0 + \dot{r}_c^{\text{int}} \tag{5.2.41}$$

$$r = \boldsymbol{\Phi}_r\hat{y}_0 + r_c^{\text{int}} \, . \tag{5.2.42}$$

As this algorithm relies heavily on linearisations, all steps from eq. (5.2.1) to eq. (5.2.42) must be repeated. For this re-computation the final dynamic orbit from eqs. (5.2.41) and (5.2.42) is now r_ϵ and $\dot{r}_\epsilon$, used to evaluate the background model and fit the initial state vectors. This is repeated until convergence is achieved. Dynamic orbit computation following this schema is thus an inherently iterative process.

5.3 Parameter Sensitivity Matrix

With $\boldsymbol{\Phi}$ now known, the parameter sensitivity matrix S can be determined. With the P force model parameters p, e.g. the Stokes coefficients of a monthly mean potential, S describes the sensitivity of the dynamic orbit to changes in those coefficients δp. Looking at just one orbit arc, a change of the force model parameters only influences all epochs $\tau > 0$, but not the initial state of the satellite y_0, as the integrals in eqs. (5.1.7) and (5.1.8) are 0 for $\tau = 0$. The initial value of the parameter sensitivity matrix is simply a matrix of zeros

$$S(0) = \mathbf{0}_{6\times P} \, . \tag{5.3.1}$$

To determine the value of S for the remaining epochs, the derivative of the satellite state

$$\dot{y}(\tau) = z(\tau) \tag{5.3.2}$$

is introduced. Taking the derivative of eq. (5.3.2) w.r.t. the initial state gives

$$\frac{\partial \dot{y}(\tau)}{\partial y_0} = \frac{\partial z(\tau)}{\partial y_0} = \frac{\partial z(\tau)}{\partial y(\tau)} \frac{\partial y(\tau)}{\partial y_0} . \tag{5.3.3}$$

Introducing the matrix

$$Z_y = \frac{\partial z(\tau)}{\partial y(\tau)} \tag{5.3.4}$$

eq. (5.3.3) can be compactly written as

$$\dot{\Phi} = Z_y \Phi , \tag{5.3.5}$$

the *differential equation of the state transition matrix*. Similarly, taking the derivative of eq. (5.3.2) w.r.t. the force model parameters gives, using first the product rule and then the chain rule,

$$\frac{\partial \dot{y}(\tau)}{\partial p} = \frac{\partial z(\tau)}{\partial p} = \frac{\partial z(\tau)}{\partial p} + \frac{\partial z(\tau)}{\partial y(\tau)} \frac{\partial y(\tau)}{\partial p} . \tag{5.3.6}$$

Note that $z(\tau)$ is a function of p both directly through $f(\tau, r(\tau), p, \ldots)$, as well as indirectly through the satellite state $y(\tau)$, which also depends on p. Introducing the matrix

$$Z_p = \frac{\partial z(\tau)}{\partial p} \tag{5.3.7}$$

eq. (5.3.6) can be compactly written as

$$\dot{S} = Z_y S + Z_p , \tag{5.3.8}$$

the *differential equation of the parameter sensitivity matrix*. Looking closer,

$$Z_p(\tau) = \begin{bmatrix} \dfrac{\partial \dot{r}(\tau)}{\partial p} \\ \dfrac{\partial \ddot{r}(\tau)}{\partial p} \end{bmatrix} = \begin{bmatrix} 0 \\ \dfrac{\partial f(\tau)}{\partial p} \end{bmatrix} , \tag{5.3.9}$$

which can be computed for all times τ. The inhomogeneous differential equation system formed by eqs. (5.3.5) and (5.3.8)

$$-Z_y \Phi + \dot{\Phi} = 0 \tag{5.3.10}$$

$$-Z_y S + \dot{S} = Z_p \tag{5.3.11}$$

can be solved for $S(\tau)$ through the approach of variation of constants, yielding

$$S(\tau) = -\Phi(\tau) \left[\int_0^\tau \Phi^{-1}(\tau') Z_p(\tau') d\tau' + C \right] . \tag{5.3.12}$$

The integration constant can be fixed to $C = 0$ due to eq. (5.3.1), resulting in

$$S(\tau) = -\Phi(\tau) \int_0^\tau \Phi^{-1}(\tau') Z_p(\tau') d\tau' , \tag{5.3.13}$$

Using this equation, the parameter sensitivity matrix for a complete orbit arc can be computed through integration from a known start value and the known quantities Φ and Z_p.

ITSG-Grace2016

<div style="text-align: right; font-size: 3em;">6</div>

This chapter will give an outline of the state of the art of GRACE data processing in the frame of the ITSG-Grace2016 gravity field solution. This information will give important background and context to the later chapters in this thesis, which detail some of the author's specific contributions to ITSG-Grace2016 and the subsequent ITSG-Grace2018 solution.

The processing, as outlined in fig. 6.1, begins with the download of GRACE level 1B data from the SDS. Following SCA/ACC sensor fusion and data screening, kinematic and dynamic orbits are determined for both GRACE-A and GRACE-B. This is followed by the estimation of stochastic models for both hl-SST and ll-SST observations, which are then used in the determination of the sought monthly Stokes coefficients. All computation steps are performed in GROOPS.

GROOPS is is the Gravity Recovery Object Oriented Programming System, an in-house multi-purpose geodetic software suite developed at IfG. GROOPS is used for all GRACE data processing at IfG, and is capable of performing all necessary processing steps to generate level 2 and level 3 products from GRACE level 1B data. To enable full GRACE-FO processing, level 1A to level 1B processing is also being integrated into GROOPS. GROOPS is written in C++, and makes extensive use of the low-level linear algebra routines defined by LAPACK and BLAS (Anderson, 1999; Blackford et al., 2002).

6.1 Data Preprocessing

The ITSG-Grace2016 gravity field solution is computed from GRACE level 1B release 2.0 data published by GFZ and JPL (GRACE, 2001). The data provided is of high quality, however some additional screening and preprocessing steps have been found to improve the gravity field solutions derived from them. These additional steps have been described in much detail by Klinger (2018). Much of the preprocessing of GRACE data will remain unchanged for the upcoming ITSG-Grace2018 release, with notable exception of the sensor fusion step to combine the star camera level 1B product (SCA1B) with the accelerometer level 1B product (ACC1B) to yield an improved orientation product. The upcoming release 3.0 of GRACE level 1B data by JPL will already include an orientation product derived from SCA/ACC sensor fusion (GRACE, 2018), which was previously computed in-house at IfG. For the purpose of this document, a SCA/ACC sensor fusion approach refined from the ITSG-Grace2016 approach

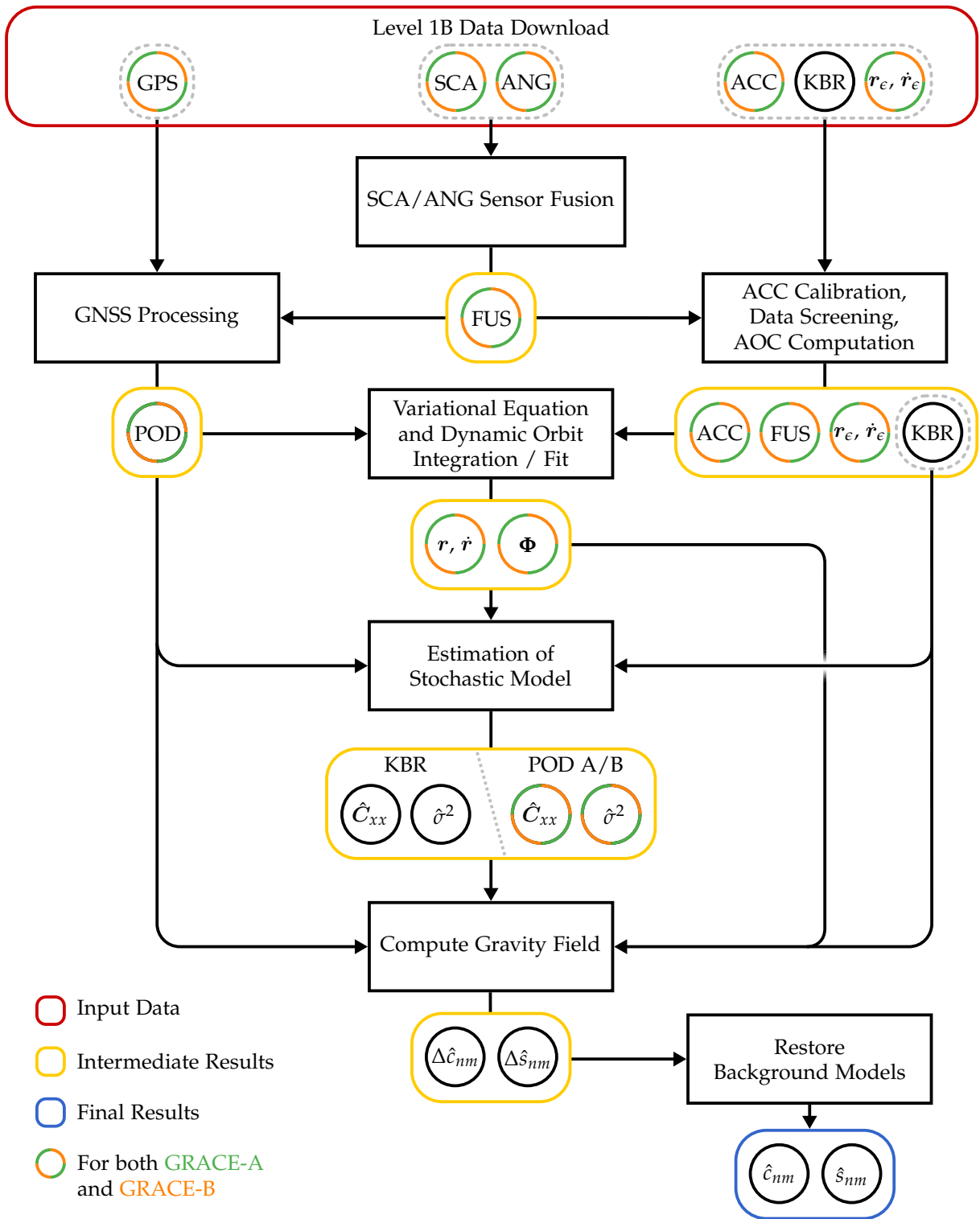Figure 6.1: Schematic for ITSG-Grace2016 level 1B to level 2 data processing. $\mathbf{\Phi}$ is the state transition matrix of the variational equations. $\boldsymbol{x}_{\mathrm{cal}}$ are the co-estimated calibration parameters for the accelerometer.

described by Klinger, 2018 making use of current release 2.0 level 1B data is presented in section 6.2.

Initially, the GRACE level 1B data is converted to a GROOPS-internal data format. The data is then screened for outliers and time periods of reduced data quality, downsampled, and interpolated, as described by Klinger (2018).

For further processing, the data is divided into continuous segments, or *arcs*. In ITSG-Grace2016, arcs of two different lengths are used. For integration of the force models and determination of the dynamic satellite orbit using variational equations, arcs of no shorter than 1 h and no longer than 24 h are created. These 24 h-arcs are the *variational arcs*. For processing of ll-SST observations, arcs of no shorter than 1 h and no longer than 3 h are used, these are the *short arcs*. Both variational and short arcs are divided at midnight each day, so that no segment spans multiple days. Where data is not available for at least one continuous hour, it is discarded.

After data preprocessing steps, the following data is available within variational arcs:

Kinematic orbits ITSG-Grace2016 uses an in-house computed kinematic orbit, the precise orbit determination (POD) product (Zehentner, 2017; Zehentner and Mayer-Gürr, 2016), computed from level 1B GPS data using the raw observation approach. In addition to spacecraft positions, this approach also gives a fully populated 3D covariance matrix at each epoch, which is used in further processing steps.
Dynamic orbit The level 1B orbit solution delivered by the SDS is used as a priori information for the in-house dynamic orbit integration.
Linear accelerations The level 1B linear accelerations are pre-calibrated using modelled accelerometer data (Klinger, 2018).
Orientation product This is a result of level 1B star camera and accelerometer sensor fusion, as described by Klinger, 2018.

In addition, the following data is available in short arcs:

Kinematic orbits The same kinematic orbits that are used in the variational arcs are also kept at hand in short arcs.
Orientation product The same is true for the orientation, which is required in the computation of the AOC, the stochastic modelling of the orientation uncertainty in chapter 8 and for the co-estimation of satellite orientations through a total least squares algorithm described in chapter 9.
KBR observations As delivered by the SDS.
Time of flight correction As delivered by the SDS.
Antenna offset correction The AOC is computed using the improved orientation product from the SCA/ACC sensor fusion.

In both the short arcs and the variational arcs, all data is now given with 5 s sampling, except for the kinematic orbits and their 3D covariance matrices, which are given with 300 s sampling.

6.2 Sensor Fusion

Klinger and Mayer-Gürr (2016) have shown that the quality of GRACE-derived gravity field solutions can be enhanced by using an improved orientation product. This orientation product is the result of a sensor fusion algorithm merging information from the star camera sensors, which is stable at longer wavelengths, with angular accelerations observed by the on-board accelerometers, which have lower noise than the star camera observations at higher frequencies. These observations are combined through a weighted least squares adjustment which yields the fused orientation parameters. This sensor fusion is performed independently for each GRACE spacecraft.

The star camera orientation product gives the rotation from the CRF to the SRF of the respective spacecraft. This rotation is given per epoch as a quaternion

$$\boldsymbol{q} = \begin{bmatrix} q_w & q_x & q_y & q_z \end{bmatrix}^{\mathsf{T}} , \tag{6.2.1}$$

with q_w the scalar part and q_x to q_z the vectorial part of the quaternion. The *angular accelerations* of the spacecraft

$$\dot{\boldsymbol{\omega}} = \begin{bmatrix} \dot{\omega}_x & \dot{\omega}_y & \dot{\omega}_z \end{bmatrix}^{\mathsf{T}} \tag{6.2.2}$$

are given in the SRF. The angular accelerations are the first derivative of the *angular velocities* $\boldsymbol{\omega}$, which are in turn the first derivatives of the orientation of the spacecraft $\boldsymbol{\alpha}$. These angles $\boldsymbol{\alpha}$ deserve some further discussion, as their value is not immediately intuitive. They describe the divergence of the actual orientation of the spacecraft from its nominal orientation with the K-Frame x-axis towards the other satellite, as described in section 4.3. This divergence is given as a set of three Euler angles roll, pitch, and yaw, as illustrated in fig. 6.2.

The nominal orientation of the spacecraft as described in section 4.3 is

$$R_{\mathrm{CRF}}^{\mathrm{NOM}} = R_{\mathrm{KF}}^{\mathrm{SRF}} R_{\mathrm{LOSF}}^{\mathrm{KF}} R_{\mathrm{CRF}}^{\mathrm{LOSF}} , \tag{6.2.3}$$

where the rotation from the LOSF to the CRF can be determined from the satellite positions, e.g. from dynamic orbits. The rotation from the KF to the SRF is computed
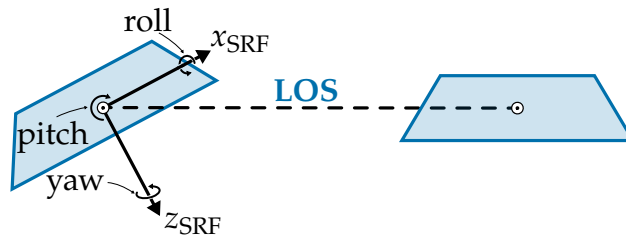

Figure 6.2: GRACE attitude in roll, pitch, and yaw angles. y_{SRF} is orthogonal to image plane.

from the calibrated KBR antenna phase centre coordinates. It is of note that for the *nominal* orientation, the KF and the LOSF coincide, so the rotation from the KF to the LOSF is the identity matrix. The nominal orientation can thus be computed analytically, without relying on orientation observations by the spacecraft. The actual orientation of the spacecraft $\tilde{R}_{\text{CRF}}^{\text{SRF}}$ is observed by the SCA. Due to the active steering of the satellites throughout science operations, the difference between these two rotations

$$
\begin{aligned}
\tilde{R}_\alpha &= \left(R_{\text{CRF}}^{\text{NOM}} \right)^{\mathsf{T}} \tilde{R}_{\text{CRF}}^{\text{SRF}} \\
&= \left(R_{\text{LOSF}}^{\text{CRF}} R_{\text{KF}}^{\text{LOSF}} R_{\text{SRF}}^{\text{KF}} \right) \tilde{R}_{\text{CRF}}^{\text{SRF}} \\
&= \left(R_{\text{LOSF}}^{\text{CRF}} R_{\text{SRF}}^{\text{KF}} \right) \tilde{R}_{\text{CRF}}^{\text{SRF}}
\end{aligned}
\tag{6.2.4}
$$

is a small angle rotation, on the order of some few milliradians (Herman et al., 2004). This attitude deviation can be written as an Euler sequence of roll, pitch, and yaw rotations with respect to the axes of the SRF

$$
\tilde{R}_\alpha = R_{z,\text{SRF}}(\text{yaw}) R_{y,\text{SRF}}(\text{pitch}) R_{x,\text{SRF}}(\text{roll}) \, .
\tag{6.2.5}
$$

The orientation angles α for one epoch τ are then

$$
\alpha(\tau) = \left[\text{roll}(\tau) \quad \text{pitch}(\tau) \quad \text{yaw}(\tau) \right]^{\mathsf{T}} \, .
\tag{6.2.6}
$$

6.2.1 Parametrization

The original implementation of the SCA/ACC sensor fusion at IfG was parametrized in terms of full rotation quaternions. This approach has some caveats: Estimating the full four quaternion parameters for a three dimensional rotation is an over-parametrization of the problem. The solution must be constrained in such a way that the length of the quaternion is unity. Further, when considering the covariance information of a single epoch's quaternion, it is clear that this dependency of the quaternion elements leads to not fully invertible covariance matrices.

The implementation described here is parametrized in terms of small angle rotations in roll, pitch, and yaw with regard to a reference orientation. This has the advantage that only three parameters must be determined per epoch. No singularities or gimbal lock can occur as, due to the active steering of the spacecraft, the rotations are always small angles. Further, the covariance matrices of each epoch are fully invertible without additional constraints. The parameter vector is

$$
x = \left[\alpha_1^{\mathsf{T}} \quad \alpha_2^{\mathsf{T}} \quad \cdots \quad \alpha_N^{\mathsf{T}} \quad x_{\text{cal}}^{\mathsf{T}} \right]^{\mathsf{T}}
\tag{6.2.7}
$$

with the α_i the orientation at each of the N epochs of a variational arc and x_{cal} some calibration parameters.

6.2.2 Star Camera Observations

In addition to the observed orientation of the spacecraft q, the nominal orientation of the spacecraft as computed from eq. (6.2.3) is also given as a quaternion q_0. The nominal orientation serves as the Taylor point for the iterative adjustment of the spacecraft orientation. Due to the difference in the rotations $\Delta\alpha$ only being small, multiplication of the quaternions yields

$$\Delta q = q_0^{-1} \cdot q \approx \begin{bmatrix} 1 \\ 0.5\Delta\alpha_x \\ 0.5\Delta\alpha_y \\ 0.5\Delta\alpha_z \end{bmatrix} . \tag{6.2.8}$$

The linearised observation equation for one epoch of star camera observations is thus

$$\Delta q_{[1:3]} = 0.5 \cdot I_{3\times3}\Delta\alpha . \tag{6.2.9}$$

The full *design matrix for the star camera observations* is then

$$A_{\text{SCA}} = 0.5 \cdot I_{3N\times3N} . \tag{6.2.10}$$

For optimal results in the data combination, a priori covariance information for the SCA observations is introduced. According to Romans (2003), one GRACE star camera head has the nominal noise characteristic

$$\Sigma = \sigma^2 \cdot \begin{bmatrix} 1 & 0 & 0 \\ 0 & 1 & 0 \\ 0 & 0 & \kappa^2 \end{bmatrix} , \tag{6.2.11}$$

expressed in the respective star camera frame. The noise for rotations about the image plane axes is at the same level, with the noise for rotations about the boresight axis worse by a factor of $\kappa \approx 8$. The a priori error of the image plane rotations is given as $\sigma \approx 6''$. The orientation of the star camera heads in the SRF is known through calibration and delivered in the *QSA* record of the GRACE sequence of events file. Further, the SCA1B data contains information on which SCA head was active for a particular epoch. This allows for variance propagation of the a priori covariance matrices to the SRF and their combination. This combined covariance matrix is then introduced as the observation weight for the SCA observation in the SCA/ACC sensor fusion.

6.2.3 Accelerometer Observations

The angular acceleration observations of the accelerometer are directly linked to the Euler angles in the SRF through double differentiation

$$\dot{\omega}(t) = \frac{\partial^2\alpha(t)}{\partial t^2} . \tag{6.2.12}$$

The linearised observations can be written as

$$\Delta \dot{\omega} = D_{\text{ACC}} \Delta \alpha \, , \tag{6.2.13}$$

where $\Delta \dot{\omega} = \dot{\omega} - \dot{\omega}_0$ and $\dot{\omega}_0$ are the angular accelerations derived from q_0 through polynomial differentiation. D_{ACC} is a double differentiation matrix based on a polynomial of degree d as described in section 2.7. D_{ACC} has a roughly block-diagonal structure, with each block of size 3×3 due to there being three angles per epoch. For a polynomial of degree $d = 2$, D_{ACC} would be

$$D_{\text{ACC}} = \begin{bmatrix} D_{0,0} & D_{0,1} & D_{0,2} & 0 & & \cdots & & 0 \\ D_{1,0} & D_{1,1} & D_{1,2} & 0 & & & & \\ 0 & D_{1,0} & D_{1,1} & D_{1,2} & & \ddots & & \vdots \\ & & & \ddots & & & & \\ \vdots & & \ddots & & D_{1,0} & D_{1,1} & D_{1,2} & 0 \\ & & & & 0 & D_{1,0} & D_{1,1} & D_{1,2} \\ 0 & & \cdots & & 0 & D_{2,0} & D_{2,1} & D_{2,2} \end{bmatrix}_{3N \times 3N} , \tag{6.2.14}$$

with

$$D_{i,j} = \overline{w}_{i,j} I_{3 \times 3} \tag{6.2.15}$$

and $\overline{w}_{i,j}$ the j-th weight factor of the differentiation polynomial computed to be evaluated at the support i. For the accelerometer observations, it is desirable to co-estimate calibration parameters such as biases or scales. These P_{cal} parameters are collected in the $3N \times P_{\text{cal}}$ matrix A_{cal}. The *design matrix for the angular accelerations* is then

$$A_{\text{ACC}} = \begin{bmatrix} D_{\text{ACC}} & A_{\text{cal}} \end{bmatrix}_{3N \times 3N + P_{\text{cal}}} . \tag{6.2.16}$$

The initial weights for the angular acceleration observations are set to the values given by (Klinger, 2018), $5 \cdot 10^{-6} \, \text{rad}/\text{s}^2/\sqrt{\text{Hz}}$ for the x- and z-axis, and $2 \cdot 10^{-7} \, \text{rad}/\text{s}^2/\sqrt{\text{Hz}}$ for the y-axis.

6.2.4 Combination

The two observation groups are combined in an iterative least squares adjustment, with variance component estimation used to determine their relative weights. The initial Taylor point for the orientation q_0 at each epoch is set to the nominal orientation of the satellite. The combined observation equation system for both SCA and ACC observations is

$$\begin{bmatrix} \Delta q_{[1:3]} \\ \Delta \dot{\omega} \end{bmatrix} = \begin{bmatrix} A_{\text{SCA}} & 0 \\ D_{\text{ACC}} & A_{\text{cal}} \end{bmatrix} \begin{bmatrix} \Delta \alpha \\ \Delta x_{\text{cal}} \end{bmatrix} . \tag{6.2.17}$$
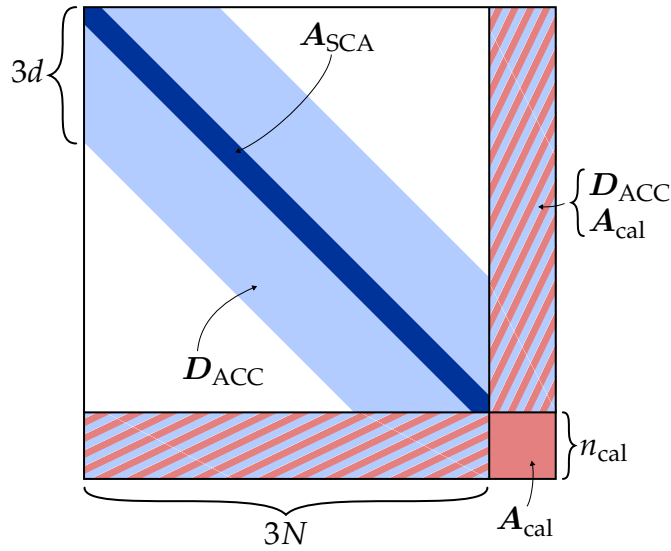
Figure 6.3: Structure of the normal equation system of the improved SCA/ACC sensor fusion, with contributing design matrices marked.

For performance reasons, the observation equations are set up and decorrelated per epoch and then combined directly at the normal equation level. The normal equation system has a kite structure. Depending on the arc length N and the chosen polynomial degree d, it can be quite sparse. The structure of the normal equation system is illustrated in fig. 6.3.

The initial orientations are improved with the adjusted $\Delta\hat{\alpha}$ to yield $\hat{q}$, which is used as q_0 for the next iteration. The estimated calibration parameters $\Delta\hat{x}_{\text{cal}}$ are applied to the angular acceleration observations, giving the new $\dot{\omega}_0$. After convergence, the $\hat{q}$ give the adjusted orientation of the satellite, the result of the SCA/ACC sensor fusion.

A further product of this approach is the covariance matrix of the adjusted parameters. This matrix is divided along the same lines as the normal equation system set up with eq. (6.2.17), and has the entries

$$\hat{\mathbf{\Sigma}}_{\hat{x}\hat{x}} = \begin{bmatrix} \hat{\mathbf{\Sigma}}_{\hat{\alpha}\hat{\alpha}} & \hat{\mathbf{\Sigma}}_{\hat{\alpha}\hat{x}_{\text{cal}}} \\ \hat{\mathbf{\Sigma}}_{\hat{\alpha}\hat{x}_{\text{cal}}}^{\mathsf{T}} & \hat{\mathbf{\Sigma}}_{\hat{x}_{\text{cal}}\hat{x}_{\text{cal}}} \end{bmatrix} \quad . \tag{6.2.18}$$

$\hat{\mathbf{\Sigma}}_{\hat{\alpha}\hat{\alpha}}$ is the fully populated complete variance-covariance matrix for the satellite orientation along the orbit arc, given in the SRF. The 3×3 blocks on the main diagonal are the covariance matrices of the orientation at that specific epoch.

6.3 Orbit Integration

For ITSG-Grace2016, the GRACE dynamic orbits are integrated using the algorithm described in chapter 5 with the improvements laid out in chapter 7. The orbits are

integrated using the models given in table 6.1, as well as the observations of the GRACE accelerometers.

Where the dynamic orbit integration algorithm as described in chapter 5 only fits the initial state of each arc to the approximate orbit used as input, GRACE offers more observations that can be employed here: POD orbits derived from hl-SST observations by the GPS receiver and the ll-SST observations of the KBR system. In ITSG-Grace2016, the dynamic orbit is also fit to both of these observation groups. Accelerometer calibration parameters x_{cal} as described in section 6.4.1 are co-estimated with the initial satellite state for each arc. The observation system for this orbit fit is

$$
\begin{bmatrix} l_{\text{sst}} \\ l_{\text{pod,A}} \\ l_{\text{pod,B}} \end{bmatrix} = \begin{bmatrix} A_{\text{sst}} & \Phi_A & \Phi_B \\ A_{\text{pod,A}} & \Phi_A & 0 \\ A_{\text{pod,B}} & 0 & \Phi_B \end{bmatrix} \begin{bmatrix} x_{\text{cal}} \\ y_{0,A} \\ y_{0,B} \end{bmatrix} , \tag{6.3.1}
$$

where the design matrices A are those described in section 6.4.3. The newly estimated initial states $\hat{y}_{0,A}$ and $\hat{y}_{0,B}$ are then used to improve the dynamic orbit estimates of GRACE-A and GRACE-B according to eq. (5.1.14). The complete process for integrating the ITSG-Grace2016 dynamic orbits consists of three steps, as illustrated in fig. 6.4.

Table 6.1: Background models for dynamic orbit integration in ITSG-Grace2016.

Effect	Model
Mean earth gravity	GOCO05s [1]
Trend	GOCO05s [1]
Annual & semi-annual oscillation	GOCO05s [1]
Atmosphere & ocean dealiasing	AOD1B RL05 [2]
Earth rotation	IERS 2010 [3]
Solid earth tides	IERS 2010 [3]
Pole tides	IERS 2010 [3]
Relativistic effects	IERS 2010 [3]
Third body forces	JPL DE421 [4]
Ocean tides	EOT11a [5]
Ocean pole tides	Desai, 2002 [6]
Atmospheric tides	Atmospheric tide loading calculator [7]

[1] Mayer-Gürr, Kvas, et al., 2015   [2] Flechtner, Dobslaw, and Fagiolini, 2014   [3] Petit and Luzum, 2010   [4] Folkner, Williams, and Boggs, 2008   [5] The EOT11a model was produced by DGFI based on multi-mission altimeter data and distributed via OpenADB (http://openadb.dgfi.badw.de). More details on the product are available in (Savcenko et al., 2012).   [6] Using coefficients published in the *IERS Conventions (2010)*.   [7] van Dam and Ray, 2010
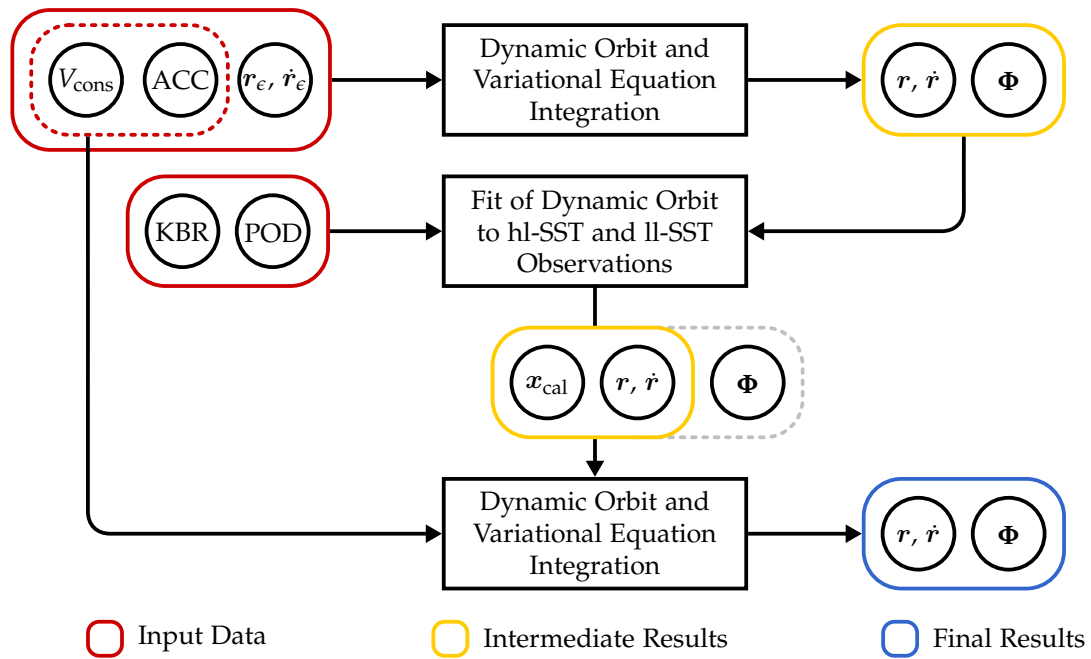
Figure 6.4: Data flow in ITSG-Grace2016 dynamic orbit integration for one spacecraft. V_cons are the background models from which the accelerations due to conservative forces are derived, as given in table 6.1. $\mathbf{\Phi}$ is the state transition matrix of the variational equations. $\boldsymbol{x}_\text{cal}$ are the co-estimated calibration parameters for the accelerometer.

An initial integration step using background models, the level 1B dynamic orbit, and the accelerometer observations as input is followed by an orbit fit to KBR and POD data, as described above. The resulting dynamic orbit and calibration parameters are used to re-integrate the orbit once more to ensure convergence. This results in the final dynamic orbit and state transition matrix, which are used in the set-up of GRACE hl-SST and ll-SST observation equations. It is important that all calibration and state parameters estimated here are also re-estimated when computing the final gravity field models, so as to not bias the solution towards the a priori models used in the orbit integration.

6.4 Functional Models

All observation equations for GRACE in ITSG-Grace2016 are derived using variational equations. After determining the dynamic orbit for both GRACE spacecraft as described in chapter 5 and section 6.3, the parameter sensitivity matrix for each spacecraft is computed from eq. (5.3.13). Here, the matrix $\boldsymbol{Z_p}$ from eq. (5.3.9) describing the dependence of the forces acting on the satellite on some parameters $\boldsymbol{p}$ is needed. At this point, recall that $\boldsymbol{f}(\tau)$ is in fact a rather complex function, describing the

superposition of accelerations due to gravitational, tidal, and non-conservative forces

$$f(\tau) = g(\tau) + \ddot{r}_{\text{ACC}}(\tau) \ . \tag{6.4.1}$$

In ITSG-Grace2016, the parameters to be estimated are divided in groups along similar lines. The first parameter group p_{grav} contains the parameters due to gravitational effects. These parameters are common to both satellites, as they move in the same conservative potential field. The second parameter group p_{sat} contains the parameters describing the dependence of the observations on non-conservative forces. These are specific to each satellite. These two sets of parameters p_{grav} and p_{sat} are *force model parameters*, and are computed through integrating the parameter sensitivity matrix in the variational equations. A third parameter group p_{sst} is neither specific to each satellite nor to the potential fields in which the satellite move, but rather describes effects due to the specific ll-SST observation system and geometry. The ll-SST parameters p_{sst} are computed using the dynamic orbits resulting from the variational equations as a Taylor point.

6.4.1 Force Model Parameters

To compute $Z_p(\tau)$, the partials of the force $f(\tau)$ w.r.t. the force model parameters are needed. The following paragraphs give a short description of how these are obtained and then integrated.

Gravity Field Parameters

In ITSG-Grace2016, both monthly mean and daily mean Stokes coefficients for each day of the month $k \in [1, K]$ are estimated. The total disturbing potential on the k-th day of the month V_k^{t} is modelled as the sum of the monthly mean potential V^{m} and the mean of the potential for that day V_k^{d}

$$V_k^{\text{t}} = V^{\text{m}} + V_k^{\text{d}} \ . \tag{6.4.2}$$

The total potential for the month can be written as a piecewise constant function

$$V^{\text{t}}(t) = V^{\text{m}} + \sum_{k=1}^{K} \delta_k(t) V_k^{\text{d}} \tag{6.4.3}$$

as illustrated in fig. 6.5, and with

$$\delta_k(t) = \begin{cases} 1 & \text{if } t \text{ is on the } k\text{-th day,} \\ 0 & \text{otherwise.} \end{cases} \tag{6.4.4}$$
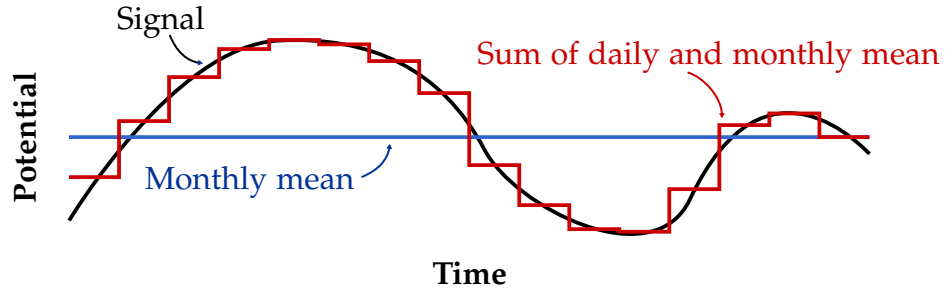
Figure 6.5: Daily total potential as piecewise constant function.

The monthly coefficients are estimated from degree 2 and order 0 to degree and order (D/O) 120, while the daily coefficients are only estimated to D/O 40. Schematically, the observation equations for the Stokes coefficients are

$$
\begin{bmatrix} l_1 \\ l_2 \\ \vdots \\ l_{K-1} \\ l_K \end{bmatrix} = \begin{bmatrix} \begin{array}{ccccc|c} \boldsymbol{A}_1^{\mathrm{d}} & \boldsymbol{0} & \cdots & \cdots & \boldsymbol{0} \\ \boldsymbol{0} & \boldsymbol{A}_2^{\mathrm{d}} & \ddots & & \vdots \\ \vdots & \ddots & \ddots & \ddots & \vdots \\ \vdots & & \ddots & \boldsymbol{A}_{K-1}^{\mathrm{d}} & \boldsymbol{0} \\ \boldsymbol{0} & \cdots & \cdots & \boldsymbol{0} & \boldsymbol{A}_K^{\mathrm{d}} \end{array} & \boldsymbol{A}^{\mathrm{m}} \end{bmatrix} \cdot \begin{bmatrix} \boldsymbol{x}_1^{\mathrm{d}} \\ \boldsymbol{x}_2^{\mathrm{d}} \\ \vdots \\ \boldsymbol{x}_{K-1}^{\mathrm{d}} \\ \boldsymbol{x}_K^{\mathrm{d}} \\ \boldsymbol{x}^{\mathrm{m}} \end{bmatrix} , \tag{6.4.5}
$$

where $\boldsymbol{A}_1^{\mathrm{d}} \ldots \boldsymbol{A}_K^{\mathrm{d}}$ are the observations equations for the daily Stokes coefficients

$$
\boldsymbol{x}_k^{\mathrm{d}} = \begin{bmatrix} c_{2,0} & \cdots & s_{40,40} \end{bmatrix}^{\mathsf{T}} , \tag{6.4.6}
$$

and $\boldsymbol{A}^{\mathrm{m}}$ are the observation equations for the monthly Stokes coefficients

$$
\boldsymbol{x}^{\mathrm{m}} = \begin{bmatrix} c_{2,0} & \cdots & s_{120,120} \end{bmatrix}^{\mathsf{T}} . \tag{6.4.7}
$$

Equivalently, $l_1 \ldots l_K$ are the observations for the individual days of the month. For the case of piecewise constant daily potential coefficients, the observation equations for the daily coefficients are identical to those of the monthly coefficients of the same degree and order. This means that the respective partials only need to be computed once, and can be re-used for both design matrix blocks, as illustrated in fig. 6.6.

The partials of the gravity field w.r.t. the Stokes coefficients are computed once for GRACE-A and once for GRACE-B (see e.g. Ilk, 1983)

$$
\boldsymbol{J}_{\mathrm{grav,A}}(\tau) = \begin{bmatrix} \dfrac{\partial \boldsymbol{g}(\tau, \boldsymbol{r}_{\mathrm{A}}(\tau))}{\partial c_{2,0}} & \cdots & \dfrac{\partial \boldsymbol{g}(\tau, \boldsymbol{r}_{\mathrm{A}}(\tau))}{\partial s_{120,120}} \end{bmatrix} , \tag{6.4.8}
$$

$$
\boldsymbol{J}_{\mathrm{grav,B}}(\tau) = \begin{bmatrix} \dfrac{\partial \boldsymbol{g}(\tau, \boldsymbol{r}_{\mathrm{B}}(\tau))}{\partial c_{2,0}} & \cdots & \dfrac{\partial \boldsymbol{g}(\tau, \boldsymbol{r}_{\mathrm{B}}(\tau))}{\partial s_{120,120}} \end{bmatrix} . \tag{6.4.9}
$$

Low degree monthly coefficients

High degree monthly coefficients
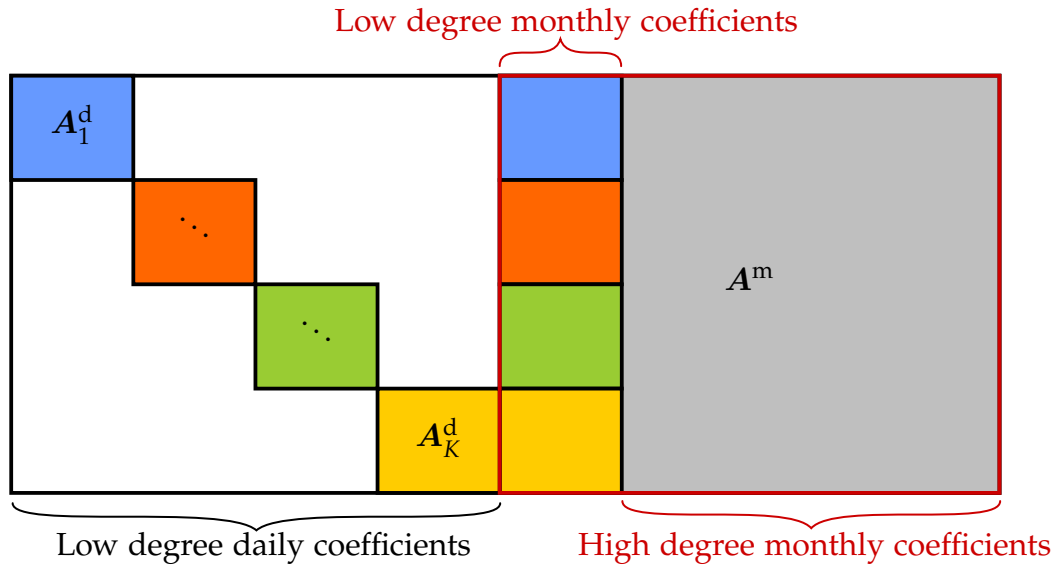
Low degree daily coefficients

Figure 6.6: Schematic of daily and monthly Stokes coefficients design matrix blocks. Identical colours indicate that the low degree daily coefficient blocks are identical to the low degree monthly coefficient blocks for the same day.

They are then inserted into eq. (5.3.9) for integration. With the K-day vector of daily Stokes coefficients

$$p_{\text{grav,d}} = \begin{bmatrix} x_1^{\text{d}} \\ \vdots \\ x_K^{\text{d}} \end{bmatrix} \qquad (6.4.10)$$

and the vector of monthly Stokes coefficients

$$p_{\text{grav,m}} = x^{\text{m}} \qquad (6.4.11)$$

the complete vector of gravity field parameters is

$$p_{\text{grav}} = \begin{bmatrix} p_{\text{grav,d}} \\ p_{\text{grav,m}} \end{bmatrix} . \qquad (6.4.12)$$

More compactly, eq. (6.4.5) can then be written as

$$l = \begin{bmatrix} A^{\text{d}} & A^{\text{m}} \end{bmatrix} \begin{bmatrix} p_{\text{grav,d}} \\ p_{\text{grav,m}} \end{bmatrix} \qquad (6.4.13)$$

With this parametrization, the equation system is not solvable directly, as the columns of A_{m} with the low degree monthly Stokes coefficients are a linear combination of the daily coefficient blocks, inducing a rank defect in the normal equation system. In ITSG-Grace2016 this problem is treated by requiring the daily solutions to have zero

mean. This is sensible, as the mean of the monthly gravity field is parametrized in the monthly mean coefficients. Further, the temporal and spatial correlations of the daily gravity fields are loosely constrained to conform to a process model derived from geophysical models.

This is implemented as a set of pseudo-observations for the geophysical model $l_{\text{gpm}} = 0$ for the daily gravity field parameters, with an associated design matrix A_{gpm} and cofactor matrix Q_{gpm}:

$$\begin{bmatrix} l \\ l_{\text{gpm}} \end{bmatrix} = \begin{bmatrix} A^{\text{d}} & A^{\text{m}} \\ A_{\text{gpm}} & 0 \end{bmatrix} \begin{bmatrix} p_{\text{grav,d}} \\ p_{\text{grav,m}} \end{bmatrix} \tag{6.4.14}$$

A more in-depth description of this procedure is out of scope for this thesis. The approach is based on the GRACE Kalman filter introduced by Kurtenbach, 2011. A complete description of the implementation details of this approach with the refinements and further development made for ITSG-Grace2016 will be able to be found in the upcoming dissertation of Andreas Kvas, expected to be released in 2019.

Satellite Parameters

The observation of the GRACE accelerometers are not only subject to random noise, but also to systematic effects due to miscalibration and instrument imperfections. In ITSG-Grace2016, calibration parameters are estimated for each accelerometer using the calibration equation

$$\ddot{r}_{\text{cal}} = S \ddot{r}_{\text{obs}} + b \, . \tag{6.4.15}$$

Here, S is a fully populated 3×3 matrix describing the accelerometer scale factors, cross-talk between the observation axes, and the misalignment of the accelerometer with the SRF. The vector b parametrizes one bias per accelerometer axis.

In ITSG-Grace2016, the entries in S are estimated as constants per day. The biases b are estimated daily as uniform cubic basis splines (UCBS) with a knot interval of 6 h. Klinger (2018) gives a comprehensive analysis of this parametrization. This results in 30 calibration parameters x_{cal} being estimated per day and satellite. The parameter vector is

$$p_{\text{sat}} = \begin{bmatrix} x_{\text{cal,A},1} \dots x_{\text{cal,A},K} & x_{\text{cal,B},1} \dots x_{\text{cal,B},K} \end{bmatrix}^{\mathsf{T}} \tag{6.4.16}$$

with the Jacobians

$$J_{\text{sat,A}}(\tau) = \begin{bmatrix} \dfrac{\partial \ddot{r}_{\text{ACC,A}}(\tau)}{\partial x_{\text{cal,A},1}} & \dots & \dfrac{\partial \ddot{r}_{\text{ACC,A}}(\tau)}{\partial x_{\text{cal,A},K}} \end{bmatrix}, \tag{6.4.17}$$

$$J_{\text{sat,B}}(\tau) = \begin{bmatrix} \dfrac{\partial \ddot{r}_{\text{ACC,B}}(\tau)}{\partial x_{\text{cal,B},1}} & \dots & \dfrac{\partial \ddot{r}_{\text{ACC,B}}(\tau)}{\partial x_{\text{cal,B},K}} \end{bmatrix}. \tag{6.4.18}$$

Integration of the Parameter Sensitivity Matrix

The parameter sensitivity matrix is integrated for each spacecraft $i = \mathrm{A}, \mathrm{B}$ using eq. (5.3.13) with

$$
\boldsymbol{Z}_{p,i}(\tau) = \begin{bmatrix} \boldsymbol{0} & \boldsymbol{0} \\ \boldsymbol{J}_{\mathrm{grav},i}(\tau) & \boldsymbol{J}_{\mathrm{sat},i}(\tau) \end{bmatrix} \tag{6.4.19}
$$

and an integration polynomial of degree 7, yielding — for each satellite — the complete variational equations

$$
\boldsymbol{\Omega}_i = \begin{bmatrix} \boldsymbol{S}_{\mathrm{grav},i} & \boldsymbol{S}_{\mathrm{sat},i} & \boldsymbol{\Phi}_i \end{bmatrix} . \tag{6.4.20}
$$

The variational equations are now available for all epochs, containing both the derivatives w.r.t. the position and the derivatives w.r.t. the velocity:

$$
\boldsymbol{\Omega}_i(\tau) = \begin{bmatrix} \boldsymbol{S}_{\mathrm{grav},i}^{r}(\tau) & \boldsymbol{S}_{\mathrm{sat},i}^{r}(\tau) & \boldsymbol{\Phi}_i^{r}(\tau) \\ \boldsymbol{S}_{\mathrm{grav},i}^{\dot{r}}(\tau) & \boldsymbol{S}_{\mathrm{sat},i}^{\dot{r}}(\tau) & \boldsymbol{\Phi}_i^{\dot{r}}(\tau) \end{bmatrix} . \tag{6.4.21}
$$

6.4.2 Low-Low SST Parameters

In ITSG-Grace2016, the KBR antenna phase centre coordinates for each spacecraft are estimated as constants, once per month. The observation equations are computed by taking the derivative of the ranging equation eq. (4.3.7) w.r.t. the KBR APC coordinates c_A and c_B. As the APCs only occur in the antenna offset correction, the derivative for an APC c_i is

$$
\frac{\partial \rho_{\mathrm{KBR}}}{\partial c_i} = \frac{\partial \left\| \boldsymbol{u} + \boldsymbol{v} \right\|}{\partial c_i} . \tag{6.4.22}
$$

The chain rule applies, with

$$
\frac{\partial \left\| \boldsymbol{u} + \boldsymbol{v} \right\|}{\partial c_i} = \frac{\partial \left\| \boldsymbol{u} + \boldsymbol{v} \right\|}{\partial \boldsymbol{v}} \frac{\partial \boldsymbol{v}}{\partial c_i} . \tag{6.4.23}
$$

Writing

$$
\left\| \boldsymbol{u} + \boldsymbol{v} \right\| = \sqrt{\langle \boldsymbol{u}, \boldsymbol{u} \rangle + \langle \boldsymbol{v}, \boldsymbol{v} \rangle + 2 \cdot \langle \boldsymbol{u}, \boldsymbol{v} \rangle} , \tag{6.4.24}
$$

the first partial in eq. (6.4.23) is

$$
\begin{aligned}
\frac{\partial \left\| \boldsymbol{u} + \boldsymbol{v} \right\|}{\partial \boldsymbol{v}} &= \frac{1}{2 \cdot \left\| \boldsymbol{u} + \boldsymbol{v} \right\|} \frac{\partial}{\partial \boldsymbol{v}} \left(\langle \boldsymbol{u}, \boldsymbol{u} \rangle + \langle \boldsymbol{v}, \boldsymbol{v} \rangle + 2 \cdot \langle \boldsymbol{u}, \boldsymbol{v} \rangle \right) \\
&= \frac{1}{\left\| \boldsymbol{u} + \boldsymbol{v} \right\|} \left(\boldsymbol{u} + \boldsymbol{v} \right)^{\mathsf{T}} .
\end{aligned} \tag{6.4.25}
$$

The second partials in eq. (6.4.23) are

$$\frac{\partial v}{\partial c_A} = -R_A \qquad \text{and} \qquad \frac{\partial v}{\partial c_B} = R_B . \qquad (6.4.26)$$

Inserting into eq. (6.4.23) gives

$$\frac{\partial \rho_{KBR}}{\partial c_A} = -\frac{(u+v)^T}{\|u+v\|} R_A , \qquad (6.4.27)$$

$$\frac{\partial \rho_{KBR}}{\partial c_B} = \frac{(u+v)^T}{\|u+v\|} R_B , \qquad (6.4.28)$$

which are the observation equations for the 6 ll-SST parameters per month:

$$p_{sst} = \begin{bmatrix} c_A \\ c_B \end{bmatrix} . \qquad (6.4.29)$$

The complete Jacobian for the ll-SST parameters is then simply

$$J_{sst} = \begin{bmatrix} \dfrac{\partial \rho_{KBR}}{\partial c_A} & \dfrac{\partial \rho_{KBR}}{\partial c_B} \end{bmatrix} . \qquad (6.4.30)$$

6.4.3 Observation Equation System

With all Jacobians available, the observation equation system for the GRACE hl-SST and ll-SST observations can be set up. The observation equations are set up for each short arc $m \in [1, M]$, using the variational equations integrated for each day of a month $k \in [1, K]$. The combined parameter vector for one short arc is

$$x_m = \begin{bmatrix} p_{grav,d} & p_{sat,A}^k & p_{sat,B}^k & p_{sst} & y_{0,A}^k & y_{0,B}^k & p_{grav,m} \end{bmatrix}^T . \qquad (6.4.31)$$

It is important to note that the estimated parameters can be the same for multiple short arcs. The monthly Stokes coefficients, for example, are only estimated once per month. The parameters $p_{sat,A}^k$, $p_{sat,B}^k$, $y_{0,A}^k$, and $y_{0,B}^k$ are estimated once per day k, and are the same for all short arcs m in this day. This must be considered when accumulating the normal equations from the individual short arcs. The peculiar ordering of the parameters, with the daily Stokes coefficients at the beginning of the parameter vector, and the monthly Stokes coefficients at the end, is due to some optimizations that can then be employed in eliminating the non-target parameters, namely all but $p_{grav,m}$, from the resulting normal equation system. These optimizations are described in Kvas (2014).

In ITSG-Grace2016 three observation groups are processed in the LSA for gravity field determination: The spacecraft positions from kinematic orbits as observed by the GPS, the ll-SST KBR range-rate observations, and the pseudo-observations constraining the daily gravity fields. Starting from the sought parameters and the known observations,

the linearised observation equation system for one short arc can be set up symbolically, giving

$$
\begin{bmatrix} \Delta l_{\text{pod,A}} \\ \Delta l_{\text{pod,B}} \\ \Delta l_{\text{sst}} \\ l_{\text{gpm}} \end{bmatrix} = \begin{bmatrix} A_{\text{pod,A}}^{\text{grav,d}} & A_{\text{pod,A}}^{\text{sat}} & 0 & 0 \\ A_{\text{pod,B}}^{\text{grav,d}} & 0 & A_{\text{pod,B}}^{\text{sat}} & 0 \\ A_{\text{sst}}^{\text{grav,d}} & A_{\text{sst,A}}^{\text{sat}} & A_{\text{sst,B}}^{\text{sat}} & A_{\text{sst}}^{\text{sst}} \\ A_{\text{gpm}}^{\text{grav,d}} & 0 & 0 & 0 \end{bmatrix} \cdots
$$
$$
\cdots \begin{bmatrix} A_{\text{pod,A}}^{\text{state}} & 0 & A_{\text{pod,A}}^{\text{grav,m}} \\ 0 & A_{\text{pod,B}}^{\text{state}} & A_{\text{pod,B}}^{\text{grav,m}} \\ A_{\text{sst,A}}^{\text{state}} & A_{\text{sst,B}}^{\text{state}} & A_{\text{sst}}^{\text{grav,m}} \\ 0 & 0 & 0 \end{bmatrix} \begin{bmatrix} \Delta p_{\text{grav,d}} \\ \Delta p_{\text{sat,A}} \\ \Delta p_{\text{sat,B}} \\ \Delta p_{\text{sst}} \\ \Delta y_{0,A} \\ \Delta y_{0,B} \\ \Delta p_{\text{grav,m}} \end{bmatrix} , \quad (6.4.32)
$$

or $l = Ax$ in short. The indices for the arc m and day k have been omitted here for clarity. In eq. (6.4.32), empty matrix segments appear where the observations do not depend on the sought parameters. The POD observations for GRACE-A, for example, depend neither on the accelerometer calibration parameters for GRACE-B nor on that spacecraft's initial state.

When accumulating the observation equations, care has to be taken to not mix up parameters referring to only a specific day with other parameters of the same type referring to another day. An ordering for the parameter vector, and accordingly the blocks in the normal equation system, has to be chosen that ensures that the correct observation equations are accumulated together. Table 6.2 gives a summary of all $P = 46\,842$ parameters estimated for a typical 31 day ITSG-Grace2016 monthly solution.

Table 6.2: Estimated parameters for a month of $K = 31$ days

Type	Parameter	Parametrization	Intervals	Per Interval	Total
Potential	c_{nm}, s_{nm}	D/O 2 to 40	Daily	957	29 967
Potential	c_{nm}, s_{nm}	D/O 2 to 120	Monthly	14 637	14 637
ACC bias	b	UCBS	Daily	21 / sat	1302
ACC scale	S	Constant	Daily	9 / sat	558
APC vector	c	Constant	Monthly	3 / sat	6
Initial State	y_0	-	Daily	6 / sat	372
Total					46 842

Observation Equations for hl-SST

The observable in hl-SST POD is the spacecraft position. The equations describing the dependence of the spacecraft position at time τ on the sought parameters x are exactly the variational equations. In ITSG-Grace2016, only the spacecraft position is used as an observable for POD. The velocity is not used, as it is only derived from the POD positions, not determined directly. The linearised observation difference is then the POD position r_{pod} reduced by the dynamic orbit position r_{dyn}:

$$\Delta l_{\mathrm{pod}} = r_{\mathrm{pod}} - r_{\mathrm{dyn}} \tag{6.4.33}$$

The design matrix for the monthly gravity field parameters for each spacecraft i is simply the appropriate parameter sensitivity matrix

$$A_{\mathrm{pod},i}^{\mathrm{grav,m}} = S_{\mathrm{grav},i}^{r} \, . \tag{6.4.34}$$

The design matrices for the daily Stokes coefficients can be computed herefrom according to section 6.4.1. The design matrices for the satellite parameters are similarly

$$A_{\mathrm{pod},i}^{\mathrm{sat}} = S_{\mathrm{sat},i}^{r} \, . \tag{6.4.35}$$

The design matrices for the satellite states are the state transition matrices

$$A_{\mathrm{pod},i}^{\mathrm{state}} = \Phi_{i}^{r} \, . \tag{6.4.36}$$

Observation Equations for ll-SST

In ITSG-Grace2016, ll-SST observations are processed at the range rate level. The range rate for the satellites COMs is given in eq. (4.3.8) as

$$\dot{\rho}_{\mathrm{COM}}(\tau) = \langle e(\tau), \dot{u}(\tau) \rangle = e^{\mathsf{T}}(\tau)\dot{u}(\tau) = \frac{1}{\|u(\tau)\|} u^{\mathsf{T}}(\tau)\dot{u}(\tau) \, . \tag{6.4.37}$$

The range rate depends on both the positions of the spacecraft, as components of u, and their velocities, as components of $\dot{u}$. For brevity, the index for the COM is omitted in the following derivations, while understanding that all ranges and range rates refer to the spacecraft COM. Similarly, the time index is also dropped. The derivative of the range rate w.r.t. to some parameters x is

$$\frac{\partial \dot{\rho}}{\partial x} = \frac{\partial \dot{\rho}}{\partial u}\frac{\partial u}{\partial x} + \frac{\partial \dot{\rho}}{\partial \dot{u}}\frac{\partial \dot{u}}{\partial x} \, . \tag{6.4.38}$$

The derivative of the range rate w.r.t. the satellite baseline is

$$\frac{\partial \dot{\rho}}{\partial u} = \frac{\partial}{\partial u}\langle e, \dot{u} \rangle = \frac{\partial}{\partial u} e^{\mathsf{T}}\dot{u} = \frac{\partial}{\partial u}\left(\frac{1}{\|u\|} u^{\mathsf{T}}\dot{u} \right) \tag{6.4.39}$$

Now, due to $\|\boldsymbol{u}\| = \left(\boldsymbol{u}^\mathsf{T}\boldsymbol{u}\right)^{1/2}$

$$\frac{\partial}{\partial \boldsymbol{u}}\frac{1}{\|\boldsymbol{u}\|} = -\frac{1}{\|\boldsymbol{u}\|^3}\boldsymbol{u}^\mathsf{T} \tag{6.4.40}$$

and

$$\frac{\partial}{\partial \boldsymbol{u}}\boldsymbol{u}^\mathsf{T}\dot{\boldsymbol{u}} = \frac{\partial}{\partial \boldsymbol{u}}\dot{\boldsymbol{u}}^\mathsf{T}\boldsymbol{u} = \dot{\boldsymbol{u}}^\mathsf{T} \ . \tag{6.4.41}$$

Putting together the chain rule, eq. (6.4.39) is

$$\begin{aligned}
\frac{\partial \dot{\rho}}{\partial \boldsymbol{u}} &= \frac{1}{\|\boldsymbol{u}\|}\dot{\boldsymbol{u}}^\mathsf{T} - \frac{1}{\|\boldsymbol{u}\|^3}\boldsymbol{u}^\mathsf{T} \cdot \left(\boldsymbol{u}^\mathsf{T}\dot{\boldsymbol{u}}\right) \\
&= \frac{1}{\rho}\dot{\boldsymbol{u}}^\mathsf{T} - \frac{1}{\|\boldsymbol{u}\|}\boldsymbol{e}^\mathsf{T} \cdot \left(\boldsymbol{e}^\mathsf{T}\dot{\boldsymbol{u}}\right) \\
&= \frac{1}{\rho}\dot{\boldsymbol{u}}^\mathsf{T} - \frac{\dot{\rho}}{\rho}\boldsymbol{e}^\mathsf{T}
\end{aligned} \tag{6.4.42}$$

The derivative of the range rate w.r.t. the differential velocity is

$$\frac{\partial \dot{\rho}}{\partial \dot{\boldsymbol{u}}} = \frac{\partial}{\partial \dot{\boldsymbol{u}}}\boldsymbol{e}^\mathsf{T}\dot{\boldsymbol{u}} = \boldsymbol{e}^\mathsf{T} \tag{6.4.43}$$

In eq. (6.4.38), the derivatives of the baseline and differential velocity can be further expanded to

$$\frac{\partial \boldsymbol{u}}{\partial \boldsymbol{x}} = \frac{\partial \boldsymbol{u}}{\partial \boldsymbol{r}_\mathrm{A}}\frac{\partial \boldsymbol{r}_\mathrm{A}}{\partial \boldsymbol{x}} + \frac{\partial \boldsymbol{u}}{\partial \boldsymbol{r}_\mathrm{B}}\frac{\partial \boldsymbol{r}_\mathrm{B}}{\partial \boldsymbol{x}} \ , \tag{6.4.44}$$

$$\frac{\partial \dot{\boldsymbol{u}}}{\partial \boldsymbol{x}} = \frac{\partial \dot{\boldsymbol{u}}}{\partial \dot{\boldsymbol{r}}_\mathrm{A}}\frac{\partial \dot{\boldsymbol{r}}_\mathrm{A}}{\partial \boldsymbol{x}} + \frac{\partial \dot{\boldsymbol{u}}}{\partial \dot{\boldsymbol{r}}_\mathrm{B}}\frac{\partial \dot{\boldsymbol{r}}_\mathrm{B}}{\partial \boldsymbol{x}} \ . \tag{6.4.45}$$

With

$$\frac{\partial \boldsymbol{u}}{\partial \boldsymbol{r}_\mathrm{A}} = \frac{\partial \dot{\boldsymbol{u}}}{\partial \dot{\boldsymbol{r}}_\mathrm{A}} = -1 \ , \tag{6.4.46}$$

$$\frac{\partial \boldsymbol{u}}{\partial \boldsymbol{r}_\mathrm{B}} = \frac{\partial \dot{\boldsymbol{u}}}{\partial \dot{\boldsymbol{r}}_\mathrm{B}} = 1 \ , \tag{6.4.47}$$

this simplifies to

$$\frac{\partial \boldsymbol{u}}{\partial \boldsymbol{x}} = \frac{\partial \boldsymbol{r}_\mathrm{B}}{\partial \boldsymbol{x}} - \frac{\partial \boldsymbol{r}_\mathrm{A}}{\partial \boldsymbol{x}} \ , \tag{6.4.48}$$

$$\frac{\partial \dot{\boldsymbol{u}}}{\partial \boldsymbol{x}} = \frac{\partial \dot{\boldsymbol{r}}_\mathrm{B}}{\partial \boldsymbol{x}} - \frac{\partial \dot{\boldsymbol{r}}_\mathrm{B}}{\partial \boldsymbol{x}} \ . \tag{6.4.49}$$

Going from generic parameters $\boldsymbol{x}$ to the specific parameters set up in ITSG-Grace2016, the derivatives of the positions and velocities of the spacecraft w.r.t. the gravity field parameters, satellite parameters, and the initial state are the variational equations from

eq. (6.4.21). With this information, the appropriate row of matrices in eq. (6.4.32) can be determined by inserting the correct partials in eq. (6.4.38). One row of the design matrix, corresponding to one point in time τ, for the monthly gravity field parameters from ll-SST observations is

$$A_{\text{sst}}^{\text{grav,m}} = \left(\frac{1}{\rho}\dot{u}^{\mathsf{T}} - \frac{\dot{\rho}}{\rho}e^{\mathsf{T}}\right)\left(S_{\text{grav,B}}^{r} - S_{\text{grav,A}}^{r}\right) + e^{\mathsf{T}}\left(S_{\text{grav,B}}^{\dot{r}} - S_{\text{grav,A}}^{\dot{r}}\right) , \quad (6.4.50)$$

again with the time τ omitted. The design matrices for the daily Stokes coefficients can be computed herefrom according to section 6.4.1. The design matrices w.r.t. to the satellite parameters for GRACE-A and GRACE-B are

$$A_{\text{sst,A}}^{\text{sat}} = \left(\frac{1}{\rho}\dot{u}^{\mathsf{T}} - \frac{\dot{\rho}}{\rho}e^{\mathsf{T}}\right)\left(-S_{\text{sat,A}}^{r}\right) + e^{\mathsf{T}}\left(-S_{\text{sat,A}}^{\dot{r}}\right) , \quad (6.4.51)$$

$$A_{\text{sst,B}}^{\text{sat}} = \left(\frac{1}{\rho}\dot{u}^{\mathsf{T}} - \frac{\dot{\rho}}{\rho}e^{\mathsf{T}}\right)\left(\ S_{\text{sat,B}}^{r}\right) + e^{\mathsf{T}}\left(\ S_{\text{sat,B}}^{\dot{r}}\right) , \quad (6.4.52)$$

and equivalently for the satellite states

$$A_{\text{sst,A}}^{\text{state}} = \left(\frac{1}{\rho}\dot{u}^{\mathsf{T}} - \frac{\dot{\rho}}{\rho}e^{\mathsf{T}}\right)\left(-\Phi_{\text{sat,A}}^{r}\right) + e^{\mathsf{T}}\left(-\Phi_{\text{sat,A}}^{\dot{r}}\right) , \quad (6.4.53)$$

$$A_{\text{sst,B}}^{\text{state}} = \left(\frac{1}{\rho}\dot{u}^{\mathsf{T}} - \frac{\dot{\rho}}{\rho}e^{\mathsf{T}}\right)\left(\ \Phi_{\text{sat,B}}^{r}\right) + e^{\mathsf{T}}\left(\ \Phi_{\text{sat,B}}^{\dot{r}}\right) . \quad (6.4.54)$$

Only the observation equations for the ll-SST parameters remain. The equations in section 6.4.2 were computed for range observations, while the observation equations for ITSG-Grace2016 are set up for range rates. The required range rate observation equations can be computed trough

$$\frac{\partial\dot{\rho}}{\partial p_{\text{sst}}} = \frac{\partial\dot{\rho}}{\partial\rho}\frac{\partial\rho}{\partial p_{\text{sst}}} . \quad (6.4.55)$$

As $\dot{\rho} = \partial\rho/\partial\tau$, eq. (6.4.55) can be written as

$$\frac{\partial\dot{\rho}}{\partial p_{\text{sst}}} = D\frac{\partial\rho}{\partial p_{\text{sst}}} , \quad (6.4.56)$$

with D a polynomial derivative matrix. In ITSG-Grace2016, a polynomial of degree 2 is used. The complete design matrix for the ll-SST parameters is (with eq. (6.4.30))

$$A_{\text{sst}}^{\text{sst}} = DJ_{\text{sst}} . \quad (6.4.57)$$

The reduced observation vector for the KBR observations $\dot{\rho}_{\text{KBR}}$ is, from the ranging equation (eq. (4.3.7)),

$$\Delta l_{\text{sst}} = \dot{\rho}_{\text{KBR}} + \Delta\dot{\rho}_{\text{AOC}} + \Delta\dot{\rho}_{\text{TOF}} + \Delta\dot{\rho}_{\text{Iono}} - \dot{\rho}_{\text{COM}} . \quad (6.4.58)$$

The sum $\dot{\rho}_{\text{KBR}} + \Delta\dot{\rho}_{\text{TOF}} + \Delta\dot{\rho}_{\text{Iono}}$ is given in the level 1B KBR product. $\dot{\rho}_{\text{COM}}$ is computed according to eq. (4.3.9). The derivative $\Delta\dot{\rho}_{\text{AOC}}$ is computed from $\Delta\rho_{\text{AOC}}$ using polynomial differentiation, as above, with orientations from the SCA/ACC sensor fusion.

6.5 Fit of Stochastic Model

To compute an optimal least squares solution of the daily and monthly Stokes coefficients, the stochastic characteristics of the observation data must be considered. In ITSG-Grace2016, four observation groups are present: the hl-SST POD observations for both GRACE-A and GRACE-B, the ll-SST KBR observations, and the pseudo-observations used to constrain the daily Stokes coefficients. Each observation group has associated residuals

$$
\begin{bmatrix} \Delta l_{\text{pod,A}} \\ \Delta l_{\text{pod,B}} \\ \Delta l_{\text{sst}} \\ l_{\text{gpm}} \end{bmatrix} = Ax + \begin{bmatrix} e_{\text{pod,A}} \\ e_{\text{pod,B}} \\ e_{\text{sst}} \\ e_{\text{gpm}} \end{bmatrix}
\tag{6.5.1}
$$

which are distributed according to their respective covariance matrices

$$
\begin{bmatrix} e_{\text{pod,A}} \\ e_{\text{pod,B}} \\ e_{\text{sst}} \\ e_{\text{gpm}} \end{bmatrix} \sim \mathrm{N}\left(0, \begin{bmatrix} \Sigma_{\text{podA}} & 0 & 0 & 0 \\ 0 & \Sigma_{\text{podB}} & 0 & 0 \\ 0 & 0 & \Sigma_{\text{sst}} & 0 \\ 0 & 0 & 0 & \Sigma_{\text{gpm}} \end{bmatrix}\right).
\tag{6.5.2}
$$

In ITSG-Grace2016, it is assumed that the observation groups are not cross-correlated. Only the structure of the covariance matrix due to the geophysical model Q_{gpm} is known a priori, the remaining covariance matrices are determined in ITSG-Grace2016 through variance component estimation.

The stochastic model is re-estimated for each generated monthly solution in a multi-step process. To this end, a GRACE monthly gravity field solution of decreased degree and order of only 60 is computed while iteratively adjusting the weights of the observation groups and refining the covariance structure of each observation group. The gravity field solution is computed at a reduced fidelity to speed up the time-consuming iteration of the computation.

6.5.1 Toeplitz Covariance Structure

The noise of the POD and KBR observations is assumed to be the result of a wide-sense stationary process, meaning that the autocovariance function of the noise signal does not vary with time, or in the case of ITSG-Grace2016, within one month. Such a process can be fully described by its autocovariance function (Etten, 2006)

$$
C_{xx}(t_1, t_2) = C_{xx}(t_2 - t_1) = C_{xx}(\Delta t) .
\tag{6.5.3}
$$

This covariance function is estimated once per observation type and month. The re-estimation for every month implies that the estimated noise model is stationary for

one month only, and can differ between any two months. Let Δt be the sampling in seconds and N the number of epochs in the arc. The covariance function for the arc can then be discretised as

$$C_{xx}^n = C_{xx}(n \cdot \Delta t) \,, \, n \in [0, N) \,. \tag{6.5.4}$$

The observations for the month have at this point been split into short arcs

$$l = \begin{bmatrix} l_1 & \dots & l_M \end{bmatrix}^\mathsf{T} \,, \tag{6.5.5}$$

each of length $N_m \leq N_{\max}$. For one arc of N_m POD or KBR observations, the cofactor matrix then has a Toeplitz structure

$$Q_{ll}^m = \begin{bmatrix} C_{xx}^0 & C_{xx}^1 & C_{xx}^2 & \cdots & C_{xx}^{N_m-1} \\ C_{xx}^1 & C_{xx}^0 & C_{xx}^1 & & C_{xx}^{N_m-2} \\ C_{xx}^2 & C_{xx}^1 & C_{xx}^0 & & C_{xx}^{N_m-3} \\ \vdots & & & \ddots & \vdots \\ C_{xx}^{N_m-1} & C_{xx}^{N_m-2} & C_{xx}^{N_m-3} & \cdots & C_{xx}^0 \end{bmatrix} \tag{6.5.6}$$

with the entries determined by the time lag and the autocovariance function of the noise signal from eq. (6.5.4). This cofactor matrix is identical for all arcs of the same observation type and the same length N. All cofactor matrices are slices of the longest possible cofactor matrix of size $N_{\max} \times N_{\max}$. The elements of the discretised covariance function C_{xx} completely define all of these cofactor matrices. This necessitates that the covariance function is also estimated for a length of $N_{\max}$, even though some arcs do not allow for the estimation of some of the longer time lags due to their shorter length $N_m < N_{\max}$.

Additionally, a variance factor is computed per observation type for each of the M short arcs of the month, giving appropriate weights to the individual arcs. These are the *arc-wise variance factors* σ_m^2, which together with the cofactor matrix give the complete covariance matrix for the arc

$$\Sigma_{ll}^m = \sigma_m^2 \cdot Q_{ll}^m \,. \tag{6.5.7}$$

A simplifying assumption is made that observations are not correlated between short arcs. This then gives the following block-diagonal covariance structure for a complete month of observations in one observation group:

$$\Sigma_{ll} = \begin{bmatrix} \Sigma_{ll}^1 & 0 & \cdots & 0 \\ 0 & \ddots & \ddots & \vdots \\ \vdots & \ddots & \ddots & 0 \\ 0 & \cdots & 0 & \Sigma_{ll}^M \end{bmatrix} \,. \tag{6.5.8}$$

As observations are treated as uncorrelated across observation groups and across individual short arcs, the observation equations for each arc can be computed and decorrelated independently of each other, and finally be accumulated at the normal equation level to compute a gravity field solution.

6.5.2 Covariance Function and Power Spectral Density

For a wide-sense stationary process such as the assumed observation noise, the co-variance function of the process and the power spectral density (PSD) of the process form a Fourier pair (Etten, 2006). As the covariance function describing the observation noise is only estimated and known in its discretised form, a discrete transform to the spectral domain is used to compute the PSD. For ITSG-Grace2016, the type I discrete cosine transform (DCT) is used (Rao and Yip, 1990). This transform implies that the covariance function is even at the origin, with

$$C_{xx}^{-n} = C_{xx}^{n} \tag{6.5.9}$$

and also even at the upper boundary of the domain, with

$$C_{xx}^{N_{\text{max}}-n} = C_{xx}^{N_{\text{max}}+n} \ . \tag{6.5.10}$$

As the DCT is a linear operator, it can be written as

$$\tilde{x} = X x \ , \tag{6.5.11}$$

with X the $N \times N$ matrix of DCT coefficients, x an $N \times 1$ vector of equidistant data points in the time domain, and $\tilde{x}$ the $N \times 1$ DCT of x. The elements of the DCT matrix X are (see e.g. Rao and Yip, 1990, p. 11)

$$X_{mn} = \sqrt{\frac{2}{N-1}} \left(k_m k_n \cos\left(\frac{mn\pi}{N-1}\right) \right) \ , \qquad m, n \in [0, N) \ , \tag{6.5.12}$$

with

$$k_i = \begin{cases} 1 & \text{if } i \neq 0 \\ \frac{1}{\sqrt{2}} & \text{otherwise.} \end{cases} \tag{6.5.13}$$

The PSD of the observation noise is then, in terms of the covariance function,

$$S_{xx} = X C_{xx} \ . \tag{6.5.14}$$

The elements of the PSD are

$$S_{xx}^{j} = S_{xx}(f_j) \ , \qquad j \in [0, N) \ . \tag{6.5.15}$$

with $f_0 = 0 \, \text{Hz}$ and f_{N-1} the Nyquist frequency of the signal. Each entry gives the amplitude of the observation noise at that specific frequency.

6.5.3 Estimation of Covariance Function

The Toeplitz cofactor matrix for each observation type can be written as a sum of N_{max} individual cofactor matrices, each only dependent on the covariance function of one

specific time lag. Let V_n be the $N_{\max} \times N_{\max}$ identity matrix for $n = 0$, and a zero matrix with only the n-th lower and upper diagonal ones otherwise, e.g. for $N_{\max} = 5$

$$V_2 = \begin{bmatrix} 0 & 0 & 1 & 0 & 0 \\ 0 & 0 & 0 & 1 & 0 \\ 1 & 0 & 0 & 0 & 1 \\ 0 & 1 & 0 & 0 & 0 \\ 0 & 0 & 1 & 0 & 0 \end{bmatrix} . \tag{6.5.16}$$

The cofactor matrix eq. (6.5.6) is then

$$Q_{ll}^m = \sum_{n=0}^{N_m-1} C_{xx}^n \cdot V_n . \tag{6.5.17}$$

Each value of the discretised covariance function corresponds to one specific covariance component V_n, and as such they can be separated using VCE. The arc-wise variance factors, the variance factor determining the weight of one individual short arc of one observation type w.r.t. all other arcs of that observation type, depend on the sum of all individual cofactor matrices associated with all time lags:

$$\Sigma_{ll}^m = \sigma_m^2 \cdot \sum_{n=0}^{N_m-1} C_{xx}^n \cdot V_n \tag{6.5.18}$$

To fit the stochastic model to the observation noise, the amplitude of the covariance function for each time lag C_{xx}^n must be determined.

If the covariance function were estimated directly in the time domain, the value for one specific time lag C_{xx}^n could however never change its sign, as the appropriate variance factor is always estimated as its square (compare eq. (2.6.8)). As the PSD is by definition always positive, this restriction does not impact its estimation. Negative values of the covariance function can then occur in the inverse DCT that give the covariance function from the estimated PSD. Thus, in ITSG-Grace2016, the PSD is estimated instead of the covariance function, even though the two are functionally interchangeable. This can be achieved in the spectral domain by determining the amplitude of the PSD at each frequency S_{xx}^j. Using VCE, the estimated amplitude for each frequency $j \in [0, N)$ can be written as

$$\hat{S}_{xx}^j = \hat{\alpha}_j^2 S_{xx}^j , \tag{6.5.19}$$

with S_{xx}^j an a priori value for the amplitude of the PSD at that frequency, and

$$\hat{\alpha}_j^2 = \frac{\tilde{\Omega}_j}{\tilde{s}_j} . \tag{6.5.20}$$

As the time lag of the covariance function, or conversely the frequency of the PSD, can appear in any of the covariance matrices Σ_{ll}^m of the M short arcs, depending

on their length, the estimator for the variance factor must also consider all of these contributions. Therefore,

$$\tilde{\Omega}_j = \sum_{m=1}^{M} \tilde{\Omega}_j^m \qquad \text{and} \qquad \tilde{s}_j = \sum_{m=1}^{M} \tilde{s}_j^m . \qquad (6.5.21)$$

The contributions to each frequency can be determined in two ways. The first is to transform the residuals and covariance components V_n to the spectral domain and then directly compute the $\tilde{\Omega}_j$ and $\tilde{s}_j$. The second option is to compute the Ω_n and s_n in the temporal domain, and then transform these to the spectral domain afterwards. The second approach is chosen, as it enables the exploitation of some time-domain symmetries in the computation, as is later explained in section 6.5.6. To this end, the contributors for each time lag $n \in [0, N)$ must be computed. With the covariance matrix for one time lag from eq. (6.5.18) and eq. (2.6.6), the square sum of residuals for one time lag in one arc is

$$\Omega_n^m = \begin{cases} \sigma_m^2 C_{xx}^n \cdot \left(\hat{e}^\mathsf{T} \Sigma_{ll}^{-\mathsf{T}} V_n \Sigma_{ll}^{-1} \hat{e} \right) & \text{if } n < N_m , \\ 0 & \text{otherwise,} \end{cases} \qquad (6.5.22)$$

while the redundancy is

$$s_n^m = \begin{cases} \sigma_m^2 C_{xx}^n \cdot \text{trace} \left(R V_n \right) & \text{if } n < N_m , \\ 0 & \text{otherwise.} \end{cases} \qquad (6.5.23)$$

In both eqs. (6.5.22) and (6.5.23), it is important to note that $\hat{e} = \hat{e}_m$, $\Sigma_{ll} = \Sigma_{ll}^m$, and $R = R_m$. This index has only been omitted for clarity. With

$$\Omega^m = \begin{bmatrix} \Omega_0^m & \dots & \Omega_{N-1}^m \end{bmatrix}^\mathsf{T} \qquad \text{and} \qquad s^m = \begin{bmatrix} s_0^m & \dots & s_{N-1}^m \end{bmatrix}^\mathsf{T} , \qquad (6.5.24)$$

the contributors to the individual frequencies of the PSD to be inserted into eq. (6.5.21) are the entries of the $N \times 1$ vectors

$$\tilde{\Omega}^m = X \Omega^m \qquad (6.5.25)$$
$$\tilde{s}^m = X s^m \qquad (6.5.26)$$

6.5.4 Estimation of Arc-wise Variance Factors

The arc-wise variance factors σ_m^2 ($m \in [1, M]$) can be estimated from the equations given in section 6.5.3. Specifically, where the covariance function was determined by estimating the amplitude of a specific frequency over all arcs, the arc-wise variance factors are determined by estimating the cumulative amplitude over all frequencies for one specific arc. The estimated variance factor for one arc is then

$$\hat{\alpha}_m^2 = \frac{\sum_{j=0}^{N-1} \tilde{\Omega}_j^m}{\sum_{j=0}^{N-1} \tilde{s}_j^m} . \qquad (6.5.27)$$

The estimated arc-wise variance factor is however *not* directly $\hat{\sigma}_m^2 = \hat{\alpha}_m^2 \sigma_m^2$. As the absolute magnitude of the covariance matrix has already been modified by adjusting the individual frequencies in the PSD, computing $\hat{\sigma}_m^2$ in this way would lead to a double consideration of the respective variance components. Instead, an intermediate quantity

$$\gamma_m^2 = \hat{\alpha}_m^2 \sigma_m^2 \tag{6.5.28}$$

is determined. The arc-wise variance factor is then this intermediate value normalized by the mean over all arcs with

$$\bar{\gamma} = \frac{1}{M} \sum_{m=1}^{M} \gamma_m \tag{6.5.29}$$

as

$$\hat{\sigma}_m^2 = \frac{\gamma_m^2}{\bar{\gamma}^2} \; . \tag{6.5.30}$$

The mean of the arc-wise variance factors is thus 1. The arc-wise variance factors only give the relative weighting of the arcs w.r.t. each other within the observation group. The covariance function determines the overall magnitude and structure of the covariance matrix for the observations.

6.5.5 Geophysical Signal

In addition to the complete stochastic model estimated for the satellite instruments, one variance factor per month is estimated for the stochastic model of the geophysical pseudo-observations. The standard apparatus for VCE given in section 2.6 is used to optimally scale the covariance matrix

$$\mathbf{\Sigma}_{\mathrm{gpm}} = \hat{\sigma}_{\mathrm{gpm}}^2 \mathbf{Q}_{\mathrm{gpm}} \; . \tag{6.5.31}$$

6.5.6 Implementation Notes

The variance component estimation as described in the previous sections is a computationally expensive algorithm, especially as multiple iterations are usually necessary to achieve good convergence. In GROOPS, the software used to compute ITSG-Grace2016, some optimizations have been implemented to reduce this computational effort. The following pages will give an overview of some of the most impactful of these optimizations. Further, some aspects will be shown where for practical reasons the computation strategy deviates from the strict theoretical derivations of the previous subsections.

Solution of Normal Equation System

After setting up and decorrelating the observation equations for each short arc, these are accumulated into the normal equation system $N\hat{x} = n$ (see eq. (2.2.7)). At this point, N contains the full normal equation system for all parameters x from eq. (6.4.32). This includes the monthly Stokes coefficients, the daily Stokes coefficients for all days of the month, as well as the satellite and state parameters. Similarly to the algorithm for decorrelation described in section 2.3, the inversion of N can be avoided by computing its Cholesky factorization

$$N = U^{\mathsf{T}}U \tag{6.5.32}$$

giving

$$U^{\mathsf{T}}U\hat{x} = n . \tag{6.5.33}$$

The least squares solution to the equation system can then be computed by sequentially solving two triangular systems:

$$\hat{x} = U^{-1}U^{-\mathsf{T}}n = U^{-1}\bar{n} . \tag{6.5.34}$$

In computing the Cholesky factorization eq. (6.5.32) use can be made of the special blocked structure of N (see e.g. Higham, 2002).

Matrix of Redundancies

In the process of determining the stochastic model, the matrix of redundancies R from eq. (2.6.8) must be computed for each short arc. Here, N is the completely accumulated normal equation system from all arcs, all other matrices refer to the m-th arc:

$$R = \Sigma_{ll}^{-1} - \Sigma_{ll}^{-1}AN^{-1}A^{\mathsf{T}}\Sigma_{ll}^{-\mathsf{T}} \tag{6.5.35}$$

Especially the product $AN^{-1}A^{\mathsf{T}}$ is expensive in this expression, as it involves the inverse of a large $P \times P$ normal equation, as well as two products with $N \times P$ matrices.

As R is never needed directly, but only in the form of the trace of the product of R with some covariance matrix V_n

$$
\begin{aligned}
s_n &= \operatorname{trace}\left(RV_n\right) \\
&= \operatorname{trace}\left(\left(\Sigma^{-1} - \Sigma^{-1}AN^{-1}A^{\mathsf{T}}\Sigma^{-\mathsf{T}}\right)V_n\right) \\
&= \operatorname{trace}\left(\Sigma^{-1}V_n - \Sigma^{-1}AN^{-1}A^{\mathsf{T}}\Sigma^{-\mathsf{T}}V_n\right) ,
\end{aligned} \tag{6.5.36}
$$

some optimizations can be introduced in the computation. First, note that the trace of a sum of matrices is equal to the sum of the traces, giving

$$s_n = \operatorname{trace}\left(\Sigma^{-1}V_n\right) - \operatorname{trace}\left(\Sigma^{-1}AN^{-1}A^{\mathsf{T}}\Sigma^{-\mathsf{T}}V_n\right) . \tag{6.5.37}$$

Further, circular permutation of the product in the trace does not change the trace. Inserting the Cholesky factorization of N, and then permuting the second trace in eq. (6.5.37) gives

$$
\begin{aligned}
s_n &= \text{trace}\left(\boldsymbol{\Sigma}^{-1}\boldsymbol{V}_n\right) - \text{trace}\left(\boldsymbol{\Sigma}^{-1}\boldsymbol{A}\boldsymbol{U}^{-1}\boldsymbol{U}^{-\mathsf{T}}\boldsymbol{A}^{\mathsf{T}}\boldsymbol{\Sigma}^{-\mathsf{T}}\boldsymbol{V}_n\right) \\
&= \text{trace}\left(\boldsymbol{\Sigma}^{-1}\boldsymbol{V}_n\right) - \text{trace}\left(\boldsymbol{U}^{-\mathsf{T}}\boldsymbol{A}^{\mathsf{T}}\boldsymbol{\Sigma}^{-\mathsf{T}}\boldsymbol{V}_n\boldsymbol{\Sigma}^{-1}\boldsymbol{A}\boldsymbol{U}^{-1}\right) .
\end{aligned}
\tag{6.5.38}
$$

At this point the rightmost trace can be approximated by using a Monte-Carlo trace estimator (Hutchinson, 1990). Hutchinson shows that for a $P \times P$ matrix $\boldsymbol{X}$,

$$
\text{trace}\left(\boldsymbol{X}\right) \approx \frac{1}{Z}\sum_{z=0}^{Z-1} \boldsymbol{z}_z^{\mathsf{T}}\boldsymbol{X}\boldsymbol{z}_z ,
\tag{6.5.39}
$$

for sufficiently large Z. Here each $\boldsymbol{z}_z$ is a random $P \times 1$ vector, with entries only 1 and -1, each with a probability of 0.5:

$$
\boldsymbol{z}_z = \begin{bmatrix} -1 & 1 & \dots & 1 & -1 \end{bmatrix}^{\mathsf{T}}
\tag{6.5.40}
$$

At this point, an evil maths trick is used in rewriting eq. (6.5.39). Let $\boldsymbol{Z}$ be a $P \times Z$ matrix of Monte Carlo vectors $\boldsymbol{z}_z$, then the sum in eq. (6.5.39) can be written as

$$
\text{trace}\left(\boldsymbol{X}\right) \approx \frac{1}{Z}\text{trace}\left(\boldsymbol{Z}^{\mathsf{T}}\boldsymbol{X}\boldsymbol{Z}\right) .
\tag{6.5.41}
$$

Here, the diagonal elements of the matrix product are exactly the component sums from eq. (6.5.39). The trace operator performs the sum over these diagonal components, neglecting the off-diagonal products of all combinations of two non-identical Monte Carlo vectors. To clarify this approach, consider a simple example where $Z = 2$. Here

$$
\begin{aligned}
\text{trace}\left(\boldsymbol{X}\right) &\approx \frac{1}{2}\text{trace}\left(\begin{bmatrix} \boldsymbol{z}_0^{\mathsf{T}} \\ \boldsymbol{z}_1^{\mathsf{T}} \end{bmatrix} \boldsymbol{X} \begin{bmatrix} \boldsymbol{z}_0 & \boldsymbol{z}_1 \end{bmatrix}\right) = \frac{1}{2}\text{trace}\left(\begin{bmatrix} \boldsymbol{z}_0^{\mathsf{T}}\boldsymbol{X}\boldsymbol{z}_0^{\mathsf{T}} & \boldsymbol{z}_0^{\mathsf{T}}\boldsymbol{X}\boldsymbol{z}_1^{\mathsf{T}} \\ \boldsymbol{z}_1^{\mathsf{T}}\boldsymbol{X}\boldsymbol{z}_0^{\mathsf{T}} & \boldsymbol{z}_1^{\mathsf{T}}\boldsymbol{X}\boldsymbol{z}_1^{\mathsf{T}} \end{bmatrix}\right) \\
&= \frac{1}{2}\left(\boldsymbol{z}_0^{\mathsf{T}}\boldsymbol{X}\boldsymbol{z}_0^{\mathsf{T}} + \boldsymbol{z}_1^{\mathsf{T}}\boldsymbol{X}\boldsymbol{z}_1^{\mathsf{T}}\right) = \frac{1}{2}\sum_{z=0}^{1} \boldsymbol{z}_z^{\mathsf{T}}\boldsymbol{X}\boldsymbol{z}_z ,
\end{aligned}
\tag{6.5.42}
$$

which is exactly the result from eq. (6.5.39). This can be further simplified by normalizing the Monte Carlo vectors to the number of realizations with $\bar{\boldsymbol{Z}} = \frac{1}{\sqrt{Z}}\boldsymbol{Z}$, giving

$$
\text{trace}\left(\boldsymbol{X}\right) \approx \text{trace}\left(\bar{\boldsymbol{Z}}^{\mathsf{T}}\boldsymbol{X}\bar{\boldsymbol{Z}}\right) .
\tag{6.5.43}
$$

Applying this trick to the second trace in eq. (6.5.38) gives

$$
s_n = \text{trace}\left(\boldsymbol{\Sigma}^{-1}\boldsymbol{V}_n\right) - \text{trace}\left(\bar{\boldsymbol{Z}}^{\mathsf{T}}\boldsymbol{U}^{-\mathsf{T}}\boldsymbol{A}^{\mathsf{T}}\boldsymbol{\Sigma}^{-\mathsf{T}}\boldsymbol{V}_n\boldsymbol{\Sigma}^{-1}\boldsymbol{A}\boldsymbol{U}^{-1}\bar{\boldsymbol{Z}}\right) ,
\tag{6.5.44}
$$

Where the left-hand trace is the simple trace from before, but the right-hand trace is now a rewritten form of the Monte-Carlo trace estimator. The right-hand trace is shifted back to its original permutation, after which the traces are combined, giving

$$
\begin{aligned}
s_n &= \operatorname{trace}\left(\mathbf{\Sigma}^{-1}\mathbf{V}_n\right) - \operatorname{trace}\left(\mathbf{\Sigma}^{-1}\mathbf{A}\mathbf{U}^{-1}\bar{\mathbf{Z}}\bar{\mathbf{Z}}^{\mathsf{T}}\mathbf{U}^{-\mathsf{T}}\mathbf{A}^{\mathsf{T}}\mathbf{\Sigma}^{-\mathsf{T}}\mathbf{V}_n\right) \\
&= \operatorname{trace}\left(\left(\mathbf{\Sigma}^{-1} - \mathbf{\Sigma}^{-1}\mathbf{A}\mathbf{U}^{-1}\bar{\mathbf{Z}}\bar{\mathbf{Z}}^{\mathsf{T}}\mathbf{U}^{-\mathsf{T}}\mathbf{A}^{\mathsf{T}}\mathbf{\Sigma}^{-\mathsf{T}}\right)\mathbf{V}_n\right) \\
&= \operatorname{trace}\left(\bar{\mathbf{R}}\mathbf{V}_n\right) \ .
\end{aligned}
\tag{6.5.45}
$$

This new quantity is an estimator for the matrix of redundancies

$$
\bar{\mathbf{R}} = \mathbf{\Sigma}^{-1} - \mathbf{\Sigma}^{-1}\mathbf{A}\mathbf{U}^{-1}\bar{\mathbf{Z}}\bar{\mathbf{Z}}^{\mathsf{T}}\mathbf{U}^{-\mathsf{T}}\mathbf{A}^{\mathsf{T}}\mathbf{\Sigma}^{-\mathsf{T}} \ ,
\tag{6.5.46}
$$

or

$$
\bar{\mathbf{R}} = \mathbf{\Sigma}^{-1} - \tilde{\mathbf{R}}\tilde{\mathbf{R}}^{\mathsf{T}}
\tag{6.5.47}
$$

with

$$
\begin{aligned}
\tilde{\mathbf{R}} &= \mathbf{\Sigma}^{-1}\mathbf{A}\mathbf{U}^{-1}\bar{\mathbf{Z}} \\
&= \mathbf{W}^{-1}\mathbf{W}^{-\mathsf{T}}\mathbf{A}\mathbf{U}^{-1}\bar{\mathbf{Z}} \\
&= \mathbf{W}^{-1}\bar{\mathbf{A}}\mathbf{U}^{-1}\bar{\mathbf{Z}} \ .
\end{aligned}
\tag{6.5.48}
$$

With $\mathbf{W}$, $\mathbf{A}$, and $\mathbf{U}$ known from previous computations, $\tilde{\mathbf{R}}$ can be computed efficiently and quickly. First the triangular system $\mathbf{U}^{-1}\bar{\mathbf{Z}}$ is solved, giving a $P \times Z$ temporary matrix. As $\mathbf{U}$ is computed from the accumulated normal equations and is identical for all short arcs, $\mathbf{U}^{-1}\bar{\mathbf{Z}}$ only needs to be computed once, and can then be reused for all short arcs. After determining the product $\bar{\mathbf{A}}\mathbf{U}^{-1}\bar{\mathbf{Z}}$, only one more triangular system needs to be solved, giving the $N \times Z$ matrix $\tilde{\mathbf{R}}$. In GROOPS, $Z = 100$, giving a very manageably small matrix $\tilde{\mathbf{R}}$, which is then used to determine $\bar{\mathbf{R}}$ using eq. (6.5.47). To summarize, this implementation avoids the explicit computation of $\mathbf{N}^{-1}$ in eq. (6.5.35). Further the computation of $\bar{\mathbf{R}}$ is reduced in complexity through exploitation of symmetries in eq. (6.5.46). Elegant application of the Monte Carlo trace estimator reduces the operations needed to compute $\tilde{\mathbf{R}}$.

Overall, this algorithm reduces the computational cost to determine $\mathbf{R}$ considerably, at the expense of a small error due to the approximation introduced by the Monte Carlo trace estimator. As the stochastic model is determined through multiple iterations, this uncertainty does however not affect the resulting model significantly.

Computation of Variance Factors

The computation of Ω_n^m and s_n^m from eqs. (6.5.22) and (6.5.23) can be optimized by not explicitly computing all matrix products involved. For a time lag $n = 0$, $\operatorname{trace}\left(\bar{\mathbf{R}}_m\mathbf{V}_n\right)$ is

trivial, as it is simply trace $(\bar{R}_m)$, with no need to compute the product. For lags $n > 0$ the trace used to compute the redundancy can be written as

$$\text{trace}\,(\bar{R}_m V_n) = \text{trace}\,\left(\bar{R}_m\,(V_n^- + V_n^+)\right) = \text{trace}\,(\bar{R}_m V_n^-) + \text{trace}\,(\bar{R}_m V_n^+) \quad (6.5.49)$$

where V_n^- is only the lower half of V_n, and V_n^+ the upper half. For e.g. $N_{\max} = 5$, these would be

$$V_2^- = \begin{bmatrix} 0 & 0 & 0 & 0 & 0 \\ 0 & 0 & 0 & 0 & 0 \\ 1 & 0 & 0 & 0 & 0 \\ 0 & 1 & 0 & 0 & 0 \\ 0 & 0 & 1 & 0 & 0 \end{bmatrix} \quad \text{and} \quad V_2^+ = \begin{bmatrix} 0 & 0 & 1 & 0 & 0 \\ 0 & 0 & 0 & 1 & 0 \\ 0 & 0 & 0 & 0 & 1 \\ 0 & 0 & 0 & 0 & 0 \\ 0 & 0 & 0 & 0 & 0 \end{bmatrix}. \quad (6.5.50)$$

With $V_n^+ = (V_n^-)^\mathsf{T}$ and $\bar{R}$ being a symmetric matrix

$$\text{trace}\,(\bar{R}_m V_n) = 2 \cdot \text{trace}\,(\bar{R}_m V_n^-)\;. \quad (6.5.51)$$

As V_n is large and sparse, it is efficient to unroll the trace of the matrix product and directly write it as a sum

$$\text{trace}\,(\bar{R}_m V_n^-) = \sum_{i=0}^{N_m - n} \bar{R}_m(i + n, i)\;. \quad (6.5.52)$$

The square sum of residuals can similarly be optimized by smartly computing

$$\hat{e}^\mathsf{T} \Sigma_{ll}^{-\mathsf{T}} V_n \Sigma_{ll}^{-1} \hat{e}\;. \quad (6.5.53)$$

First, let

$$\tilde{e} = \Sigma_{ll}^{-1} \hat{e} = W^{-1} W^{-\mathsf{T}} \hat{e} = W^{-1} \hat{\hat{e}} \quad (6.5.54)$$

which is again efficiently computed by solving a triangular system. Then

$$\begin{aligned}
\hat{e}^\mathsf{T} \Sigma_{ll}^{-\mathsf{T}} V_n \Sigma_{ll}^{-1} \tilde{e} &= \tilde{e}^\mathsf{T} V_n \tilde{e} \\
&= \tilde{e}^\mathsf{T}\,(V_n^- + V_n^+)\,\tilde{e} \\
&= \begin{cases} \tilde{e}^\mathsf{T} \tilde{e} & \text{if } n = 0, \\ 2 \cdot \tilde{e}^\mathsf{T} V_n^- \tilde{e} & \text{otherwise.} \end{cases}
\end{aligned} \quad (6.5.55)$$

This loop can again be unrolled, avoiding the product with the sparse matrix V_n^-, as

$$\tilde{e}^\mathsf{T} V_n^- \tilde{e} = \sum_{i=n}^{N_m} \tilde{e}(i) \cdot \tilde{e}(i - n)\;. \quad (6.5.56)$$

Arc-wise Variance Factors

As described in section 6.5.4, the arc-wise variance factors are normalized to remove a double-consideration of the amplitude determination. To this end, the mean of the arc-wise variance factors is determined in eq. (6.5.29). In the implementation in GROOPS, this mean is not the direct arithmetic mean of all variance factors. Instead, the mean is computed robustly by only employing the central half of the sorted values, ignoring outliers at either tail of the distribution. With the γ_m sorted according to their magnitude, the mean is then

$$\bar{\gamma} = \frac{2}{M} \sum_{m=M/4}^{3 \cdot M/4} \gamma_m \ . \tag{6.5.57}$$

Variance Factor for Geophysical Pseudo-Observations

The variance factor for the geophysical pseudo-observations $\hat{\sigma}_{\mathrm{gpm}}^2$ from eq. (6.5.31) is computed using eq. (2.6.12). As the pseudo-observations l_{gpm} are 0, the residuals are directly

$$\hat{e}_{\mathrm{gpm}} = -A_{\mathrm{gpm}} \hat{x}_{\mathrm{gpm}} \ . \tag{6.5.58}$$

Dropping the index for the geophysical process, the square sum of residuals is

$$\Omega = \hat{e}^\mathsf{T} \Sigma^{-1} \hat{e} = \hat{x}^\mathsf{T} A^\mathsf{T} \Sigma^{-1} A \hat{x} = \hat{x}^\mathsf{T} N_{\mathrm{gpm}} \hat{x} \ . \tag{6.5.59}$$

The redundancy is

$$s = N_{\mathrm{gpm}} - \mathrm{trace}\left(N_{\mathrm{gpm}} N^{-1}\right) \ . \tag{6.5.60}$$

Here, the Monte Carlo trace estimator from eq. (6.5.41) can be employed again, with

$$
\begin{aligned}
\mathrm{trace}\left(N_{\mathrm{gpm}} N^{-1}\right) &= \mathrm{trace}\left(N_{\mathrm{gpm}} U^{-1} U^{-\mathsf{T}}\right) \\
&= \mathrm{trace}\left(U^{-\mathsf{T}} N_{\mathrm{gpm}} U^{-1}\right) \\
&= \mathrm{trace}\left(\bar{Z}^\mathsf{T} U^{-\mathsf{T}} N_{\mathrm{gpm}} U^{-1} \bar{Z}\right)
\end{aligned}
\tag{6.5.61}
$$

Importantly, $U^{-1}\bar{Z}$ is the same as in eq. (6.5.48), and can be reused directly.

Estimation of the Zero-Frequency

For a zero-mean random process, the theoretical expected value of the zero frequency of the PSD is well defined. Through discretisation and approximation effects, the actual zero frequency amplitude for the PSD of such a time series can be close, or equal to, zero. In practice, this means that the estimation of the zero frequency amplitude can

be unstable, due to the quotient eq. (6.5.19) becoming ill-defined for some values of $\tilde{\Omega}_0$ and $\tilde{s}_0$. To work around this issue in ITSG-Grace2016, the zero frequency amplitude was set to the same value as that of the lowest non-zero frequency of the estimated power spectral density.

6.5.7 Summary

The input to the algorithm for the estimation of the stochastic model are the observations for hl-SST, $l_{\text{pod},A}$, $l_{\text{pod},B}$, and the ll-SST observations l_{sst}. Further, an approximation of the stochastic model for these observation types is needed. If no information is available, white noise can be assumed, with

$$S_{xx}^j = 1 \,, j \in [0, N_{\max}) \qquad \text{and} \qquad \sigma_m^2 = 1 \,, m \in [1, M] \,. \qquad (6.5.62)$$

In addition, the cofactor matrix for the geophysical process model Q_{gpm} is needed, the scale of which can also be assumed to be $\sigma_{\text{gpm}}^2 = 1$.

With this data in place, the determination of the stochastic model can begin. The iteration roughly follows the scheme presented in fig. 6.7, where the location of the individual steps in the following algorithm are marked with their respective Arabic numerals. To determine the stochastic model, for each arc and observation group

1. compute Δl, A, using the functional models from section 6.4 and the parametrization described in table 6.2, but only up to degree and order 60.
2. compute the covariance matrix Σ using eq. (6.5.62), and store the Cholesky decomposition $\Sigma = W^{\mathsf{T}}W$.
3. decorrelate the reduced observation vector and the Design matrix using eq. (2.3.4), giving $\Delta\bar{l}$, $\bar{A}$.
4. compute and accumulate the normal equations N and right hand sides n.
5. compute the Cholesky decomposition $N = U^{\mathsf{T}}U$, and solve for $\Delta\hat{x}$.
6. create a matrix of Monte Carlo vectors $\bar{Z}$, and compute $U^{-1}\bar{Z}$.
7. compute the decorrelated residuals as $\hat{e} = \Delta\bar{l} - \bar{A}\Delta\hat{x}$.
8. compute $\tilde{R}$, $\tilde{e}$, and, using them, $\tilde{\Omega}$ and $\tilde{s}$.
9. compute updated estimates of $\hat{S}_{xx}^j$, $\hat{\sigma}_m^2$ for all observation groups, as well as $\hat{\sigma}_{\text{gpm}}^2$.
10. if these quantities have not sufficiently converged, compute an updated covariance matrix $\hat{\Sigma}$ and its Cholesky decomposition, continue from the 2nd step.

Figure 6.8 gives an example of the estimated PSDs $\hat{S}_{xx}$ and the arc-wise variance factors σ^2 for the month of June 2010. Figure 6.8a shows the estimated PSD of the ll-SST observation noise, derived from the KBR residuals. The PSD exhibits a structure typical for GRACE ll-SST data. The noise spectrum shows an ascending branch above $1 \cdot 10^{-2}$ Hz, which is due to the processing of the KBR data in the range rate domain. As the range rates are derived from the observed biased ranges through differentiation, noise at higher frequencies is amplified, while noise at lower frequencies is damped. At frequencies below $1 \cdot 10^{-2}$ Hz, noise due to a combination of ACC observation errors and residual geophysical signals dominates. Both the ACC observations, and
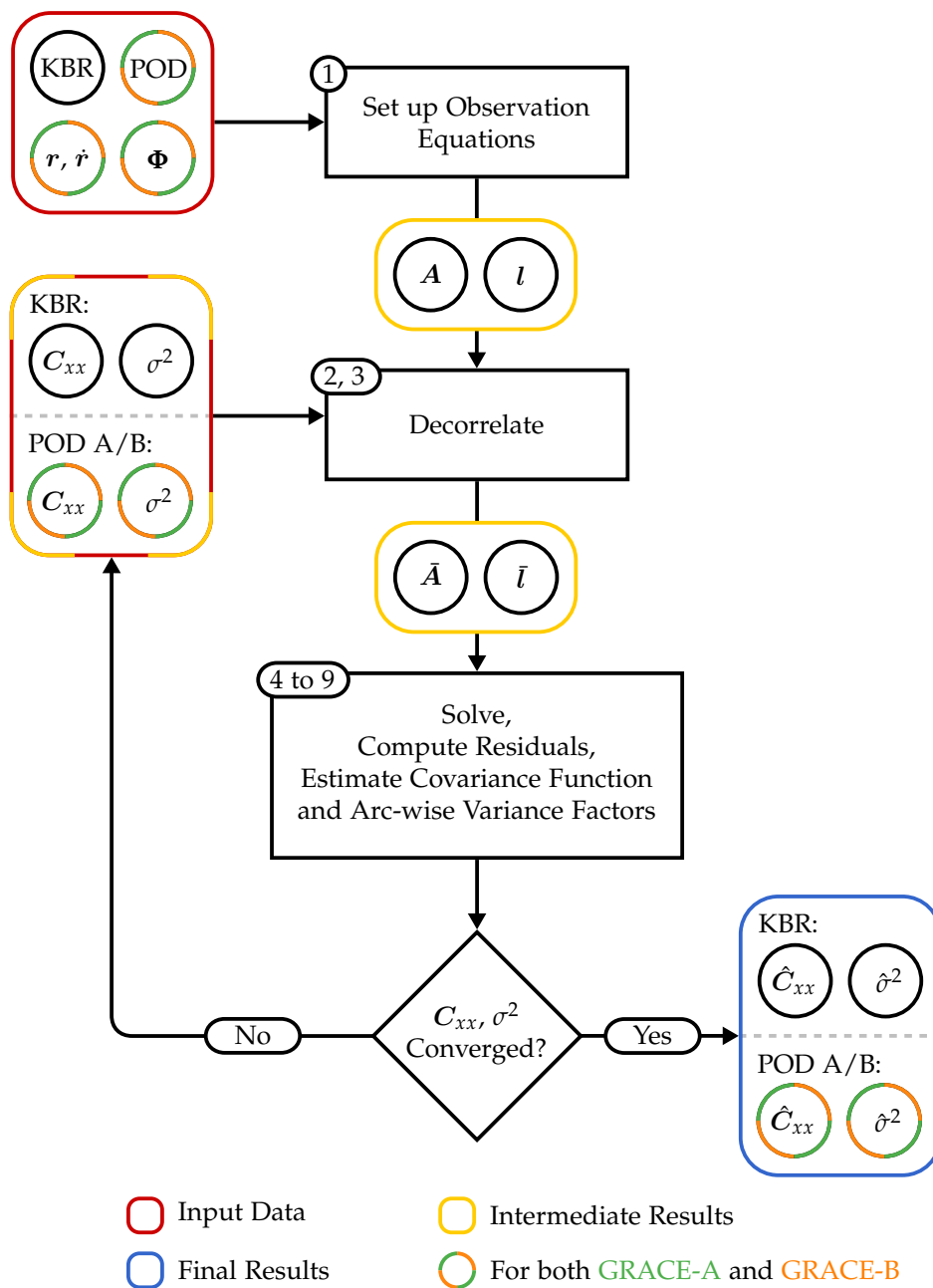
Figure 6.7: Summary of estimation of the observation covariance functions $\hat{C}_{xx}$ and arc-wise variance factors $\hat{\sigma}^2$ for KBR and POD observations. $\boldsymbol{\Phi}$ are the state transition matrices from the dynamic orbit determination, $\boldsymbol{r}, \dot{\boldsymbol{r}}$ are the dynamic orbits of the two spacecraft.

the acceleration due to conservative forces derived from the background models are integrated in the determination of the GRACE dynamic orbits (eq. (5.2.2)). Due to the integration, noise at lower frequencies is amplified, while noise at higher frequencies is damped.

Figure 6.8b shows the estimated arc-wise variance factors σ_m^2 for the ll-SST observations. Their mean is 1, due to the normalization applied in eq. (6.5.29). A systematic increase of the arc-wise variance factors can be observed during the third quarter of the month. According to Flechtner (2010), GRACE-A was commanded into attitude hold mode (AHM) on June 17, 2010, during which the pointing towards GRACE-B is not enforced as strictly, and can undergo larger variations. The time period that GRACE-A spent in AHM is shaded with a grey backdrop, and corresponds well with a period of increased arc-wise variance factors. This demonstrates how a drop in data quality was automatically detected through VCE. The arc-wise variance factors increase in value, meaning the weight of the corresponding arcs in the LSA decreases accordingly. Figures 6.8d and 6.8f show the arc-wise variance factors for the POD observations on GRACE-A and GRACE-B. As the GPS observations are not affected by the AHM, their arc-wise variance factors do not show a corresponding change during this period.

Figures 6.8c and 6.8e show the PSDs for the GRACE-A and GRACE-B POD observations. The PSDs are estimated separately for each coordinate axis in the orbit system, giving the three curves shown.

6.6 Complete solution

With the dynamic orbits determined, a functional model set up, and the stochastic characteristics of the signals estimated, a complete GRACE gravity field solution can be determined. For ITSG-Grace2016, this comprises both monthly and daily gravity fields. An ITSG-Grace2016 monthly solution is computed from all data available for that specific calendar month, beginning at 00:00:00 UTC on the 1st day of the month, and up to, but not including, 24:00:00 UTC on the last day of the month. For months with large data gaps no attempt is made to combine data from multiple months. The resulting gravity field is then the temporal mean of the time-variable gravity signal for that month. Together with the static field and long-term time-variable signal, which were introduced as a priori reference fields in the dynamic orbit integration, this gives the full mean potential for the month. This corresponds to the required step of adding the adjusted parameters to the Taylor point in any LSA, with $\hat{x} = x_0 + \Delta\hat{x}$. Monthly gravity fields are computed up to D/O 120. Expansions up to D/O 90 and 60 are then determined through truncation of the full normal equation system. All three solutions are then provided to the user community.

Daily gravity field solutions are determined using GRACE observations from 00:00:00 UTC of that day up to, but not including, 24:00:00 UTC on the same day. In addition to the GRACE observations, additional information in the form of the stochastic information on the temporal variability of gravity due to geophysical processes is
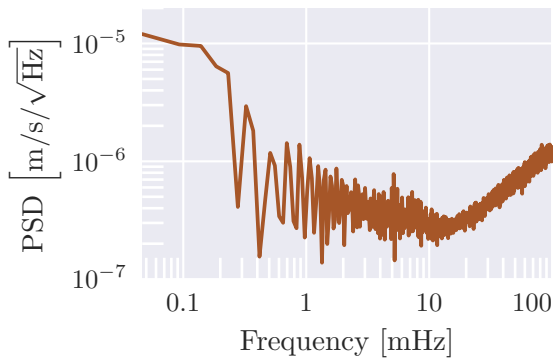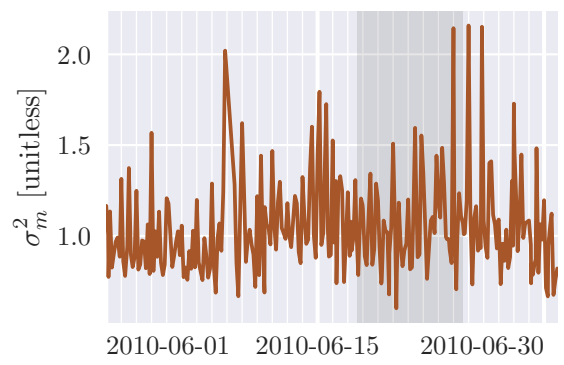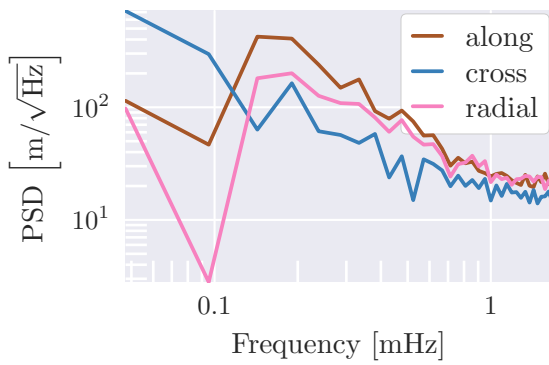
(a) SST PSD
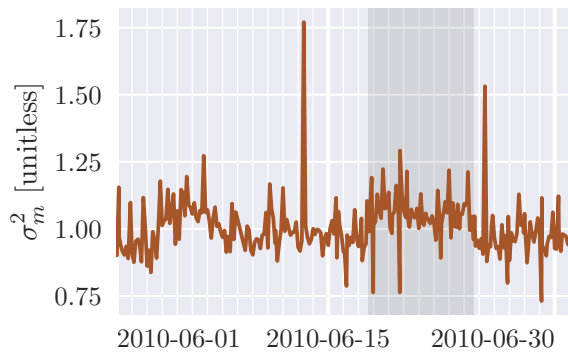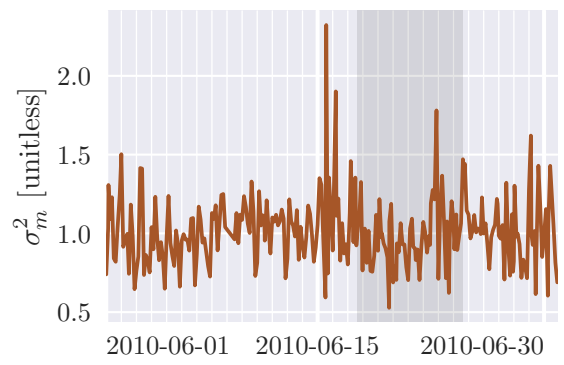
(b) SST arc-wise variance factors
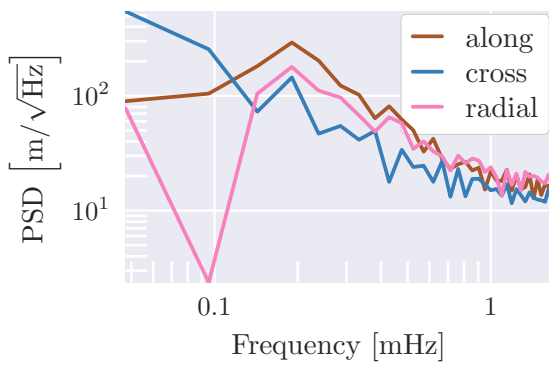
(c) POD PSD for GRACE-A

(d) POD arc-wise variance factors for GRACE-A

(e) POD PSD for GRACE-B

(f) POD arc-wise variance factors for GRACE-B

Figure 6.8: Examples of estimated PSDs (left column) and arc-wise variance factors (right column (right column)) for June 2010. The shaded areas in (b), (d) and (f) mark a time period where GRACE-A was commanded to attitude hold mode, resulting in anomalously large pointing variations.

introduced for the daily gravity field solutions. The published ITSG-Grace2016 daily gravity field solutions are determined in a separate adjustment, independently of the monthly solutions. This process is based on Kalman filtering as described by Kurtenbach, 2011, and is not presented here. A more detailed description will be given in the upcoming dissertation of Andreas Kvas, expected to be released in 2019.

6.6.1 High Degree Monthly Gravity Fields

To determine a monthly gravity field solution, observation equations are set up for the parameters listed in table 6.2, including all monthly Stokes coefficients up to degree and order 120. This is done for all observation groups, ll-SST KBR observations, and hl-SST POD observations for both GRACE-A and GRACE-B. The observation equations are decorrelated with the stochastic model derived in section 6.5, and then accumulated into a normal equation system.

Figure 6.9 illustrates the ordering of the parameters in the normal equation system, and shows the blocks containing correlations between the parameter groups. For the monthly solutions, ultimately only the monthly Stokes coefficients are of interest. To this end, all other parameters are eliminated from the normal equation system before determining its solution, as described in section 2.4. An efficient algorithm to perform this elimination specifically in the context of the ITSG-Grace2016 gravity field solution is described by Kvas (2014).

Figure 6.10 shows two gravity field solutions. The lower degree solution, determined up to D/O 60, is the solution determined in the estimation of the stochastic model, as described in section 6.5. The D/O 120 solution is the complete monthly solution as described here. The degree amplitudes of the two solutions are nearly identical up to D/O 30, where short-term temporal variations in the gravity field dominate the recovered signal. Above D/O 40, the lower degree solution shows a lower amplitude. This effect can be observed in all low-degree solutions. It is due to the truncation of the spherical harmonics expansion at too low a degree, which constrains the associated solution space and results in aliasing or leakage of unresolved signal into the solved-for Stokes coefficients (Sneeuw, 2000).

6.6.2 Lower Degree Solutions

The normal equation system for the D/O 120 solution, where all parameters but the monthly Stokes coefficients were eliminated, is reused to compute both the final D/O 90 and D/O 60 solution by simple truncation. First, all parameters for Stokes coefficients from degree 91 and order 0 to D/O 120 are cut from the normal equation system, *not* using the parameter elimination algorithm mentioned in section 6.6.1. The normal equation system is then solved, giving a monthly gravity field up to D/O 90. The process is repeated, truncating the Stokes coefficients from degree 61 and order 0 to D/O 90, then again solving the remaining system to determine a D/O 60 solution.
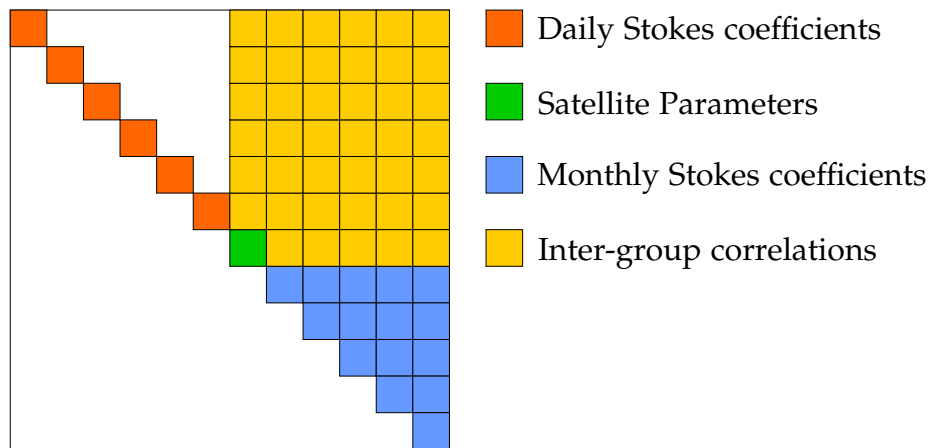
Figure 6.9: Symbolic illustration of the normal equation structure of an ITSG-Grace2016 monthly gravity field solution. Only the upper triangle is stored, as the normal equation matrix is symmetric. The individual blocks are not to scale.
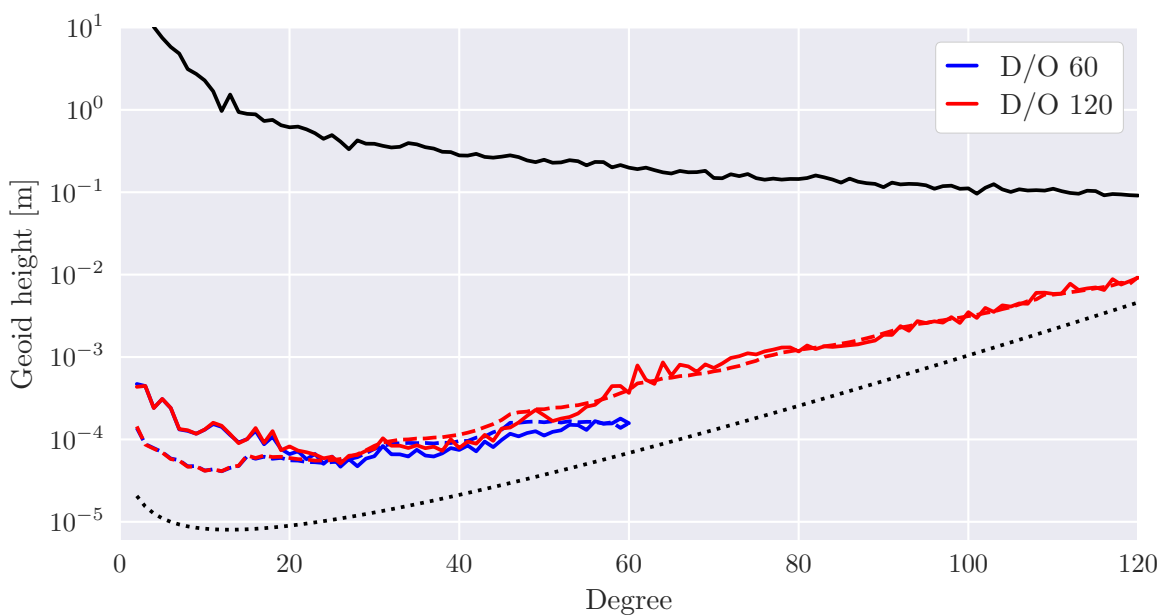

Figure 6.10: Degree Amplitude plot for June 2010. The pictured low degree and order field is a by-product of determining the stochastic model of the observables. The high degree and order field is the final product for this month.

Numerical Optimization in Orbit Integration

<div style="text-align: right;">**7**</div>

> **Attribution** This chapter, as well as chapter 5 of this thesis focusing on the variational equations and dynamic orbit integration, are an extended version of a previous publication by the author: Ellmer and Mayer-Gürr, 2017. Specifically, this chapter reproduces and expands on sections 3.6 to 5 of Ellmer and Mayer-Gürr, 2017. The content of this chapter is the result of original research carried out by the author of this thesis. Section 7.2.3 does not appear in Ellmer and Mayer-Gürr, 2017, and is first published in this work.

Dynamic orbits are an integral part of determining a gravitational field using the variational equations. All forces that are known a priori, both from reference models and from direct observations, are encapsulated in the integrated positions and velocities of the GRACE satellites along their respective orbit arcs. The use of dynamic orbit positions to determine the accelerations due to conservative forces however means that dynamic orbit integration for GRACE must be an iterative procedure.

Only when positions, velocities, and accelerations derived from an integrated dynamic orbit equal those used in its computation can one say that an equilibrium state has been reached. The dynamic orbit can then be described as self-consistent. Using a dynamic orbit as input for the orbit integration routine must then result in the same dynamic orbit as output. Any difference in the positions from the input orbit to the result can be regarded as either a defect in the orbit integration algorithm, a defect in its implementation, or as a manifestation of insufficient convergence.

This chapter details an approach to characterize the quality and analyse the convergence of the dynamic orbit integration described in chapter 5. Building on this result, the improved algorithm used in ITSG-Grace2016 will be presented. The improved algorithm ensures self-consistency of the dynamic orbits at a level that allows for consistent processing of data from the GRACE-FO laser ranging interferometer (LRI), which is expected to surpass the accuracy provided by the GRACE KBR instrument (Sheard et al., 2012).

7.1 Quality of Convergence

For real data processing, such as in the context of GRACE, the true position of the spacecraft is unknown. The obvious path for a quality check on orbit determination, the computation of position differences to some absolute ground truth, is thus not available.

Use can however be made of the iterative nature of the dynamic orbit integration. An alternative quality check can be derived from the position corrections applied at each iteration l to give the new positions at iteration $l + 1$. These are the $\boldsymbol{\Delta r_\epsilon}$ from eq. (5.2.26). Given a perfect dynamic orbit integration process consisting of a correct orbit integration implementation and error-free data, it is expected that the $\boldsymbol{\Delta r_\epsilon}$ must grow smaller with each iteration. The integrated dynamic orbit approaches the true satellite orbit, and the difference between subsequent iterations of orbits must thus vanish:

$$\lim_{l \to \infty} \boldsymbol{\Delta r_\epsilon} = \mathbf{0} \ . \tag{7.1.1}$$

For all practical considerations, constraints such as flawed algorithms or the limited precision of computations set a lower bound for the achievable repeatability of the orbit integration. This precludes the differences in eq. (7.1.1) from disappearing entirely. Instead, even as more iterations of computation are performed, the differences $\boldsymbol{\Delta r_\epsilon}$ stop to grow smaller after some computational threshold is reached. This convergence limit can be used as a benchmark to test the quality of orbit determination strategies both amongst different implementation and on their own merit, always given the same input data. The better the algorithm is designed and implemented, the smaller the ultimate limit of the position differences becomes.

Figure 7.1 shows the convergence in terms of $\boldsymbol{\Delta r_\epsilon}$ for 100 iterations of computation, based on simulated data. The exact specifications of the simulation are given later in section 7.3. At this point the magnitude of the remaining variability between iterations is of primary interest. It can be clearly seen that even after convergence, $\boldsymbol{\Delta r_\epsilon}$ does not drop much below $10\,\mu m$. As the expected ranging accuracy of the GRACE-FO LRI is expected to be smaller than $100\,nm$ (Heinzel et al., 2012), it is worth investigating avenues to improve on this result.
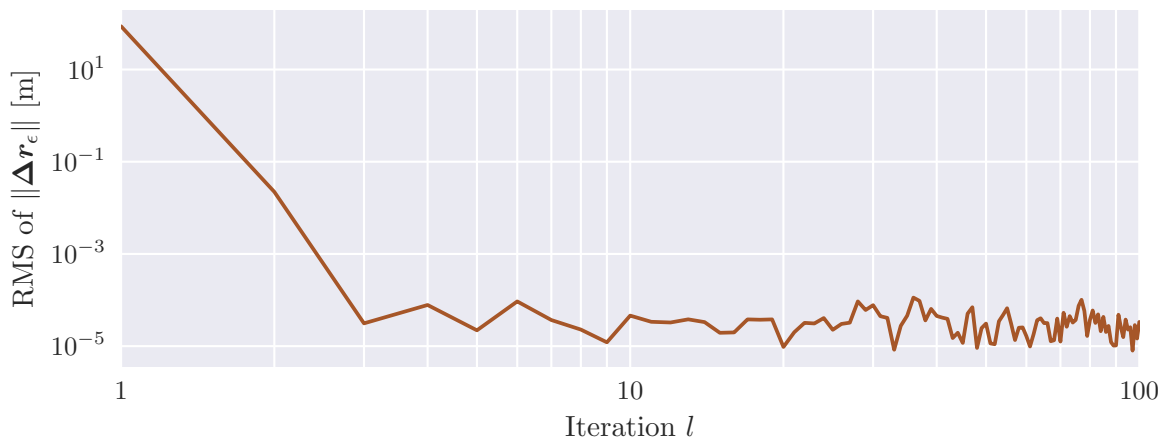

Figure 7.1: Unsatisfying convergence of dynamic orbit integration after several iterations l, expressed as the RMS of $\|\boldsymbol{\Delta r_\epsilon}\|$. From simulated data.

7.2 Improved Algorithm

An especially challenging aspect of the integration procedure presented in chapter 5 is the retention of full numerical precision in the determination of the integrated positions and velocities of eqs. (5.2.3) and (5.2.4). For longer arc lengths the numeric values of especially the integrated positions $r_{\epsilon}^{\text{int}}$ can become very large. As these integrals are accumulated, the numerical resolution of a standard double precision floating point number can cease to be sufficient to hold all of the necessary information, leading to a loss of precision in the least significant digits.

One promising approach to regaining this precision is to split the integral into two parts: The first part is numerically large, and should be solved analytically. The second part of the integral should be smaller in magnitude, and is integrated numerically. This can be seen as a more general formulation of the well-known Encke method for perturbed orbit propagation (Encke, 1852), which was also independently developed by Bond (Bond, 1849). Writing the larger part of the integral to be due to a reference force $\boldsymbol{f}_0(\tau)$, and the smaller due to a perturbing force $\Delta \boldsymbol{f}(\tau)$, the acceleration due to their sum is the full acceleration

$$\ddot{\boldsymbol{r}}(\tau) = \boldsymbol{f}(\tau) = \boldsymbol{f}_0(\tau) + \Delta \boldsymbol{f}(\tau) \, . \tag{7.2.1}$$

Equivalently to the original equation of motion, this partitioned equation can also be integrated. The reference acceleration is, along with its integrals, equivalent to eqs. (5.1.6) to (5.1.8):

$$\ddot{\boldsymbol{r}}_{\text{ref}}(\tau) = \boldsymbol{f}_0(\tau) \tag{7.2.2}$$

$$\dot{\boldsymbol{r}}_{\text{ref}}(\tau) = \dot{\boldsymbol{r}}_{\text{ref},0} + T \int_0^\tau \boldsymbol{f}_0(\tau')d\tau' \tag{7.2.3}$$

$$\boldsymbol{r}_{\text{ref}}(\tau) = \boldsymbol{r}_{\text{ref},0} + \dot{\boldsymbol{r}}_{\text{ref},0}(\tau T) + T^2 \int_0^\tau (\tau - \tau') \boldsymbol{f}_0(\tau')d\tau' \, . \tag{7.2.4}$$

In these equations, the initial values of the reference motion

$$\boldsymbol{y}_{\text{ref},0} = \begin{bmatrix} \boldsymbol{r}_{\text{ref},0} \\ \dot{\boldsymbol{r}}_{\text{ref},0} \end{bmatrix} \tag{7.2.5}$$

appear. The reference force $\boldsymbol{f}_0$ should be chosen in such a way that the integrals in eqs. (7.2.2) to (7.2.4) have analytical solutions. Computing the complete integrals of both the reference force and accelerations due to perturbing forces gives the true motion of the spacecraft, defined by

$$\ddot{\boldsymbol{r}}(\tau) = \boldsymbol{f}_0(\tau) + \Delta \boldsymbol{f}(\tau) \, , \tag{7.2.6}$$

$$\boldsymbol{r}(\tau) = \dot{\boldsymbol{r}}_0 + T \int_0^\tau \left[\boldsymbol{f}_0(\tau') + \Delta \boldsymbol{f}(\tau') \right] d\tau' \, , \tag{7.2.7}$$

$$\boldsymbol{r}(\tau) = \boldsymbol{r}_0 + \dot{\boldsymbol{r}}_0(\tau T) + T^2 \int_0^\tau (\tau - \tau') \left[\boldsymbol{f}_0(\tau') + \Delta \boldsymbol{f}(\tau') \right] d\tau' \, . \tag{7.2.8}$$

Here, the original initial state y_0 appears. The difference between the true motion and the reference motion is given by the Encke vectors $\Delta\ddot{r}$, $\Delta\dot{r}$, and Δr. Using eqs. (7.2.2) to (7.2.4) for the true motion and eqs. (7.2.6) to (7.2.8) for the reference motion they are

$$\Delta\ddot{r}(\tau) = \ddot{r}(\tau) - \ddot{r}_{\text{ref}}(\tau) = \Delta f(\tau) \, , \tag{7.2.9}$$

$$\Delta\dot{r}(\tau) = \dot{r}(\tau) - \dot{r}_{\text{ref}}(\tau) = \Delta\dot{r}_0 + T \int_0^\tau \Delta f(\tau')d\tau' \, , \tag{7.2.10}$$

$$\Delta r(\tau) = r(\tau) - r_{\text{ref}}(\tau) = \Delta r_0 + \Delta\dot{r}_0(\tau T) + T^2 \int_0^\tau (\tau - \tau')\Delta f(\tau')d\tau' \, . \tag{7.2.11}$$

The vectors $\Delta\dot{r}_0 = \dot{r}_0 - \dot{r}_{\text{ref},0}$ and $\Delta r_0 = r_0 - r_{\text{ref},0}$ are the differential initial state between the reference motion and the true motion. This formulation is now very similar to the original integration problem treated in chapter 5, with only two differences to be found: First, the original initial values of the true motion y_0 are replaced by the differential initial values

$$\Delta y_0 = \begin{bmatrix} \Delta r_0 \\ \Delta\dot{r}_0 \end{bmatrix} \, . \tag{7.2.12}$$

Second, the full force $f(\tau)$ is replaced by the disturbing force $\Delta f(\tau)$. This system can be solved with only minor adjustments to the algorithm presented in chapter 5. The complete steps are as follows:

1. Select a reference force f_0 with an associated analytically determinable reference trajectory. Compute r_{ref} and $\dot{r}_{\text{ref}}$ for the entire orbit arc. Compute the disturbing forces Δf at the approximate position r_ϵ according to eq. (7.2.1).
2. Following eqs. (5.2.12) and (5.2.13), compute the integrated Encke position and velocity

$$\Delta r_\epsilon^{\text{int}} = K_r \Delta\ddot{r}_\epsilon \, . \tag{7.2.13}$$

3. With $\bar{\Phi}_r$ as in eq. (5.2.7), solve the system

$$r_\epsilon - r_{\text{ref}} - \Delta r_\epsilon^{\text{int}} = \bar{\Phi}_r \Delta y_0 \tag{7.2.14}$$

   to compute an estimate of the differential state $\Delta\hat{y}_0$.
4. In analogy to eq. (5.2.25), the estimated coordinate difference to the true position is

$$\Delta r_\epsilon = [I - K_r T]^{-1} \left[\bar{\Phi}_r \Delta\hat{y}_0 + \Delta r_\epsilon^{\text{int}} + r_{\text{ref}} - r_\epsilon \right] \, . \tag{7.2.15}$$

5. Compute Φ_r, $\Phi_{\dot{r}}$, and $\Phi_{\ddot{r}}$ according to eqs. (5.2.30), (5.2.33) and (5.2.36).
6. Following eq. (5.2.37), use Δr_ϵ to correct the accelerations due to the disturbing forces

$$\Delta\ddot{r}_{\text{c}} = \Delta\ddot{r}_\epsilon + T\Delta r_\epsilon \, . \tag{7.2.16}$$

7. Integrate the corrected accelerations as in eqs. (5.2.38) and (5.2.39) with

$$\Delta \dot{r}_c^{int} = K_{\dot{r}} \Delta \ddot{r}_c \,, \tag{7.2.17}$$

$$\Delta r_c^{int} = K_r \Delta \ddot{r}_c \,, \tag{7.2.18}$$

and, similar to eq. (5.2.40), compute a new estimate $\Delta \hat{y}_0$ of the differential state from

$$r_\epsilon - r_{ref} - \Delta r_c^{int} = \Phi_r \Delta y_0 \,. \tag{7.2.19}$$

8. Compute the final dynamic orbit as in eqs. (5.2.41) and (5.2.42) with

$$\dot{r} = \dot{r}_{ref} + \Phi_{\dot{r}} \Delta \hat{y}_0 + \Delta \dot{r}_c^{int} \tag{7.2.20}$$

$$r = r_{ref} + \Phi_r \Delta \hat{y}_0 + \Delta r_c^{int} \tag{7.2.21}$$

This is a general formulation of what could be termed a *reduced initial value approach* to dynamic orbit determination.

7.2.1 Reference Motion

These derivations are fully independent of the choice of reference force f_0. The only prerequisite is that the equation of motion due to the reference force should be analytically solvable. If this condition were not fulfilled, the given formulations would still hold, but the numerical advantages attributed to the method might disappear. If, for example, one were to choose $f_0(\tau) = 0$ and $\Delta y_0 = y_0$, the approach would simplify into the same apparatus as presented in sections 5.2.1 to 5.2.4. In this case, the reference motion is a linear unperturbed motion through space, tangent to the satellite orbit at the first epoch. The classical choice for an analytically solvable reference motion is the Kepler ellipse, with the reference force that of a point-like or spherical Earth, or more generally the acceleration due to the central term of a more complex gravitational potential:

$$f_0(\tau) = -GM \frac{r(\tau)}{\|r(\tau)\|^3} \tag{7.2.22}$$

In his work on the perturbation of planets, Encke suggests to compute the perturbed orbit relative to such a Keplerian reference motion (Encke, 1852, 1857). Encke defines the ellipse by requiring that the position and velocity at the first epoch of the reference trajectory are identical to that of the perturbed orbit at the first epoch, or

$$r_{ref,0} = r_\epsilon(0) \qquad \text{and} \qquad \dot{r}_{ref,0} = \dot{r}_\epsilon(0) \,. \tag{7.2.23}$$

Such an ellipse is termed an *osculating* ellipse. Setting the reference motion to an osculating ellipse has the undesirable effect that the reference motion and the perturbed orbit will diverge significantly, usually after only a short period of integration. This leads to the integrals of the perturbing accelerations in eqs. (7.2.10) and (7.2.11)

becoming large again, and in consequence to the loss of any numerical advantages attributed to the method.

The separation of the reference motion and the perturbed motion is commonly quantified in the *Encke ratio*

$$\epsilon = \frac{\|\mathbf{\Delta r}\|}{\|\mathbf{r}\|} \, , \tag{7.2.24}$$

the ratio of the magnitude of the Encke vector in relation to the magnitude of the position vector. A large Encke ratio indicates a relatively speaking large numerical integrand, and consequently the loss of the numerical precision associated with the Encke method. Lundberg, Bettadpur, and Eanes (2000) state that the general recommendation is to aim for $\epsilon < 1\,\%$.

The general approach to treating large Encke ratios ϵ is rectification. Rectification means that the integration is interrupted at a certain epoch and then continued from there using a newly defined reference trajectory. In essence, this implies restarting the orbit integrator with new initial values, which are defined by the last epoch of the previous integration arc. This entails possibly negative effects on precision of the orbit arc (Milani and Nobili, 1987). The new trajectory will however again have a small ϵ, at least for some time until the deviation of the new reference trajectory from the true trajectory starts to grow again.

The first efforts to reduce the Encke ratio for long arc orbit determination, or dynamic orbit integration in general, were based on the premise of considering the secular terms induced in the satellite motion by Earth's oblateness in the reference force (Escobal, 1966; Kyner and Bennett, 1966). Closed equations exist for such a trajectory. The drift induced by Earth's oblateness in some of the Kepler elements, notably the argument of perigee and the right ascension of the ascending node, contribute significantly to the deviation of the reference trajectory from the true trajectory, especially for longer arc lengths. Liu and Hu (1997) later focused on considering higher order terms of Earth's potential, as well as higher-order secular terms, in the reference force. Lundberg, Bettadpur, and Eanes (2000) developed a long arc model that allows general variations in all six orbital elements, mentioning successful results with Encke ratios on the order of 10 % to 20 %. All of these studies have in common that they consider medium to high orbiting laser ranging satellites like the laser geodynamics satellite (LAGEOS) (Liu and Hu, 1997; Lundberg, Bettadpur, and Eanes, 2000; Lundberg, Schutz, et al., 1990) or the *Satellite de Taille Adaptée avec Réflecteurs Laser pour les Etudes de la Terre* (STARLETTE) (Lundberg, Bettadpur, and Eanes, 2000). The arc lengths considered in these works are on the order of multiple years or decades, not hours as is usual in GRACE processing.

For the considered GRACE case of a low-earth orbiter with moderate arc lengths of at most 24 h, a distinctly simpler and more elegant solution presents itself. Where the methods mentioned above consider ever-more precise refinements of the reference force, the initial parameters are always kept to be those of an osculating ellipse for the reference epoch. For GRACE, a mean static Kepler ellipse, with no temporal

modification of the Kepler parameters due to higher order terms or external perturbations proofs completely sufficient. Instead, the choice of the initial parameters of the reference orbit $y_{\text{ref},0}$ is reconsidered.

To formulate a constraint for the initial state of the reference orbit, consider that the Encke ratio $\epsilon(\tau)$ is small if the Encke vector $\Delta r(\tau)$ is small. The goal must thus be to minimize the magnitude of the Encke vectors over the whole arc. This can be written as

$$\sum_{n=0}^{N} \|\Delta r(\tau_n)\|^2 \to \min .\tag{7.2.25}$$

Knowing that the hypothetical true position of the spacecraft is arrived at by taking the sum of the reference position as a function of its initial values and the Encke vector, these positions can be written as

$$r = r_{\text{ref}}(y_{\text{ref},0}) + \Delta r .\tag{7.2.26}$$

Recognizing eq. (7.2.25) as the minimisation criteria of a classical least squares adjustment, eq. (7.2.26) can be solved in a least squares sense. To this end, the Encke vector Δr is treated as if it represented the residuals e of the least squares fit. The true positions are however not available, instead the approximate positions are used as observations for the spacecraft state at each epoch, giving

$$r_{\epsilon} = r_{\text{ref}}(y_{\text{ref},0}) + e .\tag{7.2.27}$$

This finds the initial values of the reference ellipse

$$\hat{y}_{\text{ref},0} = \begin{bmatrix} \hat{r}_{\text{ref},0} \\ \hat{\dot{r}}_{\text{ref},0} \end{bmatrix}\tag{7.2.28}$$

that lead to the minimal square sum $\Delta r^{\mathsf{T}} \Delta r$, fulfilling the condition in eq. (7.2.25). The resulting differential initial values are then

$$\Delta y_0 = y_0 - \hat{y}_{\text{ref},0} = \begin{bmatrix} r_0 \\ \dot{r}_0 \end{bmatrix} - \begin{bmatrix} \hat{r}_{\text{ref},0} \\ \hat{\dot{r}}_{\text{ref},0} \end{bmatrix} .\tag{7.2.29}$$

As $\Delta r^{\mathsf{T}} \Delta r$ is minimized and the Encke ratio is by definition positive, the solution $\hat{y}_{\text{ref},0}$ also minimizes the sum of all Encke ratios over the complete orbit arc. Figure 7.2 illustrates this optimized best-fit reference ellipse.
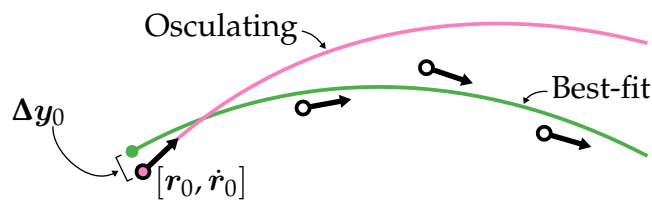

Figure 7.2: Osculating ellipse (in pink) and best-fit ellipse (in green).

7.2.2 Parametrization of Reference Motion

Traditionally, an orbital ellipse in a spherically symmetric potential is parametrised using Kepler parameters

$$\xi = \begin{bmatrix} a & e & I & \omega & \Omega & M \end{bmatrix}^\mathsf{T} . \tag{7.2.30}$$

Numerical tests have shown that this parametrisation for the reference trajectory is not sufficiently stable when using standard double precision arithmetic. This statement is supported by the results later presented in section 7.3.2. This instability could potentially be remedied by computing all parameters relating to the reference trajectory in quadruple precision arithmetic, and then converting the computed state at each epoch to double precision for the further steps. It is undesirable to port the complete orbit integration algorithm to quadruple precision arithmetic, as this is sure to lead to significant performance penalties, with expected slowdowns on the order of a factor of 5 to 10 (Bailey and Borwein, 2015).

Another solution is to parametrise the reference motion with a more stable set of orbital elements. Here, the equinoctial elements

$$\xi_e = \begin{bmatrix} a & h & k & p & q & \lambda \end{bmatrix}^\mathsf{T} \tag{7.2.31}$$

as given in Broucke and Cefola (1972) are an attractive option. In these elements, a is the semi-major axis of the ellipse. The elements h and k define the eccentricity and perigee of the orbit. The elements p and q encode the inclination of the orbital plane and the position of the ascending node. λ is the classical mean longitude. The equinoctial elements are a non-canonical set of orbit elements, with the Poincaré elements their canonical counterpart (Vallado and McClain, 2001). Danielson et al. (1995, Section 2.1) gives a concise but comprehensive introduction to their derivation and use. The transformation from an equinoctial state vector to a Cartesian state vector can mostly be performed without relying on the evaluation of trigonometric functions, making this transformation very numerically stable.

In this work all computations relating to the equinoctial elements are performed in double precision arithmetic, with the exception of the computation of λ, the mean longitude. This is the fast-moving variable defining the position of the satellite along the equinoctial orbit arc. λ is computed and stored in quadruple precision. As λ is not used in any expensive operations, the impact on overall performance is negligible. With this parametrization and implementation, the conversion from equinoctial elements to Cartesian coordinates shows sufficiently high stability. The results presented in sections 7.3.3 and 7.3.4 illustrate this statement.

7.2.3 Determination of Best-Fit Orbit

To determine the best-fit Kepler ellipse from eq. (7.2.27), the partial derivatives of the position and velocity of the satellite in the CRF w.r.t. the equinoctial elements are

needed. This is the *state transition matrix of the equinoctial elements*

$$\boldsymbol{\Phi}_e = \begin{bmatrix} \boldsymbol{\Phi}_{e,r} \\ \boldsymbol{\Phi}_{e,\dot{r}} \end{bmatrix} = \begin{bmatrix} \dfrac{\partial \boldsymbol{r}}{\partial \tilde{\boldsymbol{\xi}}_e} \\ \dfrac{\partial \dot{\boldsymbol{r}}}{\partial \tilde{\boldsymbol{\xi}}_e} \end{bmatrix} . \tag{7.2.32}$$

Similarly to the state transition matrix $\boldsymbol{\Phi}$ introduced in chapter 5, $\boldsymbol{\Phi}_e$ describes the change in the position and velocity of a spacecraft due to a change in the equinoctial elements describing its orbit. This state transition matrix contains exactly the observation equations needed to determine a best-fit equinoctial orbit $\hat{\boldsymbol{\xi}}_e$ that satisfies eq. (7.2.25) in a linearised least squares adjustment.

Danielson et al. (1995) gives the derivatives needed to compute eq. (7.2.32) in a clear and concise formalism. Beware however of wrong partial derivatives of the equinoctial element a with regard to Cartesian position and velocity as given by Danielson et al. (1995, section 2.1.6, eqs. 2 and 4). Comparison with Broucke and Cefola (1972) gives the correct partials in Danielson et al.'s notation. These are

$$\frac{\partial \boldsymbol{r}}{\partial a} = \frac{1}{a} \cdot \left(\boldsymbol{r} - \dot{\boldsymbol{r}} \frac{3t}{2} \right) \qquad \text{and} \qquad \frac{\partial \dot{\boldsymbol{r}}}{\partial a} = -\frac{1}{2a} \cdot \left(\dot{\boldsymbol{r}} - \text{GM} \frac{3\boldsymbol{r}}{\|\boldsymbol{r}\|^3} \cdot t \right) . \tag{7.2.33}$$

In this work, one equinoctial best-fit orbit is determined for each 24 h variational orbit arc. It has proven unnecessary to introduce positions and velocities from all 17 280 epochs in the orbit arc as observations. Instead, only positions from up to 100 epochs are used. The algorithm to determine the best-fit orbit is:

Select observations: Select $N = 100$ epochs from the orbit arc. Start with the first epoch, then select epochs spaced at regular intervals from the remaining arc, giving even coverage of the observations. These positions are inserted into the observation vector

$$\boldsymbol{l} = \begin{bmatrix} \boldsymbol{r}(\tau_1)^\mathsf{T} & \cdots & \boldsymbol{r}(\tau_N)^\mathsf{T} \end{bmatrix}^\mathsf{T} \tag{7.2.34}$$

Compute approximate solution: The initial guess for the best-fit equinoctial elements $\tilde{\boldsymbol{\xi}}_{e,0}$ is taken to be the osculating orbit at the first epoch.

Reduced observations: Compute the unperturbed equinoctial orbit

$$\boldsymbol{l}_0 = \begin{bmatrix} \boldsymbol{r}_{\text{ref}}(\tau_1)^\mathsf{T} & \cdots & \boldsymbol{r}_{\text{ref}}(\tau_N)^\mathsf{T} \end{bmatrix}^\mathsf{T} \tag{7.2.35}$$

and then $\Delta \boldsymbol{l} = \boldsymbol{l} - \boldsymbol{l}_0$.

Observation equations: The observation equation system is

$$\boldsymbol{A} = \begin{bmatrix} \dfrac{\partial \boldsymbol{r}(\tau_1)}{\partial \tilde{\boldsymbol{\xi}}_e} \\ \vdots \\ \dfrac{\partial \boldsymbol{r}(\tau_N)}{\partial \tilde{\boldsymbol{\xi}}_e} \end{bmatrix} = \begin{bmatrix} \boldsymbol{\Phi}_{e,r}(\tau_1) \\ \vdots \\ \boldsymbol{\Phi}_{e,r}(\tau_N) \end{bmatrix} \tag{7.2.36}$$

Update estimate: Compute the least squares estimate $\Delta \hat{x}$ using Δl and A. The updated estimate for the best-fit orbit is then

$$\hat{\xi}_e = \xi_{e,0} + \Delta \hat{x} \ . \tag{7.2.37}$$

Iterate: Until convergence is achieved. The equinoctial orbit $\hat{\xi}_e$ is then used to determine the reference force f_0 in eq. (7.2.1) and as the reference orbit in eq. (7.2.4).

7.3 Results

The following pages will give results from two separate sets of computations. The first results, presented in sections 7.3.1 to 7.3.3 are purely from simulations and illustrate the algorithms performance under ideal conditions. To this end, an orbit was simulated for a single spacecraft using the GOCO05s static gravitational potential (Mayer-Gürr, Kvas, et al., 2015). No further conservative or non-conservative forces were considered in the orbit propagation. The static potential was expanded to degree and order 60. The simulated orbit was computed using an in-house orbit propagator based on the integration polynomials presented in section 2.7.

The second set of results, given in sections 7.3.4 and 7.3.5, illustrate the performance of the algorithm for real data processing. The results were determined using real GRACE data in the context of dynamic orbit integration for the ITSG-Grace2016 gravity field solution.

All orbits, both for the simulation and for real data, were determined for an arc length of 24 h at a sampling of 5 s resulting in $N = 17\,280$ epochs. Where applicable, the Marussi tensor T was expanded to degree and order 10.

When absolute differences between coordinates are shown, such as between iterations, they are given for the along-track axis only. In all presented results the along-track axis shows, in accordance to theory (Huang and Innanen, 1983), the largest errors.

7.3.1 Encke Ratio

Figure 7.3 shows the Encke ratio for the two reference ellipses described in section 7.2.1. The first case (in pink) represents the classical Encke configuration of an osculating reference ellipse. Here, the differential initial state is $\Delta y_0 = 0$. The ellipse is congruent to the approximate orbit at the first epoch. The second case (in green) represents the best-fit reference ellipse for the orbit arc as derived in section 7.2.3. Here, the initial state is the least squares estimate $\Delta \hat{y}_0$.

The Encke ratio for the osculating orbit is 0 % at the start of the 24 h arc. It grows to larger than 1 % within 1 h, finally reaching 20 % towards the end of the arc. The Encke ratio at the final epoch corresponds to an Encke vector of 1240 km.
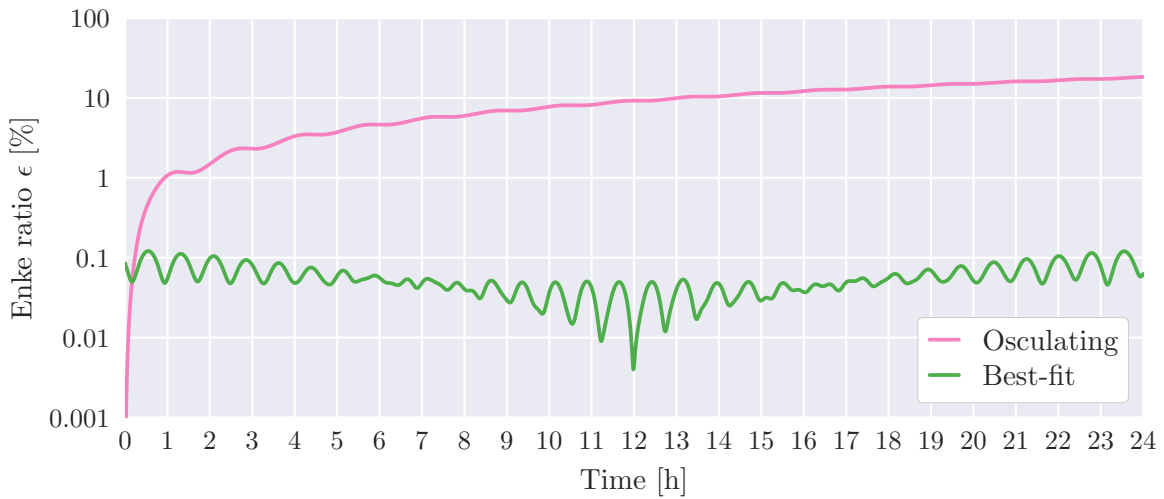
Figure 7.3: Encke ratio over one orbit arc for osculating reference orbit (in pink) and best-fit orbit (in green).

The Encke ratio for the best-fit orbit is in general much smaller, never increasing much beyond 0.1 %. The upper bound of 1 % given by Lundberg, Bettadpur, and Eanes (2000) is never reached. The Encke ratio shows approximately time-symmetric behaviour, with the lowest ratio at the centre of the orbit arc, and the largest ratios at the beginning and end. In absolute terms, the largest observed deviation of the best-fit ellipse from the perturbed motion is 8.2 km, a reduction of 99.3 % from the osculating case.

7.3.2 Convergence

As outlined in section 7.1, the convergence of the dynamic orbit solution can be taken as a benchmark indicating the correctness of the algorithm. To determine the number of iterations necessary for convergence to occur, the simulated orbit was deteriorated with Gaussian white noise. The standard deviation for the position component was set to $\sigma_r = 50\,\mathrm{m}$, that for the velocity component to $\sigma_{\dot{r}} = 0.5\,\mathrm{m/s}$.

The deteriorated orbit was inserted as the first approximate position r_ϵ into the orbit integration routine. Then, 100 iterations of integration and correction were computed for five configurations which differ in the choice and parametrisation of the reference trajectory. The first is a configuration with no reference motion, or $f_0 = 0$ in brown. The second pair consists of osculating reference ellipses, defined by $\Delta y_0 = 0$, parametrised in either Kepler elements (pink) or equinoctial elements (purple). The last pair represents the best-fit ellipses with $\Delta y_0 = \Delta \hat{y}_0$, also parametrised in either Kepler elements (green) or equinoctial elements (orange). Figure 7.4 shows the root mean square (RMS) of the corrections Δr_ϵ applied for these five configurations in each iteration cycle.
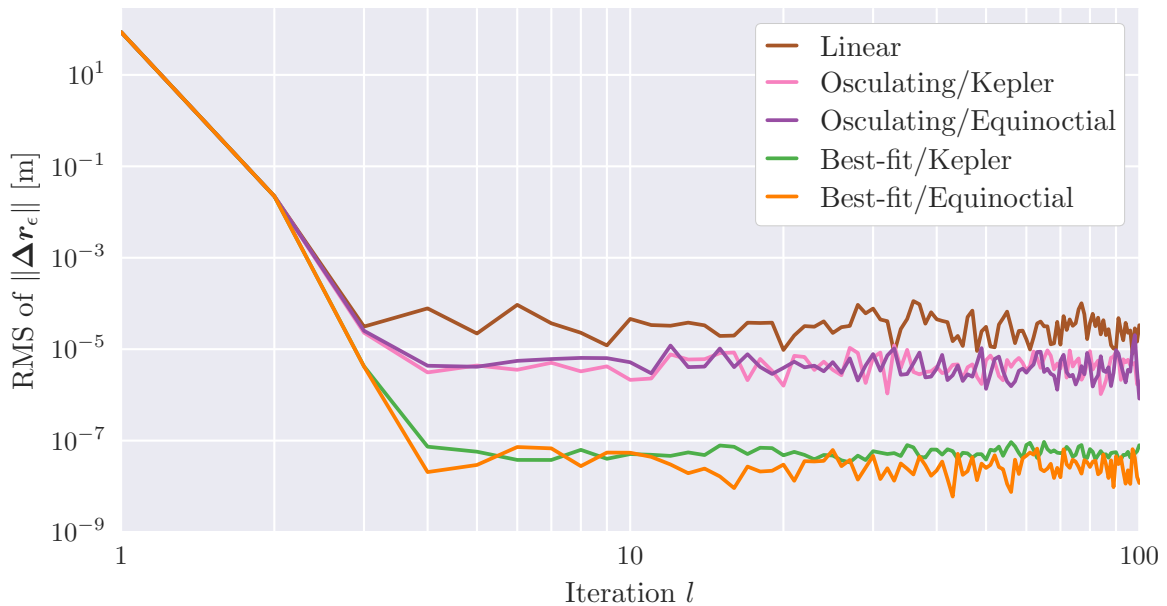
Figure 7.4: Simulated data. RMS of 3D coordinate difference $\|\Delta r_\epsilon\|$ for a complete arc after each iteration l.

For the first two iterations, no difference in convergence between the configurations is apparent, with the changes in positions for all configurations quickly shrinking from tens of metres to around 1 cm. The convergence behaviour starts to differ from the third iteration. Here, the configuration with no reference acceleration (brown) can be easily identified as the one with the worst convergence. The RMS of the corrections never decreases below 10 μm. The two configurations using the osculating reference ellipse and Kepler elements (pink) or equinoctial elements (purple) also exhibit comparatively large position differences between iterations, never falling much below 10 μm. The two configurations using a best-fit reference ellipse, either with Kepler elements (green) or equinoctial elements (orange), show the smallest differences, reaching an equilibrium at changes below 100 nm. All configurations have converged after four iterations, showing no significant reduction in inter-iteration differences thereafter.

7.3.3 Absolute Differences from Simulated Data

The following results are based on the corrections Δr_ϵ obtained after a generous number of 80 iterations, picked at random from the available results. The exact numeric values are only representative, as they of course change from iteration to iteration. The spectral behaviour of the differences is however rather consistent. Figure 7.5 shows the differences $\Delta r_\epsilon^{\mathrm{along}}$ of the in-track coordinate component for one complete day. Figures 7.5a and 7.5b show the coordinate differences in the spatial domain at two different scales. Figure 7.5c shows the PSDs of the coordinate differences, allowing for interpretation of frequency-dependent patterns therein.
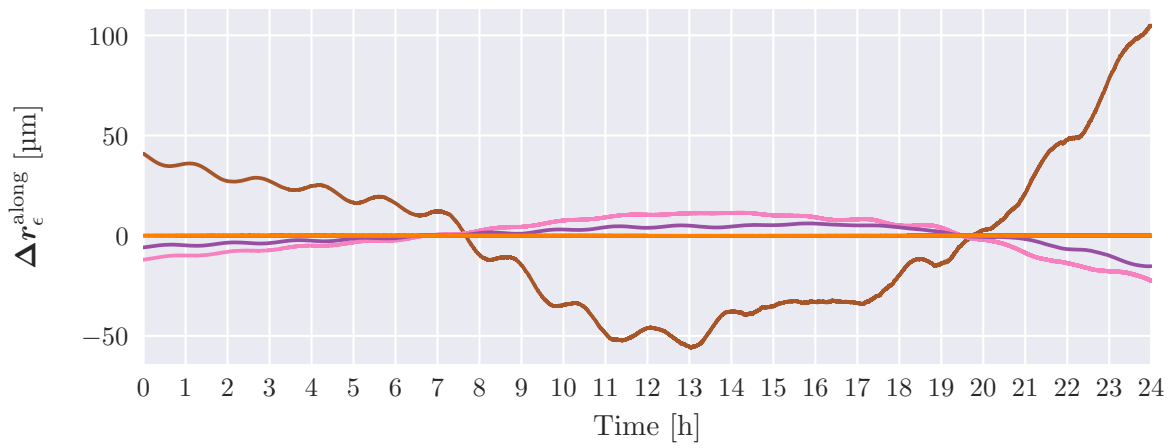
(a) Spatial domain for all configurations.
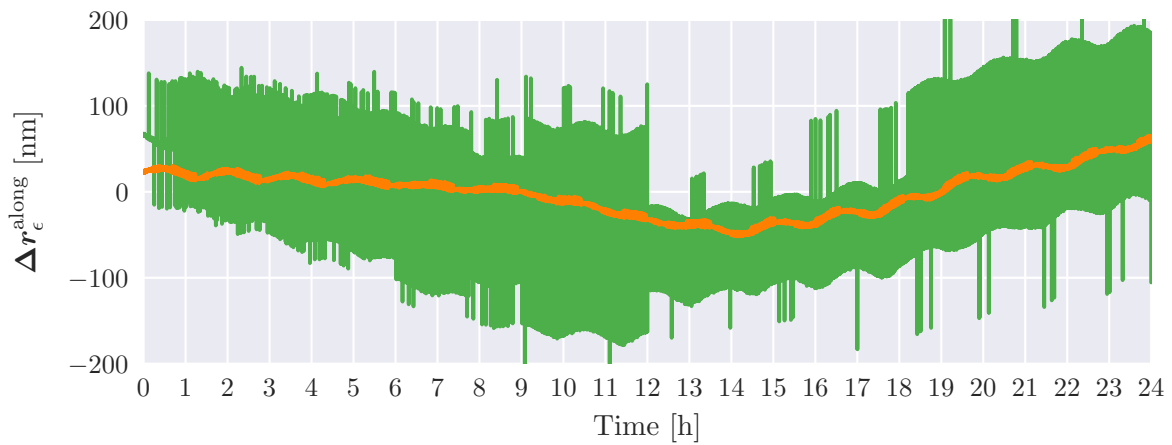
(b) Spatial domain for best-fit configurations.
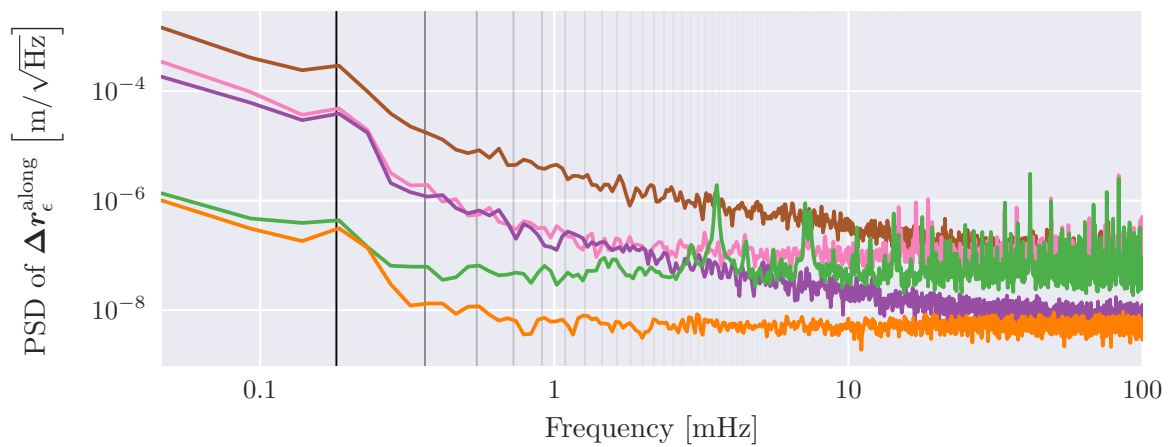
(c) Spectral domain for all configurations.

Figure 7.5: Simulated data. In-Track coordinate differences $\Delta r_\epsilon^{\text{along}}$ between iterations in both the spatial and spectral domain after convergence. The vertical grey lines in (c) denote multiples of the orbital frequency, with the leftmost line showing one cycle per revolution. Colours denoting the configurations are the same as in fig. 7.4.

In fig. 7.5a, the configuration using no reference acceleration (brown) can be identified as the one with the largest coordinate differences. This matches the observations from fig. 7.4. The configurations using the osculating reference ellipse (pink and purple) also show comparatively large errors. For all configurations the magnitude of the differences is smallest at around 8 h and 20 h, not at the beginning of the arc as might be expected. This is due to the re-estimation of the initial state from eqs. (5.2.40) and (7.2.19), fitting the integrated orbit to the approximate positions r_ϵ. The corrections applied to the best-fit configurations (green and orange) can not be seen at this scale. Figure 7.5b shows a magnification of only the best-fit cases. Here it becomes clear that the corrections for the best-fit configuration using equinoctial elements (orange) are smaller than those for the best-fit configuration using Kepler elements (green).

The differences and similarities between the five configurations become most clear not in the spatial domain but when observing the PSDs of the corrections $\Delta r_\epsilon^{\text{along}}$. The PSDs were computed using Welch's method with a segment length of 6 h, and are displayed in fig. 7.5c. The vertical grey lines in fig. 7.5c denote multiples of the orbital frequency, starting at approximately one cycle per 89 min for the leftmost line. The best-performing configuration of a best-fit reference ellipse parametrised in equinoctial elements (orange) shows white noise behaviour at frequencies higher than two cycles per revolution. Significantly, the magnitude of the corrections in the high-frequency part of the spectrum is at the level of the numerical resolution of a double precision floating point number at orbital altitude. For this configuration, machine precision is completely exhausted here. This is not the case for the best-fit ellipse parametrised in Kepler elements (green), which shows a consistently higher power for all frequencies above two cycles per revolution. This clearly illustrates the advantages of the equinoctial parametrisation over the Kepler parametrisation. Both configurations show some residual error at very long wavelengths.

At low frequencies, the configurations based on the osculating reference orbit (pink and purple) show much larger deviations. The corrections for these orbits at one cycle per revolution are two orders of magnitude larger than those of the two best-fit ellipse configurations (green and orange). At higher frequencies, the corrections of the osculating configuration using Kepler elements (pink) asymptotically approach those of the best-fit configuration also using Kepler elements (green). The same holds true for the two equinoctial ellipses, with the osculating configuration (purple) almost reaching the level of the best-fit ellipses (orange) at the Nyquist frequency. Also at higher frequencies, the osculating configuration employing equinoctial elements (purple) displays corrections smaller than those of the best-fit orbit with Kepler elements (green). At very high frequencies close to the Nyquist frequency, the configurations employing Kepler elements (pink and green) show no significant improvements over using no reference acceleration at all (brown).

Not shown in fig. 7.5, the coordinate differences Δr_ϵ in the cross-track and radial axes show similar spectral behaviour. The magnitude of the differences is however smaller by approximately two orders of magnitude.

7.3.4 Application to real GRACE data

In addition to the simulations discussed in sections 7.3.2 and 7.3.3 the dynamic orbit computation was also carried out with real data in the context of the ITSG-Grace2016 gravity field solutions (Klinger, Mayer-Gürr, et al., 2016; Mayer-Gürr, Behzadpour, et al., 2016). In addition to the static GOCO05s potential, these orbits now include accelerations due to conservative forces from several more background models (see table 6.1 for details). Further, direct observations of accelerations due to non-conservative forces from the GRACE accelerometers are included in the integration. The orbits are fit to GRACE ll-SST and hl-SST observations as described in section 6.3.

Figure 7.6 shows that neither of the Kepler-parametrised configurations (pink and green) shows any improvement over the implementation not employing a reference acceleration (brown). For real data, the superiority of the best-fit reference trajectory is confirmed when studying the configurations using equinoctial elements. Neither of the equinoctial configurations (purple and orange) show the large drop in quality when switching to real data that was observed in the Kepler-parametrised configurations (pink and green). The increase in residual power at one cycle per revolution is still present in all solutions, but the magnitude remains smallest for the best-fit equinoctial configuration (orange).

Overall, the best-fit trajectory parametrised in equinoctial elements (orange) is superior to the other configurations in the same way as could be seen in the simulated data. The comparative impact of this improved methodology is significantly larger for real data than could be expected from the less complex data used in the simulations of section 7.3.3.
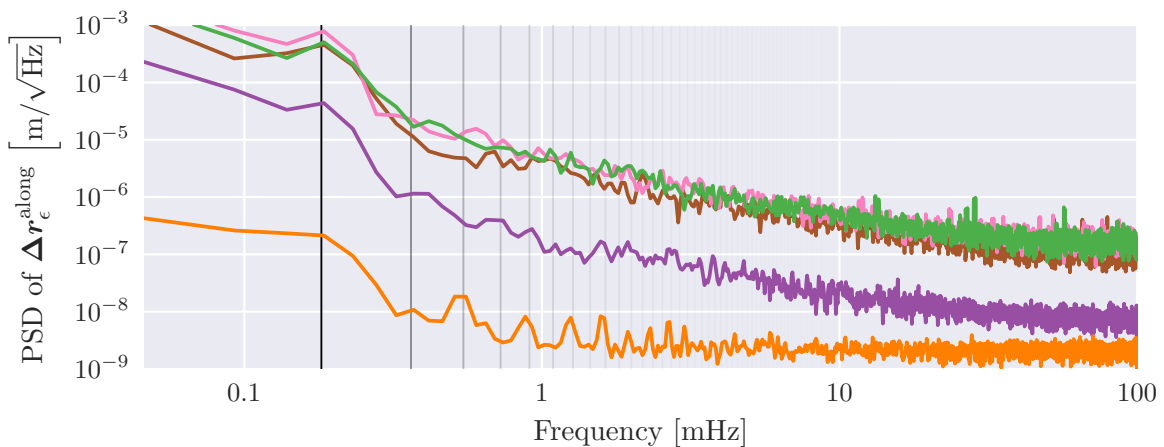
Figure 7.6: Real data. In-Track coordinate differences after convergence for real GRACE orbits. Colours denoting the configurations are the same as in figs. 7.4 and 7.5.

7.3.5 Propagation to Ranging Measurement

The final integrated dynamic GRACE orbits are used at many steps in gravity field determination, as laid out in chapter 5. In eq. (6.4.58) a linearisation of the GRACE ll-SST KBR observations is computed from the dynamic orbits using eq. (4.3.9). Here, both orbits r_A and r_B for GRACE-A and GRACE-B are used. The impact of the dynamic orbit noise on the term used to reduce the ranging measurement can be computed from eq. (4.3.2),

$$\rho_{\mathrm{COM}} = \|u\| = \|r_B - r_A\| \ .$$

The norm of the position difference is

$$\|r_B - r_A\| = \sqrt{\Delta x^2 + \Delta y^2 + \Delta z^2} \tag{7.3.1}$$

regardless of the choice of reference frame. Let both r_A and r_B be given in the SRF of either satellite, for example arbitrarily GRACE-A. Then x is approximately the along-track, y the cross-track, and z the radial difference in position. From eq. (7.3.1), simple error propagation gives

$$\sigma^2_{\rho_{\mathrm{COM}}} = 2 \left[\left(\frac{\Delta x}{\|u\|} \right)^2 \sigma^2_x + \left(\frac{\Delta y}{\|u\|} \right)^2 \sigma^2_y + \left(\frac{\Delta z}{\|u\|} \right)^2 \sigma^2_z \right] \ . \tag{7.3.2}$$

With x being the along-track axis, the partials can be approximated with

$$\frac{\Delta x}{\|u\|} \approx 1 \tag{7.3.3}$$

and

$$\frac{\Delta y}{\|u\|} \approx \frac{\Delta z}{\|u\|} \approx 0 \ . \tag{7.3.4}$$

This gives the standard deviation of the derived baseline as

$$\sigma_{\rho_{\mathrm{COM}}} = \sqrt{2} \sigma_x \ . \tag{7.3.5}$$

The uncertainty of the orbit in the along-track axis due to the integration algorithm is given by the PSDs displayed in fig. 7.6. After variance propagation with eq. (7.3.5), the PSDs can directly be differentiated in the frequency domain to compute the uncertainty of the reduction term in the range rate domain:

$$\sigma_{\dot{\rho}_{\mathrm{COM}}}(f) = 2\pi f \cdot \sigma_{\rho_{\mathrm{COM}}}(f) \tag{7.3.6}$$

The resulting PSDs are displayed in fig. 7.7. Here, the solid black line shows an error estimate for the GRACE KBR instrument. The dashed black line is an error estimate for the GRACE-FO laser ranging interferometer. All tested configurations lead to a
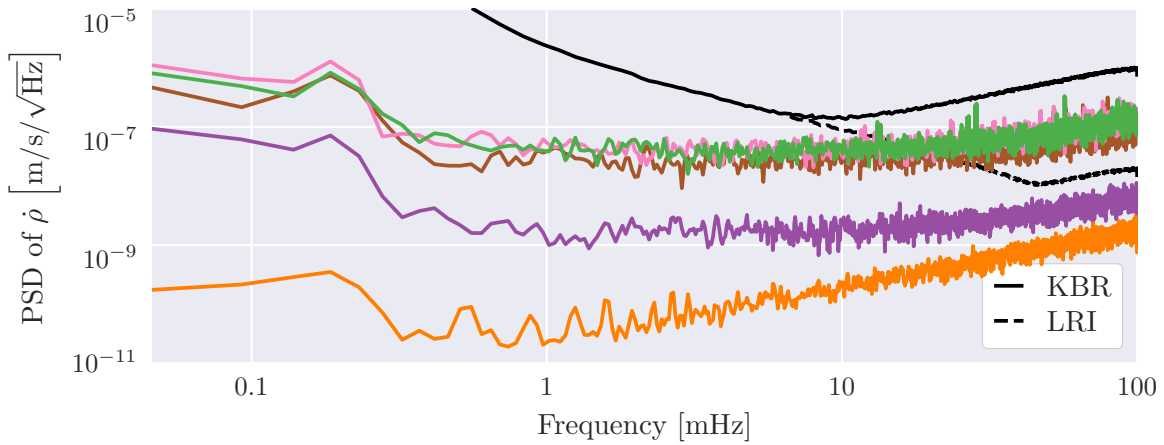
Figure 7.7: Real data. Propagation of orbit noise to range rate measurement $\dot{\rho}$. Solid black is a noise model for the GRACE KBR and ACC instrument noise, Dashed black is a noise model for the GRACE-FO LRI and ACC instruments. The other colours are the same as in figs. 7.4 to 7.6.

range-rate error smaller than the precision of the current KBR instrument on GRACE (solid black line) across the entire frequency spectrum.

In the branch of the error spectrum that is dominated by the KBR noise, above $\approx 10\,\mathrm{mHz}$, the accuracy of the configuration using no reference motion (brown) as well as the uncertainty of both the Kepler configurations (pink and green) are well above the performance estimate for the LRI (dashed black line). Both configurations using equinoctial elements (purple and orange) are below the LRI noise level over the complete spectrum. As could be expected, the equinoctial configuration based on the best-fit reference ellipse (orange) also shows the lowest noise in this domain.

The KBR noise spectrum in fig. 7.7 is based on spectral analysis of real GRACE SST residuals. The performance estimate for the LRI is based on real GRACE ACC data, a description of the noise characteristics of the LRI (Heinzel et al., 2012), and an optimistic assumption of a 50-fold improvement of the ranging accuracy with regard to the KBR instrument (Flechtner, 2012).

7.4 Discussion

An improved algorithm for dynamic orbit determination was developed, paying particular attention to its applicability to GRACE-FO data processing. The existing methodology was refined by applying Encke's method, directly eliminating the large contribution of the central term of Earth's gravitational potential on the numerically integrated accelerations. Encke's method was then refined in two separate ways: First, the osculating reference ellipse proposed by Encke was replaced by a rigorously optimized best-fit reference ellipse. Such a best-fit ellipse significantly reduces the

uncertainty observed at low frequencies in the dynamic orbits. Complicated higher-order or time-variable parametrizations of the reference ellipse can thus be avoided, keeping the complexity of the implementation low. Further, the reference ellipse was transformed from a parametrisation in classical Kepler elements to a parametrisation in equinoctial elements. Without changing the geometry of the ellipse, this improved the stability of the derived reference motion mainly at higher frequencies. The resulting orbits combining both of these improvements reach machine precision at frequencies above two cycles per orbital revolution.

The uncertainty of the original and improved dynamic orbits were compared with the uncertainty of GRACE and GRACE-FO ll-SST ranging observations through error propagation to the range rate domain. It was shown that the improved orbits are now self-consistent to well below the expected precision of the GRACE-FO LRI instrument. This represents an improvement of several orders of magnitude over previous results achieved at IfG. Such an improvement can be important as the dynamic orbits are used as a Taylor point in the linearisation of the observation equations for gravity field recovery from GRACE, and later GRACE-FO. Any extraneous errors that originate in the processing chain, and do not arise directly from the observations, should be avoided.

The largest significance of this work can be found in the reduction of the in-track variability between iterations by several orders of magnitude, as it is the component with the largest influence on the GRACE ll-SST ranging observations. It is conceivable to further reduce this error using an ensemble approach. In such an approach, the results of each iteration after convergence would be treated as a separate realisation of the dynamic orbit. An ensemble of such realisations could then be directly used to compute an orbit of best agreement, possibly reducing the integration error at each individual epoch.

The assessment of the effectiveness of the equinoctial best-fit reference ellipse presented in this work is very specific to the GRACE orbital configuration and chosen arc length. For the case of GRACE precession of the orbital plane during the integration period is negligible, which ensures a consistently small Encke ratio. The method is thus directly applicable to satellites in similar orbital configurations such as the European Space Agency's gravity field and steady-state ocean circulation explorer (GOCE) mission (Drinkwater et al., 2003) or the Swarm constellation (Friis-Christensen, Lühr, and Hulot, 2006). For satellites in other orbits, or for longer arcs, the effect of nodal precession might need to be considered. The nodal precession of the orbital plane is dependent on the spacecraft's inclination (Brouwer, 1959), and is smallest for polar orbits. The Encke ratio would thus increase at a faster rate for a satellite at any other inclination than GRACE. A better approximation of such an orbit could be made by introducing a co-precessing ellipse, which would keep the Encke ratio smaller for longer integration periods. Such an ellipse would also again allow for longer integration periods, as shown by Escobal, 1966; Kyner and Bennett, 1966. Jezewski (1983a,b) gives an analytical solution for such a reference motion, where the precession of the ellipse is due to Earth's oblateness.

Importantly, this method improves only on the processing of the data, leading to a dynamic orbit that is more compatible with the observations and models used in its integration. The method is *not* able to compensate for deficiencies in the input data. Given noisy accelerometer data or imperfect background models, application of this method would not lead to dynamic orbits that are necessarily closer to the true position of the spacecraft, but merely fit the noisy observations and models better.

Spectral analysis of orbit differences from real GRACE data after convergence shows that some extraneous oscillations remain in the orbits. These oscillations are largest at frequencies at or below one cycle per revolution. They can also be attributed to the static nature of the employed reference ellipse. The presented results are however satisfactory for applications in GRACE processing. For this use, the critical part of the error spectrum begins only at much higher frequencies, where stability better than that expected of the GRACE-FO LRI instrument was achieved (cf. fig. 7.7).

The applicability of the often suggested method of rectifying the reference orbit to GRACE dynamic orbit integration is uncertain. Continuous orbit arcs are of high desirability in the context of integrating the variational equations and dynamic orbits, as the number of satellite states to be estimated is kept low. Milani and Nobili (1987) give a refined algorithm for an orbit rectification method which can be used without restarting the integration procedure and thus introducing a new satellite state at that epoch. In the integration method presented in this text, the state transition matrix of the variational equations is modified using corrections computed from the Marussi tensor. Given this circumstance, it is not immediately clear how the method outlined by Milani and Nobili can be applied to the presented modified Encke approach.

Star Camera Observations and Uncertainties

<div style="text-align: right">8</div>

In the processing strategy employed for ITSG-Grace2016, an accurate stochastic model is indispensable to determining a high-quality gravity field solution. In the regime used to estimate the stochastic model, which was described in section 6.5, the complete noise spectrum for the ll-SST observations was modelled as resulting from exactly one stationary process. The estimated covariance function was subsequently scaled by an arc-wise variance factor. This scaling equally affects all time lags of the covariance function, or equivalently all frequencies of the PSD. It does not change the assumption of stationarity within one arc, but only scales the variance of the stationary process. These arc-wise variance factors, in effect, can be regarded as a fudge factor for unmodelled variations in the observation noise.

Analysis of the arc-wise variance factors for ITSG-Grace2016 has shown that they are at times correlated with the magnitude and change of the satellite pointing angles with respect to the line of sight frame. The magnitude of these angles maps directly into the magnitude of the antenna offset correction. As the satellites are subject to active steering and pointing variations due to environmental effects, the variance in the AOC over one month of observations, or even one arc, can decidedly not be regarded as the result of a stationary process.

This chapter introduces an additional non-stationary stochastic model for the antenna offset correction. This new AOC stochastic model is derived from the full orientation covariance matrices obtained in the improved sensor fusion described in section 6.2. The impact of introducing this a priori information on the non-stationary AOC noise alongside the estimated stationary stochastic model (see section 6.5) is analysed. The combined stochastic models are used to estimate a time series of GRACE monthly gravity field solutions, based on the ITSG-Grace2016 processing chain. The focus in the analysis will not be on the gravity field solutions themselves, but on the stochastic model and post-fit residuals in the ll-SST observable. The impact on the estimated Stokes coefficients will be analysed in chapter 9, together with the gravity field solutions estimated therein.

8.1 The Antenna Offset Correction in the ll-SST Observation Equation

The antenna offset correction is one of many corrections applied to the ll-SST KBR observations. The reduced observation vector for the low-low satellite-to-satellite

tracking observable (see eq. (6.4.58)) can be condensed to

$$\Delta l_{\text{sst}} = \dot{\rho}_{\text{sst}} + \Delta \dot{\rho}_{\text{AOC}} + e \qquad (8.1.1)$$

with $\dot{\rho}_{\text{sst}}$ the *reduced range rate*

$$\dot{\rho}_{\text{sst}} = \dot{\rho}_{\text{KBR}} + \Delta \dot{\rho}_{\text{TOF}} + \Delta \dot{\rho}_{\text{Iono}} - \dot{\rho}_{\text{COM}} \ . \qquad (8.1.2)$$

Before, only one stochastic model was estimated for the ll-SST observations under the assumption of stationarity. A priori knowledge of the spacecraft orientation uncertainties can be exploited to separate the noise due to the non-stationary AOC process from the remaining noise. The remaining noise sources will continue to be treated under the assumption of stationarity.

In effect, the stochastic model will be

$$\hat{\dot{\rho}}_{\text{sst}} = \dot{\rho}_{\text{sst}} + \hat{e}_{\text{sst}} \ , \qquad \hat{e}_{\text{sst}} \sim N\left(0, \boldsymbol{\Sigma}_{\text{sst}}\right) \qquad (8.1.3)$$
$$\Delta \hat{\dot{\rho}}_{\text{AOC}} = \Delta \dot{\rho}_{\text{AOC}} + \hat{e}_{\text{AOC}} \ , \qquad \hat{e}_{\text{AOC}} \sim N\left(0, \boldsymbol{\Sigma}_{\Delta \dot{\rho}_{\text{AOC}}}\right) \qquad (8.1.4)$$

with $\boldsymbol{\Sigma}_{\text{sst}}$ determined through VCE as discussed in section 6.5, and $\boldsymbol{\Sigma}_{\Delta \dot{\rho}_{\text{AOC}}}$ to be discussed in the following sections. The complete stochastic model for the reduced observations Δl_{sst} is obtained through variance propagation as

$$\boldsymbol{\Sigma}_{ll} = \boldsymbol{\Sigma}_{\text{sst}} + \boldsymbol{\Sigma}_{\Delta \dot{\rho}_{\text{AOC}}} \ . \qquad (8.1.5)$$

8.1.1 Uncertainties in Computing the Antenna Offset Correction

As discussed in section 6.2, the adapted ITSG-Grace2016 sensor fusion algorithm gives complete variance-covariance matrices for the orientation of the GRACE satellites. Let these be $\hat{\boldsymbol{\Sigma}}_{\hat{\alpha}\hat{\alpha}}^{\text{A}}$ for GRACE-A and $\hat{\boldsymbol{\Sigma}}_{\hat{\alpha}\hat{\alpha}}^{\text{B}}$ for GRACE-B. These covariances represent the uncertainty of the small angle rotation from the nominal orientation of the satellite to the observed instantaneous orientation. This is the rotation $\tilde{\boldsymbol{R}}_\alpha$ from eq. (6.2.4).

For one epoch, the AOC as given in eq. (4.3.6) can be approximated through

$$\Delta \rho_{\text{AOC}} = \langle \boldsymbol{R}_{\text{A}} \boldsymbol{c}_{\text{A}}, \boldsymbol{e} \rangle + \langle \boldsymbol{R}_{\text{B}} \boldsymbol{c}_{\text{B}}, \boldsymbol{e} \rangle \ , \qquad (8.1.6)$$

where $\boldsymbol{R}_s, s \in \text{A}, \text{B}$ is the observed rotation from the SRF to the CRF, $\tilde{\boldsymbol{R}}_{\text{CRF}}^{\text{SRF}}$, for that satellite. The APC vectors are given in the SRF, the satellite baseline $\boldsymbol{e}$ in the CRF. Rewriting eq. (8.1.6), the AOC can also be expressed in terms of the three-dimensional *opening angle* β between the APC vector and the satellite baseline:

$$\Delta \rho_{\text{AOC}} = \|\boldsymbol{c}_{\text{A}}\| \cdot \cos \beta_{\text{A}} + \|\boldsymbol{c}_{\text{B}}\| \cos \cdot \beta_{\text{B}} \ , \qquad \beta_s = \arccos \left\langle \frac{1}{\|\boldsymbol{c}_s\|} \boldsymbol{R}_s \boldsymbol{c}_s, \boldsymbol{e} \right\rangle . \quad (8.1.7)$$

The opening angle for GRACE-A is visualized in fig. 8.1. This formulation is useful to keep in mind as, due to the small values of β, the opening angle can often be used as a proxy for the magnitude of the AOC that is intuitive to conceptualize and classify.
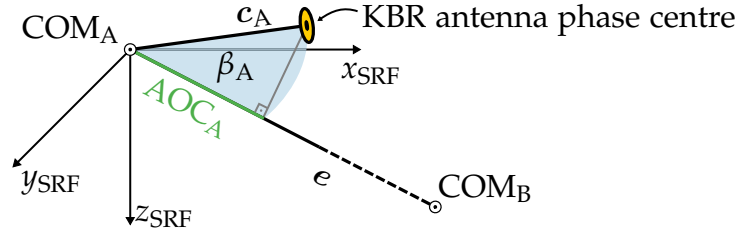
Figure 8.1: Opening angle for GRACE-A antenna phase centre vector.

In theory, all quantities involved in the computation of the AOC are subject to some uncertainty. The uncertainty of the spacecraft orientation is known to some extent from the SCA/ACC sensor fusion, but as this fusion is based on a priori assumptions on the noise of the SCA and ACC observables, it can only be regarded as an approximation of the true uncertainties. The APC vectors c_A and c_B are determined through in-orbit calibration manoeuvres, and as such can not be expected to be error-free. Similarly, the baseline e is determined from the integrated dynamic orbits, and is certain to not represent the true relative positions of the satellites.

The remainder of this chapter will focus on the uncertainty in the satellite orientation and its consideration in the gravity field adjustment, based on the formulation given in eq. (8.1.6).

8.1.2 AOC Covariance From Sensor Fusion

The AOC as described in eq. (8.1.6) is a sum of two identical component summands, with only the rotation and APC vector specific to each satellite. It is thus sufficient to investigate variance propagation for only one summand, as the result for the other is then trivially obtained through substitution of these two quantities. To make this derivation easier to follow, the APC vector c and the satellite baseline e will be subscripted with the coordinate system they are given in. The contribution to the AOC for one satellite is

$$
\begin{aligned}
\Delta \rho_{\text{AOC}}^{s} &= \left\langle \tilde{R}_{\text{CRF}}^{\text{SRF}} c_{\text{SRF}}, e_{\text{CRF}} \right\rangle \\
&= \left(\tilde{R}_{\text{CRF}}^{\text{SRF}} c_{\text{SRF}} \right)^{\mathsf{T}} e_{\text{CRF}} \\
&= c_{\text{SRF}}^{\mathsf{T}} \left(\tilde{R}_{\text{CRF}}^{\text{SRF}} \right)^{\mathsf{T}} e_{\text{CRF}} .
\end{aligned}
\tag{8.1.8}
$$

The SCA/ACC sensor fusion gives uncertainties for small angle rotations in the SRF, but the rotary $\tilde{R}_{\text{CRF}}^{\text{SRF}}$ is a large rotation. So for variance propagation purposes, a suitable transformation is needed. To this end, a similar decomposition of the rotation as used in eq. (6.2.5) is employed, with

$$
\tilde{R}_{\text{CRF}}^{\text{SRF}} = R_{\text{CRF}}^{\text{NOM}} \tilde{R}_{\text{NOM}}^{\text{SRF}} .
\tag{8.1.9}
$$

Here, $R_{\text{CRF}}^{\text{NOM}}$ is the rotation to the CRF from the nominal orientation of the spacecraft as described in section 4.3, with the KBR antenna pointing to the other spacecraft. This rotary is computed from the satellite orbits and the calibrated APC coordinates and is assumed to be error-free. The remaining rotation $\tilde{R}_{\text{NOM}}^{\text{SRF}}$ from the SRF to the nominal orientation is the inverse of the small-angle Euler rotation sequence described in eqs. (6.2.4) and (6.2.5):

$$\tilde{R}_{\text{NOM}}^{\text{SRF}} = \tilde{R}_{\alpha}^{\mathsf{T}} \tag{8.1.10}$$

This is the rotation for which the covariance matrix was determined in the sensor fusion algorithm of section 6.2. Substituting these rotations in eq. (8.1.8) gives

$$
\begin{aligned}
\Delta \rho_{\text{AOC}}^s &= c_{\text{SRF}}^{\mathsf{T}} \left(R_{\text{CRF}}^{\text{NOM}} \tilde{R}_{\text{NOM}}^{\text{SRF}} \right)^{\mathsf{T}} e_{\text{CRF}} \\
&= c_{\text{SRF}}^{\mathsf{T}} \left(\tilde{R}_{\text{NOM}}^{\text{SRF}} \right)^{\mathsf{T}} \left(R_{\text{CRF}}^{\text{NOM}} \right)^{\mathsf{T}} e_{\text{CRF}} \\
&= c_{\text{SRF}}^{\mathsf{T}} \tilde{R}_{\text{SRF}}^{\text{NOM}} R_{\text{NOM}}^{\text{CRF}} e_{\text{CRF}} .
\end{aligned}
\tag{8.1.11}
$$

The rightmost product in eq. (8.1.11), $R_{\text{NOM}}^{\text{CRF}} e_{\text{CRF}}$, is the satellite baseline expressed in the nominal orientation of the spacecraft. There is no need to explicitly calculate this vector, though, as by definition it is exactly the direction of the APC vector expressed in the SRF, as illustrated in fig. 8.2. In other words, the satellite baseline in the nominal orientation is

$$R_{\text{NOM}}^{\text{CRF}} e_{\text{CRF}} = \frac{c_{\text{SRF}}}{\|c_{\text{SRF}}\|} . \tag{8.1.12}$$

Inserting into eq. (8.1.11) then gives

$$\Delta \rho_{\text{AOC}}^s = \frac{1}{\|c_{\text{SRF}}\|} \cdot c_{\text{SRF}}^{\mathsf{T}} \tilde{R}_{\text{SRF}}^{\text{NOM}} c_{\text{SRF}} , \tag{8.1.13}$$

and finally, using eq. (8.1.10)

$$\Delta \rho_{\text{AOC}}^s = \frac{1}{\|c_{\text{SRF}}\|} \cdot c_{\text{SRF}}^{\mathsf{T}} \tilde{R}_{\alpha} c_{\text{SRF}} . \tag{8.1.14}$$

The partial derivative of the AOC w.r.t. the small angle rotations α is then, via the chain rule

$$\frac{\partial \Delta \rho_{\text{AOC}}^s}{\partial \alpha} = \frac{\partial \Delta \rho_{\text{AOC}}^s}{\partial \text{vec}\left(\tilde{R}_{\alpha}\right)} \frac{\partial \text{vec}\left(\tilde{R}_{\alpha}\right)}{\partial \alpha} . \tag{8.1.15}$$

With the APC vector c now understood to be given in the SRF, and using the ordering for matrix derivatives as described in eq. (2.1.7), the first partial is

$$
\begin{aligned}
\frac{\partial \Delta \rho_{\text{AOC}}^s}{\partial \text{vec}\left(\tilde{R}_{\alpha}\right)} &= \frac{1}{\|c\|} \cdot c^{\mathsf{T}} \otimes c^{\mathsf{T}} \\
&= \frac{1}{\|c\|} \cdot \begin{bmatrix} c_x c_x & c_x c_y & c_x c_z & c_y c_x & c_y c_y & c_y c_z & c_z c_x & c_z c_y & c_z c_z \end{bmatrix} .
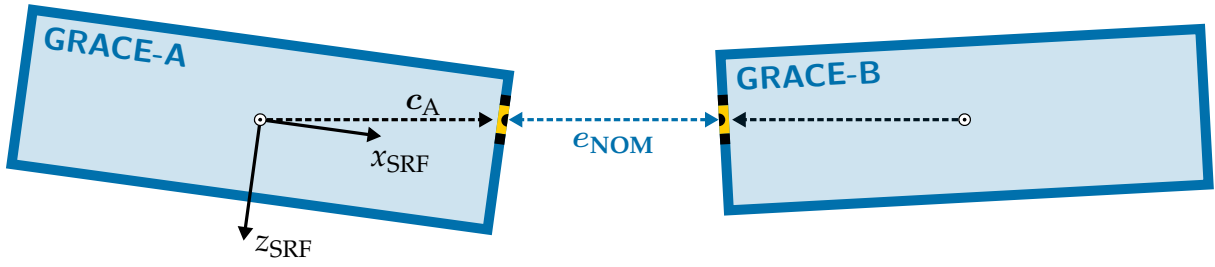\end{aligned}
\tag{8.1.16}
$$

Figure 8.2: Orientation of spacecraft in nominal attitude with APC vector

The second partial depends on the chosen Euler sequence used to represent the small-angle rotation $\tilde{\boldsymbol{R}}_\alpha$. After analytically forming the complete rotary as described in eq. (6.2.5), partials w.r.t. to roll, pitch, and yaw are taken. For the Euler sequence from eq. (6.2.5) used here, these can for example be found in Diebel, 2006, section 8.11. For the individual Euler rotations, the derivatives are

$$
\frac{\partial \tilde{\boldsymbol{R}}_\alpha}{\partial \text{roll}} = \begin{bmatrix} 0 & s_{\text{pitch}} c_{\text{roll}} c_{\text{yaw}} - s_{\text{roll}} s_{\text{yaw}} & s_{\text{pitch}} s_{\text{roll}} c_{\text{yaw}} + s_{\text{yaw}} c_{\text{roll}} \\ 0 & -s_{\text{pitch}} s_{\text{yaw}} c_{\text{roll}} - s_{\text{roll}} c_{\text{yaw}} & -s_{\text{pitch}} s_{\text{roll}} s_{\text{yaw}} + c_{\text{roll}} c_{\text{yaw}} \\ 0 & -c_{\text{pitch}} c_{\text{roll}} & -s_{\text{roll}} c_{\text{pitch}} \end{bmatrix} , \quad (8.1.17)
$$

$$
\frac{\partial \tilde{\boldsymbol{R}}_\alpha}{\partial \text{pitch}} = \begin{bmatrix} -s_{\text{pitch}} c_{\text{yaw}} & s_{\text{roll}} c_{\text{pitch}} c_{\text{yaw}} & -c_{\text{pitch}} c_{\text{roll}} c_{\text{yaw}} \\ s_{\text{pitch}} s_{\text{yaw}} & -s_{\text{roll}} s_{\text{yaw}} c_{\text{pitch}} & s_{\text{yaw}} c_{\text{pitch}} c_{\text{roll}} \\ c_{\text{pitch}} & s_{\text{pitch}} s_{\text{roll}} & -s_{\text{pitch}} c_{\text{roll}} \end{bmatrix} , \quad (8.1.18)
$$

$$
\frac{\partial \tilde{\boldsymbol{R}}_\alpha}{\partial \text{yaw}} = \begin{bmatrix} -s_{\text{yaw}} c_{\text{pitch}} & -s_{\text{pitch}} s_{\text{roll}} s_{\text{yaw}} + c_{\text{roll}} c_{\text{yaw}} & s_{\text{pitch}} s_{\text{yaw}} c_{\text{roll}} + s_{\text{roll}} c_{\text{yaw}} \\ -c_{\text{pitch}} c_{\text{yaw}} & -s_{\text{pitch}} s_{\text{roll}} c_{\text{yaw}} - s_{\text{yaw}} c_{\text{roll}} & s_{\text{pitch}} c_{\text{roll}} c_{\text{yaw}} - s_{\text{roll}} s_{\text{yaw}} \\ 0 & 0 & 0 \end{bmatrix} , \quad (8.1.19)
$$

with $s_{\text{roll}} = \sin(\text{roll})$, $c_{\text{roll}} = \cos(\text{roll})$, and equivalently for pitch and yaw. Using the correct ordering, the full matrix-vector derivative is

$$
\frac{\partial \operatorname{vec}\left(\tilde{\boldsymbol{R}}_\alpha\right)}{\partial \boldsymbol{\alpha}} =
$$

$$
\begin{bmatrix} 0 & -s_{\text{pitch}} c_{\text{yaw}} & -s_{\text{yaw}} c_{\text{pitch}} \\ 0 & s_{\text{pitch}} s_{\text{yaw}} & -c_{\text{pitch}} c_{\text{yaw}} \\ 0 & c_{\text{pitch}} & 0 \\ s_{\text{pitch}} c_{\text{roll}} c_{\text{yaw}} - s_{\text{roll}} s_{\text{yaw}} & s_{\text{roll}} c_{\text{pitch}} c_{\text{yaw}} & -s_{\text{pitch}} s_{\text{roll}} s_{\text{yaw}} + c_{\text{roll}} c_{\text{yaw}} \\ -s_{\text{pitch}} s_{\text{yaw}} c_{\text{roll}} - s_{\text{roll}} c_{\text{yaw}} & -s_{\text{roll}} s_{\text{yaw}} c_{\text{pitch}} & -s_{\text{pitch}} s_{\text{roll}} c_{\text{yaw}} - s_{\text{yaw}} c_{\text{roll}} \\ -c_{\text{pitch}} c_{\text{roll}} & s_{\text{pitch}} s_{\text{roll}} & 0 \\ s_{\text{pitch}} s_{\text{roll}} c_{\text{yaw}} + s_{\text{yaw}} c_{\text{roll}} & -c_{\text{pitch}} c_{\text{roll}} c_{\text{yaw}} & s_{\text{pitch}} s_{\text{yaw}} c_{\text{roll}} + s_{\text{roll}} c_{\text{yaw}} \\ -s_{\text{pitch}} s_{\text{roll}} s_{\text{yaw}} + c_{\text{roll}} c_{\text{yaw}} & s_{\text{yaw}} c_{\text{pitch}} c_{\text{roll}} & s_{\text{pitch}} c_{\text{roll}} c_{\text{yaw}} - s_{\text{roll}} s_{\text{yaw}} \\ -s_{\text{roll}} c_{\text{pitch}} & -s_{\text{pitch}} c_{\text{roll}} & 0 \end{bmatrix} .
$$

$$(8.1.20)$$

With these derivatives, the variance of the satellite orientation observation from the SCA/ACC sensor fusion can be propagated to the AOC for one spacecraft. As the AOC at one epoch only depends on the orientation at that epoch, the matrix of partials is block diagonal, with

$$
\boldsymbol{F}_\alpha^s = \begin{bmatrix} \frac{\partial \Delta \rho_{\mathrm{AOC}}^s(\tau_1)}{\partial \boldsymbol{\alpha}(\tau_1)} & & 0 \\ & \ddots & \\ 0 & & \frac{\partial \Delta \rho_{\mathrm{AOC}}^s(\tau_N)}{\partial \boldsymbol{\alpha}(\tau_N)} \end{bmatrix}_{N \times 3N} . \tag{8.1.21}
$$

With $\Delta \dot{\rho}_{\mathrm{AOC}} = \partial \Delta \rho_{\mathrm{AOC}} / \partial \tau$ the full AOC covariance matrix in the range rate domain for one spacecraft is

$$
\boldsymbol{\Sigma}_{\Delta \dot{\rho}_{\mathrm{AOC}}}^s = \boldsymbol{D} \boldsymbol{F}_\alpha^s \hat{\boldsymbol{\Sigma}}_{\hat{\alpha}\hat{\alpha}}^s \left(\boldsymbol{D} \boldsymbol{F}_\alpha^s \right)^{\mathsf{T}} , \tag{8.1.22}
$$

with $\boldsymbol{D}$ the polynomial differentiation matrix from eq. (6.4.56). The complete AOC covariance matrix considering the influence of both GRACE-A and GRACE-B is

$$
\boldsymbol{\Sigma}_{\Delta \dot{\rho}_{\mathrm{AOC}}} = \boldsymbol{\Sigma}_{\Delta \dot{\rho}_{\mathrm{AOC}}}^{\mathrm{A}} + \boldsymbol{\Sigma}_{\Delta \dot{\rho}_{\mathrm{AOC}}}^{\mathrm{B}} . \tag{8.1.23}
$$

Figure 8.3 shows the AOC covariance matrices due to the orientation uncertainty together with the Toeplitz covariance matrix constructed from the estimated covariance function for one short arc in June 2010. In ITSG-Grace2016, this is arc 134 of the month, containing data from 13:35:45 UTC to 16:35:40 UTC on June 17, 2018. Figures 8.3b and 8.3c show that the overall magnitude of the AOC covariance matrices is much smaller than that of the Toeplitz covariance matrix, displayed in fig. 8.3a. Figures 8.3d and 8.3e show magnified views of the AOC covariance matrices. Due to blinding by the sun or the moon, there are times when only one SCA head is active and considered in the sensor fusion. These times are marked in red in the margins of the matrix plots. They correspond well to larger variances on the off-diagonal elements of the covariance matrices.

During this arc, at around 15:00:00, GRACE-A was commanded to attitude hold mode. Due to the deteriorated pointing accuracy, the opening angle β_{A} for GRACE-A starts to increase. This can be observed in the increased magnitude of the AOC covariance matrix in fig. 8.3b. The effect is much clearer when focusing only on the main diagonal elements of the covariance matrices, as displayed in fig. 8.4. Here, the relation of the increased opening angle and the increase in the propagated standard deviation σ for GRACE-A (in green) can be clearly seen. Note that the standard deviation is given on a logarithmic scale. The increase in opening angle for GRACE-A by a factor of ≈ 2 to ≈ 3 leads to an increase in the AOC standard deviation for GRACE-A of approximately one order of magnitude. The main diagonal elements of the AOC covariance matrix for GRACE-A (in green) are however still smaller than those of the Toeplitz matrix (in blue). The timing of the increase in opening angle corresponds to the beginning of the increase in the arc-wise variance factors previously observed in fig. 6.8.
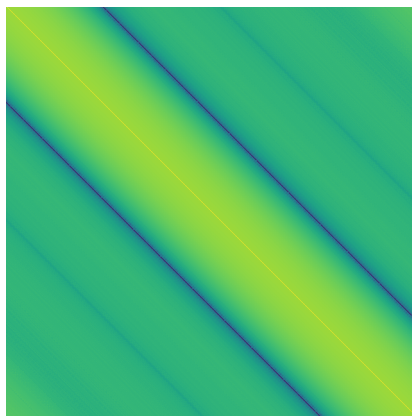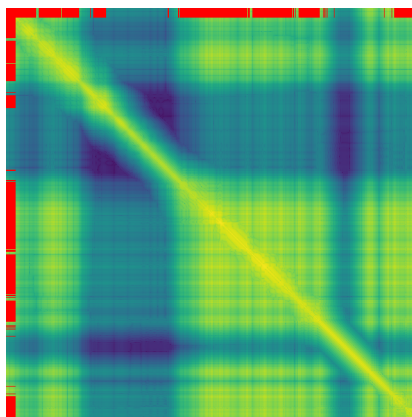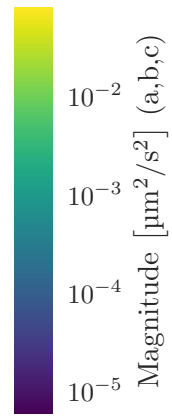
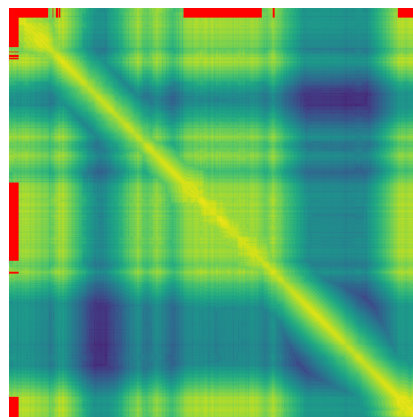(a) Stationary covariance.
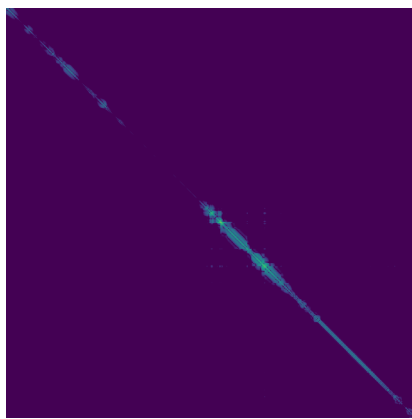
(b) $\Sigma_{\Delta\dot{\rho}_{\text{AOC}}}$ GRACE-A
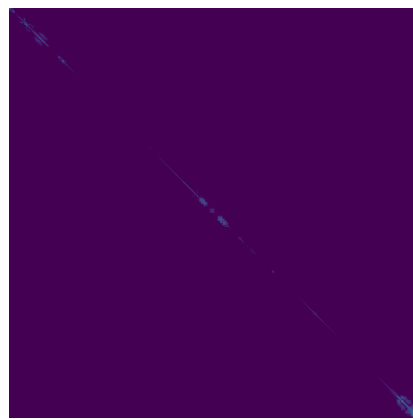
(c) $\Sigma_{\Delta\dot{\rho}_{\text{AOC}}}$ GRACE-B

(d) $\Sigma_{\Delta\dot{\rho}_{\text{AOC}}}$ GRACE-A

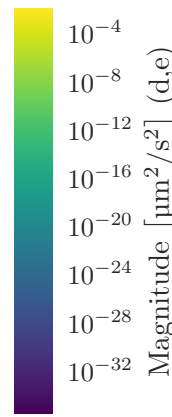(e) $\Sigma_{\Delta\dot{\rho}_{\text{AOC}}}$ GRACE-B

Figure 8.3: Full temporal covariance matrices in the range-rate domain for one short arc in June 2010. (a) shows the estimated Toeplitz matrix due to the assumed stationary noise component. (b) and (c) show the covariances due to orientation uncertainty in the AOC at the same scale. (d) and (e) show a magnified view of the AOC covariance matrices. Here, periods where only one SCA head was active on the respective spacecraft are marked in red.
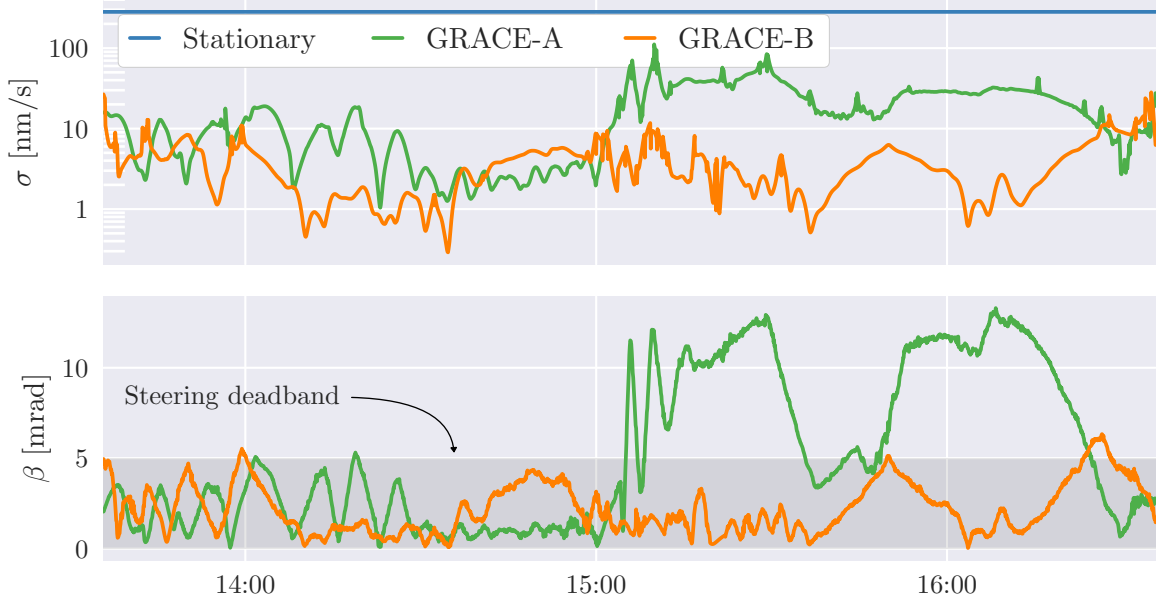
Figure 8.4: Square root of main diagonal elements of covariance matrices in fig. 8.3, σ, and opening angle β for both spacecraft. In the top panel, the blue line shows the zero time-lag variance factor of the estimated stationary covariance function. The main diagonal of the AOC covariance matrix due to GRACE-A is shown in green, and that of the covariance matrix due to GRACE-B in orange. The bottom panel shows the opening angle β for the two satellites in the same colours. The darker shaded area indicates the nominal active steering deadband.

8.2 Updated Stochastic Model

Having obtained detailed knowledge of the structure of the AOC covariance matrix, this information can be taken into consideration in defining and estimating the stochastic model for the ll-SST observation equations, as outlined in eq. (8.1.5). The stochastic model defined in eq. (6.5.18) is extended with the AOC covariance matrices for GRACE-A and GRACE-B to give

$$\boldsymbol{\Sigma}_{ll}^{m} = \sigma_m^2 \cdot \sum_{n=0}^{N_m-1} C_{xx}^n \cdot \boldsymbol{V}_n + \sigma_{\text{AOC,A}}^2 \boldsymbol{\Sigma}_{\Delta\dot{\rho}_{\text{AOC}}}^{A} + \sigma_{\text{AOC,B}}^2 \boldsymbol{\Sigma}_{\Delta\dot{\rho}_{\text{AOC}}}^{B} \tag{8.2.1}$$

The variance propagation from the orientation uncertainty to the AOC was performed independently for each spacecraft, and for each short arc. The covariance matrices are then introduced into the stochastic model as cofactor matrices. This extends the model defined by the purely stationary process described by eq. (6.5.18) with information on the non-stationary behaviour of the AOC noise. To allow for imperfections in the result of the SCA/ACC sensor fusion algorithm, one additional variance factor $\sigma_{\text{AOC},s}^2$ was estimated per spacecraft $s \in [A, B]$, per month. As the propagation of variances

from the orientation uncertainty to the AOC is purely linear, this variance factor can also be taken to represent a scaling of the uncertainty in the satellite orientation, as obtained from the SCA/ACC sensor fusion.

The estimation of the ll-SST covariance function as described in section 6.5 remains unchanged, with one variance factor per time lag. The total number of estimated variance factors for all ll-SST observations in one month is thus: $N_{max} = 2160$ variance factors, one for for each time lag (3 h arcs at 5 s sampling); $M = 248$ arc-wise variance factors (31 days with eight 3 h arcs each); and 2 additional variance factors for the AOC covariance matrices.

8.3 Results

The GRACE time series was reprocessed with the updated stochastic model described in the previous sections. For some months, especially in 2002, this was not possible due to issues with the release 2.0 level 1B data. In December 2002, for example, the sca_id field in the SCA1B data file is set to the value 5, which is not defined in the level 1B user documentation (Case, Kruizinga, and Wu, 2010). As this is the flag that describes which SCA heads were used in the determination of the satellite attitude no meaningful AOC covariance can be computed for this period. These months were thus excluded from further analysis. In total, 152 monthly solutions were processed spanning the period from February 2003 to June 2017.

The following sections will give an overview of the AOC covariance matrices' impact on several aspects of the stochastic model. Further, the post-fit residuals of one particularly interesting month will be analysed. As the improved stochastic model does not have as strong of an impact on the overall monthly gravity field solution as the co-estimation of the satellite orientation later introduced in chapter 9 this aspect will not be discussed here explicitly. For compactness, it will be illuminated together with the results in section 9.3.

8.3.1 AOC Variance Factors

The distribution of the monthly AOC variance factors for the processed GRACE time series is illustrated in fig. 8.5. The displayed probability density functions (PDFs) were determined using a non-parametric kernel density estimator (e.g. Rosenblatt, 1956).

If the a priori orientation uncertainty estimate from the SCA/ACC sensor fusion were accurate, and no other unmodelled effects were present, the expected values for the monthly AOC variance factors would be 1. The estimates, however, show a mean of slightly above 2 (2.30 for GRACE-A and 2.26 for GRACE-B). These increased means indicate that the estimates of the orientation uncertainty from the SCA/ACC sensor fusion are possibly too optimistic.
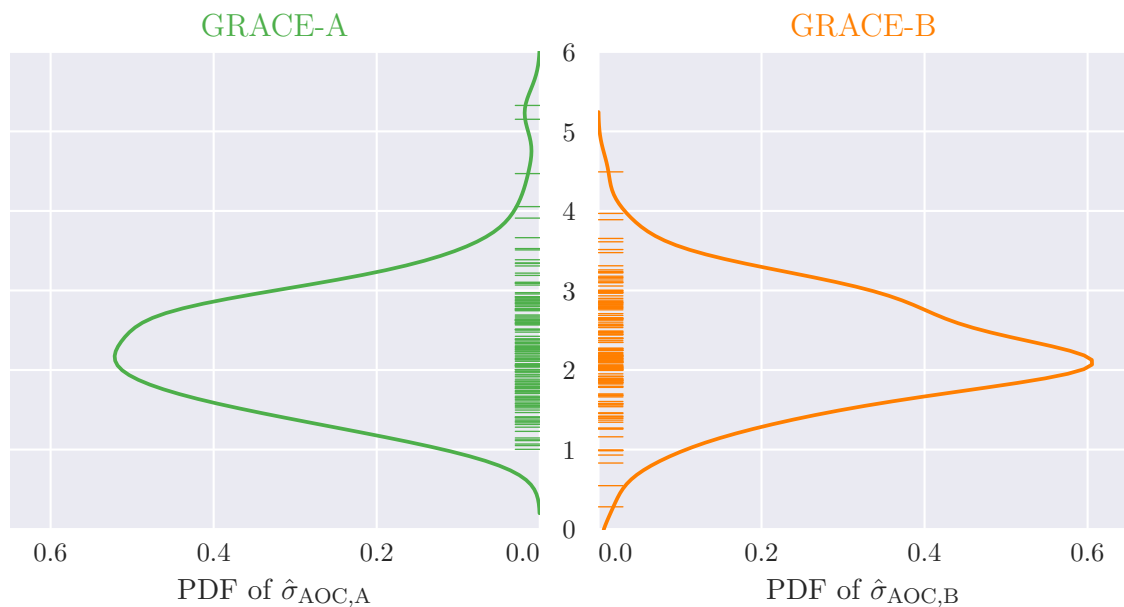
Figure 8.5: Kernel density estimate of PDFs of estimated AOC variance factors $\hat{\sigma}_{AOC,\,A/B}$ for complete GRACE time series. Each barb represents one variance factor for one month.
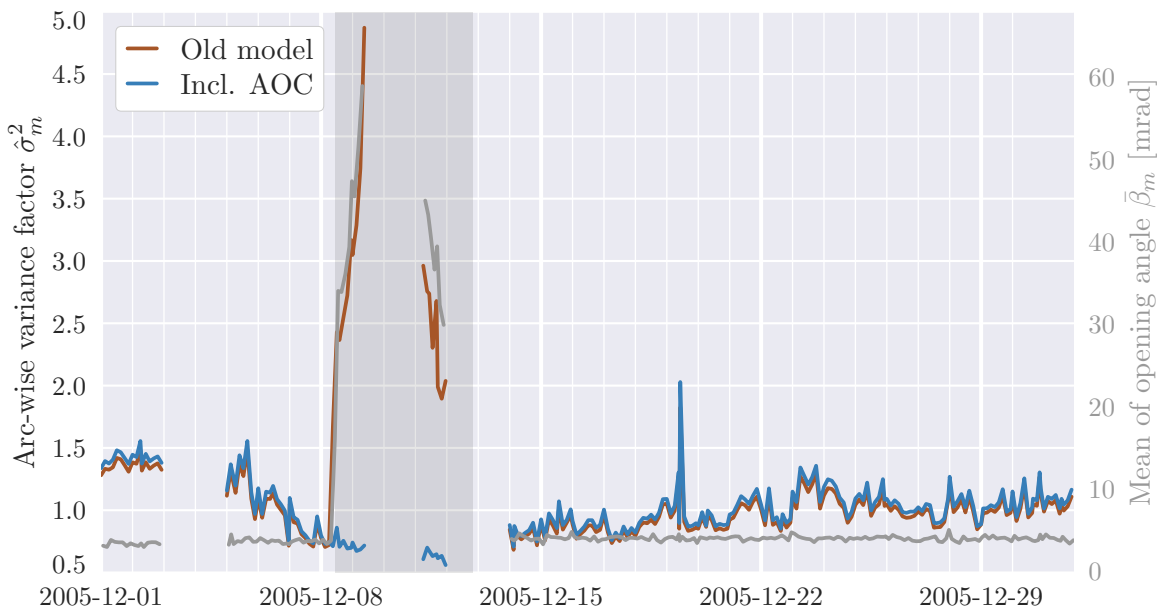
8.3.2 Arc-wise Variance Factors

The AOC covariance matrices, scaled by their variance factors, are expected to model some of the increased noise in observations with large opening angles. It is thus expected that the increase in the arc-wise variance factors for the stationary noise component previously observed for these time periods should, to some extent, disappear. One such period is the time that GRACE-A spent in attitude hold mode in June 2010, mentioned before in section 6.5 and seen in the arc-wise variance factors displayed in fig. 6.8b.

Figure 8.6a illustrates the arc-wise variance factors for the same data in June 2010, using the improved stochastic model. The arc-wise variance factors for the stochastic model considering only the estimated stationary covariance function (in brown) again shows the increase in arc-wise variance factors during the period of increased opening angles (darker shaded area). Introducing the a priori AOC covariance information for this month (in blue), the estimated arc-wise variance factors are noticeably closer to 1 during this period. The same effect can be observed in other periods of increased opening angles, for example the orbit swap manoeuvre in December 2005 when both GRACE-A and GRACE-B were commanded to attitude hold mode. In addition the 1° pitch bias that keeps the KBR horns in alignment was removed, leading to very large angles during the periods when a KBR link was established. Figure 8.6b shows that during this period the arc-wise variance factors for the processing using the AOC covariance information (in blue) are again much improved.
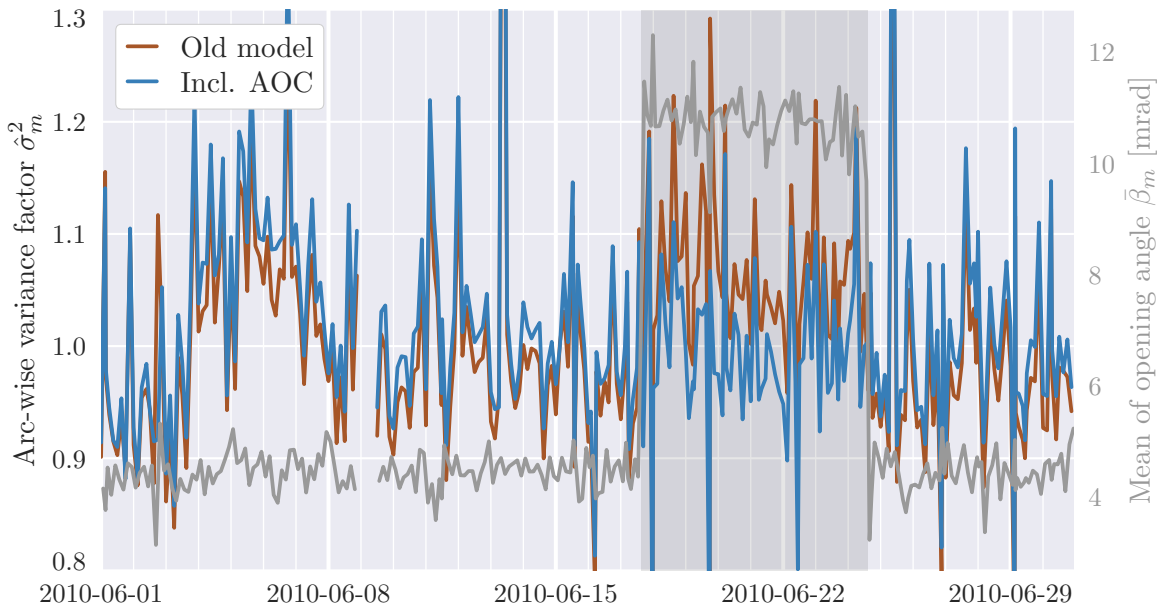
(a) Arc-wise variance factors for June 2010. The shaded area indicates the period that GRACE-A spent in attitude hold mode.

(b) Arc-wise variance factors for December 2005. The shaded area indicates the period during which GRACE-A and GRACE-B were in attitude hold mode, and where some data was lost due to a GRACE-B orbit trim manoeuvre.

Figure 8.6: Ll-SST arc-wise variance factors $\hat{\sigma}_m^2$ for two months with periods of deteriorated data quality. (a) GRACE-A was commanded to AHM to allow investigation of a system anomaly. (b) Increased opening angles for both spacecraft during a scheduled orbit swap manoeuvre.

Correlation with Opening Angle

The presented results from June 2010 and December 2005 suggest that the arc-wise variance factors are indeed correlated with periods of larger opening angles. This hypothesis can be tested by computing Pearson's product-moment correlation coefficient r between the arc-wise variance factors and the mean opening angles for each month. The distribution of all correlation coefficients, one for each month, is then studied. The mean of the opening angle for both satellites for one arc m with N_m epochs is

$$\bar{\beta}_m = \frac{1}{2N_m} \sum_{n=1}^{N_m} \left(\beta_n^{\text{A}} + \beta_n^{\text{B}} \right) \, . \tag{8.3.1}$$

Figure 8.7 shows the distribution of the monthly correlation coefficients for the processed GRACE time series. If the observation geometry, represented through the mean opening angle, had no impact on the arc-wise variance factors, the correlation coefficients would be expected to scatter around 0. Due to the distribution of both the mean opening angle and the arc-wise variance factor estimates, some spurious correlation is to be expected. The probability distribution for the old model considering only the stationary covariance function (in brown) is not centred at 0. The shift of the distribution towards positive correlations indicates that arc-wise variance factors and the mean opening angles are positively correlated. Introducing the AOC covariance information largely eliminates this shift (in blue). This indicates that the correlation of observation geometry and arc-wise variance factors is largely removed by use of the improved stochastic model.

Numerically, the mean of the correlation coefficients is reduced from 0.15 in the original processing to 0.03 when considering the AOC covariance matrices.
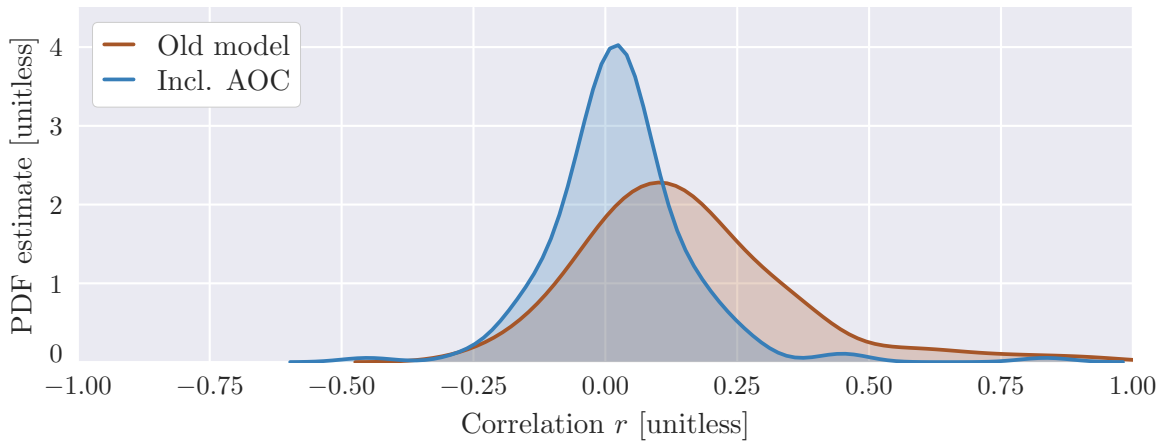
Figure 8.7: Distribution of correlation coefficients r between arc-wise variance factors $\hat{\sigma}_m^2$ and mean opening angles $\bar{\beta}_m$. One correlation coefficient was estimated per month.

8.3.3 Covariance Function

When only considering a stationary covariance function in the determination of the stochastic model, this covariance function will be estimated to best fit all power in the residuals, both from stationary and non-stationary noise processes. The non-stationary effects thus alias into the stationary covariance function, as there is no avenue to model them in this framework. The newly introduced information about some of the non-stationary noise in the form of the AOC covariance matrices should model some of this observed power in the residuals, reducing aliasing into the stationary covariance function.

Figure 8.8a shows the estimated covariance functions, displayed as PSDs, for the previously discussed month of December 2005. In the PSD estimated according to the old noise model (in brown), such aliasing is clearly visible in the shaded area. The lower bound of the shaded area is set to 3.3 mHz, which is the dominant frequency in the GRACE pointing variations after February 2004 for GRACE-A and after January 2005 for GRACE-B (Bandikova, 2015). The upper bound of the shaded area is at 20 mHz, where noise in the SCA observations at harmonics of the orbital frequency of the spacecraft starts to be dominated by purely stochastic effects (Inácio et al., 2015).

This result can be compared to a month of "good" data without such abnormally large opening angles, e.g. April 2008 (cf. fig. 8.8b). Here, the PSD for the old model is virtually identical to that of the new model determined using the AOC covariance matrices. During this normal operation, the effect due to the orientation uncertainty is small enough to be dominated by other noise sources.

It could be argued that the strict modelling of the AOC uncertainty is not necessary, as the arcs most affected by these errors are down-weighted in the VCE through application of large arc-wise variance factors. Comparison of the PSDs in fig. 8.8a shows that this is however not correct. The aliasing in the PSD estimated in the old model is not only present in the arcs affected by large opening angles, but in all arcs of the month. While arcs with large opening angles are downweighted, and thus lose influence on the monthly solution, all remaining arcs are decorrelated with a clearly wrong covariance function, introducing systematic effects into the solution. It has been demonstrated here that correct modelling of the AOC covariance mitigates this undesired effect of aliasing into the stationary covariance function.

The overall magnitude of the average change in the PSD can be observed in the mean of all monthly PSDs for the processed time series. The mean of the PSDs is computed once per frequency, per processing strategy. These PSDs are displayed in fig. 8.9. The lower noise level in the highlighted band is clearly visible in the mean PSD obtained when using AOC covariance matrices (in brown). It is also interesting to note that the PSD computed under consideration of the AOC covariance information (in blue) follows the expected linear progression of the KBR-branch of the noise spectrum to a lower frequency, down to ≈10 mHz, as opposed to ≈20 mHz for the old model (in brown).
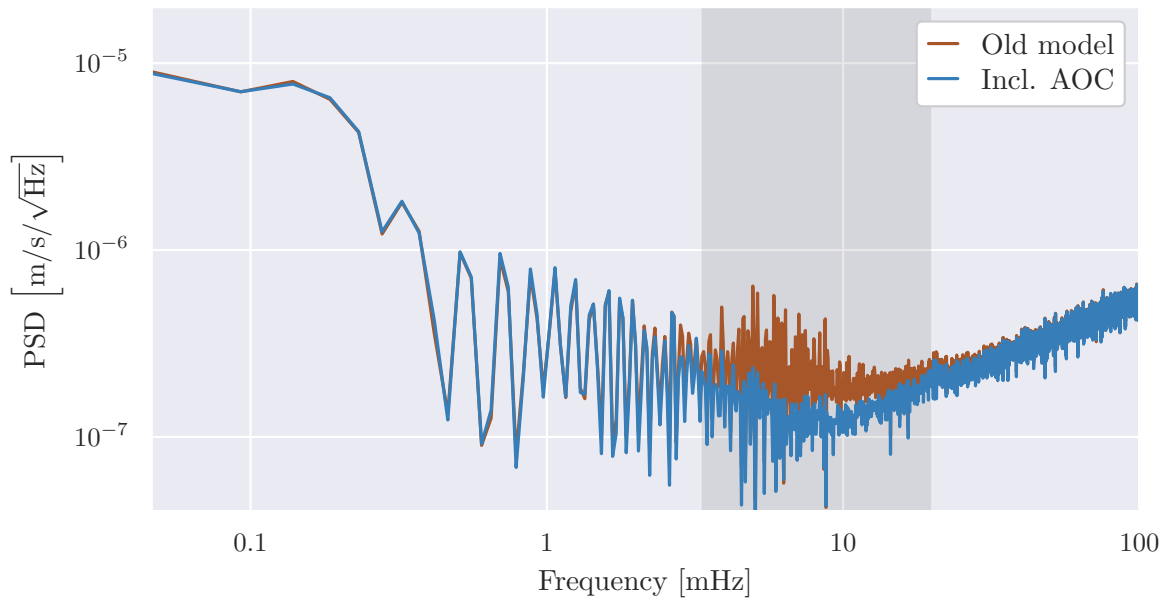
(a) Estimated PSDs for December 2005.
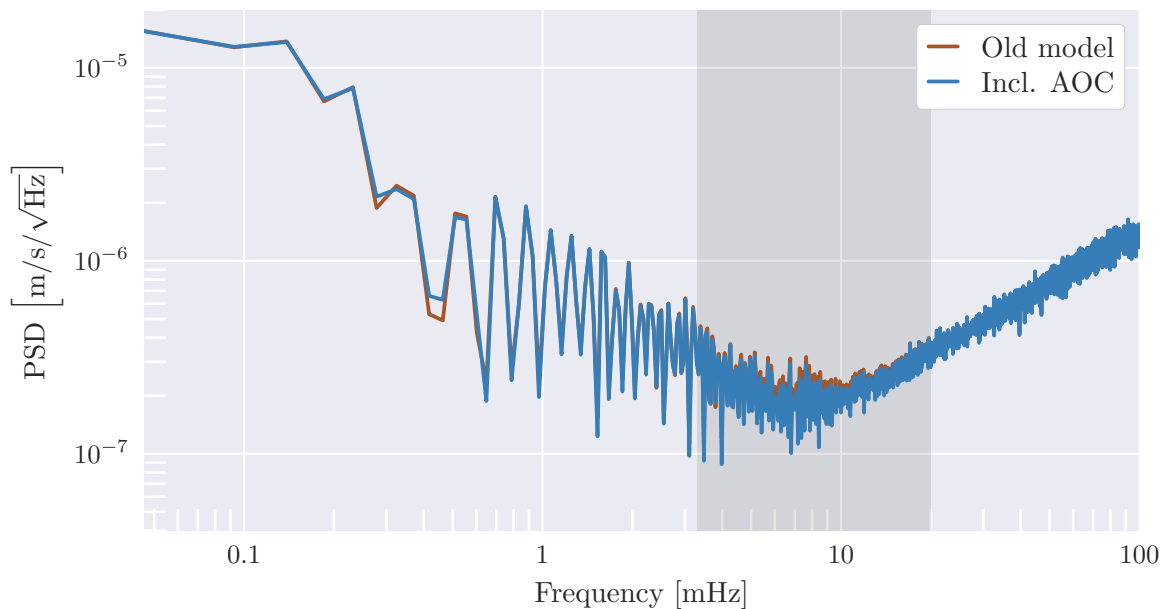
(b) Estimated PSDs for April 2008.

Figure 8.8: Estimated stationary noise PSD, without considering full AOC covariance matrices (in brown) and when taking them into account (in blue). (a) shows the PSDs for a month containing "bad" data with large opening angles, (b) shows the PSDs for a "good" month without such anomalies. The shaded area spans from 3.3 mHz to 20 mHz and indicates the band where a strong influence of non-stationary errors due to orientation uncertainty is expected.
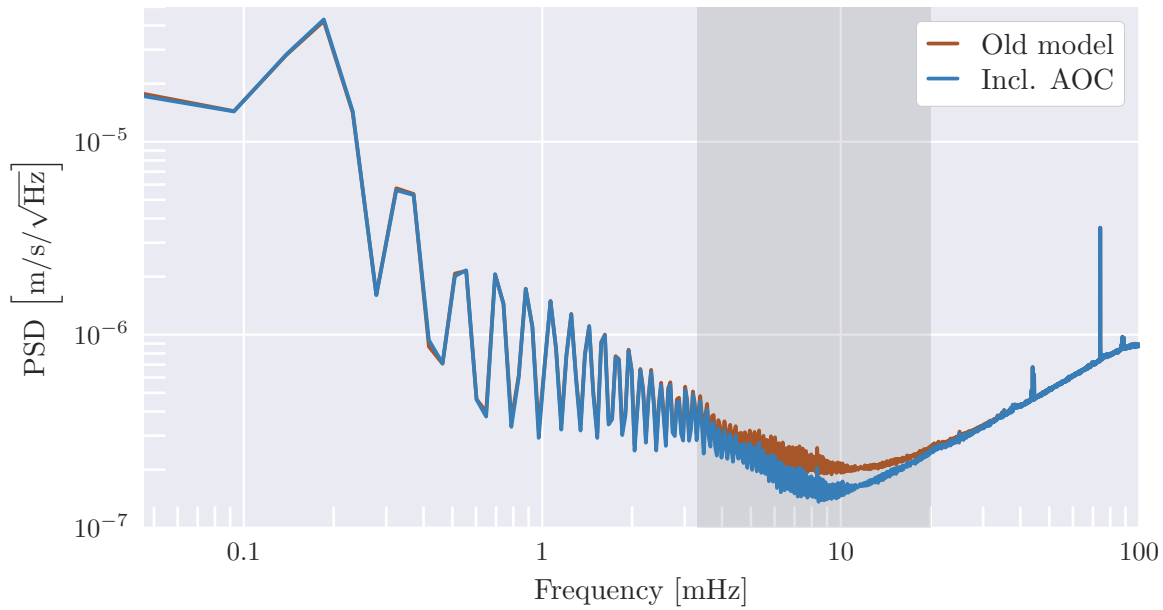
Figure 8.9: Mean PSDs for the old processing model (in brown) and considering full AOC covariance matrices (in blue). The new model shows decreased power in the band strongly influenced by uncertainties in the spacecraft orientation. The shaded frequency band has the same bounds as in fig. 8.8.

8.3.4 Impact on Residuals

As the estimated residuals $\hat{e}$ are a superposition of residuals due to a stationary noise process and due to the non-stationary AOC noise, they can be disentangled to give the residuals attributed to each of the individual sources with

$$\hat{e}_{\text{sst}} = \boldsymbol{\Sigma}_{\text{sst}} \left(\boldsymbol{\Sigma}_{\text{sst}} + \boldsymbol{\Sigma}_{\Delta\dot{\rho}_{\text{AOC}}} \right)^{-1} \hat{e} \tag{8.3.2}$$

and

$$\hat{e}_{\text{AOC}} = \boldsymbol{\Sigma}_{\Delta\dot{\rho}_{\text{AOC}}} \left(\boldsymbol{\Sigma}_{\text{sst}} + \boldsymbol{\Sigma}_{\Delta\dot{\rho}_{\text{AOC}}} \right)^{-1} \hat{e} \;. \tag{8.3.3}$$

Figure 8.10 shows the PSDs of all three groups of residuals — combined, stationary, and non-stationary — for June 2010. It can be seen that the power in the non-stationary residuals (blue) is even larger than that of the stationary residuals (green) in the highlighted frequency-band, where a large impact of the orientation uncertainty is expected.

It must be said, however, that a PSD is decidedly the wrong instrument to display this information, as stationarity of the signal is a fundamental assumption when computing the PSD. Figure 8.10 could lead one to assume that the AOC residuals have the same quite high power at a frequency of $\approx 6\,\text{mHz}$ to $\approx 10\,\text{mHz}$ throughout the complete month, with no discernible variability from one time segment to another. This is however not true, as will be illustrated in fig. 8.11. The non-stationary nature of
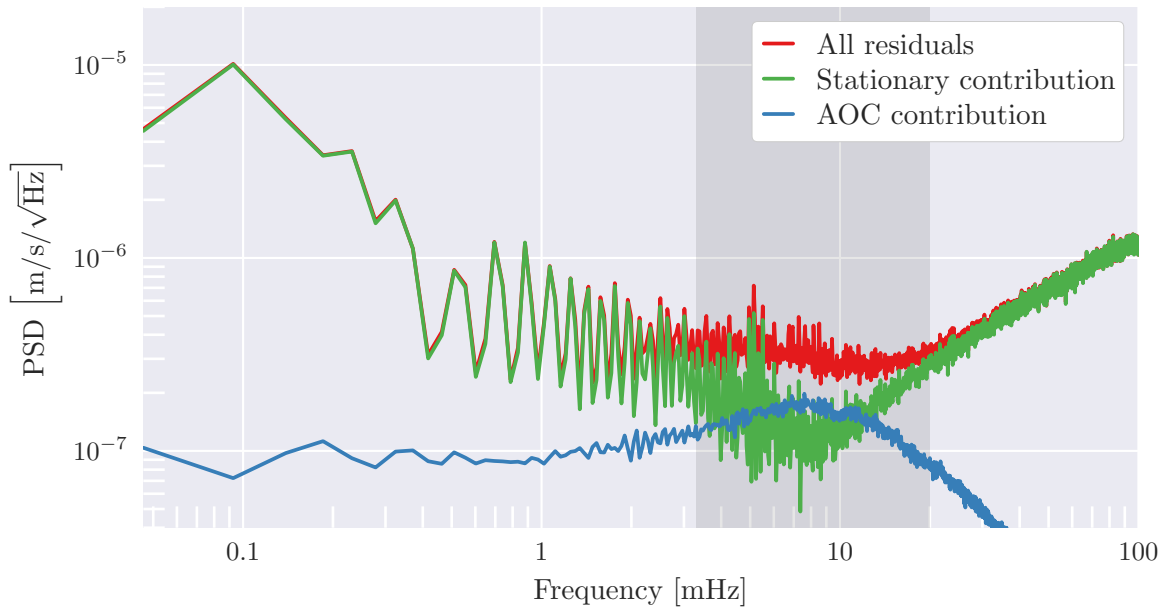
Figure 8.10: PSDs of the residuals for June 2010. The combined residuals $\hat{e}$ are shown in red. The PSD for the disentangled residuals due to stationary effects $\hat{e}_{sst}$ is shown in green. The PSD for the residuals due to the non-stationary effects $\hat{e}_{AOC}$ is shown in blue. The shaded frequency band has the same bounds as in fig. 8.8.

the noise due to the AOC uncertainty must be taken into account when studying these residuals.

To capture the variability of the power in the estimated residuals not only in the frequency domain but also with time, a wavelet decomposition is computed for $\hat{e}$, $\hat{e}_{sst}$, and $\hat{e}_{AOC}$ using the Daubechies 5 wavelet (see e.g. Mallat, 2009) . The length of the time series allows for 11 levels of decomposition, where each level corresponds to a specific frequency band. Each of these levels is then re-synthesized individually, giving 11 time series of residuals, each only containing signals at the frequency band corresponding to the decomposition level. These residual series were then divided into 3 h intervals. The power of the signal in each frequency band and each interval was then computed as the RMS over the residuals in that bin. Figure 8.11 shows the resulting time-frequency-power diagram for the ll-SST residuals of June 2010.

The top panel of fig. 8.11 shows the power of the combined residuals $\hat{e}$ (red). During the time periods of an increased opening angle (vertical grey lines), a small but consistent increase in power is visible at frequencies above $\approx 3\,\text{mHz}$ (top horizontal grey line). A further increase in power can be observed on June 2, 2010, where no correspondingly large increase in opening angle is observed (cf. fig. 8.6a). A third, smaller, increase occurs on June 13, 2010.

The middle panel of fig. 8.11 shows the power of the residuals due to stationary processes $\hat{e}_{sst}$ (green). The power distribution is mostly homogeneous over time, as would be expected from a stationary process. Several small spikes of power can still be
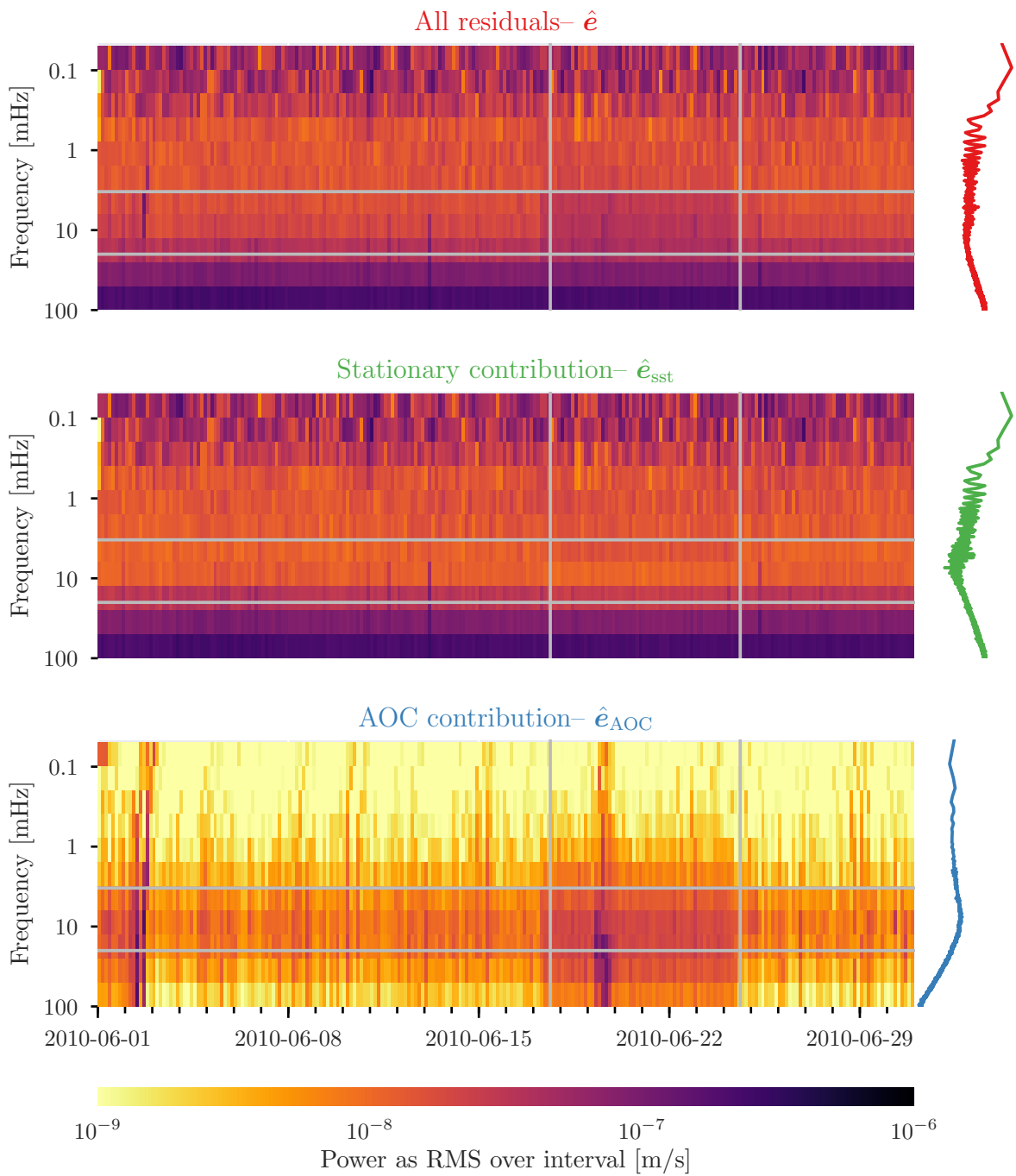
Figure 8.11: Time-frequency-power diagram of combined (top panel) and disentangled (lower two panels) residuals due to stationary and non-stationary effects for June 2010. The fill colour of each small rectangle represents the power in the estimated residuals for that specific 3 h interval and frequency range. The right margin displays the PSDs from fig. 8.10 corresponding to the respective diagram. The vertical grey lines mark the area of increased opening angle β, corresponding to the shaded area in fig. 8.6a. The horizontal grey lines mark the frequency band where a larger power is expected, corresponding to the shaded areas in figs. 8.8 to 8.10.

identified, most prominent amongst them the spike on June 13, 2010. The first and last increase in power can however not be identified in the plot any more.

These increases in power are prominently visible in the lower panel of fig. 8.11, which shows the power of the residuals due to the AOC uncertainty $\hat{e}_{AOC}$ (blue). The increase in power over a large range of frequencies during the long period of large opening angles starting on June 17, 2010 is now clearly identifiable here. Indeed, the increase in power is not limited to the frequency band identified previously (horizontal grey lines), but can also be observed at frequencies above 20 mHz. KBR system noise is dominant in this frequency band and obscures this signal during normal operations. The PSD for the non-stationary AOC contribution (blue in fig. 8.10, also right margin of bottom panel in fig. 8.11) actually shows a consistent decrease in power with increased frequency, illustrating the unsuitability of the tool "PSD" to study this signal.

A similar increase in power over a wide frequency spectrum can be observed in the peak on June 2, 2010, which is clearly visible in the AOC contribution to the residuals. As opposed to the period of increased opening angle later in the month, which is noted in the SDS monthly report for June 2010 (Flechtner, 2010), there is no indication of anomalous observations given for this time period. Possible sources of the increased AOC residual power at this time could also be found not in the observation geometry but in the SCA/ACC sensor fusion covariance matrices. Larger than normal SCA noise due to e.g. increased blinding could lead to reduced accuracies in the orientation estimate and in turn the AOC. Similarly, an origin in the angular rate observations could also play a role.

Figure 8.12 shows the time-frequency-power diagram for the AOC contribution during the first days of June 2010 in the upper panel. The lower panel shows the opening angle β for GRACE-A and GRACE-B. The increase in power on June 2, 2010 corresponds roughly to some attitude excursions for GRACE-B. In general, the pointing for GRACE-B seems to undergo larger variations during this time span. For these two days, peaks in the opening angle could possibly be interpreted to correspond roughly to increased power in the residuals, although such a generalization should only be made cautiously and be subjected to further analysis. This is however a further indication that the AOC covariance matrices to some extent represent the true stochastic behaviour of the AOC, and that they are a valuable addition to the stochastic model for processing GRACE data.

8.4 Discussion

This chapter focused on investigating the effects of uncertainties in the satellite orientation on the determination of the antenna offset correction used in correcting GRACE KBR ll-SST data. The impact of the orientation uncertainty on other uses of the satellite orientation, such as in rotating the on-board accelerometer observations to the CRF for force integration, were not studied.
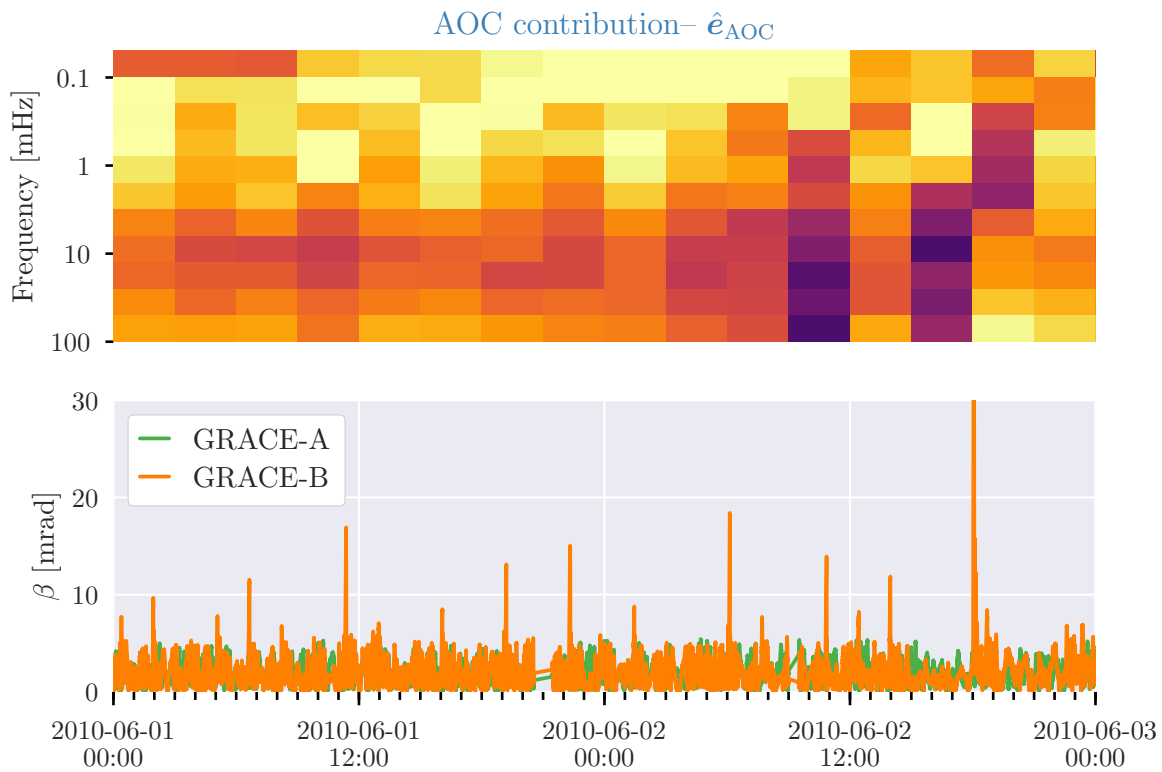
Figure 8.12: Time-frequency-power diagram of disentangled residuals due to non-stationary effects for the first two days of June 2010 (top panel, colourbar identical to fig. 8.11). The bottom panel shows the opening angle β for GRACE-A and GRACE-B during the same time period.

The noise due to the AOC uncertainty was shown to be non-stationary, and can thus not be described using the purely stationary noise model estimated in ITSG-Grace2016. A rigorous stochastic model for the AOC was developed through variance propagation based on full variance-covariance information for the satellite orientations. This information, with one covariance matrix per short arc per spacecraft, was then introduced into the stochastic model for the GRACE ll-SST observations.

This additional information had several positive effects on the estimated stochastic model. The arc-wise variance factors for arcs with larger than normal opening angles no longer show consistently and abnormally large values. The previous stochastic model correctly identified these arcs to have inferior data quality, but the approach of simple scaling of the stationary covariance function does not do justice to the complex and time-variable characteristics of the AOC signal during these arcs. The presented augmented approach correctly models periods of increased variances and correlations in the AOC, leading to improved results in the estimation of the stationary component of the stochastic model.

The estimated stationary covariance functions for months with periods of increased opening angles no longer show aliasing in the frequency band most affected by the AOC uncertainty. In turn, the remaining arcs of these months are now decorrelated

with a "cleaner" covariance function. This not only improves the stochastic model for the few arcs that do contain anomalous data, but for all remaining arcs of the month as well.

It is important to note that modelling the errors in the antenna offset correction correctly does not necessarily lead to a *reduction* of the overall residuals. What this new model does allow for is the *attribution* of a certain fraction of the observed residuals to one of the two noise sources: The stationary noise due to the ll-SST system, or the non-stationary noise due to the AOC.

Co-Estimation of Orientation Parameters

The full orientation covariance matrix from the SCA/ACC sensor fusion not only allows for the disentanglement of the AOC residuals from the stationary ll-SST residuals. Having a complete stochastic model of both observation types — ll-SST KBR observations as well as the orientation observations — there is no longer a need to consider the orientation of the spacecraft as fixed.

This chapter will describe the process of co-estimating improved orientations of the GRACE satellites at each epoch, together with the Stokes coefficients, in one least squares adjustment. Where the previous chapter only focused on the effects of the orientation uncertainty on the derived antenna offset correction, the following pages will outline a strategy of directly targeting improvements in the original noisy observations from the SCA/ACC sensor fusion.

The assumption of a fixed, non-stochastic, perfectly observed orientation must of course introduce errors into the recovered gravity field. An attempt was made to model these errors in chapter 8 by describing the uncertainty in the AOC. Taking this thought to its logical conclusion, estimation of an improved "best-fit" satellite orientation will further allow for the computation of an improved AOC, reducing the resulting error in the recovered gravity field.

The complete ll-SST observable and the estimated Stokes coefficients depend on the AOC. The ultimate independent variable for the AOC is the spacecraft orientation. To properly model this dependency, an algorithm must be employed that allows for variations in both the dependent and independent variables. Many such approaches exist, known by several names. Amongst them are total least squares, error-in-variables, the generalized case of adjustment theory, mixed model, or Gauß-Helmert model (see e.g. Amiri-Simkooei and Jazaeri, 2012; Golub and van Loan, 1980; Koch, 1997; L. Lenzmann and E. Lenzmann, 2004; Niemeier, 2008; Reinking, 2008; Schaffrin, 2007; Snow, 2012). In essence, these algorithms describe the same approach: the linearisation of the functional relationship is not only computed about the Taylor point for the unknowns x_0, but also about approximate values for both dependent and independent observables l_0. Both parameters and observables are then improved iteratively.

This chapter will start by presenting the theoretical basis of one such algorithm, the total least squares (TLS) algorithm as outlined by Reinking, 2008. This approach will be contrasted to a formulation of the problem in the classical Gauß-Markov apparatus. The practical constraints in implementing a TLS algorithm for GRACE gravity field recovery will be enumerated, leading to a summary of the strategy employed to reprocess the GRACE time series.

Results of the performed reanalysis will be presented, focusing on time series of estimated Stokes coefficients, their formal errors, and derived quantities such as equivalent water heights. Monthly estimates for the GRACE antenna phase centre vectors will be given and contrasted with those from the ITSG-Grace2016 processing chain. The sections regarding Stokes coefficient and APC vectors will include results from the processing chain including AOC covariance matrices only, as described in chapter 8.

9.1 Uncertainties in Independent Variables

This section will outline two formalisms that can be used to treat the problem of independent variables of a stochastic nature. Their outlines will be given in a generalized notation, before the application to GRACE processing is discussed in section 9.2. For both formulations, there shall be two sets of observations, a set of independent observations l_{ind}, and a set of associated dependent observations l_{dep}. These observations are used to estimate some parameters $\hat{x}$. The classical example for such a configuration is the estimation of a straight line, with the independent variable the ordinate of an observed point x_n, the dependent variable the coordinate of the point y_n, and the sought parameters the intercept and slope of the line.

The functional model connecting the observation groups and the parameter vector is

$$l_{\text{dep}} = f(l_{\text{ind}}, x) + e_{\text{dep}} , \tag{9.1.1}$$

which in the classical linearisation in the Gauß-Markov model according to eq. (2.2.1) would lead to the observation equations

$$l_{\text{dep}} - f(l_{\text{ind}}, x_0) = \left. \frac{\partial f(l_{\text{ind}}, x)}{\partial x} \right|_{x_0} (x - x_0) + e_{\text{dep}} \tag{9.1.2}$$

or

$$\Delta l_{\text{dep}} = A \Delta x + e_{\text{dep}} . \tag{9.1.3}$$

The residuals in eq. (9.1.3) are attributed exclusively to a misfit in the dependent observations l_{dep}. The uncertainty in the independent variables is not considered in this formalism. The fundamental idea behind the approach commonly termed TLS is to introduce a second matrix of residuals E_A as

$$\Delta l_{\text{dep}} = (A + E_A) \Delta x + e_{\text{dep}} . \tag{9.1.4}$$

The norm of both e_{dep} and E_A is then minimized together (see e.g. Golub and van Loan, 1980). Here, E_A allows for variations in A due to the uncertainty in l_{ind}.

9.1.1 Total Least Squares as Gauß-Markov Model with Derived Observations

Reinking gives a derivation of the solution to the TLS problem in eq. (9.1.4) that relies on the removal of the distinction between dependent and independent variables. Rather, all variables are collected in one vector

$$l = \begin{bmatrix} l_{\text{dep}} \\ l_{\text{ind}} \end{bmatrix} . \tag{9.1.5}$$

This section will give a summary of the algorithm published in Reinking, 2008. Building on this summary, the resulting normal equation system is analysed in preparation for later comparisons with the algorithm presented in section 9.1.2. Reinking's algorithm begins by restating the problem eq. (9.1.1) in the Gauß-Helmert model as

$$G\left(\hat{x}, \hat{l}\right) = \hat{l}_{\text{dep}} - f\left(\hat{l}_{\text{ind}}, \hat{x}\right) = 0 . \tag{9.1.6}$$

The functional G is then linearised about both the parameters and observations, giving

$$G\left(x_0, l_0\right) + \left.\frac{\partial G}{\partial x}\right|_{x_0, l_0} \Delta x + \left.\frac{\partial G}{\partial l}\right|_{x_0, l_0} \Delta l = 0 \tag{9.1.7}$$

or, more compactly,

$$G_0 + A_x \Delta x + F \Delta l = 0 . \tag{9.1.8}$$

With $\Delta l = \hat{l} - l_0 = l - e - l_0$, eq. (9.1.8) is

$$G_0 + A_x \Delta x + F\left(l - e - l_0\right) = 0 \tag{9.1.9}$$
$$-Fl - \left(G_0 - Fl_0\right) = A_x \Delta x - Fe \tag{9.1.10}$$

Here, it is important to note that the residuals e are actually residuals in both the dependent and independent variables:

$$e = \begin{bmatrix} e_{\text{dep}} \\ e_{\text{ind}} \end{bmatrix} . \tag{9.1.11}$$

Reinking now defines the *derived observations* λ as

$$\lambda = -Fl . \tag{9.1.12}$$

With

$$\lambda_0 = \left(G_0 - Fl_0\right) , \tag{9.1.13}$$
$$e_\lambda = -Fe , \tag{9.1.14}$$

and $\Delta\boldsymbol{\lambda} = \boldsymbol{\lambda} - \boldsymbol{\lambda}_0$ this gives the equation system

$$\Delta\boldsymbol{\lambda} = \boldsymbol{A}_x\Delta\boldsymbol{x} + \boldsymbol{e}_\lambda \ . \tag{9.1.15}$$

Equation (9.1.15) is a reformulation of the Gauß-Helmert problem eq. (9.1.6) as a Gauß-Markov problem with derived observations. Given covariance information for $\boldsymbol{l}_{\text{ind}}$ and $\boldsymbol{l}_{\text{dep}}$ as

$$\boldsymbol{\Sigma}_{ll} = \begin{bmatrix} \boldsymbol{\Sigma}_{\text{dep}} & \boldsymbol{\Sigma}_{\text{cro}} \\ \boldsymbol{\Sigma}_{\text{cro}}^{\mathsf{T}} & \boldsymbol{\Sigma}_{\text{ind}} \end{bmatrix} \tag{9.1.16}$$

the covariance matrix for the derived observations $\boldsymbol{\lambda}$ follows from eq. (9.1.12) through variance propagation as

$$\boldsymbol{\Sigma}_{\lambda\lambda} = \boldsymbol{F}\boldsymbol{\Sigma}_{ll}\boldsymbol{F}^{\mathsf{T}} \ . \tag{9.1.17}$$

The solution to eq. (9.1.15) is then simply that of eq. (2.2.3),

$$\Delta\hat{\boldsymbol{x}} = \left(\boldsymbol{A}_x^{\mathsf{T}}\boldsymbol{\Sigma}_{\lambda\lambda}^{-1}\boldsymbol{A}_x \right)^{-1} \boldsymbol{A}_x^{\mathsf{T}}\boldsymbol{\Sigma}_{\lambda\lambda}^{-1}\Delta\boldsymbol{\lambda} \ . \tag{9.1.18}$$

Neitzel and Petrovic, 2008; Reinking, 2008 assert that this gives the same solution as directly solving for the TLS problem formulated in eq. (9.1.4) using classical methods such as those presented by e.g. Golub and van Loan, 1980.

Estimated Residuals and Observations

Evaluating eq. (9.1.18) gives estimated residuals $\hat{\boldsymbol{e}}_\lambda$ in the derived observations $\boldsymbol{\lambda}$. From eq. (9.1.14) it is known that $\boldsymbol{e}_\lambda = -\boldsymbol{F}\boldsymbol{e}$. Direct comparison with the identity

$$\begin{aligned} \boldsymbol{e}_\lambda &= \boldsymbol{\Sigma}_{\lambda\lambda}\boldsymbol{\Sigma}_{\lambda\lambda}^{-1}\boldsymbol{e}_\lambda \\ &= \boldsymbol{F}\boldsymbol{\Sigma}_{ll}\boldsymbol{F}^{\mathsf{T}}\boldsymbol{\Sigma}_{\lambda\lambda}^{-1}\boldsymbol{e}_\lambda \end{aligned} \tag{9.1.19}$$

allows one to identify that

$$\hat{\boldsymbol{e}} = -\boldsymbol{\Sigma}_{ll}\boldsymbol{F}^{\mathsf{T}}\boldsymbol{\Sigma}_{\lambda\lambda}^{-1}\hat{\boldsymbol{e}}_\lambda \ . \tag{9.1.20}$$

Having computed $\hat{\boldsymbol{e}} = \begin{bmatrix} \hat{\boldsymbol{e}}_{\text{dep}} & \hat{\boldsymbol{e}}_{\text{ind}} \end{bmatrix}^{\mathsf{T}}$ using eq. (9.1.20), the estimated dependent and independent observations are

$$\hat{\boldsymbol{l}}_{\text{dep}} = \boldsymbol{l}_{\text{dep}} - \hat{\boldsymbol{e}}_{\text{dep}} \qquad \text{and} \qquad \hat{\boldsymbol{l}}_{\text{ind}} = \boldsymbol{l}_{\text{ind}} - \hat{\boldsymbol{e}}_{\text{ind}} \ . \tag{9.1.21}$$

The Taylor points for the observations in the next iteration of the adjustment are then $\hat{\boldsymbol{l}}_{\text{dep}}$ and $\hat{\boldsymbol{l}}_{\text{ind}}$. Note that the residuals are always added to the original observations, not the Taylor point of the current iteration.

Normal Equation System

Going beyond the derivations given by Reinking, 2008, his apparatus can be taken to completion by directly setting up the normal equation system for the sought parameters $\hat{x}$. To this end, the matrices in eq. (9.1.8) are analysed and expanded, so that they can later be substituted into eq. (9.1.18). First, note that

$$A_x = \left.\frac{\partial G}{\partial x}\right|_{x_0,l_0} = -\left.\frac{\partial f}{\partial x}\right|_{x_0,l_0} = -A \ . \tag{9.1.22}$$

Further,

$$F = \left[\left.\frac{\partial G}{\partial l_{\text{dep}}}\right|_{x_0,l_0} \quad \left.\frac{\partial G}{\partial l_{\text{ind}}}\right|_{x_0,l_0}\right] = \left[I \quad -\left.\frac{\partial f}{\partial l_{\text{ind}}}\right|_{x_0,l_0}\right] = \left[I \quad -F_{\text{ind}}\right] \ . \tag{9.1.23}$$

With eqs. (9.1.17) and (9.1.23), the covariance matrix of the derived observations is

$$
\begin{aligned}
\Sigma_{\lambda\lambda} &= \begin{bmatrix} I & -F_{\text{ind}} \end{bmatrix} \begin{bmatrix} \Sigma_{\text{dep}} & \Sigma_{\text{cro}} \\ \Sigma_{\text{cro}}^{\mathsf{T}} & \Sigma_{\text{ind}} \end{bmatrix} \begin{bmatrix} I^{\mathsf{T}} \\ -F_{\text{ind}}^{\mathsf{T}} \end{bmatrix} \\
&= \Sigma_{\text{dep}} - F_{\text{ind}}\Sigma_{\text{cro}}^{\mathsf{T}} - \Sigma_{\text{cro}}F_{\text{ind}}^{\mathsf{T}} + F_{\text{ind}}\Sigma_{\text{ind}}F_{\text{ind}}^{\mathsf{T}} \ ,
\end{aligned} \tag{9.1.24}
$$

giving the normal equation in the Reinking apparatus

$$N_{\text{R}} = A^{\mathsf{T}} \left(\Sigma_{\text{dep}} - F_{\text{ind}}\Sigma_{\text{cro}}^{\mathsf{T}} - \Sigma_{\text{cro}}F_{\text{ind}}^{\mathsf{T}} + F_{\text{ind}}\Sigma_{\text{ind}}F_{\text{ind}}^{\mathsf{T}}\right)^{-1} A \ . \tag{9.1.25}$$

To compute the right-hand side n_{R}, eqs. (9.1.12) to (9.1.14) must be expanded. With

$$\lambda = -\begin{bmatrix} I & -F_{\text{ind}} \end{bmatrix} \begin{bmatrix} l_{\text{dep}} \\ l_{\text{ind}} \end{bmatrix} = -l_{\text{dep}} + F_{\text{ind}}l_{\text{ind}} \tag{9.1.26}$$

$$Fl_0 = \begin{bmatrix} I & -F_{\text{ind}} \end{bmatrix} \begin{bmatrix} l_{\text{dep},0} \\ l_{\text{ind},0} \end{bmatrix} = l_{\text{dep},0} - F_{\text{ind}}l_{\text{ind},0} \tag{9.1.27}$$

$$G_0 = l_{\text{dep},0} - f_0 \tag{9.1.28}$$

the *reduced derived observations* are

$$
\begin{aligned}
\Delta\lambda &= \lambda - \lambda_0 = \lambda - (G_0 - Fl_0) = \lambda - G_0 + Fl_0 \\
&= -l_{\text{dep}} + F_{\text{ind}}l_{\text{ind}} - l_{\text{dep},0} + f_0 + l_{\text{dep},0} - F_{\text{ind}}l_{\text{ind},0} \\
&= -l_{\text{dep}} + f_0 + F_{\text{ind}}l_{\text{ind}} - F_{\text{ind}}l_{\text{ind},0} \\
&= -\left(l_{\text{dep}} - f_0\right) + F_{\text{ind}}\left(l_{\text{ind}} - l_{\text{ind},0}\right) \\
&= -\left(\left(l_{\text{dep}} - f_0\right) - F_{\text{ind}}\left(l_{\text{ind}} - l_{\text{ind},0}\right)\right) \\
&= -\left(\Delta l_{\text{dep}} - F_{\text{ind}}\Delta l_{\text{ind}}\right) \ .
\end{aligned} \tag{9.1.29}
$$

At this point it is important to note that Δl_{dep} is the reduced observation as it appears in the classical Gauß-Markov model in section 2.2, not simply $l_{\text{dep}} - l_{\text{dep},0}$. In fact, the

Taylor point for the dependent observations $l_{\text{dep},0}$ completely cancels from eq. (9.1.29). In the equation for the reduced derived observations, the term concerning the independent observations can be considered as a *correction term* for the reduced dependent observations, or

$$\Delta\Delta l_{\text{dep}} = F_{\text{ind}}\Delta l_{\text{ind}} \ . \tag{9.1.30}$$

With eqs. (9.1.22), (9.1.24) and (9.1.29) the right-hand side of the normal equation system is

$$\boldsymbol{n}_{\text{R}} = \boldsymbol{A}^{\mathsf{T}} \left(\boldsymbol{\Sigma}_{\text{dep}} - \boldsymbol{F}_{\text{ind}}\boldsymbol{\Sigma}_{\text{cro}}^{\mathsf{T}} - \boldsymbol{\Sigma}_{\text{cro}}\boldsymbol{F}_{\text{ind}}^{\mathsf{T}} + \boldsymbol{F}_{\text{ind}}\boldsymbol{\Sigma}_{\text{ind}}\boldsymbol{F}_{\text{ind}}^{\mathsf{T}} \right)^{-1} \left(\Delta l_{\text{dep}} - \boldsymbol{F}_{\text{ind}}\Delta l_{\text{ind}} \right) \ . \tag{9.1.31}$$

9.1.2 Total Least Squares as Gauß-Markov Model with Eliminated Observations

In this section, a different formulation for the treatment of uncertainties in the dependent variables is proposed. Where Reinking, 2008 started from an extended observation vector (eq. (9.1.5)), this formulation, perhaps equivalently, will begin with introducing the independent variables into an extended parameter vector

$$\boldsymbol{\xi} = \begin{bmatrix} \boldsymbol{x} \\ l_{\text{ind}} \end{bmatrix} \ . \tag{9.1.32}$$

This formulation pursues the goal of not only estimating the adjusted parameters $\hat{\boldsymbol{x}}$ and the adjusted dependent variable $\hat{l}_{\text{dep}}$, but to also determine a least squares estimate for the independent variable $\hat{l}_{\text{ind}}$. The functional model eq. (9.1.1) is extended with a second relationship describing the observations of the independent variable

$$l_{\text{dep}} = \boldsymbol{f}\left(l_{\text{ind}}, \boldsymbol{x}\right) + \boldsymbol{e}_{\text{dep}} \tag{9.1.33}$$

$$l_{\text{ind}} = \boldsymbol{g}\left(l_{\text{ind}}\right) + \boldsymbol{e}_{\text{ind}} \ . \tag{9.1.34}$$

This second relationship is of course simply

$$\boldsymbol{g}\left(l_{\text{ind}}\right) = l_{\text{ind}} \ . \tag{9.1.35}$$

This results in an extended observation vector identical to that of Reinking,

$$l = \begin{bmatrix} l_{\text{dep}} \\ l_{\text{ind}} \end{bmatrix} \ . \tag{9.1.36}$$

Linearising eqs. (9.1.33) and (9.1.34) at the Taylor point of the approximate values for the parameters and the independent variable yields

$$l_{\text{dep}} = \boldsymbol{f}\left(l_{\text{ind},0}, \boldsymbol{x}_0\right) + \left.\frac{\partial \boldsymbol{f}}{\partial \boldsymbol{x}}\right|_{\boldsymbol{x}_0, l_{\text{ind},0}} \Delta\boldsymbol{x} + \left.\frac{\partial \boldsymbol{f}}{\partial l_{\text{ind}}}\right|_{\boldsymbol{x}_0, l_{\text{ind},0}} \Delta l_{\text{ind}} + \boldsymbol{e}_{\text{dep}} \ , \tag{9.1.37}$$

$$l_{\text{ind}} = \boldsymbol{g}\left(l_{\text{ind},0}\right) \quad + \left.\frac{\partial \boldsymbol{g}}{\partial \boldsymbol{x}}\right|_{\boldsymbol{x}_0, l_{\text{ind},0}} \Delta\boldsymbol{x} + \left.\frac{\partial \boldsymbol{g}}{\partial l_{\text{ind}}}\right|_{\boldsymbol{x}_0, l_{\text{ind},0}} \Delta l_{\text{ind}} + \boldsymbol{e}_{\text{ind}} \ . \tag{9.1.38}$$

More compactly, this is

$$\begin{bmatrix} \Delta l_{\text{dep}} \\ \Delta l_{\text{ind}} \end{bmatrix} = \begin{bmatrix} A & F_{\text{ind}} \\ 0 & I \end{bmatrix} \begin{bmatrix} \Delta x \\ \Delta l_{\text{ind}} \end{bmatrix} + \begin{bmatrix} e_{\text{dep}} \\ e_{\text{ind}} \end{bmatrix}. \tag{9.1.39}$$

It is important to note that the two occurrences of Δl_{ind} in eq. (9.1.39) refer to two separate variables. The first is the linearisation of the independent variable about the Taylor point, $\Delta l_{\text{ind}} = l_{\text{ind}} - g\left(l_{\text{ind},0}\right)$. The second is the parameter to be estimated in the LSA. The independent variable does not depend on the parameters x. The covariance matrix of the combined observation vector is the same as in the previous model, given in eq. (9.1.16). The weight matrix for the combined observation vector is then

$$P = \Sigma_{ll}^{-1} = \begin{bmatrix} \Sigma_{\text{dep}} & \Sigma_{\text{cro}} \\ \Sigma_{\text{cro}}^{\mathsf{T}} & \Sigma_{\text{ind}} \end{bmatrix}^{-1} = \begin{bmatrix} P_{\text{dep}} & P_{\text{cro}} \\ P_{\text{cro}}^{\mathsf{T}} & P_{\text{ind}} \end{bmatrix}. \tag{9.1.40}$$

Using the matrix inversion lemma (see e.g. Bernstein, 2009, Proposition 2.8.7), the elements of P are:

$$\begin{aligned} P_{\text{dep}} &= \Sigma_{\text{dep}}^{-1} + \Sigma_{\text{dep}}^{-1}\Sigma_{\text{cro}}\left(\Sigma_{\text{ind}} - \Sigma_{\text{cro}}^{\mathsf{T}}\Sigma_{\text{dep}}^{-1}\Sigma_{\text{cro}}\right)^{-1}\Sigma_{\text{cro}}^{\mathsf{T}}\Sigma_{\text{dep}}^{-1} \\ &= \left(\Sigma_{\text{dep}} - \Sigma_{\text{cro}}\Sigma_{\text{ind}}^{-1}\Sigma_{\text{cro}}^{\mathsf{T}}\right)^{-1} \end{aligned} \tag{9.1.41}$$

$$\begin{aligned} P_{\text{cro}} &= -\Sigma_{\text{dep}}^{-1}\Sigma_{\text{cro}}\left(\Sigma_{\text{ind}} - \Sigma_{\text{cro}}^{\mathsf{T}}\Sigma_{\text{dep}}^{-1}\Sigma_{\text{cro}}\right)^{-1} \\ &= -\left(\Sigma_{\text{dep}} - \Sigma_{\text{cro}}\Sigma_{\text{ind}}^{-1}\Sigma_{\text{cro}}^{\mathsf{T}}\right)^{-1}\Sigma_{\text{cro}}\Sigma_{\text{ind}}^{-1} \end{aligned} \tag{9.1.42}$$

$$\begin{aligned} P_{\text{cro}}^{\mathsf{T}} &= -\left(\Sigma_{\text{ind}} - \Sigma_{\text{cro}}^{\mathsf{T}}\Sigma_{\text{dep}}^{-1}\Sigma_{\text{cro}}\right)^{-1}\Sigma_{\text{cro}}^{\mathsf{T}}\Sigma_{\text{dep}}^{-1} \\ &= -\Sigma_{\text{ind}}^{-1}\Sigma_{\text{cro}}^{\mathsf{T}}\left(\Sigma_{\text{dep}} - \Sigma_{\text{cro}}\Sigma_{\text{ind}}^{-1}\Sigma_{\text{cro}}^{\mathsf{T}}\right)^{-1} \end{aligned} \tag{9.1.43}$$

$$\begin{aligned} P_{\text{ind}} &= \left(\Sigma_{\text{ind}} - \Sigma_{\text{cro}}^{\mathsf{T}}\Sigma_{\text{dep}}^{-1}\Sigma_{\text{cro}}\right)^{-1} \\ &= \Sigma_{\text{ind}}^{-1} + \Sigma_{\text{ind}}^{-1}\Sigma_{\text{cro}}^{\mathsf{T}}\left(\Sigma_{\text{dep}} - \Sigma_{\text{cro}}\Sigma_{\text{ind}}^{-1}\Sigma_{\text{cro}}^{\mathsf{T}}\right)^{-1}\Sigma_{\text{cro}}\Sigma_{\text{ind}}^{-1} \end{aligned} \tag{9.1.44}$$

Normal Equation System

The normal equation for this Gauß-Markov model is

$$\begin{aligned} \begin{bmatrix} N_{11} & N_{12} \\ N_{12}^{\mathsf{T}} & N_{22} \end{bmatrix} &= \begin{bmatrix} A^{\mathsf{T}} & 0 \\ F_{\text{ind}}^{\mathsf{T}} & I \end{bmatrix} \begin{bmatrix} P_{\text{dep}} & P_{\text{cro}} \\ P_{\text{cro}}^{\mathsf{T}} & P_{\text{ind}} \end{bmatrix} \begin{bmatrix} A & F_{\text{ind}} \\ 0 & I \end{bmatrix} \\ &= \begin{bmatrix} A^{\mathsf{T}}P_{\text{dep}} & A^{\mathsf{T}}P_{\text{cro}} \\ F_{\text{ind}}^{\mathsf{T}}P_{\text{dep}} + P_{\text{cro}}^{\mathsf{T}} & F_{\text{ind}}^{\mathsf{T}}P_{\text{cro}} + P_{\text{ind}} \end{bmatrix} \begin{bmatrix} A & F_{\text{ind}} \\ 0 & I \end{bmatrix} \\ &= \begin{bmatrix} A^{\mathsf{T}}P_{\text{dep}}A & A^{\mathsf{T}}P_{\text{dep}}F_{\text{ind}} + A^{\mathsf{T}}P_{\text{cro}} \\ F_{\text{ind}}^{\mathsf{T}}P_{\text{dep}}A + P_{\text{cro}}^{\mathsf{T}}A & P_{\text{ind}} + P_{\text{cro}}^{\mathsf{T}}F_{\text{ind}} + F_{\text{ind}}^{\mathsf{T}}P_{\text{cro}} + F_{\text{ind}}^{\mathsf{T}}P_{\text{dep}}F_{\text{ind}} \end{bmatrix}. \end{aligned} \tag{9.1.45}$$

The right-hand side of the system is

$$
\begin{bmatrix} n_1 \\ n_2 \end{bmatrix} = \begin{bmatrix} A^\mathsf{T} & 0 \\ F_{\mathrm{ind}}^\mathsf{T} & I \end{bmatrix} \begin{bmatrix} P_{\mathrm{dep}} & P_{\mathrm{cro}} \\ P_{\mathrm{cro}}^\mathsf{T} & P_{\mathrm{ind}} \end{bmatrix} \begin{bmatrix} \Delta l_{\mathrm{dep}} \\ \Delta l_{\mathrm{ind}} \end{bmatrix}
$$

$$
= \begin{bmatrix} A^\mathsf{T} P_{\mathrm{dep}} & A^\mathsf{T} P_{\mathrm{cro}} \\ F_{\mathrm{ind}}^\mathsf{T} P_{\mathrm{dep}} + P_{\mathrm{cro}}^\mathsf{T} & F_{\mathrm{ind}}^\mathsf{T} P_{\mathrm{cro}} + P_{\mathrm{ind}} \end{bmatrix} \begin{bmatrix} \Delta l_{\mathrm{dep}} \\ \Delta l_{\mathrm{ind}} \end{bmatrix}
$$

$$
= \begin{bmatrix} A^\mathsf{T} P_{\mathrm{dep}} \Delta l_{\mathrm{dep}} + A^\mathsf{T} P_{\mathrm{cro}} \Delta l_{\mathrm{ind}} \\ \left(F_{\mathrm{ind}}^\mathsf{T} P_{\mathrm{dep}} + P_{\mathrm{cro}}^\mathsf{T} \right) \Delta l_{\mathrm{dep}} + \left(F_{\mathrm{ind}}^\mathsf{T} P_{\mathrm{cro}} + P_{\mathrm{ind}} \right) \Delta l_{\mathrm{ind}} \end{bmatrix} . \tag{9.1.46}
$$

Parameter elimination

Now the independent parameters are eliminated from the normal equation system as given by eq. (9.1.45) (see section 2.4). After some simplification, this gives

$$
N_{\mathrm{E}} = A^\mathsf{T} P_{\mathrm{E}} A . \tag{9.1.47}
$$

with

$$
P_{\mathrm{E}} = P_{\mathrm{dep}} - \left(P_{\mathrm{dep}} F_{\mathrm{ind}} + P_{\mathrm{cro}} \right)
$$
$$
\left(P_{\mathrm{ind}} + P_{\mathrm{cro}}^\mathsf{T} F_{\mathrm{ind}} + F_{\mathrm{ind}}^\mathsf{T} P_{\mathrm{cro}} + F_{\mathrm{ind}}^\mathsf{T} P_{\mathrm{dep}} F_{\mathrm{ind}} \right)^{-1} \left(F_{\mathrm{ind}}^\mathsf{T} P_{\mathrm{dep}} + P_{\mathrm{cro}}^\mathsf{T} \right) . \tag{9.1.48}
$$

For the right-hand side as given by eq. (9.1.46), parameter elimination yields

$$
n_{\mathrm{E}} = A^\mathsf{T} P_{\mathrm{dep}} \Delta l_{\mathrm{dep}} + A^\mathsf{T} P_{\mathrm{cro}} \Delta l_{\mathrm{ind}}
$$
$$
- \left(A^\mathsf{T} P_{\mathrm{dep}} F_{\mathrm{ind}} + A^\mathsf{T} P_{\mathrm{cro}} \right) \left(P_{\mathrm{ind}} + P_{\mathrm{cro}}^\mathsf{T} F_{\mathrm{ind}} + F_{\mathrm{ind}}^\mathsf{T} P_{\mathrm{cro}} + F_{\mathrm{ind}}^\mathsf{T} P_{\mathrm{dep}} F_{\mathrm{ind}} \right)^{-1}
$$
$$
\left(\left(F_{\mathrm{ind}}^\mathsf{T} P_{\mathrm{dep}} + P_{\mathrm{cro}}^\mathsf{T} \right) \Delta l_{\mathrm{dep}} + \left(F_{\mathrm{ind}}^\mathsf{T} P_{\mathrm{cro}} + P_{\mathrm{ind}} \right) \Delta l_{\mathrm{ind}} \right)
$$
$$
= A^\mathsf{T} P_{\mathrm{E}} \Delta l_{\mathrm{dep}} + A^\mathsf{T} P_l \Delta l_{\mathrm{ind}} , \tag{9.1.49}
$$

with

$$
P_l = P_{\mathrm{cro}} - \left(P_{\mathrm{dep}} F_{\mathrm{ind}} + P_{\mathrm{cro}} \right)
$$
$$
\left(P_{\mathrm{ind}} + P_{\mathrm{cro}}^\mathsf{T} F_{\mathrm{ind}} + F_{\mathrm{ind}}^\mathsf{T} P_{\mathrm{cro}} + F_{\mathrm{ind}}^\mathsf{T} P_{\mathrm{dep}} F_{\mathrm{ind}} \right)^{-1} \left(F_{\mathrm{ind}}^\mathsf{T} P_{\mathrm{cro}} + P_{\mathrm{ind}} \right) . \tag{9.1.50}
$$

9.1.3 Equivalence of Approaches

Given the simplifying assumption that

$$
\Sigma_{\mathrm{cro}} = 0 , \tag{9.1.51}
$$

the two approaches from sections 9.1.1 and 9.1.2 are identical. The proof is obtained by comparing the normal equation systems for both approaches under the condition that $\mathbf{\Sigma}_{\mathrm{cro}} = \mathbf{0}$. For the approach due to Reinking, the simplified normal equation system is obtained directly from eqs. (9.1.25) and (9.1.31) as

$$N_{\mathrm{R}} = A^{\mathsf{T}} P_{\mathrm{R}} A \qquad \text{and} \qquad n_{\mathrm{R}} = A^{\mathsf{T}} P_{\mathrm{R}} \left(\Delta l_{\mathrm{dep}} - F_{\mathrm{ind}} \Delta l_{\mathrm{ind}} \right) \tag{9.1.52}$$

with the weight matrix in the Reinking system

$$P_{\mathrm{R}} = \left(\mathbf{\Sigma}_{\mathrm{dep}} + F_{\mathrm{ind}} \mathbf{\Sigma}_{\mathrm{ind}} F_{\mathrm{ind}}^{\mathsf{T}} \right)^{-1} . \tag{9.1.53}$$

For the normal equation system derived using parameter elimination with

$$N_{\mathrm{E}} = A^{\mathsf{T}} P_{\mathrm{E}} A \qquad \text{and} \qquad n_{\mathrm{E}} = A^{\mathsf{T}} P_{\mathrm{E}} \Delta l_{\mathrm{dep}} + A^{\mathsf{T}} P_l \Delta l_{\mathrm{ind}} , \tag{9.1.54}$$

letting $\mathbf{\Sigma}_{\mathrm{cro}} = \mathbf{0}$ results in the weights from eqs. (9.1.41) to (9.1.44) simplifying to

$$P_{\mathrm{dep}} = \mathbf{\Sigma}_{\mathrm{dep}}^{-1} , \qquad P_{\mathrm{ind}} = \mathbf{\Sigma}_{\mathrm{ind}}^{-1} \qquad \text{and} \qquad P_{\mathrm{cro}} = \mathbf{0} . \tag{9.1.55}$$

Again using the matrix inversion lemma, this gives a simplified version of eq. (9.1.48). The first weight matrix for the normal equation system due to the parameter elimination algorithm is

$$\begin{aligned}
P_{\mathrm{E}} &= \mathbf{\Sigma}_{\mathrm{dep}}^{-1} - \mathbf{\Sigma}_{\mathrm{dep}}^{-1} F_{\mathrm{ind}} \left(\mathbf{\Sigma}_{\mathrm{ind}}^{-1} + F_{\mathrm{ind}}^{\mathsf{T}} \mathbf{\Sigma}_{\mathrm{dep}}^{-1} F_{\mathrm{ind}} \right)^{-1} F_{\mathrm{ind}}^{\mathsf{T}} \mathbf{\Sigma}_{\mathrm{dep}}^{-1} \\
&= \left(\mathbf{\Sigma}_{\mathrm{dep}} + F_{\mathrm{ind}} \mathbf{\Sigma}_{\mathrm{ind}} F_{\mathrm{ind}}^{\mathsf{T}} \right)^{-1} \\
&= P_{\mathrm{R}} .
\end{aligned} \tag{9.1.56}$$

With $P_{\mathrm{E}} \equiv P_{\mathrm{R}}$, it directly follows that $N_{\mathrm{E}} \equiv N_{\mathrm{R}}$. It remains to show that the right-hand side of the systems are identical as well. When letting $\mathbf{\Sigma}_{\mathrm{cro}} = \mathbf{0}$ the weight matrix P_l from eq. (9.1.50) is

$$\begin{aligned}
P_l &= -\mathbf{\Sigma}_{\mathrm{dep}}^{-1} F_{\mathrm{ind}} \left(\mathbf{\Sigma}_{\mathrm{ind}}^{-1} + F_{\mathrm{ind}}^{\mathsf{T}} \mathbf{\Sigma}_{\mathrm{dep}}^{-1} F_{\mathrm{ind}} \right)^{-1} \mathbf{\Sigma}_{\mathrm{ind}}^{-1} \\
&= - \left(\mathbf{\Sigma}_{\mathrm{dep}} + F_{\mathrm{ind}} \mathbf{\Sigma}_{\mathrm{ind}} F_{\mathrm{ind}}^{\mathsf{T}} \right) F_{\mathrm{ind}} \mathbf{\Sigma}_{\mathrm{ind}} \mathbf{\Sigma}_{\mathrm{ind}}^{-1} \\
&= - \left(\mathbf{\Sigma}_{\mathrm{dep}} + F_{\mathrm{ind}} \mathbf{\Sigma}_{\mathrm{ind}} F_{\mathrm{ind}}^{\mathsf{T}} \right) F_{\mathrm{ind}} \\
&= -P_{\mathrm{R}} F_{\mathrm{ind}}
\end{aligned} \tag{9.1.57}$$

Inserting eqs. (9.1.56) and (9.1.57) into eq. (9.1.49) gives

$$\begin{aligned}
n_{\mathrm{E}} &= A^{\mathsf{T}} P_{\mathrm{R}} \Delta l_{\mathrm{dep}} + A^{\mathsf{T}} \left(-P_{\mathrm{R}} F_{\mathrm{ind}} \right) \Delta l_{\mathrm{ind}} \\
&= A^{\mathsf{T}} P_{\mathrm{R}} \Delta l_{\mathrm{dep}} - A^{\mathsf{T}} P_{\mathrm{R}} F_{\mathrm{ind}} \Delta l_{\mathrm{ind}} \\
&= A^{\mathsf{T}} P_{\mathrm{R}} \left(\Delta l_{\mathrm{dep}} - F_{\mathrm{ind}} \Delta l_{\mathrm{ind}} \right) \\
&= n_{\mathrm{R}}
\end{aligned} \tag{9.1.58}$$

With $N_{\mathrm{R}} \equiv N_{\mathrm{E}}$ and $n_{\mathrm{R}} \equiv n_{\mathrm{E}}$, it is proven that both approaches give the same results. It stands to reason that this equivalence should also hold for $\mathbf{\Sigma}_{\mathrm{cro}} \neq \mathbf{0}$. Numerical tests support this hypothesis, but a rigorous proof for this conjecture is not known to the author.

9.2 Application to GRACE

GRACE KBR range-rate observations are described by the ranging equation (compare eq. (4.3.7))

$$f(x, \alpha) = \dot{\rho}_{\text{KBR}} = \dot{\rho}_{\text{COM}}(x) - \Delta\dot{\rho}_{\text{AOC}}(x, \alpha) - \Delta\dot{\rho}_{\text{TOF}} - \Delta\dot{\rho}_{\text{Iono}} + e . \tag{9.2.1}$$

Here, the dependent observable is the ll-SST KBR range rate $\dot{\rho}_{\text{KBR}}$. The independent observables are the satellite orientation α_s for both GRACE spacecraft. The sought parameters x are those described in section 6.4: The force model parameters, the satellite parameters, and the ll-SST parameters. The observation equations for these parameters, as summarized in eq. (6.4.32), are unchanged. They are collected and linearised in the Taylor point for the parameters and the satellite orientation

$$f_0(x_0, \alpha_0) = \dot{\rho}_{\text{COM}}(x_0) - \Delta\dot{\rho}_{\text{AOC}}(x_0, \alpha_0) - \Delta\dot{\rho}_{\text{TOF}} - \Delta\dot{\rho}_{\text{Iono}} . \tag{9.2.2}$$

The Taylor point for the force model parameters is given by the background models and the dynamic orbits integrated therein. The Taylor point for the satellite orientation is simply the observed satellite orientation as obtained from the SCA/ACC sensor fusion. The influence of the linearisation about the Taylor point on the time-of-flight correction and the ionospheric correction is omitted.

The design matrix for the ll-SST observations A is unchanged from the equations laid out in section 6.4, with the exception of the entries for the APC coordinates in eq. (6.4.30). The observation equations for the APC must now be linearised about the current Taylor point for the orientation at every iteration. The expanded observation vector is

$$l = \begin{bmatrix} \dot{\rho}_{\text{KBR}} \\ \alpha_{\text{A}} \\ \alpha_{\text{B}} \end{bmatrix} . \tag{9.2.3}$$

The Jacobian of the AOC in the range rate domain w.r.t. the orientation of one spacecraft was previously computed in chapter 8. With D the polynomial differentiation matrix and $F_\alpha^s = \partial\Delta\dot{\rho}_{\text{AOC}}^s/\partial\alpha_s$ from eq. (8.1.21), the full Jacobian for both the ll-SST and the orientation observations in the Reinking model (compare eq. (9.1.23)) is

$$F = \begin{bmatrix} I & -DF_\alpha^{\text{A}} & -DF_\alpha^{\text{B}} \end{bmatrix} . \tag{9.2.4}$$

With the full covariance matrix

$$\Sigma_{ll} = \begin{bmatrix} \Sigma_{\text{sst}} & 0 & 0 \\ 0 & \Sigma_{\hat{\alpha}\hat{\alpha}}^{\text{A}} & 0 \\ 0 & 0 & \Sigma_{\hat{\alpha}\hat{\alpha}}^{\text{B}} \end{bmatrix} \tag{9.2.5}$$

the weight matrix of the equation system is

$$P_R = \left(\Sigma_{\text{sst}} + DF_\alpha^A \Sigma_{\hat{\alpha}\hat{\alpha}}^A \left(DF_\alpha^A \right)^\mathsf{T} + DF_\alpha^B \Sigma_{\hat{\alpha}\hat{\alpha}}^B \left(DF_\alpha^B \right)^\mathsf{T} \right)^{-1}$$

$$= \left(\Sigma_{\text{sst}} + \Sigma_{\Delta\dot{\rho}_{\text{AOC}}}^A + \Sigma_{\Delta\dot{\rho}_{\text{AOC}}}^B \right)^{-1}. \tag{9.2.6}$$

Here, Σ_{sst} is the estimated stationary covariance matrix for the ll-SST observations, and $\Sigma_{\Delta\dot{\rho}_{\text{AOC}}}^A$ and $\Sigma_{\Delta\dot{\rho}_{\text{AOC}}}^B$ are the AOC covariance matrices from chapter 8. The observation groups are uncorrelated. The covariance matrix of the derived observations is thus identical to the complete arc-wise covariance matrix of the improved stochastic model described in eq. (8.2.1). Also identical to the approach of chapter 8, a complete set of variance factors, one for each time lag in the stationary covariance function, one for each short arc, and one for each spacecraft's AOC covariance per month, are co-estimated.

The reduced derived observation from eq. (9.1.29) is then

$$\Delta\lambda = - \left(\dot{\rho}_{\text{KBR}} - f_0(x_0, \alpha_0) - DF_\alpha^A (\alpha_A - \alpha_{0A}) - DF_\alpha^B (\alpha_B - \alpha_{0B}) \right), \tag{9.2.7}$$

with the Taylor point for the orientation the observations thereof in the first iteration, and the estimated orientation thereafter. With this information, the normal equation system can be formed, and $\Delta\hat{x}$ and $\hat{e}_\lambda$ are determined in the usual way. Using eqs. (9.1.20) and (9.1.21), the estimated additions to the satellite orientation are

$$\Delta\hat{\alpha}_A = \hat{\Sigma}_{\hat{\alpha}\hat{\alpha}}^A \left(DF_\alpha^A \right)^\mathsf{T} P_R \hat{e}_\lambda \qquad \text{and} \qquad \Delta\hat{\alpha}_B = \hat{\Sigma}_{\hat{\alpha}\hat{\alpha}}^B \left(DF_\alpha^B \right)^\mathsf{T} P_R \hat{e}_\lambda, \tag{9.2.8}$$

with the final updated estimated orientations

$$\hat{\alpha}_A = \alpha_A - \Delta\hat{\alpha}_A \qquad \qquad \text{and} \qquad \qquad \hat{\alpha}_B = \alpha_B - \Delta\hat{\alpha}_B. \tag{9.2.9}$$

Practical Considerations

The algorithm used to co-estimate orientation parameters only affects the covariance matrix and reduced observations for the ll-SST observables. The hl-SST component of the equation system remains unaffected. In GROOPS, the co-estimation of the satellite orientation has been implemented in parallel to the iterative estimation of the stochastic model with a degree and order 60 gravity field solution. This means that the updated orientation is not used to re-integrate the dynamic orbits, as this step is already completed at this point. Further, the updated estimates for the KBR antenna phase centre vectors are not used in the linearisation of the observation equations or for computing the updated AOC. Under regular observation conditions the opening angle β is small for both spacecraft. This is an unfavourable configuration for a stable estimate of the APC vectors. Until convergence of the stochastic model and the spacecraft orientation is achieved, estimates of the APC vectors fluctuate wildly. Allowing these vectors to vary at this point prohibits convergence of the system and leads to chaotic results.

For each iteration in this estimation, the updated orientation is used to recompute

1. the design matrix for the APC vectors, as in eq. (6.4.30);
2. an updated antenna offset correction, as in eq. (4.3.6);
3. updated AOC covariance matrices $\Sigma^s_{\Delta\dot{\rho}_{AOC}}$, linearised at the new estimated orientation as in eq. (8.1.22);
4. and an updated correction term for the ll-SST observation, as in eq. (9.1.30).

These additional steps lengthen the computation time per iteration significantly. The stochastic model estimated in section 8.2 is used as a priori information to speed up convergence. The estimated stochastic model and the estimated orientations are then used in the computation of the full high degree and order gravity field solution.

9.3 Results

The GRACE time series was again reprocessed, using the updated stochastic model as first introduced in chapter 8 and co-estimating improved satellite orientations as described in section 9.2. The following sections will give analysis of this time series, focusing on the estimated stochastic model, the estimated orientations, and the estimated monthly gravity fields. In addition to again highlighting some specific months representing several levels of data quality, the complete time series will also be analysed and contrasted to the previously computed solutions.

9.3.1 Stochastic Model and Residuals

The initial inclusion of the stochastic information on the non-stationary AOC in the form of AOC covariance matrices had a large impact on the estimated stochastic model. The impact was noticeable both in terms of PSD and in terms of arc-wise variance factors. The same disentanglement of stationary and non-stationary noise sources is also present and unchanged in the TLS approach. The estimated stochastic models are consequently largely identical. The additional co-estimation of the satellite orientation is of course expected to have an effect on the ll-SST residuals, as in total a larger number of parameters is estimated. Figure 9.1 gives an indication that this effect can not be very large, as the PSD estimated from the new residuals (pink) is largely identical to that computed only under consideration of the AOC covariances (blue). Figure 9.1 shows the PSD for a month of sub-par data quality, the PSDs for months of good data quality are similarly identical to those computed with AOC covariances only.

A small improvement can however be observed when studying the correlation between the arc-wise variance factors and the mean opening angles for the respective arcs, as displayed in fig. 9.2. For the TLS solution, the mean of the correlation coefficients is reduced from 0.03 to 0.01. This is a much smaller improvement than what was previously achieved by introducing the AOC covariance matrices. Nevertheless, it is important to note that the co-estimation of the satellite orientation does not have a negative impact on either component of the stochastic model.
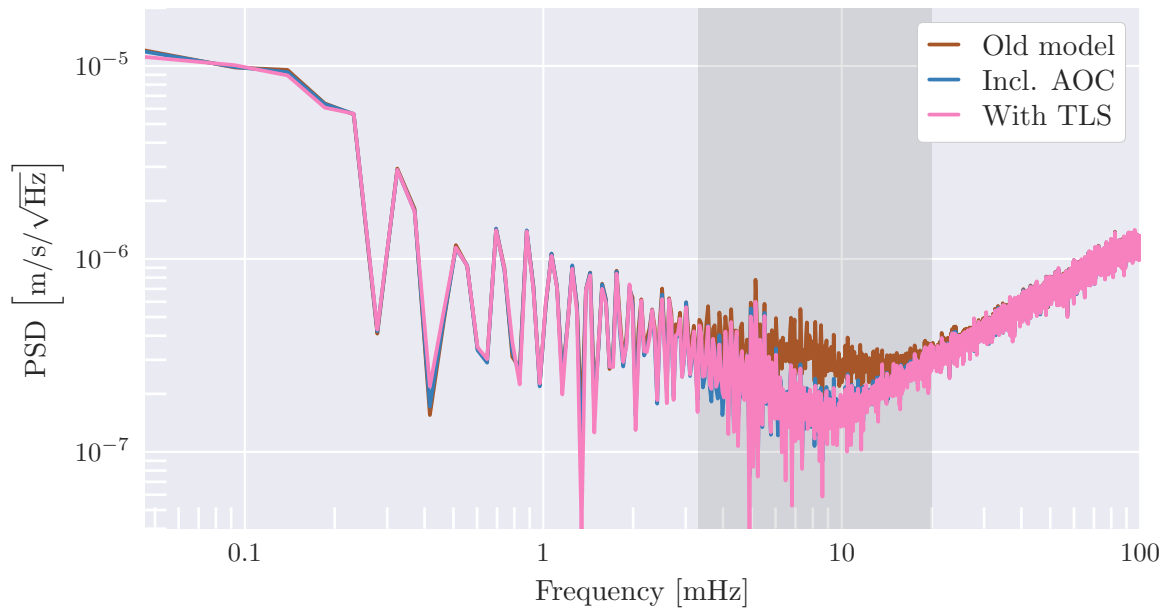
Figure 9.1: Estimated stationary noise PSD without considering full AOC covariance matrices (in brown), when taking them into account (in blue), and when co-estimating satellite orientation (in pink), for June 2010. The shaded area is the same as in fig. 8.8.
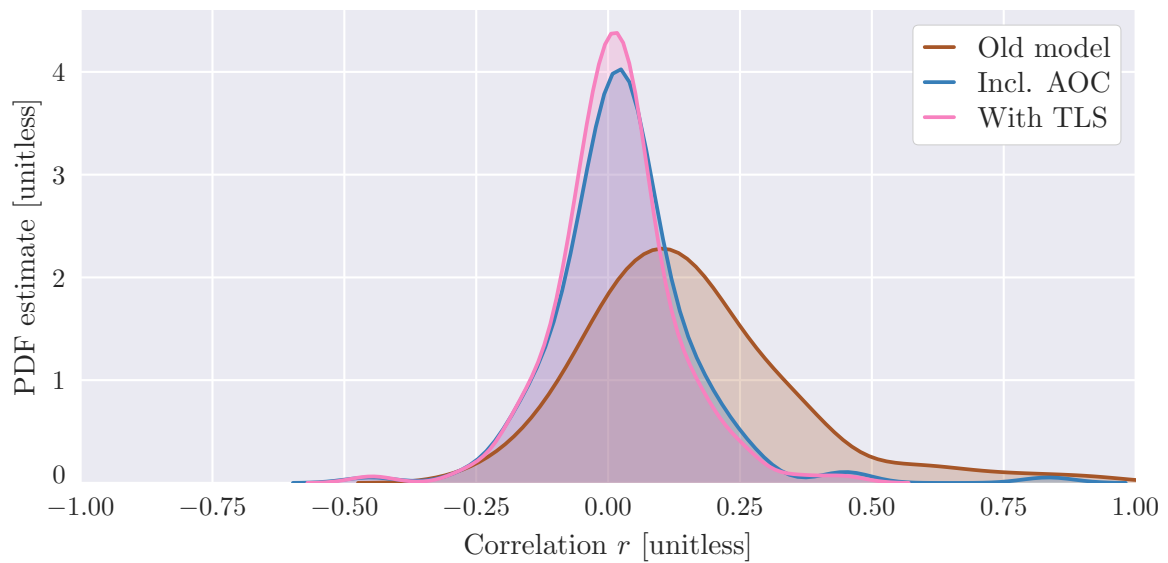
Figure 9.2: Distribution of correlation coefficients r between arc-wise variance factors $\hat{\sigma}_m^2$ and mean opening angles $\bar{\beta}_m$. One correlation coefficient was estimated per month.

9.3.2 Estimated Satellite Orientation

The TLS algorithm gives a least squares estimate for improved orientation quaternions for the two GRACE spacecraft. Investigating noise in the orientation through numerical simulations has shown that two processing steps are particularly sensitive to orientation uncertainties. These are the computation of the antenna offset correction, and the computation of the design matrix for parameters that directly depend on the satellite orientation such as the antenna phase centre vectors. The rotation of the accelerometer data into the CRF, as required for dynamic orbit integration, is for example not as sensitive to noise in the orientation.

As shown by Harvey, 2016, the release 2.0 spacecraft orientations are subject to a bug in the on board star camera software, leading to defective data in the SCA1B data files. As of the time of this writing, no corrected data is generally available. This known deficiency in the source data, together with the sensitivity of certain parameters to the spacecraft orientation discussed above, serves as motivation for the co-estimation of the satellite orientations.

Where the SCA/ACC sensor fusion only considers sensors on one GRACE spacecraft, the TLS estimate of the orientation also includes observations by the very high precision ll-SST KBR link in the orientation estimate. The KBR range rate observations give an additional constraint on the relative motion of the satellites w.r.t. each other. Full covariance information on both the orientation parameters and on the KBR observable allows for the combination of these heterogeneous observation types. It must be expected that the additional KBR observations would have a negligible impact on the adjusted orientation parameters if their noise were too high with respect to the orientation observations from the SCA/ACC sensor fusion.

Figure 9.3 shows the TLS estimate of the satellite orientation of both GRACE spacecraft for a 3 hour segment of data on June 11, 2010. This particular segment was chosen as it shows rather unremarkable satellite orientations. No large excursions from the steering deadband occur during this time period. The SCA/ACC sensor fusion orientation α, used as a Taylor point in the estimation, is plotted in the background (brown), overlaid by the TLS result $\hat{\alpha}$ (in pink) and the difference between the two $\Delta\hat{\alpha}$ (in blue). The areas shaded with a darker background mark periods of time where only one SCA head was active on the respective spacecraft. During these times, the uncertainty of the satellite orientation resulting from the SCA/ACC sensor fusion is naturally higher (compare e.g. fig. 8.3).

The top row of fig. 9.3 shows the roll angles of the two GRACE spacecraft. The TLS estimate for this angle is virtually unchanged from the SCA/ACC sensor fusion estimate. This result is reassuring as, due to the geometry of the observations, the inter-satellite link is comparatively insensitive to changes in satellite roll. The lower two rows of fig. 9.3 show the satellite pitch and yaw rotations, respectively. For these angles the difference between the a priori fusion orientation and the TLS estimate is consistently small for periods where both SCA heads are active. It is only when observations are based on only one SCA head that the TLS estimate significantly
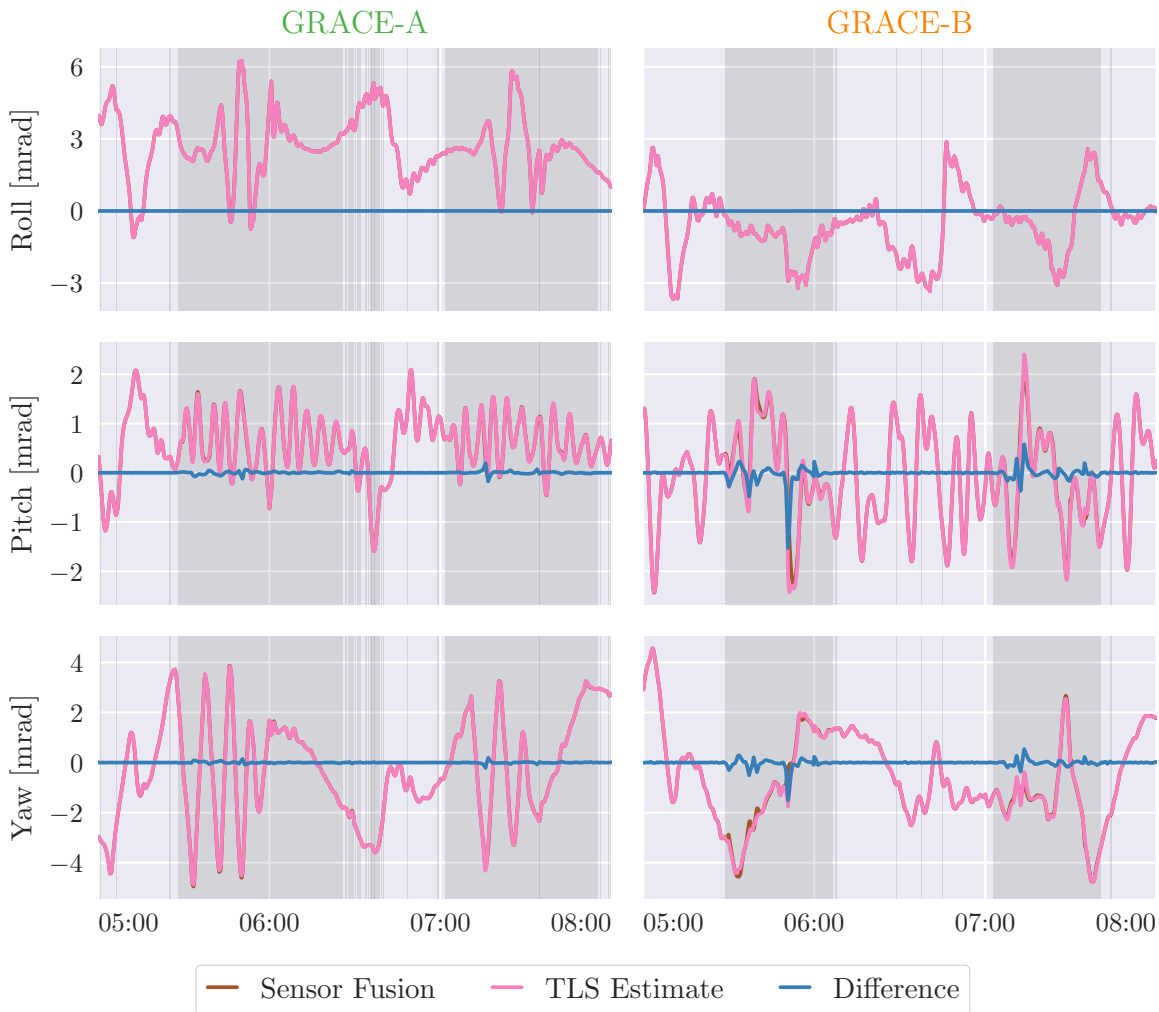
Figure 9.3: TLS estimate of satellite orientation (in pink), orientation from sensor fusion (in brown), and difference (in blue), for 3 hours on June 11, 2010. The roll, pitch, and yaw angles are given w.r.t. the nominal attitude. Darker shaded areas show times where only one star camera head was active on the respective spacecraft. Note the different scales for each angle.

diverges. This is striking, as it suggests that the noise floor of the KBR instrument in the frequency band affecting the satellite orientation is located exactly between the noise levels achievable with only one or with two SCA heads. The deviation of the TLS estimate from the a priori orientation is still mostly small, though. For the whole month of June 2010, the largest corrections observed are 0.7 mrad for GRACE-A and 1.9 mrad for GRACE-B. In general, it can be observed that the corrections are larger for GRACE-B.

Figure 9.4 gives the distributions of the estimated improvements for the satellite orientations $\Delta\hat{\alpha}_s$ for the complete processed GRACE time series. The left column is limited to a statistic of the periods where only one SCA head was active on the
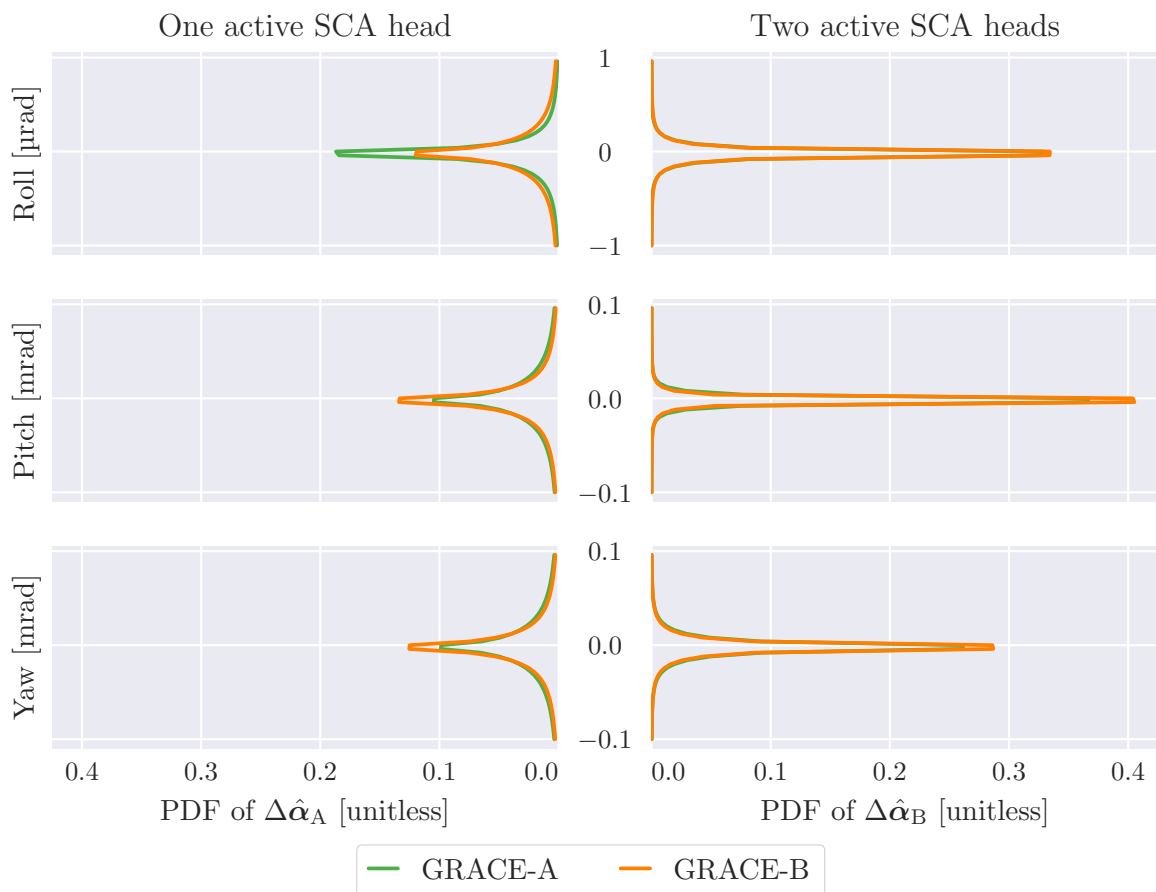
Figure 9.4: TLS estimate of improvement of satellite orientation for one active SCA head (left column), and two active heads (right column). The estimate for GRACE-A is plotted in green, that for GRACE-B in orange. Note that the scale is different for the roll angle (top row).

respective spacecraft, covering 37.8 % of the total timespan for GRACE-A and 37.1 % of the total timespan for GRACE-B. The right column gives the statistics for the remaining time periods, where observations from both SCA heads are included in the SCA1B product.

Note that in fig. 9.4, the correction for roll is given in µrad, while those for pitch and yaw are given in mrad. For periods where both heads are active, shown in the right column of fig. 9.4, there is no noticeable difference in the distribution of the corrections for the two satellites. For all three angles, the correction is on average smaller when both heads are active, which confirms the observations made in fig. 9.3. When only one SCA head is active, the correction in roll is larger for GRACE-A (green) than it is for GRACE-B (orange). This behaviour is reversed for the pitch and yaw angles, where the correction for GRACE-B (orange) is larger. The overall magnitude of the correction is, on average, rather small. For the complete time series corrections larger in magnitude than 1 mrad, as observed in fig. 9.3, are uncommon.

9.3.3 Effect on Antenna Offset Correction

After each iteration of the TLS adjustment the estimated orientations are used to re-compute the antenna offset correction. This leads to a new improved antenna offset correction that is slightly different from the initial AOC computed from the SCA/ACC sensor fusion orientation. As the AOC is a non-stationary process, analysing its change in the spectral domain would be fallacious. Instead, the change of magnitude of the AOC at each epoch is analysed, which is not dependent on the absolute value of the AOC. For a month of regular data, e.g. April 2008, the mean magnitude of the AOC is $\approx 3.8 \cdot 10^{-8}$ m/s. The mean of the estimated correction due to the improved TLS orientation estimate for the same month is $\approx 3.5 \cdot 10^{-9}$ m/s, which is roughly one order of magnitude smaller. For other months, the magnitude of both the AOC and the correction can be significantly larger.

Figure 9.5 shows the distribution of these deviations

$$d_{\mathrm{AOC}}(\tau) = \frac{\mathrm{AOC}_{\mathrm{new}}(\tau)}{\mathrm{AOC}_{\mathrm{old}}(\tau)} - 1 \qquad (9.3.1)$$

in percent. A value below $0\,\%$ indicates that the new AOC for that epoch is smaller than the original, a value larger than $0\,\%$ represents an increased AOC. As these deviations are computed in the range-rate domain, a translation of this change into a statement on the magnitude of the opening angle β is not directly possible. Instead, a smaller value for d_{AOC} indicates a slower change in the opening angle, with a larger value representing a faster change. All curves are skewed very slightly towards negative values, indicating that the TLS estimate of the orientation tends to dampen high-velocity motion in the satellite pointing.
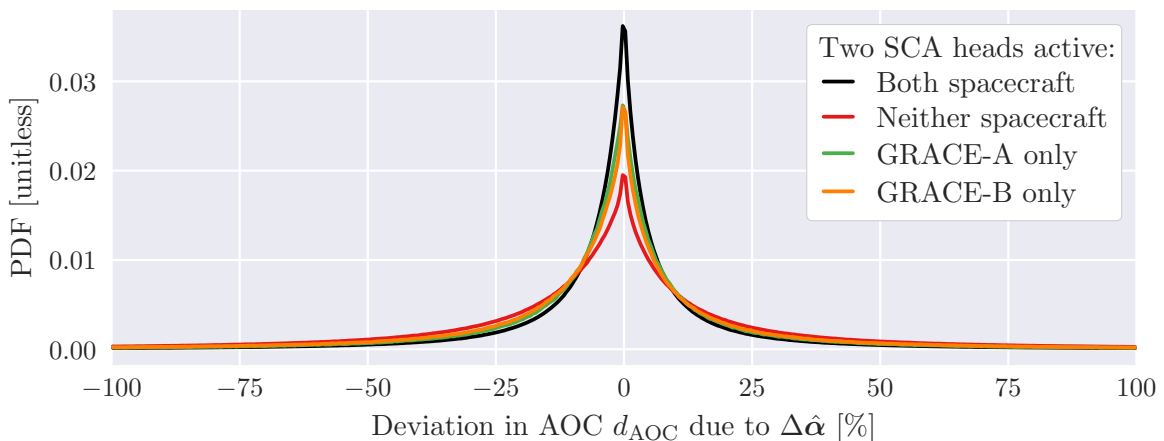
Figure 9.5: Distribution of change in AOC due to improved orientation in relation to the magnitude of the original AOC. The data sets underlying the separate distributions were selected according to how many SCA heads were active for the respective epochs.

Figure 9.5 shows that the change in AOC is smallest when all SCA heads are active (black, 57.8 % of epochs), and largest when both spacecraft operate on one head only (red, 33.7 % of epochs). Not conforming with the results from section 9.3.2, the change is almost identical when one SCA head is inactive on GRACE-B only (orange, 5.27 % of epochs), as when GRACE-A is the sole spacecraft operating with one SCA head (green, 3.2 % of epochs).

9.3.4 Estimated Antenna Phase Centre Vectors

In the least squares adjustment for the Stokes coefficients, the KBR antenna phase centre vectors for GRACE-A and GRACE-B were co-estimated (compare section 6.4.2). The following results are based on the APC estimates obtained from within the determination of the stochastic model. The estimated APC vector for one satellite s is

$$\hat{c}_s = c_s + \Delta\hat{c}_s \, , \tag{9.3.2}$$

where c_s is the a priori calibrated KBR APC for the satellite, which was used as a Taylor point in the estimation. The in-orbit calibrated APC coordinates obtained from the GRACE sequence of events file are given in table 9.1. Alongside the calibrated values, the formal errors from the adjustment for $\Delta\hat{c}$ are given for an example month of good data quality. The formal errors are given for the adjustment using the old stochastic model, the model including AOC covariance matrices, and the TLS solution. Note that the formal errors do not vary much between months, and that they are small, on the order of some micrometres. The estimated improvements $\Delta\hat{c}$ to the published calibrated APCs for the processed time series are displayed in fig. 9.6. Results for the period after August 2016, which are very strongly affected by the disabled accelerometer on GRACE-B (Flechtner, 2016), are excluded from the analysis in this section.

Table 9.1: Calibrated KBR APC coordinates and formal errors from their estimation for April 2008.

	Calibrated value	$\sigma_{\text{Old model}}$	$\sigma_{\text{Incl. AOC}}$	$\sigma_{\text{With TLS}}$
GRACE-A				
x_{APC}	1.445 m	5.241 µm	5.308 µm	5.437 µm
y_{APC}	−0.423 µm	0.018 µm	0.018 µm	0.018 µm
z_{APC}	2.278 µm	0.021 µm	0.021 µm	0.020 µm
GRACE-B				
x_{APC}	1.444 m	10.062 µm	10.052 µm	10.095 µm
y_{APC}	0.576 µm	0.031 µm	0.030 µm	0.030 µm
z_{APC}	3.304 µm	0.041 µm	0.041 µm	0.041 µm

Table 9.2: Empirical mean and standard deviation of KBR APC estimates computed from complete time series. Values relative to published calibrated APCs.

	$\Delta\hat{x}_{\mathrm{APC}}$ [cm]	$\Delta\hat{y}_{\mathrm{APC}}$ [mm]	$\Delta\hat{z}_{\mathrm{APC}}$ [mm]
GRACE-A			
Old model	-23.35 ± 15.51	0.74 ± 0.20	-1.12 ± 0.36
Incl. AOC	-25.28 ± 12.88	0.72 ± 0.18	-1.15 ± 0.33
With TLS	-2.50 ± 20.48	0.50 ± 0.18	-0.86 ± 0.52
GRACE-B			
Old model	-22.96 ± 18.23	-0.46 ± 0.16	-0.37 ± 0.64
Incl. AOC	-24.03 ± 15.60	-0.44 ± 0.14	-0.40 ± 0.57
With TLS	-4.44 ± 14.22	-0.29 ± 0.19	0.04 ± 0.54

The panels in fig. 9.6 show the difference $\Delta\hat{c}_s$ from the calibrated KBR APC vectors to the estimated APC vectors in the SRF. The top two panels show the differences in the x-coordinate for GRACE-A and GRACE-B. It is immediately obvious that the original estimate for the x-coordinate (brown) has a strong negative bias for both GRACE-A and GRACE-B. This bias is much larger than the formal errors given in table 9.1 would suggest. Introducing the AOC covariance information (blue) does not eliminate this bias but does reduce the spread of the estimates slightly (compare table 9.2). The estimate using TLS (pink) almost completely eliminates this bias. The estimate does however retain a rather large standard deviation. This can to some extent be explained by the unfavourable observation geometry, as the APC vector is better determinable with larger opening angles β, which overall are uncommon during science operations. The discrepancy between formal errors and empirical standard deviation is however not fully explained by this circumstance, suggesting the continued presence of some unmodelled systematics. This might still well be due to the systematic errors in the SCA1B data described by Harvey, 2016.

The estimated y component on both GRACE-A and GRACE-B shows a clear signal with a roughly annular period. At least for GRACE-A, this is much reduced when employing the TLS estimate. In general, the co-estimation of the APC vectors gives best results in time periods of "good" data quality, roughly from 2006 to 2011. Outside of these periods, the scatter is higher, especially towards the end of the mission lifetime, where the accelerometer on GRACE-B was powered off (not pictured).

The estimated APC vectors can also be interpreted as a misalignment of the K-Frame with the SRF (e.g. Horwath et al., 2011). The rotation from the SRF to the K-Frame expressed by the estimated APCs is described by the relationship

$$\hat{c} = \|\hat{c}\| \cdot R_{\mathrm{SRF}}^{\mathrm{KF}} \begin{bmatrix} 1 & 0 & 0 \end{bmatrix}^{\mathsf{T}}, \tag{9.3.3}$$

with $R_{\mathrm{SRF}}^{\mathrm{KF}}$ a small angle rotation as in eq. (6.2.5).
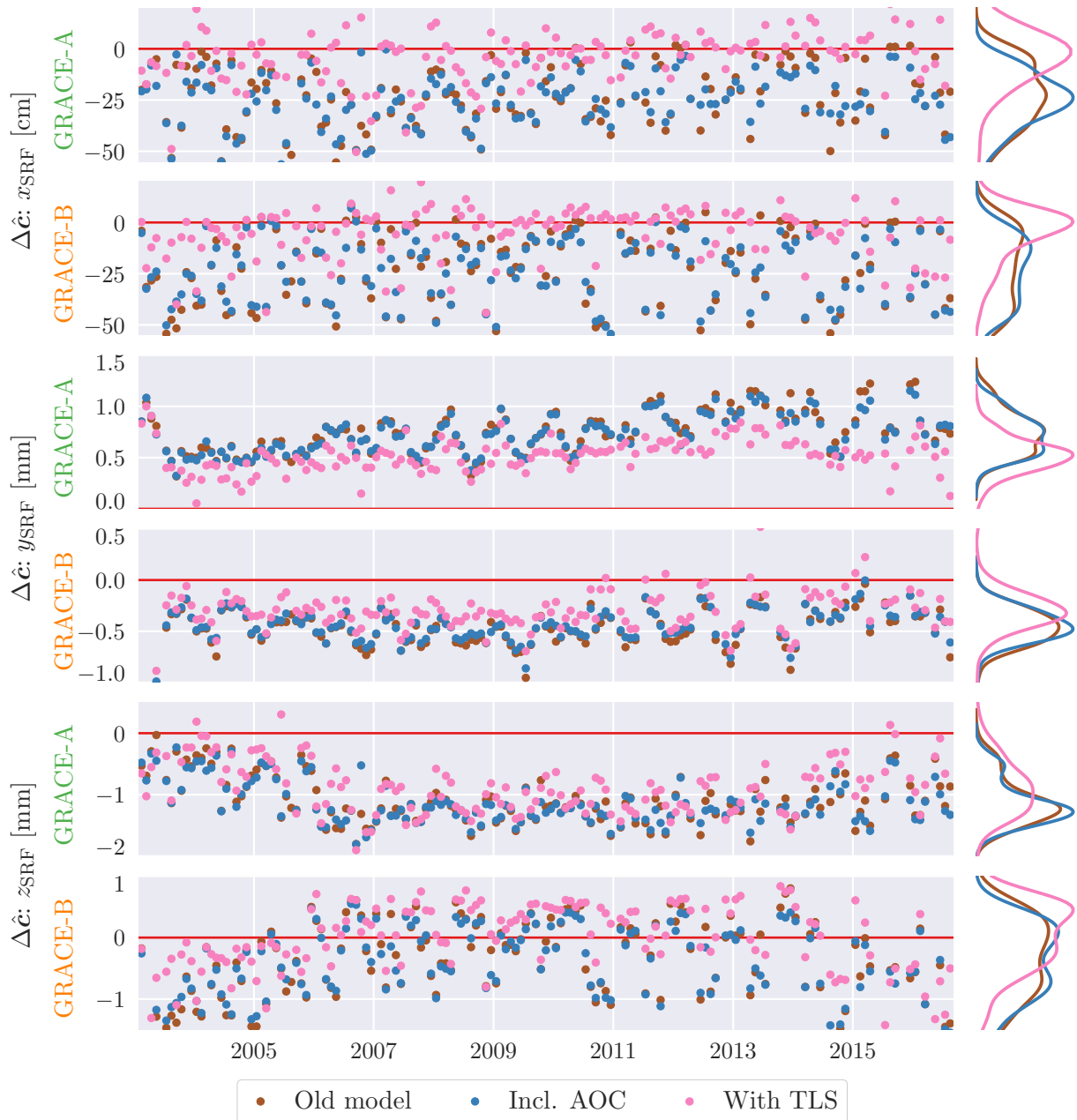
Figure 9.6: Monthly estimates for the KBR APC vectors for the old model (brown), when using AOC covariance matrices (blue), and for the TLS estimate (pink), given in the SRF. The red $\Delta\hat{c} = 0$ line indicates no deviation from the a priori calibrated APCs. The right margin shows a scaled kernel density estimate for the distribution of the coordinate estimates. Note that the plot scales are identical for the same coordinates on GRACE-A and GRACE-B, but differ between the x, y, and z-coordinates.
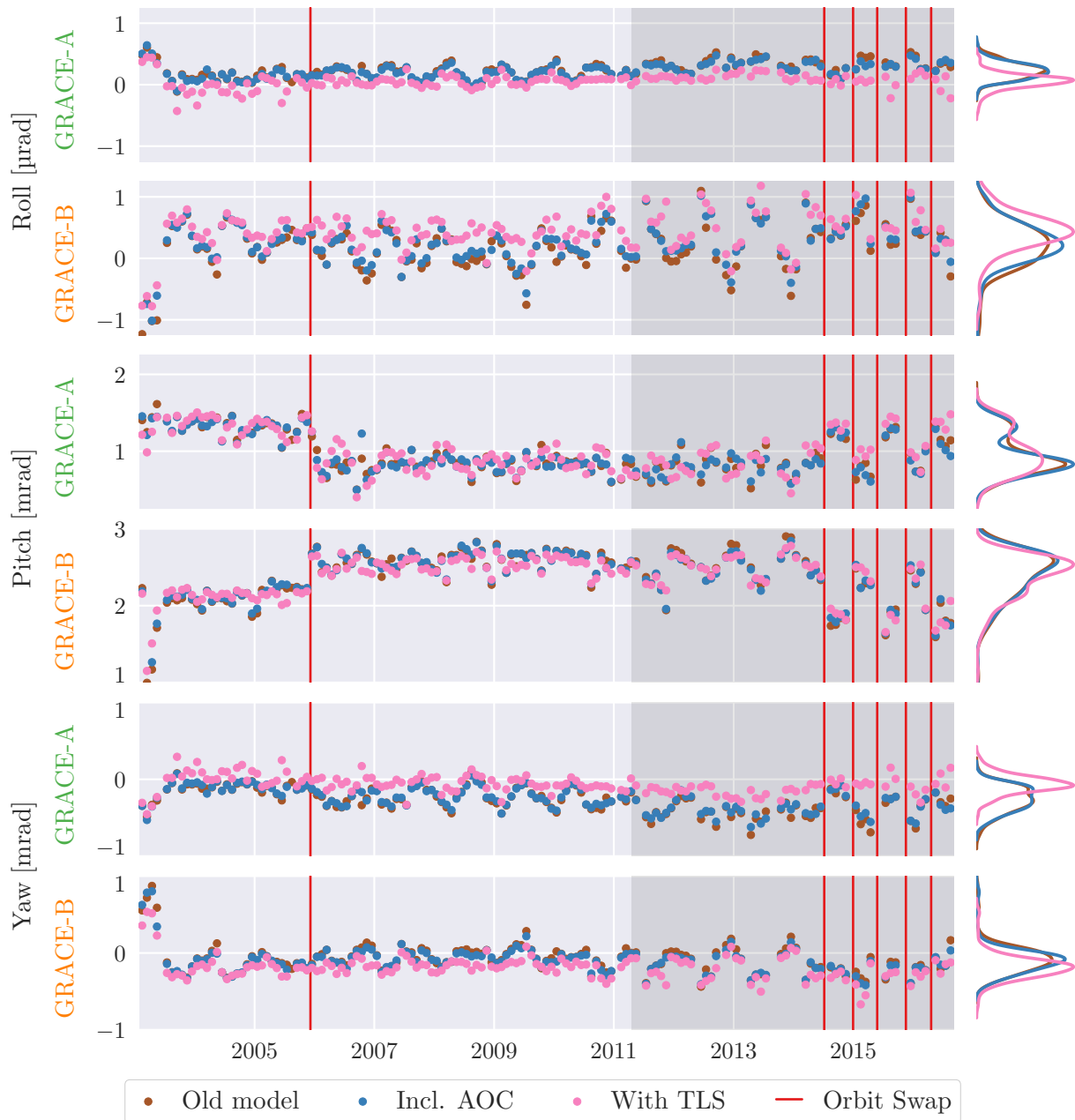
Figure 9.7: Monthly estimates for the KF to SRF misalignment expressed in Euler angles. Results given for the old model (brown), when using AOC covariance matrices (blue), and for the TLS estimate (pink). The vertical red lines indicate orbit swap manoeuvres. The shaded area indicates the time period of reduced thermal management. The right margin shows a scaled kernel density estimate for the distribution of the estimated Euler angles. Note that the scales are identical for the same angles on GRACE-A and GRACE-B, but differ between the roll, pitch, and yaw-angles.

Figure 9.7 shows the Euler angles computed from the estimates $\hat{c}_A$ and $\hat{c}_B$ for the studied period. In this representation, some characteristics of the estimated APCs appear much clearer than in the Cartesian representation of fig. 9.6. The stabilizing effect of the TLS estimate can clearly be observed, especially in the roll and yaw angles for GRACE-A, and to a lesser extent in the same angles for GRACE-B. Compared to later data, the first months of 2003 show a noticeably more unstable estimate of the APC vectors. An attempt was made to correlate the large jumps in June 2003 with important events, such as COM or KBR calibration manoeuvres, but this was not successful. The jump could possibly be simply due to the inferior data quality at the beginning of the mission lifetime.

The estimated pitch angle misalignments for both spacecraft show a striking symmetry, with the misalignment angle for GRACE-A decreasing when that for GRACE-B increases, and vice versa. Comparison with important events in the GRACE mission lifetime reveals that the large jumps in the estimated pitch angle misalignment occur at the same times as orbit swaps of the satellites. This strongly indicates that this effect depends on a systematic effect in the GRACE attitude determination, and not on a geophysical effect aliasing into the estimate. It also partly confirms previous results by Horwath et al., 2011, where a similar jump was observed in estimated daily pitch and yaw misalignment biases at the 2005 satellite swap manoeuvre. Horwath et al. however do not observe the mirrored behaviour in the pitch jump, rather both pitch angles decrease in their estimate. Further, the yaw angle misalignment has a much larger magnitude for Horwath et al., on the order of 2 mrad. In the presented solution the estimate is, in first approximation, median-free. Where Horwath et al., 2011 did not make a statement on the temporal variability of the misalignment angles, apart from the jump at the December 2005 satellite swap, the longer time series estimated here allows for the identification of such behaviour.

In general, the periodicity in the roll and yaw estimates are much more easily identifiable in this representation, as opposed to the Cartesian plot in fig. 9.6. Spectral analysis revealed that the largest amplitude is found at one cycle per 322 d, which corresponds to one full revolution of the longitude of the ascending node for the GRACE orbital plane. The observed period indicates an influence of the orientation of the spacecraft in inertial space on the APC estimate. The most obvious explanation would be an effect on the satellites due to the changing angles of incidence of solar radiation. This would also explain the jumps in the pitch angle at orbit swap manoeuvres, when the satellites quickly rotate by 180° in their orbit. The effect of such a rotation on the inertial orientation is the same as that of a rotation of the orbital plane by 180°. Other sources, like an origin in e.g. the field of view of the star camera assembly or the miscalibrated release 2.0 SCA1B data can however not be discounted outright.

Due to the dependency on the leader-follower configuration, the pitch misalignment estimates for both GRACE-A and GRACE-B show a bimodal distribution. Both other misalignment angles are unimodally distributed. The spread of the TLS estimates of the misalignment angles over the time series is either comparable to or smaller than that of the other two approaches. Interestingly, the reduction of active thermal

management in 2011 does not seem to have a strong impact on most of the estimated misalignment angles, with the exception being the roll angle on GRACE-B.

9.3.5 Gravity Field Solutions

This section presents the final full degree and order gravity field solutions first computed using the original ITSG-Grace2016 stochastic model, then incorporating AOC covariance matrices, and finally using the TLS approach.

Degree Amplitudes

Figure 9.8 shows degree amplitude graphs for two representative months. In a month of good data, shown in fig. 9.8a, the solution computed using the non-stationary AOC covariance matrices (blue) is almost identical to the standard old solution (brown). The TLS solution (pink) shows slightly lower amplitudes above degree and order ≈50. The magnitude of the improvement (dotted pink) is on the order of the expected GRACE baseline accuracy.

The improvement is much more pronounced for June 2010, shown in fig. 9.8b, where data quality is deteriorated due to larger than normal opening angles. Here, both of the new solutions differ from the old model by more than the GRACE baseline accuracy. Especially the TLS solution (pink) shows much smaller amplitudes at very high degrees, where noise is expected to dominate the recovered signal.

In general, the TLS solution shows larger differences than the solution using the AOC covariances only. This also holds for the months not pictured here.

Spatial Domain

Figures 9.9 and 9.10 show equivalent water height maps for the same two example months of good and deteriorated data quality. The reference mean field and long-term signals — both from the GOCO05s model — were removed from the monthly solutions. A 300 km Gaussian filter was applied to the datasets. The isotropic Gaussian filter was chosen instead of one of the more advanced non-isotropic filters (see e.g. Kusche, 2007; Swenson and Wahr, 2006) to retain information on the change of the potential in north-south direction. For similar reasoning, a conservatively small filter radius was selected, which allows for the retention of some high-frequency patterns in the signal after smoothing.

For both shown months, the major spatial features of the monthly gravity variations are recovered in all three configurations (top and left columns). For the month of good data, the differences between the old stochastic model and the model including AOC covariance matrices, shown in fig. 9.9c, is small and mostly globally homogeneous. Figure 9.9e shows the differences of the TLS solution w.r.t. the old stochastic model,
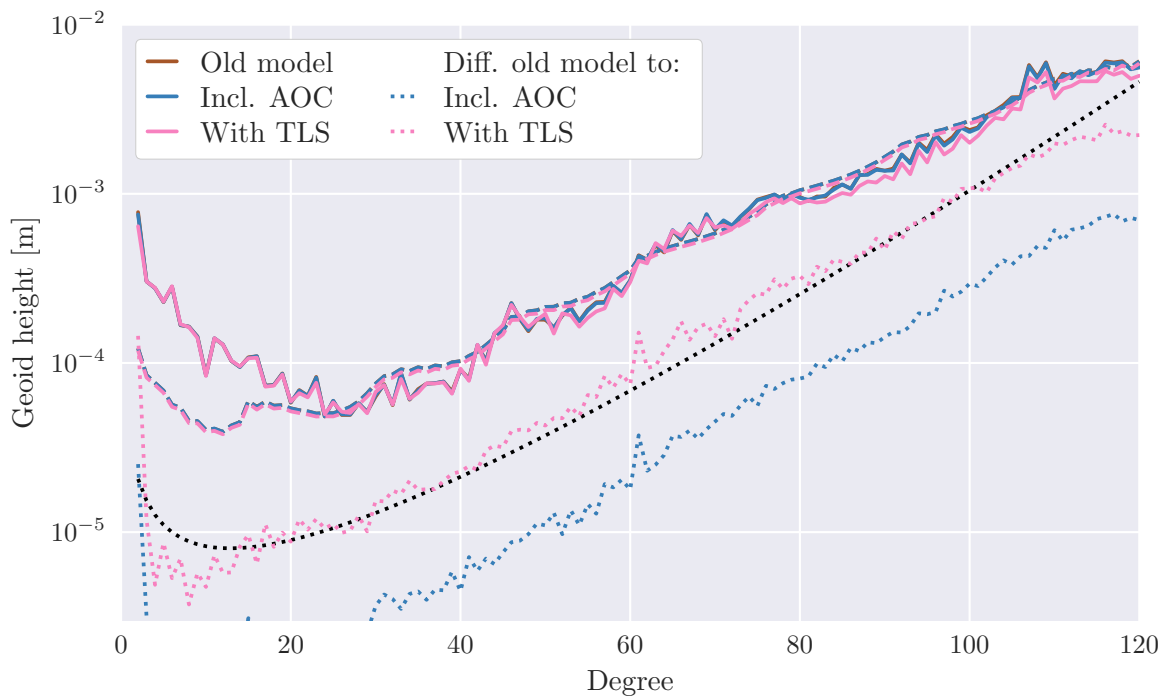
(a) Degree amplitudes for April 2008 (good data).
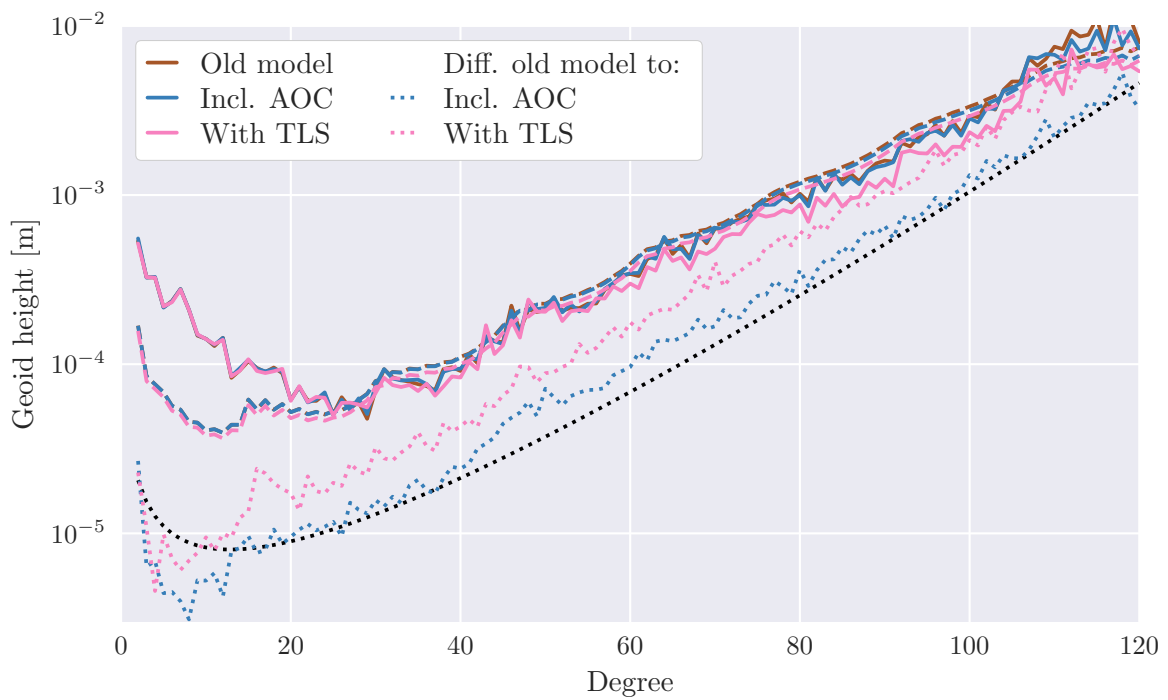
(b) Degree amplitudes for June 2010 (bad data).

Figure 9.8: Degree amplitudes in geoid height using the old stochastic model (in brown), when taking AOC covariances into account (in blue), and for the TLS solution (in pink). (a) shows a month of good data quality. (b) shows a month of deteriorated quality due to larger than usual opening angles.

(a) Old stochastic model.

(b) Using AOC covariance.

(c) Difference AOC covariance - old model.

(d) TLS solution.

(e) Difference TLS solution - old model.

Equivalent water height [cm] (a,b,d)

Equivalent water height [cm] (c,e)
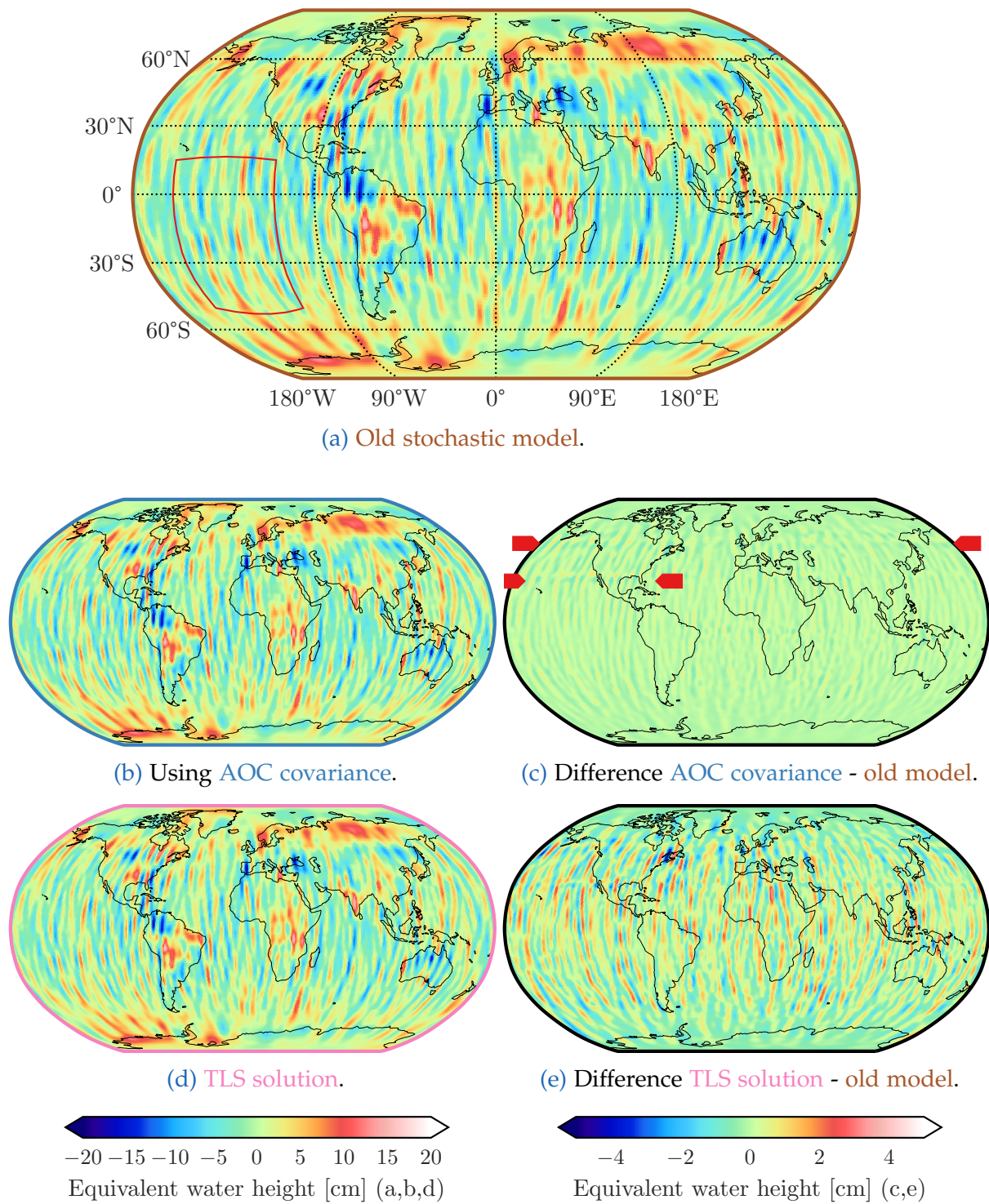
Figure 9.9: Equivalent water height maps for April 2008, a month of good data. The top and left column shows the monthly gravity field variations for the three computed solutions. The right column shows the difference of the improved solutions w.r.t. the reference solution. A 300 km Gaussian filter was applied to the data. Note the different scale for (c), (e).

(a) Old stochastic model.

(b) Using AOC covariance.

(c) Difference AOC covariance - old model.

(d) TLS solution.

(e) Difference TLS solution - old model.

Equivalent water height [cm] (a,b,d)

Equivalent water height [cm] (c,e)
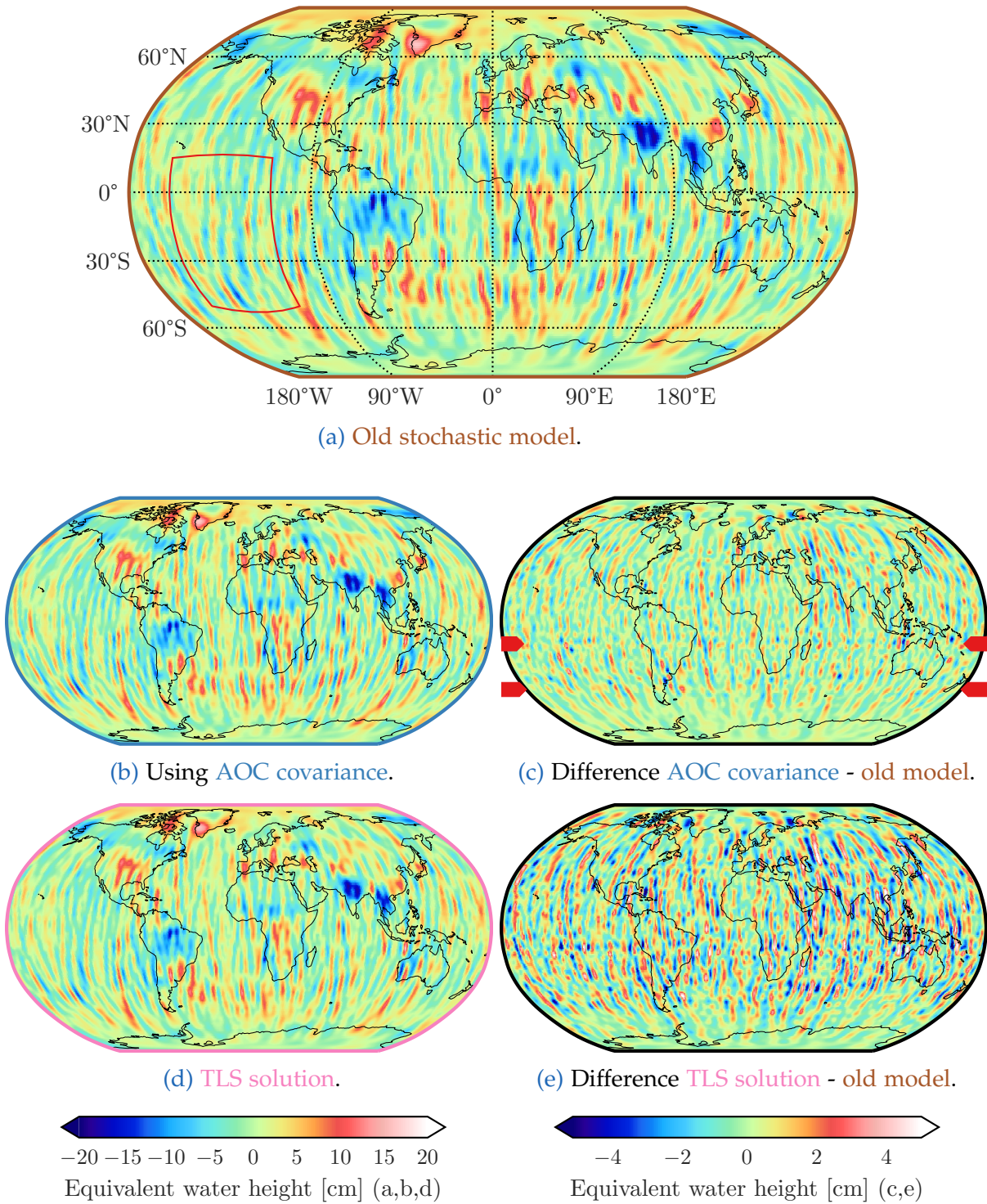
Figure 9.10: Equivalent water height maps for June 2010, a month of deteriorated data. The top and left column shows the monthly gravity field variations for the three computed solutions. The right column shows the difference of the improved solutions w.r.t. the reference solution. A 300 km Gaussian filter was applied to the solutions. Note the different scale for (c), (e).

which is similarly homogeneous, but larger in magnitude. It could be argued that in both figs. 9.9c and 9.9e some systematic differences (compare red markers) can be seen at ≈50 °N and at ≈30 °N, here especially in Mexico and off the west coast of North America. This signal on its own is however not strong enough to draw any definitive conclusion from it.

For June 2010, the month of deteriorated quality due to larger opening angles, the differences are in general larger and more spatially distinct. Especially at southern mid-latitudes, two bands of increased differences can be seen in both figs. 9.10c and 9.10e, representing the differences due to the AOC covariance matrices and TLS respectively (compare red markers). The latitudes of these bands correspond roughly to the latitudes of the northern bands observed in figs. 9.9c and 9.9e. These northern bands are not as distinct for June 2010, but they are still present.

Table 9.3 gives the average EWH RMS for these two monthly solutions, for all three processing strategies and for different geographical areas. The RMS is evaluated globally and separately over the continents and oceans. Using perfect background models and flawless processing, the RMS over the oceans would be expected to be close to zero, as no time-variable signal should remain in this area. Over the continents however, the signal of the hydrological cycle and the other processes described in chapter 3 should remain visible in the results. To further isolate the ocean signal from possible interference from continental signals, a separate remote area in the south Pacific was analysed. This is the area marked in red in figs. 9.9a and 9.10a.

Table 9.3: Global and geographically restricted RMS of recovered equivalent water heights for April 2008, a month of good data; and June 2010, a month of deteriorated data. A 300 km Gaussian filter was applied to the data.

Period / Area	Old model [cm]	Incl. AOC [cm]	With TLS [cm]
April 2008			
Global	3.81	3.81	3.72
Continents	4.60	4.60	4.55
Ocean	3.44	3.43	3.33
Pacific patch	3.43	3.41	3.19
June 2010			
Global	3.95	3.97	3.76
Continents	4.79	4.82	4.66
Ocean	3.55	3.57	3.33
Pacific patch	3.22	3.27	2.97

Table 9.3 shows that for all areas, the RMS of the solution using AOC covariance matrices is not much smaller than that of the solution computed using the old stochastic model. For June 2010, it is even larger in all areas, though within a margin that is difficult to attach a qualitative meaning to. The TLS solution shows reduced RMSs for all study areas in both months. Here, the RMS reduction over the continents is smaller than that over the ocean, and it is largest for the pacific patch area. This supports the conclusion that the TLS solution reduces orientation-induced noise in the solution without overly damping the magnitude of the recovered signal.

Temporal Domain

The time series of computed monthly solutions is also analysed in the temporal domain. Some months of reduced data quality were excluded from this analysis. The inclusion of these outliers strongly skewed the results and prohibited meaningful interpretation of the created time series and statistics. Specifically, the excluded months were 2004-01, 2004-09, 2012-04, 2012-06, 2015-01, and 2015-02 due to repeat or near-repeat orbit geometry; as well as 2017-03 and 2017-06 due to unavailability of ACC observations for GRACE-B and the subsequent use of "transplanted" ACC observations from GRACE-A.

Temporal variability - spatial domain   Figure 9.11 shows the temporal variability of the three computed time series. The variability was computed as the RMS for each point on a $1° \times 1°$ geographical grid, once for each complete time series. Only the inter-monthly variability was considered. Annual, semi-annual, and secular signals were removed prior to computation of the variability. A 300 km Gaussian filter was applied. Figure 9.11e shows that the variability in the TLS solution is clearly reduced in distinct bands in the northern and southern mid-latitudes, and around the equator. The reduction in variability is larger over the oceans than over land. For the solution using the AOC covariance matrices, the reduction has a mean of 0.015 cm over land and 0.020 cm over the ocean. For the TLS solution, the reduction is 0.111 cm and 0.165 cm over land and the ocean, respectively. In opposition to the overall trend of a reduction in variability, some areas of large signals, especially the Amazon basin and southern Africa, show a slight increase in variability.

Overall, the magnitude of the reduction in variability is not very large. It is encouraging that variability over land is reduced by a smaller factor than over the ocean. This supports the theory that correct handling of the non-stationary errors due to the satellite pointing leads to a better recovery of the sought signal, while noise in the recovered solution is damped. The reduction is larger for the TLS case than for the AOC covariance only case. As a larger number of parameters is estimated, it is reasonable to expect less noise remaining in the solution. What cannot be seen in fig. 9.11e is a systematic damping of temporal variability where large hydrological signals are expected, which is encouraging.

(a) Old stochastic model.

(b) Using AOC covariance.　　(c) Difference AOC covariance - old model.

(d) TLS solution.　　(e) Difference TLS solution - old model.

Equivalent water height [cm] (a,b,d)　　Equivalent water height [cm] (c,e)
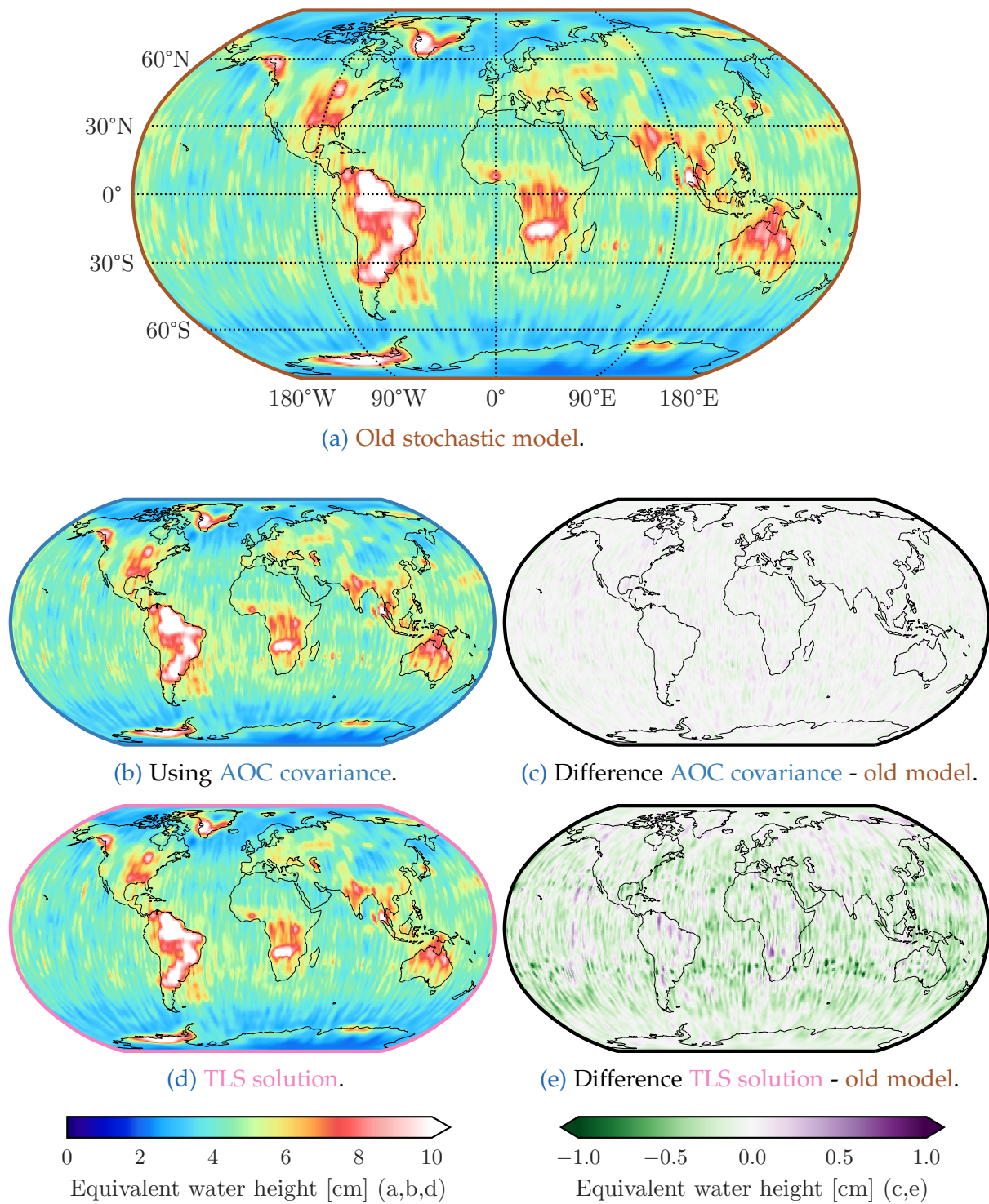
Figure 9.11: Global temporal variability of monthly gravity field solutions in equivalent water height. The top and left column shows the variability of the computed solution as the RMS over the time series. The right column shows the difference of the variability of the improved solutions w.r.t. the reference solution. A 300 km Gaussian filter was applied to all solutions.

Time series of RMS ratios   Table 9.3 presented the RMSs of several geographically restricted areas for two selected months. The same RMSs were also computed for the remaining months of the time series, again using a 300 km Gaussian filter. Then, for both of the improved solutions, a ratio was formed between the RMSs of the improved solutions (blue and pink) and the RMS of the reference solution (old stochastic model, brown). These ratios are displayed in fig. 9.12.

The ratio is displayed instead of absolute RMS values for two main reasons: Due to a variety of factors such as observation geometry and gaps in the underlying data, the magnitude of the RMS for one area can vary considerably from month to month. This makes inter-monthly comparisons of absolute differences difficult to interpret, as these in turn also vary from month to month. Further, the differences in EWH RMS between the solutions are small compared to their magnitude, which makes them disappear at these larger scales.

When considering the ratios, a value of less than 100 % indicates that the RMS of the reprocessed solution is smaller than that of the reference solution. The value for the solution computed using the old model is always 100 %, as this is the reference solution. Figure 9.12 shows that for all areas, the RMS of the solution including AOC covariance matrices (blue) is of comparable magnitude as that of the reference solution. Within the scatter of the time series, neither a clear increase nor a distinct decrease of the RMS can be observed. This does not hold for the time series of TLS solutions (pink), where the ratio is below 100 % for almost all months. The mean of the RMS reduction for the TLS series is 3.3 % globally, 2.3 % over land, 4.1 % over the oceans, and 5.1 % for the pacific patch. This confirms that for the TLS solution the reduction in RMS is higher in areas where noise is expected to be a larger factor of the recovered gravity field, and smaller where signal is expected to be larger.

For the solution using AOC covariances only (blue), the mean reductions in RMS are 0.36 % globally, 0.25 % over land, 0.44 % over the oceans, and 0.46 % for the pacific patch. Although the patterns in the magnitude of the reductions match those of the TLS solution, the means are small in relation to the scatter of the time series, and caution should be applied when drawing qualitative conclusions from this data.

Temporal variability - spectral domain   Where observing the temporal variability in the spatial domain allows for insights into the geographical localisation of specific features, the required filtering hides a lot of the variability at small spatial scales. To give a fuller impression of the characteristics of the computed solutions at these scales, the temporal RMS for each solution was also computed in the spectral domain, once for each Stokes coefficient. For the improved solutions, a ratio was again formed with the reference solution using the old stochastic model. Values below 100 % again indicate a RMS reduction. These results are shown in fig. 9.13.

The ratio for the solution using AOC covariance matrices is shown in fig. 9.13c. The most striking feature here is a reduction of the variability in the zonal and near-zonal coefficients above roughly degree 40. Correspondingly, a small increase in variability
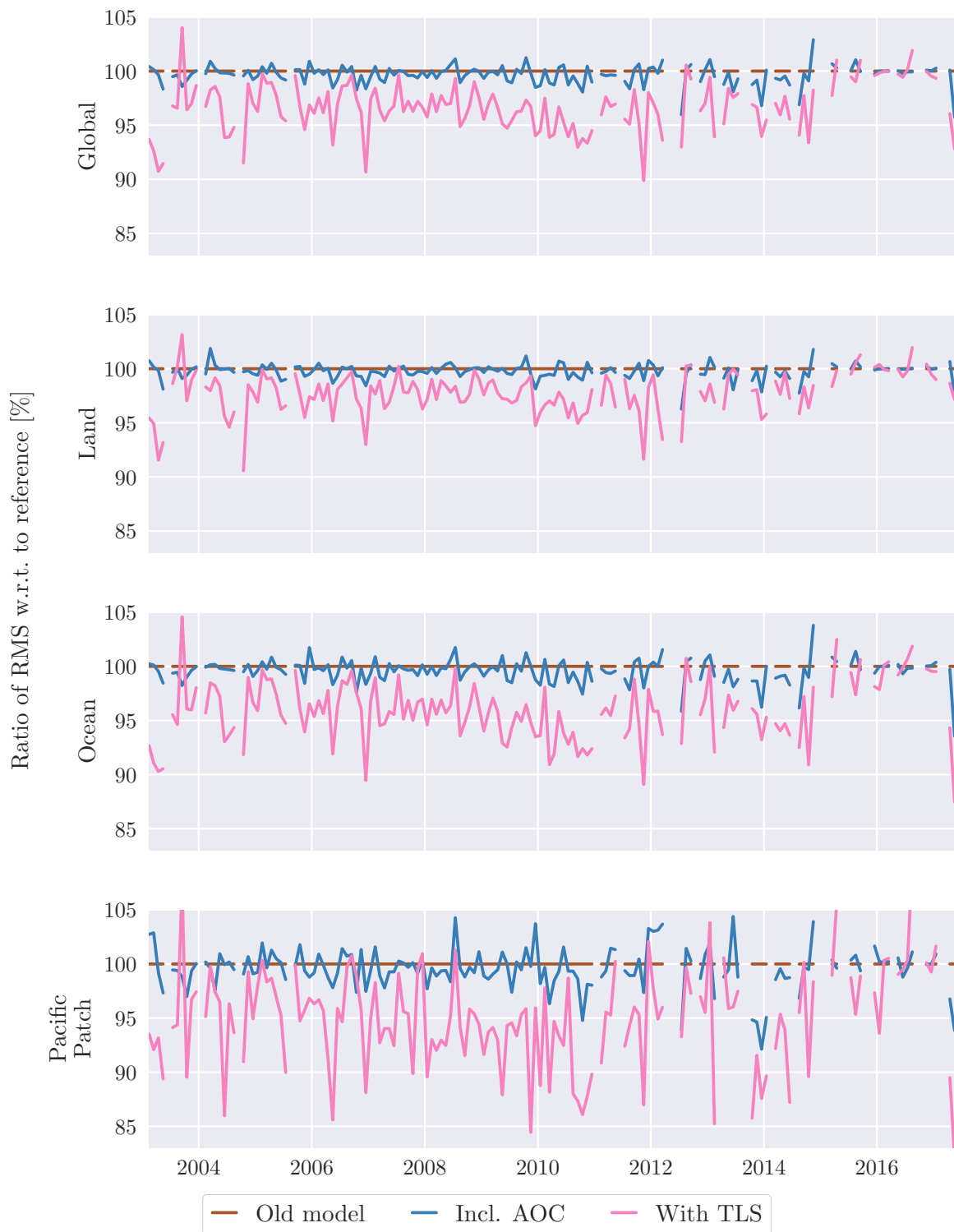
Figure 9.12: Time series of ratios of geographically restricted root mean squares of each solution w.r.t. the reference solution using the old stochastic model (brown). Prior to computation of the RMSs, a 300 km Gaussian filter was applied to the solutions.

can be observed at the first orbital resonant frequency of approximately order 16. For higher degrees, a reduction in variability can also be observed for tesseral coefficients.

The ratio for the TLS solution, displayed in fig. 9.13e, shows similar features, but with a larger magnitude. The reduction in variability in the zonal and high-order tesseral Stokes coefficients is again present. In contrast to the ratios for the solution using AOC covariance matrices only, there does not appear to be an increase in variability at the first orbital resonant frequency. For medium orders, a decrease in variability can be observed between multiples of the resonant frequency, while Stokes coefficients at the resonant frequencies themselves show relatively little change. Higher degree non-zonal Stokes coefficients of all orders decrease in variability at a similar magnitude, with no obvious correlation to the resonant frequencies.

It is expected that the variability should remain relatively unchanged at degrees below approximately 30, as strong temporal signals are expected at these scales. In general, this is the case for both solutions. The TLS solution however shows a strong reduction in variability for the zonal Stokes coefficients of degrees 17 to 20 (see inset in fig. 9.13e). Because of the sharp jump of variability and the strict limitation to zonal Stokes coefficients, a geophysical origin of this signal can be ruled out. A back-of-the-envelope calculation gives the temporal frequency that these Stokes coefficients correspond to for the GRACE spacecraft on their polar orbits. For a revolution period of $T_{\text{rev}} \approx 89\,\text{min}$, the lower bound of the affected frequency spectrum, where the reduction in variability is smaller ($c_{17,0}$), is $1/(T_{\text{rev}}/17) \approx 3.2\,\text{mHz}$. The corresponding frequency for the upper bound, formed by the degree 20 zonal Stokes coefficient is $1/(T_{\text{rev}}/20) \approx 3.7\,\text{mHz}$. This band encompasses, again, the dominant frequency in the pitch angle variations of the GRACE spacecrafts, $3.3\,\text{mHz}$ (Bandikova, Flury, and Ko, 2012), which was previously encountered in section 8.3.3. This leads to the conclusion that the TLS estimate reduces noise in these Stokes coefficients, and that this noise originated in GRACE pointing variations at the appropriate frequencies.

Figure 9.13e shows a sharp decrease in temporal variability for the TLS solution between near-zonal Stokes coefficients of degree 60 and 61. A geophysical source for this pattern is unlikely. Instead, the chosen processing strategy is the most likely origin for this artefact. The estimation of the stochastic model and the satellite orientation was only performed while co-estimating a gravity field up to D/O 60. The resulting orientations were used together with the stochastic model to compute a full D/O 120 field. As no such jump exists in the solution considering AOC covariances only (fig. 9.13c), it stands to reason that this approach is not suitable in the process of TLS orientation estimation. Rather, the iterative co-estimation of the orientation should be performed with a full D/O 120 gravity field.

9.4 Discussion

This chapter described the application of the total least squares approach of least squares adjustment to the combined estimation of GRACE-derived gravity fields and
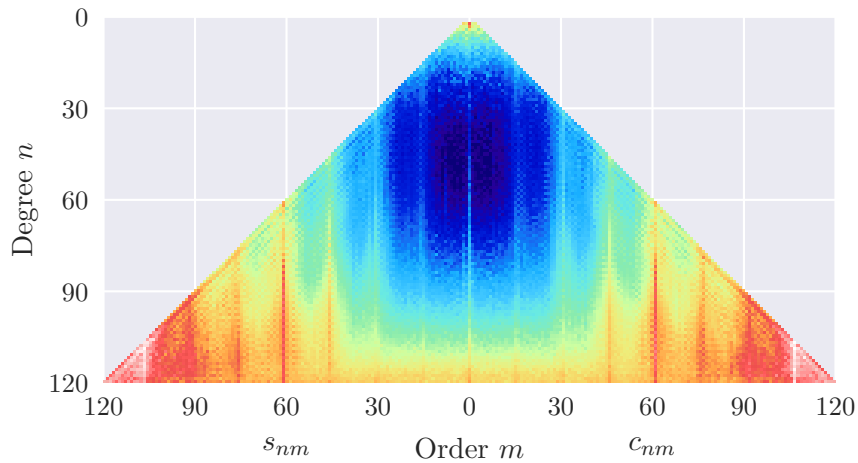
(a) Old stochastic model.
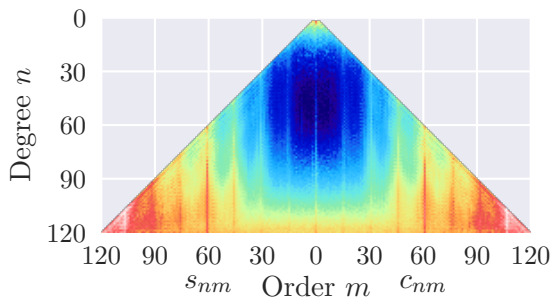
(b) Using AOC covariance.
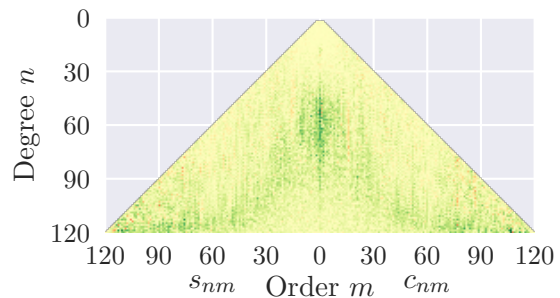
(c) Ratio of AOC covariance / old model.
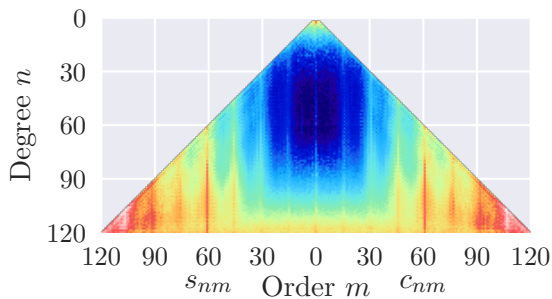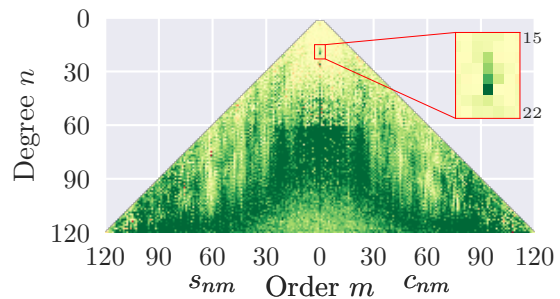
(d) TLS solution.

(e) Ratio of TLS solution / old model.

Figure 9.13: (a), (b) and (d) show the temporal variability of the computed monthly gravity field solutions as RMS over the time series in the spectral domain. (c) and (e) show the ratio of the RMS of the respective improved solution and the reference solution for each Stokes coefficient. No filter was applied to the solutions.

improved satellite orientations. Importantly, it was shown that the TLS approach described by Reinking, 2008 is equivalent to the widely used practice of parameter elimination in a classical Gauß-Markov model, given correct linearisation at every iteration step and uncorrelated observation groups.

The estimation of the satellite orientations was integrated into the processing strategy at the same stage where the stochastic model for GRACE SST observations is determined. In this context, the full SCA/ACC sensor fusion and AOC covariance matrices derived in chapter 8 formed important building blocks. Without these prerequisites, using ll-SST observations in the determination of the improved orientations would not be possible.

The estimated stochastic model was not strongly affected by use of the TLS algorithm. The estimated orientations are plausible, and the variations in orientation estimated by the algorithm follow the constraints introduced through the a priori covariance information. Over the complete analysed time span, the estimates differ more from the orientation provided through SCA/ACC sensor fusion for periods where only one SCA head is active on the respective spacecraft.

One major result is the improvement in the estimate of the antenna phase centre vectors through this approach. Where the estimate contained a large bias in the previous scenarios, using the TLS algorithm almost completely eliminates the bias. A large standard deviation remains, however. Crucially, this standard deviation is larger than that obtained through the formal errors of the least squares adjustment. This leads to the conclusion that further investigation is needed to either locate and model the remaining factors leading to this biased estimate, or to conclusively show the limits of co-estimation of the GRACE APC vectors in normal science operations. One promising avenue could be to follow the approach laid out by Horwath et al., 2011 and only estimate the deviations of the pitch and yaw components of the APC. The length of the APC vector would then be held constant at the value obtained from dedicated in-orbit KBR calibration manoeuvres. This approach could be combined with the TLS orientation estimate, which was shown to provide a more stable estimate of exactly these two angles.

At the level of monthly gravity field solutions, the TLS estimate showed improvements especially for months containing non-nominal observations, such as periods of increased opening angles due to operational constraints on the GRACE satellites. The influence of the TLS estimate can be studied most clearly not at the level of individual monthly solutions, but when analysing their temporal variability. In the spatial domain, the variability is decreased more over the oceans than over land, which in first approximation indicates a reduction of noise, and not a damping of signal. Analysis in the spectral domain clearly showed that the variability of the Stokes coefficients corresponding to the GRACE pitch angle variations in geographical extent and frequency were amongst those most improved. However, some clear processing artefacts were visible for Stokes coefficients of degrees higher than 60, indicating that there is a need to further refine the processing chain incorporating a TLS estimate of the satellite orientations.

Conclusion and Outlook 10

The presented research, building on the foundation of the state of the art GRACE level 1B to level 2 data pipeline at IfG, furthers diverse aspects of GRACE data processing. The improved stochastic model described in chapter 8 and the treatment of uncertainties in independent variables outlined in chapter 9 can bring immediate observable improvements to the processing of GRACE data. This is not the case for the first presented topic, the optimization of the dynamic orbit integration (chapter 7).

The previously existing implementation of dynamic orbit integration is of sufficient fidelity for traditional GRACE processing. This was proven by variance propagation of an error estimate for the dynamic orbits to the range-rate domain, and comparison with GRACE ll-SST noise models. The same investigation showed that the stability of the classical approach could prove insufficient for GRACE-FO processing, where the new laser ranging interferometer is expected to provide higher-precision observations of the inter-satellite separation. To ameliorate this deficiency, an improved dynamic orbit integration algorithm based on a modified Encke method using a rigorously optimized reference trajectory parametrised in equinoctial elements was introduced. Using this parametrisation, the stability of the integration is expected to be sufficient for GRACE-FO processing. This implementation was already used in the ITSG-Grace2016 series of gravity field solutions. It is also expected to be used for the upcoming ITSG-Grace2018 solutions. At the time of writing, GRACE-FO was successfully launched, and initial data from the early operations phase showed the satellite instrumentation to work as expected. Should GRACE-FO LRI data become available towards the end of 2018, the results presented in chapter 7 will be able to be verified using real data.

The description and rigorous evaluation of the effect of the spacecraft orientation uncertainty on the ll-SST antenna offset correction, outlined in chapter 8, has improved understanding of the error spectrum of real GRACE observations. The derived stochastic model for the AOC explains spurious power observed in the estimated monthly KBR PSDs, located in the frequency band associated with inter-satellite pointing variations. This power was shown to be the result of aliasing of the unmodelled non-stationary noise of the AOC into the estimated monthly stationary PSD. Disentanglement of these noise sources allows for the decorrelation of all observations in the month with a more appropriate PSD, unaffected by transient noise in only parts of the observations. Further, the variance factors used to weigh individual observation arcs were strongly correlated with the inter-satellite opening angle. Arcs with higher opening angles were consistently downweighted. This is of course desired behaviour, as the observations in these arcs are affected by higher noise. Describing the variations of the ll-SST uncertainty on an epoch-by-epoch basis is however highly preferable, as it allows for a more

granular weighting of observations, not necessarily downweighing parts of one arc because anomalous data was detected at other times during the same arc.

Even though the method of deriving AOC covariance matrices from the results of an in-house SCA/ACC sensor fusion was proven to be helpful in the analysis of GRACE data, its applicability to e.g. the ITSG-Grace2018 release is uncertain. The ITSG-Grace2018 series of gravity field solutions will be based on the release 3.0 dataset of GRACE level 1B data provided by JPL. The SCA1B product of the release 3.0 data will contain satellite orientations derived from a SCA/ACC sensor fusion computed at JPL (GRACE, 2018). The fusion computed at JPL will be based on a Kalman filter approach, and full covariance matrices will not be available to the processing community. This prohibits the computation of a meaningful SCA/ACC sensor fusion at IfG, as the necessary raw data is no longer available in unprocessed form. It could be possible to compute an approximate orientation covariance matrix using available data and use this information to derive the AOC covariance matrices. This approach has not yet been studied in detail. For GRACE-FO, full level 1A data is expected to be released (Wen et al., 2018). This will again allow for the determination of the spacecraft orientation through sensor fusion, but now based on directly employing level 1A data. The resulting covariance matrices can then be used in the determination of AOC covariance matrices for GRACE-FO.

Building on the full arc-wise information of the orientation uncertainty, the satellite orientation was co-estimated in the least squares adjustment for the Stokes coefficients. In previous solutions up to ITSG-Grace2016, the orientations of the spacecraft were assumed fixed and error-free, which is clearly not true. The equivalence of two formalisms for the treatment of uncertainties in independent variables was proven, namely the TLS algorithm as formulated by Reinking, 2008 and a formulation based on classical parameter elimination. Employing this apparatus, co-estimation of spacecraft orientations led to a more stable estimate of the KBR antenna phase centres, especially improving on the previously strongly biased length estimate. The main impact of the changed parametrisation on the recovered gravity field solutions was a reduction in temporal variability over the ocean. This can reasonably be interpreted to correspond to a reduction in noise. In the spectral domain, the reduction in variability was especially prominent for some Stokes coefficients whose spatial patterns correspond to the dominant pitch-motion of the GRACE satellites. Spectral analysis shows an abrupt drop in temporal variability at spherical harmonics of order 61. This is cause for caution, as it implies that the chosen processing strategy — co-determination of the stochastic model and initial approximation of the satellite orientations in an adjustment up to D/O 60, followed by a full adjustment up to D/O 120 — is the cause of these processing artefacts. Further studies are needed to investigate this effect, preferably recomputing the stochastic model and orientations together with a full D/O 120 solution. The conclusions drawn in the spatial domain should however remain largely unaffected by this artefact, as the 300 km Gauss filter applied to the solutions prior to analysis has a cut-off far below the D/O 60 threshold.

As the TLS algorithm depends on somewhat accurate covariance information, this approach will not be used in the ITSG-Grace2018 gravity field solutions, due to the

reasons mentioned above. Further, the release 3.0 SCA1B data product will include improvements in the provided satellite orientations. Particularly, several errors previously present in the orientation determination chain were found and fixed in this release (GRACE, 2018). It remains to be investigated whether these large improvements to the SCA1B data can make a co-estimation of the satellite orientation unnecessary. As the fundamental data needed to form the orientation covariance matrices will again be available for GRACE-FO, the orientation co-estimation could be applied for this mission.

List of Abbreviations

Bibliography

Amiri-Simkooei, Alireza and Shahram Jazaeri (2012). "Weighted Total Least Squares Formulated by Standard Least Squares Theory." In: *Journal of Geodetic Science* 2.2. DOI: 10.2478/v10156-011-0036-5 (cit. on p. 119).

Anderson, E., ed. (1999). *LAPACK Users' Guide*. 3rd ed. Software, environments, tools. Philadelphia: Society for Industrial and Applied Mathematics. 407 pp. ISBN: 978-0-89871-447-0 (cit. on p. 41).

Bailey, David and Jonathan Borwein (2015). "High-Precision Arithmetic in Mathematical Physics." In: *Mathematics* 3.2, pp. 337–367. DOI: 10.3390/math3020337 (cit. on p. 86).

Bandikova, Tamara (2015). "The Role of Attitude Determination for Inter-Satellite Ranging." OCLC: 955489510 ISBN: 978-3-7696-5170-6. Dissertation. Hannover: Gottfried Wilhelm Leibniz Universität. 153 pp. (cit. on p. 111).

Bandikova, Tamara, Jakob Flury, and Ung-Dai Ko (2012). "Characteristics and Accuracies of the GRACE Inter-Satellite Pointing." In: *Advances in Space Research* 50.1, pp. 123–135. DOI: 10.1016/j.asr.2012.03.011 (cit. on p. 150).

Bernstein, Dennis S. (2009). *Matrix Mathematics: Theory, Facts, and Formulas*. 2nd ed. OCLC: ocn243960539. Princeton, N.J: Princeton University Press. 1139 pp. ISBN: 978-0-691-13287-7 978-0-691-14039-1 (cit. on p. 125).

Berry, Matthew M. and Liam M. Healy (2004). "Implementation of Gauss-Jackson Integration for Orbit Propagation." In: *The Journal of the Astronautical Sciences* 52.3, pp. 331–357. URL: http://hdl.handle.net/1903/2202 (visited on 2017-01-26) (cit. on p. 33).

Bettadpur, Srinivas V. (2012). *GRACE Product Specification Document*. URL: ftp://podaac.jpl.nasa.gov/allData/grace/docs/ProdSpecDoc_v4.6.pdf (visited on 2018-07-03) (cit. on pp. 23, 24).

Beutler, Gerhard and Leos Mervart (2010). *Methods of Celestial Mechanics. Vol. 1: Physical, Mathematical, and Numerical Principles*. OCLC: 838311365. Berlin: Springer. 464 pp. ISBN: 978-3-540-26870-3 (cit. on pp. 29, 33).

Björck, Åke (1996). *Numerical Methods for Least Squares Problems*. Society for Industrial and Applied Mathematics. DOI: 10.1137/1.9781611971484 (cit. on p. 8).

Blackford, L. Susan et al. (2002). "An Updated Set of Basic Linear Algebra Subprograms (BLAS)." In: *ACM Transactions on Mathematical Software* 28.2, pp. 135–151. DOI: 10.1145/567806.567807 (cit. on p. 41).

Bond, William Cranch (1849). "Encke's Comet." In: *Monthly Notices of the Royal Astronomical Society* 9.5, pp. 106–107. DOI: 10.1093/mnras/9.5.106 (cit. on p. 81).

Broucke, R. A. and P. J. Cefola (1972). "On the Equinoctial Orbit Elements." In: *Celestial mechanics* 5.3, pp. 303–310. DOI: 10.1007/BF01228432 (cit. on pp. 86, 87).

Brouwer, Dirk (1959). "Solution of the Problem of Artificial Satellite Theory without Drag." In: *The Astronomical Journal* 64, p. 378. DOI: 10.1086/107958 (cit. on p. 96).

Case, Kelley, Gerhard Kruizinga, and Sien-Chong Wu (2010). *GRACE Level 1B Data Product User Handbook*. URL: ftp://podaac.jpl.nasa.gov/allData/grace/docs/Handbook_1B_v1.3.pdf (visited on 2014-07-22) (cit. on p. 107).

Danielson, Donald A. et al. (1995). *Semianalytic Satellite Theory*. Monterey, CA, USA: Naval Postgraduate School. URL: http://hdl.handle.net/10945/24428 (visited on 2015-06-12) (cit. on pp. 86, 87).

Desai, Shailen D. (2002). "Observing the Pole Tide with Satellite Altimetry." In: *Journal of Geophysical Research* 107.C11. DOI: 10.1029/2001JC001224 (cit. on p. 49).

Diebel, James (2006). *Representing Attitude: Euler Angles, Unit Quaternions, and Rotation Vectors*. URL: https://www.astro.rug.nl/software/kapteyn/_downloads/attitude.pdf (visited on 2018-07-04) (cit. on p. 103).

Dobslaw, Henryk et al. (2014). *Updating ESA's Earth System Model for Gravity Mission Simulation Studies: 1. Model Description and Validation*. Scientific Technical Report STR14/07. DOI: 10.2312/GFZ.b103-14079 (cit. on p. 15).

Drinkwater, M. R. et al. (2003). "GOCE: ESA's First Earth Explorer Core Mission." In: *Earth Gravity Field from Space — From Sensors to Earth Sciences*. Ed. by G. Beutler et al. Vol. 18. Space Sciences Series of ISSI. Dordrecht, Netherlands: Kluwer Academic Publishers, pp. 419–432. DOI: 10.1007/978-94-017-1333-7_36 (cit. on p. 96).

Ellmer, Matthias and Torsten Mayer-Gürr (2017). "High Precision Dynamic Orbit Integration for Spaceborne Gravimetry in View of GRACE Follow-On." In: *Advances in Space Research* 60.1, pp. 1–13. DOI: 10.1016/j.asr.2017.04.015 (cit. on pp. 29, 79).

Encke, Johann Franz (1852). "Über eine neue Methode der Berechnung der Planetenstörungen." In: *Astronomische Nachrichten* 33.26. In german, pp. 377–398. DOI: 10.1002/asna.18520332602 (cit. on pp. 2, 81, 83).

Encke, Johann Franz (1857). "Über die allgemeinen Störungen der Planeten." In: *Berliner astronomisches Jahrbuch*. Vol. 82. In german. Ferd. Dümmler's Verlag, pp. 319–397 (cit. on p. 83).

Escobal, P. R. (1966). "Non-Two-Body Reference Orbit for Encke's Method." In: *AIAA Journal* 4.5, pp. 930–932. DOI: 10.2514/3.3573 (cit. on pp. 84, 96).

Etten, Wim van (2006). *Introduction to Random Signals and Noise*. OCLC: ocm61859925. John Wiley & Sons. 255 pp. ISBN: 978-0-470-02411-9 (cit. on pp. 61, 63).

Flechtner, Frank (2010). *GRACE Science Data System Monthly Report June 2010*. GFZ. URL: ftp://podaac.jpl.nasa.gov/allData/grace/docs/newsletters/GRACE_SDS_NL_1006.pdf (visited on 2018-03-07) (cit. on pp. 74, 116).

Flechtner, Frank (2012). "Status of the GRACE Follow-on Mission." Joint GSTM / SPP Final Colloquium (Potsdam). URL: https://media.gfz-potsdam.de/gfz/sec12/GSTM-2012/GSTM2012-A1.zip (visited on 2018-07-04) (cit. on p. 95).

Flechtner, Frank (2016). *GRACE Science Data System Monthly Report November 2016*. GFZ. URL: ftp://podaac.jpl.nasa.gov/allData/grace/docs/newsletters/GRACE_SDS_NL_1611.pdf (visited on 2018-03-07) (cit. on p. 136).

Flechtner, Frank, Henryk Dobslaw, and Elisa Fagiolini (2014). *AOD1B Product Description Document for Product Release 05*. Rev. 4.2. URL: ftp://podaac.jpl.nasa.gov/allData/grace/docs/AOD1B_20140520.pdf (visited on 2014-07-22) (cit. on p. 49).

Folkner, William M., James G. Williams, and Dale H. Boggs (2008). "The Planetary and Lunar Ephemeris DE 421." In: *The Interplanetary Network Progress Report*. 42 178, pp. 1–34. URL: https://ipnpr.jpl.nasa.gov/progress_report/42-178/178C.pdf (visited on 2018-07-04) (cit. on p. 49).

Förstner, Wolfgang (1979). "Ein Verfahren zur Schätzung von Varianz-und Kovarianzkomponenten." In: *Allgemeine Vermessungsnachrichten* 86.11-12. In german, pp. 446–453 (cit. on p. 11).

Friis-Christensen, Eigil, H. Lühr, and Gauthier Hulot (2006). "Swarm: A Constellation to Study the Earth's Magnetic Field." In: *Earth, planets and space* 58.4, pp. 351–358. DOI: 10.1186/BF03351933 (cit. on p. 96).

Frommknecht, Björn (2008). *Integrated Sensor Analysis of the GRACE Mission*. Vol. 617. Dissertationen C. München: Deutsche Geodätische Kommision bei der Bayerischen Akademie der Wissenschaften. ISBN: 3 7696 5056 5 (cit. on p. 17).

Golub, Gene H. and Charles F. van Loan (1980). "An Analysis of the Total Least Squares Problem." In: *SIAM Journal on Numerical Analysis* 17.6, pp. 883–893. DOI: 10.1137/0717073 (cit. on pp. 119, 120, 122).

GRACE (2001). *GRACE Level 1B JPL Release 2.0*. Dataset. DOI: 10.5067/GRJPL-L1B02 (cit. on p. 41).

GRACE (2018). *GRACE Level 1B JPL Release 3.0*. Dataset. URL: https://podaac.jpl.nasa.gov/dataset/GRACE_L1B_GRAV_JPL_RL03 (visited on 2018-06-01) (cit. on pp. 41, 154, 155).

Harvey, Nate (2016). "GRACE Star Camera Noise." In: *Advances in Space Research* 58.3, pp. 408–414. DOI: 10.1016/j.asr.2016.04.025 (cit. on pp. 132, 137).

Heinzel, Gerhard et al. (2012). "Laser Ranging Interferometer for GRACE Follow-On." In: *Journal of Geodesy* 86.12, pp. 1083–1095. DOI: 10.1007/s00190-012-0566-3 (cit. on pp. 80, 95).

Herman, J et al. (2004). "Attitude Control for GRACE the First Low-Flying Satellite Formation." In: *Proceedings of the 18th International Symposium on Space Flight Dynamics*. Munich, Germany: Jointly organised by DLR/ESOC, p. 6. URL: www.issfd.org/ISSFD_2004/papers/P0106.pdf (visited on 2018-07-04) (cit. on p. 45).

Higham, Nicholas J. (2002). *Accuracy and Stability of Numerical Algorithms*. 2nd ed. Philadelphia: Society for Industrial and Applied Mathematics. 680 pp. ISBN: 0-89871-521-0 (cit. on p. 67).

Hofmann-Wellenhof, B. and Helmut Moritz (2005). *Physical Geodesy*. 1st ed. Wien; New York: Springer. 403 pp. ISBN: 978-3-211-23584-3 (cit. on p. 17).

Horwath, Martin et al. (2011). "Improved GRACE Science Results after Adjustment of Geometric Biases in the Level-1B K-Band Ranging Data." In: *Journal of Geodesy* 85.1, pp. 23–38. DOI: 10.1007/s00190-010-0414-2 (cit. on pp. 137, 140, 152).

Huang, T.-Y. and K. A. Innanen (1983). "The Accuracy Check in Numerical Integration of Dynamical Systems." In: *The Astronomical Journal* 88, pp. 870–876. DOI: 10.1086/113374 (cit. on p. 88).

Hutchinson, M.F. (1990). "A Stochastic Estimator of the Trace of the Influence Matrix for Laplacian Smoothing Splines." In: *Communications in Statistics - Simulation and Computation* 19.2, pp. 433–450. DOI: 10.1080/03610919008812866 (cit. on p. 68).

Ilk, Karl Heinz (1983). *Ein Beitrag zur Dynamik ausgedehnter Körper: Gravitationswechselwirkung*. Vol. 288. Dissertationen C. In german. München: Deutsche Geodätische Kommision bei der Bayerischen Akademie der Wissenschaften. 181 pp. ISBN: 978-3-7696-9338-6 (cit. on p. 52).

Inácio, Pedro et al. (2015). "Analysis of Star Camera Errors in GRACE Data and Their Impact on Monthly Gravity Field Models." In: *Journal of Geodesy* 89.6, pp. 551–571. DOI: 10.1007/s00190-015-0797-1 (cit. on p. 111).

Jekeli, Christoph (1981). *Alternative Methods to Smooth the Earth's Gravity Field*. Columbus, Ohio, USA: Department of Civil and Environmental Engineering and Geodetic Science, The Ohio State University. URL: http://hdl.handle.net/2060/19820014947 (visited on 2017-07-04) (cit. on p. 20).

Jezewski, D. J. (1983a). "A Noncanonical Analytic Solution to theJ 2 Perturbed Two-Body Problem." In: *Celestial Mechanics* 30.4, pp. 343–361. DOI: 10.1007/BF01375505 (cit. on p. 96).

Jezewski, D. J. (1983b). "An Analytic Solution for the J2 Perturbed Equatorial Orbit." In: *Celestial Mechanics* 30.4, pp. 363–371. DOI: 10.1007/BF01375506 (cit. on p. 96).

Kim, Jeongrae and Byron D. Tapley (2002). "Error Analysis of a Low-Low Satellite-to-Satellite Tracking Mission." In: *Journal of Guidance, Control, and Dynamics* 25.6, pp. 1100–1106. DOI: 10.2514/2.4989 (cit. on p. 27).

Kirschner, Michael, Oliver Montenbruck, and Srinivas V. Bettadpur (2001). "Flight Dynamics Aspects of the GRACE Formation Flying." In: *2nd International Workshop on Satellite Constellations and Formation Flying*, pp. 19–20. URL: http://citeseerx.ist.psu.edu/viewdoc/download?doi=10.1.1.556.3828&rep=rep1&type=pdf (cit. on p. 27).

Klinger, Beate (2018). "A Contribution to GRACE Time-Variable Gravity Field Recovery: Improved Level-1B Data Pre-Processing Methodologies." Dissertation. Graz University of Technology (cit. on pp. 41, 43, 47, 54).

Klinger, Beate and Torsten Mayer-Gürr (2016). "The Role of Accelerometer Data Calibration within GRACE Gravity Field Recovery: Results from ITSG-Grace2016." In: *Advances in Space Research* 58.9, pp. 1597–1609. DOI: 10.1016/j.asr.2016.08.007 (cit. on p. 44).

Klinger, Beate, Torsten Mayer-Gürr, et al. (2016). "The New ITSG-Grace2016 Release." In: *EGU General Assembly*. Vienna. URL: http://dx.doi.org/10.13140/RG.2.1.1856.7280 (visited on 2016-07-05) (cit. on p. 93).

Koch, Karl-Rudolf (1997). *Parameterschätzung und Hypothesentests in linearen Modellen*. In german. Bonn: Dümmler. ISBN: 978-3-427-78923-9 (cit. on pp. 7, 119).

Kurtenbach, Enrico (2011). "Entwicklung eines Kalman-Filters zur Bestimmung kurzzeitiger Variationen des Erdschwerefeldes aus Daten der Satellitenmission GRACE." In german. Dissertation. Bonn: Friedrich-Wilhelms-Universität (cit. on pp. 54, 76).

Kusche, Jürgen (2007). "Approximate Decorrelation and Non-Isotropic Smoothing of Time-Variable GRACE-Type Gravity Field Models." In: *Journal of Geodesy* 81.11, pp. 733–749. DOI: 10.1007/s00190-007-0143-3 (cit. on p. 141).

Kvas, Andreas (2014). "Estimation of Short- and Long-Term Temporal Variations in Earth's Gravity Field from GRACE Data in a Combined Least Squares Adjustment."

Master's thesis. Graz: Graz University of Technology. URL: https://pure.tugraz.at/portal/files/16893989/2014_Kvas_GR (cit. on pp. 56, 76).

Kyner, W. F. and M. M. Bennett (1966). "Modified Encke Special Perturbation Method." In: *The Astronomical Journal* 71, p. 579. DOI: 10.1086/109965 (cit. on pp. 84, 96).

Lenzmann, Lothar and Enno Lenzmann (2004). "Strenge Auswertung des nichtlinearen Gauß-Helmert-Modells." In: *AVN* 2.2004. In german (cit. on p. 119).

Liu, Lin and Song-jie Hu (1997). "On the Choice and Rectification of Reference Orbit in the Modified Encke's Method." In: *Chinese Astronomy and Astrophysics* 21.1, pp. 118–126. DOI: 10.1016/S0275-1062(97)00015-5 (cit. on p. 84).

Lundberg, John B., Srinivas V. Bettadpur, and R. J. Eanes (2000). "Long Arc Orbit Determination Solutions Using Encke's Method." In: *Applied mathematics and computation* 113.1, pp. 43–53. DOI: 10.1016/S0096-3003(99)00086-7 (cit. on pp. 84, 89).

Lundberg, John B., B. E. Schutz, et al. (1990). "The Application of Encke's Method to Long Arc Orbit Determination Solutions." In: *AAS/AIAA Astrodynamics Conference 1989*. Stowe, VT, United States. URL: http://ntrs.nasa.gov/search.jsp?R=19900059778 (visited on 2015-06-03) (cit. on p. 84).

Mallat, S. G. (2009). *A Wavelet Tour of Signal Processing: The Sparse Way*. 3rd ed. Amsterdam; Boston: Elsevier/Academic Press. 805 pp. ISBN: 978-0-12-374370-1 (cit. on p. 114).

Mayer-Gürr, Torsten (2006). "Gravitationsfeldbestimmung aus der Analyse kurzer Bahnbögen am Beispiel der Satellitenmissionen CHAMP und GRACE." In german. Dissertation. Bonn: Friedrich-Wilhelms-Universität. URL: http://dgk.badw.de/fileadmin/docs/c-675.pdf (visited on 2013-07-31) (cit. on pp. 12, 18, 31, 35).

Mayer-Gürr, Torsten, Saniya Behzadpour, et al. (2016). *ITSG-Grace2016 - Monthly and Daily Gravity Field Solutions from GRACE*. Dataset. DOI: 10.5880/icgem.2016.007 (cit. on p. 93).

Mayer-Gürr, Torsten, Andreas Kvas, et al. (2015). "The New Combined Satellite Only Model GOCO05s." EGU General Assembly (Vienna) (cit. on pp. 49, 88).

Milani, Andrea and Anna M. Nobili (1987). "Integration Error over Very Long Time Spans." In: *Celestial mechanics* 43.1, pp. 1–34. DOI: 10.1007/BF01234550 (cit. on pp. 84, 97).

Montenbruck, Oliver and Eberhard Gill (2000). *Satellite Orbits*. Springer-Verlag Berlin Heidelberg New York. 369 pp. ISBN: 978-3-642-58351-3 (cit. on p. 29).

NASA (2002). *GRACE Launch Press Kit*. URL: https://www.jpl.nasa.gov/news/press_kits/gracelaunch.pdf (visited on 2018-07-05) (cit. on p. 24).

Neitzel, Frank and Svetozar Petrovic (2008). "Total Least Squares im Kontext der Ausgleichung nach kleinsten Quadraten am Beispiel der ausgleichenden Geraden." In: *ZfV* 133. In german, pp. 141–148. URL: https://www.geodesy.tu-berlin.de/fileadmin/fg261/Publikationen/Neitzel_Petrovic_zfv_3_2008.pdf (visited on 2016-09-20) (cit. on p. 122).

Niemeier, Wolfgang (2008). *Ausgleichungsrechnung: statistische Auswertemethoden*. In german. Berlin: De Gruyter. ISBN: 978-3-11-019055-7 (cit. on pp. 7, 9, 10, 119).

Petit, Gérard and Brian Luzum, eds. (2010). *IERS Conventions (2010)*. Frankfurt am Main: Verlag des Bundesamts für Kartographie und Geodäsie. 179 pp. ISBN: 3-89888-989-6 (cit. on pp. 16, 25, 49).

Rao, K. Ramamohan and P. C. Yip (1990). *Discrete Cosine Transform: Algorithms, Advantages, Applications*. Boston: Academic Press. 490 pp. ISBN: 978-0-12-580203-1 (cit. on p. 63).

Reinking, Jörg (2008). "Total Least Squares." In: *ZfV* 133. In german, pp. 384–389. URL: http://geodaesie.info/system/files/privat/zfv_2008_6_Reinking.pdf (visited on 2016-02-26) (cit. on pp. 119, 121–124, 127, 128, 152, 154).

Romans, L (2003). *Optimal Combination of Quaternions from Multiple Star Cameras*. Memorandum. JPL. URL: ftp://podaac.jpl.nasa.gov/allData/grace/docs/quaternion_memo.pdf (visited on 2018-07-05) (cit. on p. 46).

Rosenblatt, Murray (1956). "Remarks on Some Nonparametric Estimates of a Density Function." In: *The Annals of Mathematical Statistics* 27.3, pp. 832–837. DOI: 10.1214/aoms/1177728190 (cit. on p. 107).

Savcenko, Roman et al. (2012). *EOT11a - Global Empirical Ocean Tide Model from Multi-Mission Satellite Altimetry*. Dataset. DOI: 10.1594/PANGAEA.834232 (cit. on p. 49).

Schaffrin, Burkhard (2007). "Connecting the Dots: The Straight-Line Case Revisited." In: *ZfV* 132.06/2007, p. 10 (cit. on p. 119).

Sheard, B. S. et al. (2012). "Intersatellite Laser Ranging Instrument for the GRACE Follow-on Mission." In: *Journal of Geodesy* 86.12, pp. 1083–1095. DOI: 10.1007/s00190-012-0566-3 (cit. on p. 79).

Sneeuw, Nicolaas (2000). "A Semi-Analytical Approach to Gravity Field Analysis from Satellite Observations." Dissertation. Technische Universität München. URL: http://tumb1.biblio.tu-muenchen.de/publ/diss/bv/2000/sneeuw.html (visited on 2013-07-31) (cit. on p. 76).

Snow, Kyle (2012). "Topics in Total Least-Squares Adjustment within the Errors-In-Variables Model: Singular Cofactor Matrices and Prior Information." Dissertation. Columbus, Ohio, USA: Ohio State University. URL: http://hdl.handle.net/1811/78619 (visited on 2018-07-05) (cit. on p. 119).

Stanton, Richard et al. (1998). *GRACE Science & Mission Requirements Document*. URL: https://geodesy.geology.ohio-state.edu/course/refpapers/Grace_smrd.pdf (visited on 2018-07-05) (cit. on p. 23).

Swenson, Sean and John Wahr (2006). "Post-Processing Removal of Correlated Errors in GRACE Data." In: *Geophysical Research Letters* 33.8. DOI: 10.1029/2005GL025285 (cit. on pp. 20, 141).

Tapley, Byron D. et al. (2004). "The Gravity Recovery and Climate Experiment: Mission Overview and Early Results." In: *Geophysical Research Letters* 31.9. DOI: 10.1029/2004GL019920 (cit. on p. 23).

Vallado, David Anthony and Wayne D. McClain (2001). *Fundamentals of Astrodynamics and Applications*. 2. ed. 12. OCLC: 248390162. Dordrecht: Kluwer Academic Publishers. 958 pp. ISBN: 978-1-881883-12-8 978-0-7923-6903-5 (cit. on p. 86).

Van der Vorst, H. A. (1992). "Bi-CGSTAB: A Fast and Smoothly Converging Variant of Bi-CG for the Solution of Nonsymmetric Linear Systems." In: *SIAM Journal on Scientific and Statistical Computing* 13.2, pp. 631–644. DOI: 10.1137/0913035 (cit. on p. 38).

Van Dam, Tonie and R. D. Ray (2010). *S1 and S2 Atmospheric Tide Loading Effects for Geodetic Applications*. Dataset. URL: http://geophy.uni.lu/ggfc-atmosphere/tide-loading-calculator.html (visited on 2015-03-17) (cit. on p. 49).

Wahr, John, Mery Molenaar, and Frank Bryan (1998). "Time Variability of the Earth's Gravity Field: Hydrological and Oceanic Effects and Their Possible Detection Using GRACE." In: *Journal of Geophysical Research: Solid Earth* 103.B12, pp. 30205–30229. DOI: 10.1029/98JB02844 (cit. on p. 18).

Wen, Hui Ying et al. (2018). *GRACE Follow-On Level-1 Data Product User Handbook*. URL: ftp://podaac-ftp.jpl.nasa.gov/allData/gracefo/docs/Level1DataProductUserHandbook.pdf (visited on 2018-06-18) (cit. on p. 154).

Wu, Sien-Chong, Gerhard Kruizinga, and Willy Bertiger (2006). *Algorithm Theoretical Basis Document for GRACE Level-1B Data Processing V1. 2*. URL: ftp://podaac-ftp.jpl.nasa.gov/GeodeticsGravity/grace/L1B/JPL/RL02/docs/ATBD_L1B_v1.2.pdf (visited on 2014-07-22) (cit. on p. 27).

Zehentner, Norbert (2017). "Kinematic Orbit Positioning Applying the Raw Observation Approach to Observe Time Variable Gravity." Dissertation. URL: https://graz.pure.elsevier.com/en/publications/kinematic-orbit-positioning-applying-the-raw-observation-approach (visited on 2018-07-05) (cit. on p. 43).

Zehentner, Norbert and Torsten Mayer-Gürr (2016). "Precise Orbit Determination Based on Raw GPS Measurements." In: *Journal of Geodesy* 90.3, pp. 275–286. DOI: 10.1007/s00190-015-0872-7 (cit. on pp. 29, 43).